UNIVERSITÀ DEGLI STUDI DI PADOVA

Dipartimento di Fisica e Astronomia "Galileo Galilei"

Master Degree in Astrophysics and Cosmology

Final dissertation

Studying Near Earth Asteroids in the context of the European Project Neorocks: a focus on the Binary Asteroid Didymos, the Target of the DART/HERA Missions

Thesis supervisor

Prof. Monica Iazzarin

Thesis co-supervisor

Dr. Fiorangela La Forgia

Dr. Paolo Ochner

Candidate

Andrea Farina

Academic Year 2023/24

"I speak to the star sometimes.

They don't talk back, but they listen."

Abstract

Near-Earth Objects (NEOs) are asteroids and comets whose trajectory can pass within 1.3 AU of the Sun. (65803) Didymos is a binary asteroid, whose moon (Dimorphos) was struck by the Double Asteroid Redirection Test (DART) spacecraft. The DART is a planetary defense demonstration mission by NASA's Planetary Defense Coordination Office (PDCO) to prove the effectiveness of the kinetic impactor technique in the event of a small asteroid approaching Earth. Following the impact, the revolution period of Dimorphos is 11.372 ± 0.017 (3σ) hours, with a period variation of -33.0 ± 1.0 (3σ) minutes. In this study, I conducted spectroscopic analysis of the Didymos system after the DART impact between 18^{th} October 2022 and 27^{th} December 2022, using spectra obtained by the Copernico and Galileo Telescopes located at the Astronomical Observatory of Asiago. The Didymos system is classified as S-type according to the Bus and DeMeo taxonomy. No variation in the spectral slope of the spectra was found during a full rotation of Didymos system approximately 19 days after the impact of DART. Additionally, I present the analysis of 49 NEOs collected by the Asiago telescope between December 2019 and March 2024 for the NEOROCKs project. The NEOs were taxonomically classified according to the Bus and DeMeo and Mahkle taxonomies. My results were compared with various works in the literature.

Keywords: NEOs ; Didymos ; DART; NEOROCKS

Contents

List of Tables

List of Figures

Glossary

AFP Asteroid Family Portal.

AIM Asteroid Impact Mission.

AU Astronomical Unit.

BIM Backward Integration Method.

BYORP Binary YORP.

CCD Charge-Coupled Device.

CRE Cosmic-Ray Exposure.

DRACO Didymos Reconnaissance and Asteroid Camera for Optical navigation.

ECA Earth-Crossing Asteroid.

ECAS Eight-Colour Asteroid Survey.

EVF Ejection Velocity Field.

HCM Hierarchical Clustering Method.

IMB Inner Main Belt.

IRAF Image Reduction and Analysis Facility.

IRAS Infrared Astronomical Satellite.

m.y. million years.

MBA Main Belt Asteroids.

MC Mars Crossers.

MITHNEOS MITHawaii Near-Earth Object Spectroscopic Survey.

ML Machine Learning-based.

MMB Middle Main Belt.

NEA Near-Earth Asteroid.

NEC Near-Earth Comet.

NEO Near-Earth Object.

OMB Outer Main Belt.

PCA Principal Component Analysis.

PHA Potentially Hazardous Asteroid.

PHO Potentially Hazardous Object.

PPCA Probabilistic PCA.

S3OS2 Small Solar System Objects Spectroscopic Survey.

SMASSI Small Main-Belt Asteroid Spectroscopic Survey Phase I.

SMASSII Small Main-Belt Asteroid Spectroscopic Survey Phase II.

SsODNet3 Solar System Open Database Network.

TA Trojan Asteroid.

ToO Target of Opportunity.

WISE Wide Field Infrared Survey Explorer.

YORP Yarkovsky-O'Keefe-Radzievskii-Paddack.

Introduction

Asteroids are relatively small objects, ranging from a few meters to hundreds of kilometers in diameter, and comets are celestial bodies mainly composed of ice, dust, and rocks, exhibiting long tails when they approach the Sun. Unlike comets, asteroids do not exhibit activities such as the release of dust, gases, or small particles. Asteroids are residuals from the primordial material and planetesimals that did not build planets during the formation of the Solar System. This thesis work focuses on the study of near-Earth objects (NEOs), which include asteroids and comets whose trajectory can pass within 1.3 AU of the Sun. Specifically, my study is concentrated on near-Earth asteroids (NEAs). It is important to note that this does not mean that NEOs are continuously close to the Earth, but rather that their motion occasionally brings them close to the Sun and potentially close to the Earth. Studying NEOs is crucial due to the potential danger they represent to the Earth's population. Therefore, studying their orbits and sizes is crucial in order to calculate the probability of a collision with our planet. Some of them are remnants of planetesimals that led to the formation of planets, making them crucial for the study of the origin and evolution of the Solar System. Another important reason to study NEOs is their proximity to Earth, which helps us understand the possibility that they brought the water and organic-rich material to early Earth. This allows for a description of the formation of life on Earth from a dynamic and physical point of view, studying NEOs is also fundamental in assessing the orbital evolution of small bodies in the context of gravitational perturbations from major planets and YORP, Yarkovsky, and space weathering effects. Potentially hazardous asteroids (PHAs) are NEAs that cross a minimum distance of 0.05 AU (which constitutes about 7.5 million km) from Earth and have an absolute magnitude H not exceeding 22 mag.

Spectroscopy is an important tool for studying the surface composition of NEAs, in fact, the mineral grains on the surface of the asteroid absorb or scatter sunlight. The spectrum can have different slopes/features depending on the physical and optical properties of these grains. From the early years of studying NEOs, several surveys have been conducted to collect various spectro-photometric data. Some of the most important surveys include the Eight-Colour Asteroid Survey, developed in the mid-1980s, which is based on spectrophotometric imaging of 600 asteroids; the Small Main-Belt Asteroid Spectroscopic Survey Phase II (SMASSII), which consists of 1447 observed asteroids; and the Small Solar System Objects Spectroscopic Survey (S3OS2), which consists of 800 observed asteroids. Thanks to these surveys, the largest taxonomic classifications of asteroids have been developed: Tholen's classification, Bus and Binzel's, Bus and DeMeo's, and Mahkle's.

This thesis work is divided into four main chapters. The first chapter provides general information on the characteristics of asteroids, NEOs, and the importance of resonances as the main causes of NEO formation (3:1 mean motion and ν_6 resonances with Jupiter are the main resonances that give rise to NEOs from the Main Belt). It also covers the significance of the Yarkovsky and YORP effects. The second chapter provides an overview of asteroid spectroscopy, including taxonomic classifications and the importance of asteroid families and their relationship to NEOs.

The main objective of this thesis is described in chapters 3 and 4. During my research, I observed several NEAs using the Copernico and Galileo telescopes at the Asiago Astrophysical Observatory. A specific observational strategy was followed, with a preference for PHAs due to their higher risk of impact on Earth. The observation of NEAs was followed by data reduction and analysis. Collecting data is important for adding information about NEAs in various existing surveys. Specifically, taxonomic classification is essential for understanding the surface composition of NEAs and, together with their dimensions, the potential damage they could cause in the event of impact on our planet.

In my thesis study, I had the opportunity to investigate the Didymos binary system, whose satellite was struck by the Double Asteroid Redirection Test (DART) spacecraft. DART is a planetary defense demonstration mission managed by NASA's Planetary Defense Coordination Office (PDCO). The main goal of the mission is the impact of DART on Dimorphos, the satellite of (65803) Didymos. The launch took place on 24 November 2021 and the impact on Dimorphos occurred on 26 September 2022 at 23.14 UT. The aim of the DART mission is to demonstrate that the kinetic impactor is a successful technique to deviate for planetary defence in the case of a small asteroid approaching Earth. In addition, the Italian Space Agency (ASI) integrated DART with a 6U CubeSat named the Light Italian CubeSat for Imaging of Asteroids (LICIACube). LICIACube provided documentation of the impact of DART and its immediate consequences.

On 26 September 2022 at 23:14 UT, DART impacted Dimorphos at a velocity of 6.6 km/s, giving it a large momentum in a range of 2.2 and 4.9. On 11 October 2022, NASA announced that the DART impact had reduced Dimorphos' orbital period by 32 minutes, according to ground observations. In conclusion, they determined a post-impact period of 11.372 ± 0.017 (3σ) hours with a period variation of -33.0 ± 1.0 (3σ) minutes.

In chapter 3, I described the study and analysis of data from the Didymos-Dimorphos binary system after the DART space mission. My analysis is based on the spectroscopic study of the Didymos binary system in the days and months following the impact of DART. Observations were made between October 18^{th}, 2022 and December 27^{th}, 2022 using two telescopes: the Copernico 1.82 m telescope (INAF Astronomical Observatory of Padova, situated atop Mount Ekar) and the Galileo 1.22 m telescope, both located in Asiago, Italy. My studies have been compared with other observations performed before and after the impact of DART. Didymos has various taxonomic classifications in the literature. The impact of DART on Dimorphos has allowed to study the internal composition of an asteroid and the spectral evolution of the ejecta. My goal was to taxonomically classify the Didymos system after the impact of DART and spectroscopically study an entire rotation of Didymos to determine if there were any variations in the spectral slope due to the dust ejected from the impact with Dimorphos. The third chapter includes also a study on the importance of the orientation of the spectrograph slit along the atmospheric refraction of the target studied at different angular positions from the observatory's zenith. My conclusions and those of other researchers will be compared/confirmed of the future HERA space mission, developed as part of the European Space Agency's (ESA) Space Security Programme. The Hera mission will arrive at the end of January or early February 2027, at the Didymos system to study its subsurface, interior properties and the study of the possible crater formed by DART. In addition, the result of the kinetic impactor test will be measured, providing valuable information for the development of techniques for planetary defense, mining extraction, and scientific purposes. The planetary defence programme has boosted the study of NEOs, in particular their physical and dynamical properties. Therefore, it is crucial to determine the orbit of a NEO to assess the probability of impact on our planet, its chemical composition and its physical properties in order to predict the impact on Earth and the possible crater it could form. For this reason, several projects have developed to survey NEOs. Due to new ground-based telescopes, a large amount of data on NEOs is being collected, leading to the need for different follow-upprograms/projects to study the physical properties of NEOs. These programs must ensure access to their long-term archiving for everyone, as well as maintain and evolve the corresponding data products. The NEO Rapid Observation, Characterization and Key Simulations (NEOROCKS) Collaborative Research Project is an EU-funded project started in January 2020 to address the topic "Improvement of our knowledge of the physical characteristics of the NEO population". NEOROCKs aims to improve our understanding of the physical characteristics, origin, and evolution of NEOs for planetary defense.

Chapter 4 introduces the NEOROCKS project and its objectives. The second part of the chapter describes my contribution to this project. My data collection is based on the acquisition and analysis of five years of observations made with the Asiago telescopes mentioned above. The observational campaign began in December 2019 and is still ongoing as of 12 March 2024. My work is based on analysing data from 49 NEOs and classifying them taxonomically according to the Bus and DeMeo and Mahkle taxonomy. I also conducted a data analysis by comparing our results with various works in the literature. The observational campaign will continue for another two years with the aim of classifying and studying as many NEOs as possible to contribute to the planetary defence programme of our planet.

Chapter 1

The Asteroids

The first 200 million years (m.y.) after the formation of the Solar System were not preserved on any planet due to geological processes such as erosion, metamorphism, and remelting. The study of asteroids and meteorites enables us to reconstruct what happened in the earlier phases of the formation of the Solar System. The Solar System was formed approximately 4.56 m.y. ago from a protoplanetary disk made up of dust and gas surrounding our star. Small objects were formed from material and planetesimals that did not form planets: these objects became the asteroid population.

Asteroids are crucial components of the Solar System's and Earth's history; however, they also represent a danger to our planet because they occasionally come close to Earth and their fall can cause destruction or mass extinctions such as the one that happened to the dinosaurs 65 m.y. ago (Chixchulub impact 65 Myr ago, responsible for the K-T mass extinction [27], see fig. 1.1). Following the initial bombardments during the early Solar System formation, the frequency of asteroid impacts on Earth has decreased. Asteroids of a few tens of meters in size fall once a century and cause little damage. For instance, the impacts with asteroids that occurred in Chelyabinsk in 2013 led to the destruction of an entire city, while the impact in Tunguska in 1908 caused destruction to the forest. The impacts of asteroids hundreds of meters in size occur once every thousand years, whereas the impacts of larger asteroids of several kilometers or more are extremely rare, occurring only once every 80 m.y. Given the number of asteroids that cross the Earth's orbit, their study is of vital importance to better understand their physical properties, their role in the formation of the Solar System and last but not least, to avoid future impacts with our planet [9] (see fig. 1.2).

1.1 General Characteristics of Asteroids

The Solar System's small body population includes asteroids, comets, and meteoroids formed by the destruction of these objects [28]. Asteroids are relatively small, ranging from a few meters to hundreds of kilometers in diameter. They lack an atmosphere and are made up of metals and rocks. Otherwise comets, asteroids do not exhibit the release of dust, gases, or meteoroids, among other activities [29]. The Solar System has two primary asteroid belts: the Main Belt located between 2 and 4 Astronomical Units (AU), and the Kuiper belt situated beyond Neptune's orbit between 30 and 50 AU. The Kuiper belt contains a variety of small objects, such as comets, asteroids, and remnants from the formation of the solar system. The Main Belt consists of asteroids ranging in size from 1 meter to 1000 km (like

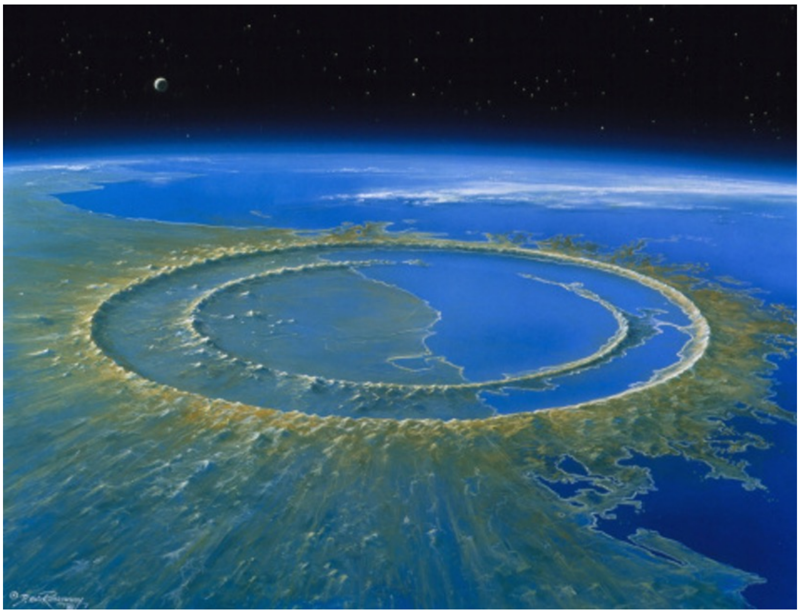

Figure 1.1: around 66 m.y. ago, a massive asteroid, with a diameter of fourteen kilometers, crashed into the Caribbean region, causing a catastrophic incident that severely affected life on our planet and resulted in the extinction of the dinosaurs. Presently, the impact location, which is a crater spanning 200 kilometers, is concealed under 600 meters of sediment beneath the Caribbean Sea. Figure taken from https://craterexplorer.ca

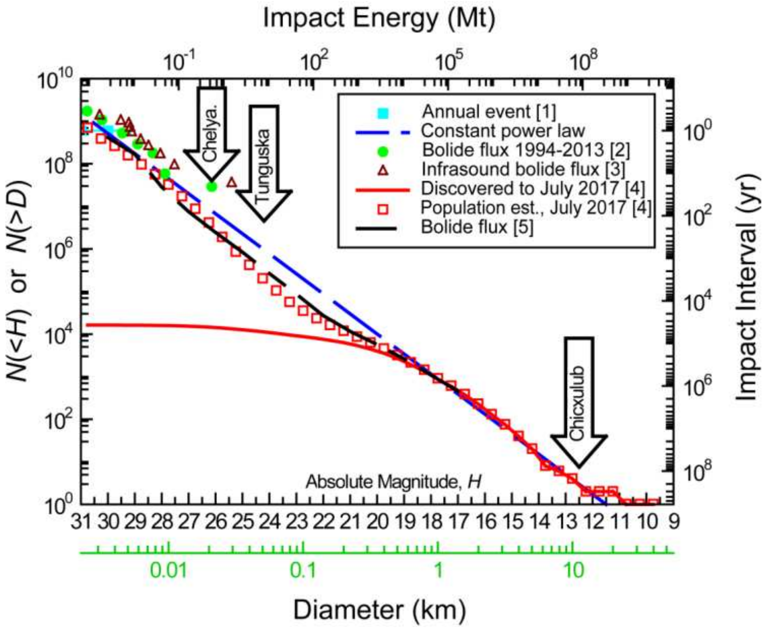

Figure 1.2: cumulative NEO population estimate from various surveys. The numbers in brackets correspond to the following references: [1] Brown et al. [4]; [2] Boslough et al. [5]; [3] Silber et al. [6]; [4] Stokes et al. [7]; [5] Tricarico [8]. Chelya in the arrow on the far left stands for Chelyabinsk. Figure taken from Silber (2018) [9].

Ceres). They complete one orbit around the Sun in 3 to 10 years on a slightly elliptical orbit with a small inclination to the ecliptic plane and in the same direction as Earth [28]. In 1801, Giuseppe Piazzi discovered the first asteroid: Ceres (now classified as a dwarf planet). Pallas, located around the same orbital distance, was the second asteroid discovered.
On the other hand, comets are active small bodies in the Solar System. Whipple identified comets as conglomerates of frozen gas and dust. As comets move closer to the Sun, some of their gases evaporate to form a coma and tail. Asteroids and comets have been established to have formed generally from different sources according to their internal composition [28] despite there are serveral transition objecta and possibile overlapping populations.
As of 12 March 2024 there are 1350492 asteroids and 4581 comets (https://www.minorplanetcenter.net/mpc/summary). The regions that contain asteroids are categorized as follows:

- **Near Earth Objects (NEOs)** refer to small bodies that move within proximity of Earth (see Section 1.2.3).
- **Mars Crossers (MC)** refer to objects that cross the orbit of Mars, i.e. bodies whose perihelion lies between the perihelion and aphelion of Mars. In particular, the number of MC is four times greater than the number of NEO population.
- **Main Belt Asteroids (MBA)** are the region between Mars and Jupiter, between 2 and 4.3 AU, where most asteroids are found in the Solar System. Kirkwood gaps are regions created in the Main Belt as a result of Jupiter's influence through orbital resonances (see Section 1.2.1). Consequently, this region is divided into several groups. Hungaria, Inner Main Belt (IMB), Middle Main Belt (MMB), Outer Main Belt (OMB), Cybele and Hilda.
    - **Hungaria** is a dynamic region of asteroids located between 1.8 and 2 AU [30]. The asteroids exhibit high inclination values between 16 and 35 degrees with a low eccentricity, below 0.1. It is separated by the resonance v_6 and the mean motion resonance 4:1 with Jupiter [30]; the name is derived from the asteroid (432) Hungaria. The secular resonance v_6 occurs when the precession frequency of the asteroids longitude of perihelion is equal to the sixth secular frequency of the planetary system [10]. Mean motion resonances occur when the ratio between the orbital period of an asteroid and a planet is close to a ratio of small integers. This happens with Jupiter in the inner Solar System and with Neptune in the outer Solar System.
    - **Inner Main Belt** is a region where asteroids are confined by mean motion resonances 4:1 and 3:1 with Jupiter; and their semimajor axis is between 2.06 and 2.50 AU. Asteroids have an eccentricity below 0.3 and an inclination of less than 15 degrees [31].
    - **Middle Main Belt** asteroids have a semimajor axis ranging from 2.5 to 2.8 AU: these boundaries are delineated between the 3:1 and 5:2 resonances with Jupiter.
    - **Outer Main Belt** refers to the region where asteroids have a semimajor axis between 2.8 and 3.3 AU, and its boundaries are established between the 5:2 and 2:1 mean motion resonances.
    - **Cybele** region is between 3.3 and 3.7 AU and is between 2:1 and 5:3 mean motion resonances with Jupiter [32]. It has a eccentricity of less than 0.3 and an

    inclination of less than 25 degrees. The region takes its name from the asteroid (65) Cybele.

  - **Hilda** asteroids are situated between 3.7 and 4.2 AU and are located in the 3:2 resonance with Jupiter [33]. These asteroids exhibit an eccentricity greater than 0.07 and an inclination less than 20 degrees. The name of the family derived from the asteroid (153) Hilda.

- **Trojan Asteroids (TA)** orbit near the Lagrangian equilibrium points L4 and L5 of the planet and are approximately 60 degrees ahead of and behind the planet on its orbit [34]. The first Trojan asteroid was discovered by Max Wolf around Jupiter and was named (588) Achilles [34]. In 1990, the first Trojan Mars asteroid, named (5261) Eureka, was discovered. The first Neptunian Trojan, identified in 2001, is known as 2001 QR322.

- **Centaurs** are objects that pass through the orbit of the Giant Planets and come from the Kuiper Belt and Scattered Disk (a circumstellar disk populated by small icy objects in the solar system; it is located at a distance of 30-35 AU and can extend beyond 100 AU). Their main gravitational influence is from the gas giants and their satellites [35]. Their location is approximately between 5.4 and 30 (AU), although this distance has not yet been precisely determined.

- **Trans-Neptunian Objects** (TNOs) refer to all celestial bodies located in the Solar System beyond Neptune's orbit, and they are divided into multiple regions. The Kuiper Belt is important for the formation of the Solar System: it is the farthest point where planetesimals can be found [36]. This belt is classified into several components:

  - **Cold component:** is located between 42 and 47 AU. The cold component of the Kuiper belt formed locally and never had a large mass, never exceeding one-tenth of Earth's mass. In the cold component exists objects with almost circular orbits and low inclination. The average diameter of the objects studied is 100 km and most of them are binary [36].
  - **Hot component:** is located between 30 and 35 AU. In the hot component, the planetary disk had a mass of 20-30 Earth masses, able to form a hot belt and a sufficiently populated scattered disk. Objects in the hot population have more eccentric and inclined orbits. These celestial bodies are believed to originate in the inner portion of the planetesimal disk, situated between 15 and 30 AU. Due to the gravitational influence of Neptune, they were forced outward during the migration of Neptune, leading to their instability. The size of the objects observed is generally around 3000 km and they contain less ice compared to the cold population.
  - **Scattered Disk:** extend even further, possibly up to 1000 AU and it is what remains today of the objects that have been scattered by Neptune since the beginning of the Solar System and have not found a stable orbit. Many objects in this population are in mean motion resonance with Neptune and therefore can live on non-encountering orbits for a long time, before going back to scattered dynamics. This disk contains 0.5-1% of the original planetesimals of the trans-Neptunian disk, making this zone very massive compared to other zones around Neptune. However, it is an unstable disk, creating a flow of objects towards the

region of the giant planets such as the Centaurs and towards the interior of the solar system such as the comets of the Jupiter family. Objects in the scattered disk have highly eccentric and inclined orbits, with a perihelion distance of 30-40 AU and aphelion distances reaching several hundred AU [36].

- **Fossilized Scattered Disk:** extend even further, possibly up to 1000 AU and it is a region of the Kuiper Belt that has a similar orbital distribution (a,e) to the scattered disk, but with greater distances from the perihelion, so they are beyond the reach of Neptune's scattering action. These are bodies that were once part of the scattered disk and were then transported to larger semimajor axes by encounters with Neptune. In the fossilized disk they are objects with orbits similar to those of the scattered disk, but formed in the outer part of the planetesimal disk, over 50 AU. They have perihelion distances of 40 AU, and some, like Sedna, have very elongated orbits that take them to distances of thousands of AU. The size distribution closely follows that of the cold population, but with a greater presence of small objects [36].
- **Resonance Objects:** refer to those that were entrapped in mean-motion resonances with Neptune during its migration [36]. The resonances 3:2 (Plutini $\sim$ 39.5 AU), 2:1 (Twotini $\sim$ 47.8 AU) and 5:2 (Cubitini $\sim$ 55.4 AU) are the most populated [36]. Resonance objects have eccentric and inclined orbits, but they are dynamically protected from resonance, which prevents them from approaching Neptune too closely. Their size distribution is similar to the hot population, but they have a higher proportion of larger objects, such as Pluto and Haumea.
- **Oort Cloud:** contains the final trans-Neptunian objects, and it is a spherical cloud comprising comets situated between 2000 and 200000 AU from the Sun. The cometary nuclei exhibit high stability because the Sun's radiation is very weak at this distance.

1.2 Near-Earth Objects

Understanding resonance dynamics is the key to understanding the processes that lead to asteroids becoming NEOs. Prior to the discovery of this effect, it was generally believed that the removal of asteroids from the main asteroid belt could occur only through collisions. These collisions impart an ejecta velocity of $\sim$ 100 m/s, but this is insufficient to achieve planet-crossing orbits [37]. The 3:1 and ν_6 resonances are the main resonances that give rise to NEOs from the Main Belt [38].

1.2.1 The origin of NEOs

J. G. Williams was the first to attribute significant importance to the resonance effects [39]. His work demonstrated that asteroids in close proximity to the ν_6 resonance periodically intersect the orbit of Mars and have secular eccentricity oscillations with an amplitude exceeding 0.25. Furthermore, in 1983, Wisdom [40] has demonstrated that a 3:1 resonance has similar effects: the eccentricity of resonant bodies can have rapid and large oscillations with amplitude exceeding 0.3 for the body to cross the orbit of Mars. Since these discoveries, greater attention was been paid to the 3:1 and ν_6 resonances in the Main Belt as the main sources of NEOs. In 1990, Wheterill used Monte Carlo methods to hypothesize that the resonances of ν_6 and 3:1 are continuously supplied by collisions or catastrophic events that occur in the Main Belt [38]. This ensures that the resonance regions are continuously supplied with enough material to maintain the population of NEO in a steady state. In the following years, a large number of NEOs were discovered and studied through simulations of test particles placed in the NEO region or in transport resonances, over time scales of millions of years. It was immediately observed that NEOs with $a < 2.5$ AU can easily collide with the Sun, reducing their dynamic life to just a few m.y. [38]. Therefore, Monte Carlo methods were insufficient to explain the behavior of NEOs. The development of new numerical integration methods has allowed consideration of a large number of particles in determining the static dynamics of NEOs. These new methods have enabled us to describe the population of NEOs as we know it today.

Orbital resonances refer to a system in which two or more objects orbit the same primary with orbital mean motions in a small number ratio [41]. The resonant effect modifies the eccentricity of the asteroids. There are two forms of resonance: powerful and diffusive. The key difference lies in the fact that powerful resonances exhibit gaps in the Main Belt asteroid distribution. There are numerous diffusive resonances, while the main resonances of the powerful class are the secular resonance ν_6 at the inner edge of the asteroid belt and the mean motion resonance with Jupiter 3:1, 5:2 and 2:1 [10]. The figure 1.3 illustrates the distribution of NEOs, Mars crossers and main belt asteroids in terms of semimajor axis, eccentricity and inclination [10]. It also shows resonances ν_6, 3:1, 5:2, and 2:1.

The secular resonance ν_6 occurs when the asteroid's perihelion longitude precession frequency matches the sixth secular frequency (a long-term orbital oscillation that occurs approximately every six orbital periods, caused by gravitational perturbations in the Solar System) of the planetary system [10]. The latter can be identified with the mean precession frequency of Saturns longitude of perihelion, but it is also relevant in the secular oscillation of the eccentricity of Jupiter. The resonance ν_6 defines the inner limit of the main belt (see fig. 1.3): the first dotted curve represents the resonance ν_6 and its effect decreases with distance. This resonance can be divided into two regions, both 0.04 AU wide: the powerful and the border regions. In the first region, the resonance causes an increase in eccentricity, leading the asteroids towards the orbit of Earth or Venus, and in some cases towards the Sun. The average lifetime of asteroids in the ν_6 resonance is 2 m.y., while the average time to become an Earth-Crossing Asteroid (ECA) is about 0.5 m.y: 80% will collide with the Sun, while 12% will be ejected into a hyperbolic orbit [42].The mean time spent in the NEO region is 6.5 m.y. and the mean probability of a collision with the Earth is about 10^{-2} [43]. In the border region, the resonance effect is small, but it can cause asteroids to cross the orbit of Mars.

The 3:1, 5:2 and 2:1 mean-motion resonances with Jupiter are located at $\sim$ 2.5, 2.8 and 3.28 AU, respectively. The former is divided into two regions: a narrow central and larger border region. Asteroids within the central region periodically cross the orbit of Mars because of regular oscillations in their eccentricity. On the other hand, asteroids in the border region can quickly reach Earth-crossing and even Sun-grazing orbits [44]. A body from the central region can easily cross the border region and quickly enter the NEO region through encounters with Mars. The median time required to cross the orbit of Earth is 1 m.y. and the mean lifetime is 2 m.y.

The 5:2 mean-motion resonance is closest to Jupiter, which causes rapid changes in eccentricity. According to Morbidelli (1993) [45], most of these asteroids are ejected onto a

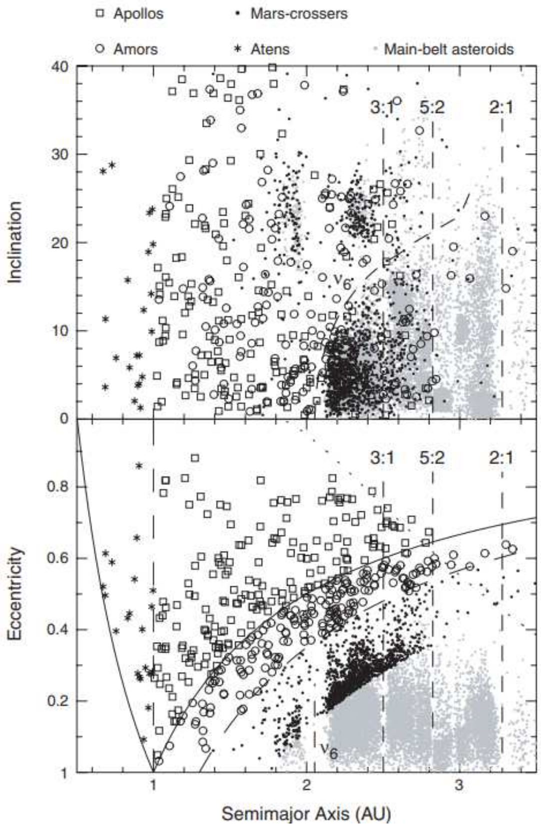

Figure 1.3: illustrates two graphs showing the distribution of NEOs, Mars-belt asteroids and main belt asteroids. The x-axis represents the semimajor axis, while the y-axis represents the inclination. The four main resonances are represented by dotted lines: ν_6, 3:1, 5:2, and 2:1. The legend of the asteroids is located above the figure. In the bottom figure, the solid curve bounds the Earth-crossing region; the dashed curve delimits the Amor region at q = 1.3 AU, and the dashed vertical line denotes the boundary between the Aten and Apollo populations. Figure taken from Morbidelli (2002) [10].

hyperbolic orbit toward Earth's orbit. The dynamical structure of 2:1 resonance is very complicated. Therefore, there is a significant gap in the asteroids distribution and no mechanisms are available to destabilize their motion in a short time. The mean time spent in the NEO region for the 3:1, 5:2, and 2:1 resonance is 2.2, 0.4 and 0.1 m.y, respectively. In addition, the mean collision probability with Earth, integrated over the lifetime in the Earth-crossing regions, is 2.5×10^{-3}, 2×10^{-4}, and 5×10^{-5}, respectively.

In the Main Belt, there are hundreds of thin resonances, called diffusive resonances. The main-belt asteroid becomes too chaotic as a result of these resonances, despite the weak chaoticity effect. Three types of these resonance are present: high-order mean-motion resonances with Jupiter (where the orbital frequencies are in a ratio of large integer numbers); three-body resonances with Jupiter and Saturn (where an integer combination of the orbital frequencies of the asteroid, Jupiter, and Saturn is equal to zero), and mean-motion resonances with Mars [10]. The asteroids cross the orbit of Mars in the inner belt and the orbit of Jupiter in the outer belt with a time span ranging from 10^7 to billions of years [46]. Morbidelli and Nesvorny [47] discovered that approximately two asteroids, with a diameter

exceeding 5 km, traverse the orbit of Mars each m.y.
There are three groups of Mars-crossers: Intermediate Mars-Crossers (IMC) located before the resonance ν_6, Hungaria with $1.77 < a < 2.06$ AU and $i > 15°$, and Phocaea with $2.1 < a < 2.5$ AU and $i > 18°$. For the IMC group, the time to reach the orbit of Earth is $\sim$ 60 m.y.; about two bodies larger than 5 km become NEOs every m.y. [48] and they remain in the NEO region for 3.75 m.y. [49]. The median time to reach Eart-crossing orbits from two groups of high inclined Mars-crossers exceeds 100 m.y [50].
In addition to resonances, NEOs are also influenced by close planetary encounters. During these encounters, the body's semimajor axis and velocity can vary because of the geometry and mass of the planet. The variation of the semimajor axis depends on the eccentricity and inclination, which affect the Tisserand parameter T respect to the encountered planet. The Tisserand parameter is defined as:

$$T = \frac{a_p}{a} + 2\sqrt{\frac{a(1-e^2)}{a_p}}\cos(i) \tag{1.1}$$

where a_p and a are the semimajor axes of the planet and asteroid respectively, e is the eccentricity and i is the inclination of the body. If only the effects of planetary encounters are taken into account and the inclination is neglected, a body would move on a curve in the plane (a,e) defined by T=constant. These curves are transverse to the mean motion resonances and most secular resonances, so the body is transported from one resonance to another. It is remembered that resonances keep the semimajor axis constant by changing eccentricity and inclination. In conclusion, the dynamics of NEOs is influenced by both the iteration between resonant dynamics and close encounters [51]. Most NEOs are either ejected on hyperbolic orbits by Jupiter or colliding with the Sun.

1.2.2 Yarkovsky and YORP effects: influences on the NEO population

The Yarkovsky effect was discovered in a singular way. Ivan O. Yarkovsky, a Russian engineer, wrote a small pamphlet [52], where he explained that a prograde-rotating planet should produce a transverse acceleration of its motion, helping to balance the aerodynamic drag assumed by the presence of the aether. Ernst J. Opik discovered Yarkovsky's lost work and brought it to western Europe. Yarkovsky's work was wrong, but it gave Opik the idea to explain that the orbits of small objects orbiting the Sun are modified by the absorption and re-emission of sunlight [53]. Additionally, Vladimir V. Radzievskii and his colleagues [54] suggested that the rotation of a body could be influenced by the thrust of photons. Stephen J. Paddack and John O'Keefe developed this idea: the rotation of these bodies was not caused by reflected sunlight but rather by their irregular shape and thermal radiation. This led to the development of the Yarkovsky-O'Keefe-Radzievskii-Paddack (YORP) effect as an alter ego of the Yarkovsky effect. Radzievskii's researchers introduced the idea that the acceleration could be due to radiation from synchronous planetary satellites [55]. This idea led to the birth of the binary YORP effect (BYORP), first studied by Cuk and Burns [56]. Today, the Yarkovski and YORP effects are fundamental to study minor bodies in planetary science and have become important for space missions [57].

1.2.2.1 Yarkovsky effect

In the past it was thought that the only effects that describe the motion of an asteroid were gravitational force and collisions. The classical model considers these two effects only to describe the history of the main belt and inner Solar System populations [38]. According to this model, asteroids can occasionally collide with each other at velocities as high as of 5 km/s [58], causing cratering and fragmentation. In the case of the larger impacts, such as collins can lead to the formation of asteroid families, after the ejection of the bodies fragments at both a velocity of 100 m/s [59]. These objects, with the right velocity and trajectory, can enter the powerful and diffusive resonance zone caused by the planets [60]. Because of these resonances, asteroids can reach the orbits of inner planets, although most of them collide with the Sun or are ejected into the outer Solar System after a close encounter with Jupiter [42]. This classical model is very useful for describing the asteroid population, but it has some inconsistencies with observations:

- the fresh ejecta are injected directly into the resonances, and the dynamic lifetime of the bodies in these powerful resonances is only a few m.y. [42]. Thus, it is expected that there is an abundance of meteorites with short Cosmic-Ray Exposure (CRE) ages and a paucity of long-lived meteorites. However, observations show that stony meteorites have a CRE age of about 10 m.y., while iron meteorites have a CRE age between 0.1 and 10 billion years (b.y) [61], [62]. Only a few asteroids are younger than 10 m.y old. Typically, their age is similar to or much longer than the dynamical life of Earth-crossing asteroids.

- The orbits of the terrestrial planets are crossed by 5- kilometer-sized asteroids of different taxonomic types [49]. Many perturbation events between large and spectrally different asteroids are necessary to maintain this population in a stable state. These are the only events capable of bringing kilometer-sized fragments into suitable resonant "escape hatches". Most of these perturbations originate in the inner and central main belt [63], it is expected that there are numerous families in these regions. However, observations indicate that there are few families in these regions, and most of the progenitors of kilometer-sized inner solar system asteroids derive from dynamically stable regions far from the resonance escape hatches [11]. Therefore, direct injection of asteroidal fragments into resonances is too inefficient to maintain these asteroids in a stable state, resulting in a low size-frequency distribution of kilometer-sized NEOs [64].

- After impact, larger fragments are launched at high velocities of as high as 100 m/s from impact site, whereas smaller asteroids travel to more distant regions from the cluster center [65]. The results obtained from the peak velocities of size-distributions indicate that the velocities obtained are lower than those predicted [11].

- Collisions between asteroids are expected to generate a wide velocity distribution, described by a Maxwellian frequency distribution [66], [67]. However, it has been observed that small asteroids ($D < 10$ km) have velocities that are either very high or very low when these data are described by a Maxwellian distribution [68], [69].

The classical model is incomplete therefore it is believed that the Yarkovsky effect is responsible for these discrepancies. This is a non gravitational force that can cause objects, between

0.1 m and 20 km in size, to move inward or outward at varying velocity depending on their orbit, spin, and material properties. The Yarkovsky effect is caused by the diurnal heating of a spinning object in space. This force may cause significant secular effects on the orbits of small celestial bodies, such as meteoroids or small asteroids [53].
Yarkovsky's **diurnal effect** is shown in Fig. 1.4a: the Sun is at the center, and it is assumed that a spherical asteroid orbits around it. The body's axis of rotation is perpendicular to the orbital plane. As the asteroid rotates, it absorbs radiation on the side facing the Sun and radiates heat into space, mainly in the infrared part of the spectrum. The asteroid experiences a greater thrust on its hotter face due to the higher amount of energy and momentum being radiated compared to its cooler face. Additionally, the asteroid experiences a sharper thrust in the opposite direction to the Sun. If the asteroid did not have thermal inertia, the temperature distribution would be symmetric about the subsolar point and the meteorid would experience a net force radially outward from the Sun [11]. However, all bodies have thermal inertia that causes a delay, thus the hottest point is actually in the afternoon and not at the subsolar point. The asteroid has an outward radial component and a component

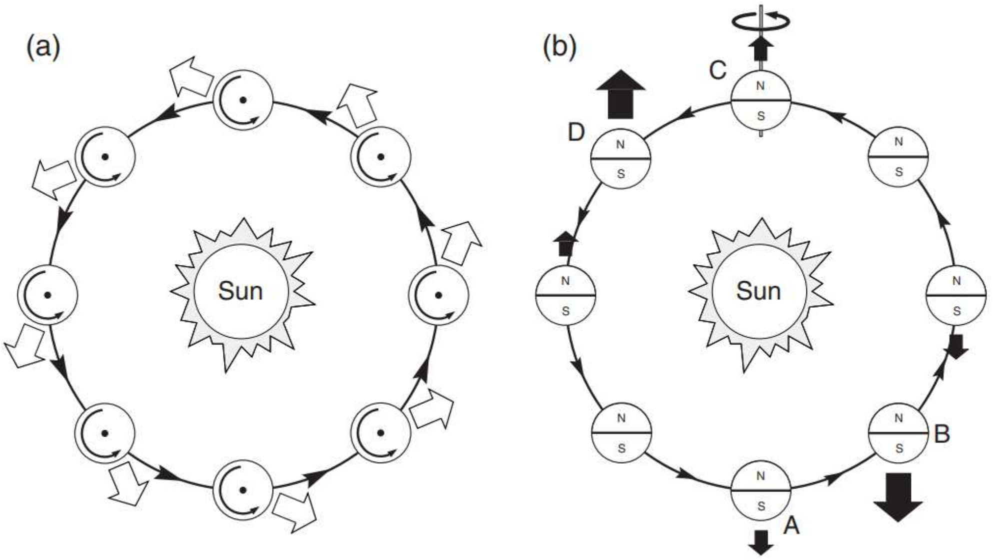

Figure 1.4: (a) The diurnal Yarkovsky effect: the Sun, in the center, the circle is an asteroid orbit and its rotation axis is perpendicular to its orbital plane. A portion of the solar radiation is absorbed and later emitted, creating a thermal force directed along the wide arrows. In this scenario, thermal reradiation is most concentrated around 2:00 p.m. on the spinning asteroid, leading to a consistent radiation recoil force pointing roughly at 2:00 a.m. Consequently, the object experiences an outward spiral motion due to the along-track component. If the asteroid were to undergo retrograde rotation, the orbit would instead spiral inward.
(b) The seasonal Yarkovsky effect, with the asteroid's spin axis lying within the orbital plane. The alternating heating and cooling of the "northern" and "southern" hemispheres generate a thermal force aligned with the spin axis. As a result of thermal inertia, the strength of the reradiation force varies along the orbit; even though the maximum sunlight exposure occurs at points A and C for each hemisphere, the resultant radiative forces reach their peak at positions B and D. As a result, the overall effect on one revolution consistently leads the object to spiral downward. Figure taken from Bottke (2002) [11].

along its orbit. The along-track component causes a secular increase in the semimajor axis, changing the orbit of the asteroid (in the figure it is shown as a prograde sense of rotation). However, if the asteroid orbits retrograde sense (see the Figure 1.4a), its orbit would narrow. Additionally, if the axis of rotation were perpendicular to the orbit, there would be no diurnal effect. The diurnal effect depends on the proximity of a celestial body to the Sun, the inclination of its axis of rotation, and its physical characteristics [11].

The Yarkovsky effect also has a **seasonal component**, where the axis of rotation lies in the orbital plane. As shown in Fig. 1.4b, solar radiation will be strongest in the northern region at point A and in the southern region at point C. However, as with the diurnal effect, there will be a delay, and it will be warmer at point B than at A and at point D than at C. During this cycle, the opposite hemisphere from the Sun will be colder and the component of the force along the axis of rotation will vary. For small eccentricities, this force will always oppose the motion of the asteroid. The effect is independent of the rotation of the asteroid and acts as a drag, causing the asteroid to disintegrate over time. This effect is influenced by the proximity of the asteroid to the Sun and the inclination of its orbit. When the axis of rotation is normal to the orbital plane, the effect becomes zero [11].

1.2.2.2 YORP effect

The YORP effect was first introduced by Runbicam (2000) [70]: it is caused by torques resulting from the Yarkovsky forces that affect the rotational velocity and orientation of the rotation axis of asteroids and meteoroids. The two primary sources of this effect are reflection and reemission. Consider a spherical asteroid with two wedges connected to the equator, as shown in Fig. 1.5, the energy emitted by the two wedges can cause torque as a result of their different shapes. According to such rotation, the wedge-produced YORP torque spins the object up. On the contrary, if the body happened to spin in the opposite direction, the YORP torque will slow it down. The YORP torque alters the obliquity of the asteroids, creating the YORP cycle. As shown in Fig. 1.5, a rapidly rotating asteroid will increase its obliquity more and more until it reaches large values. At this point, the axial torque changes sign, and the object begins to slow down its rotation. The YORP effect may spin objects up for a while, but when obliquity becomes large, it causes them to turn again, creating a cycle. This effect depends on the shape, size, distance from the Sun, and orientation of an asteroid. It can accelerate the rotation of small objects up so fast that they are forced to change their shape and/or mass loss. The YORP effect is significant because of its ability to cause both slow and fast rotational velocities for small asteroids on short timescales. Furthermore, it is related to the size of objects, which explains the variations in velocity as a function of the size of the object [11].

Another effect associated with YORP is Binary YORP. According to them, an asymmetrically shaped secondary asteroid in a binary system acts as a tangential force on its orbit. When the secondary body maintains synchronicity with the primary, it undergoes acceleration or deceleration, causing an expansion or contraction of its orbit. This effect occurs only when one of the two bodies is synchronous with its orbit and can result in a spiral towards each other or an escape within a short period. This interaction also determines the lifetime of binary asteroids due to BYORP, which is typically around 100,000 years, and then the system will be destroyed. To learn more about the different models of this effect, refer to the paper Vokrouhlicky [57].

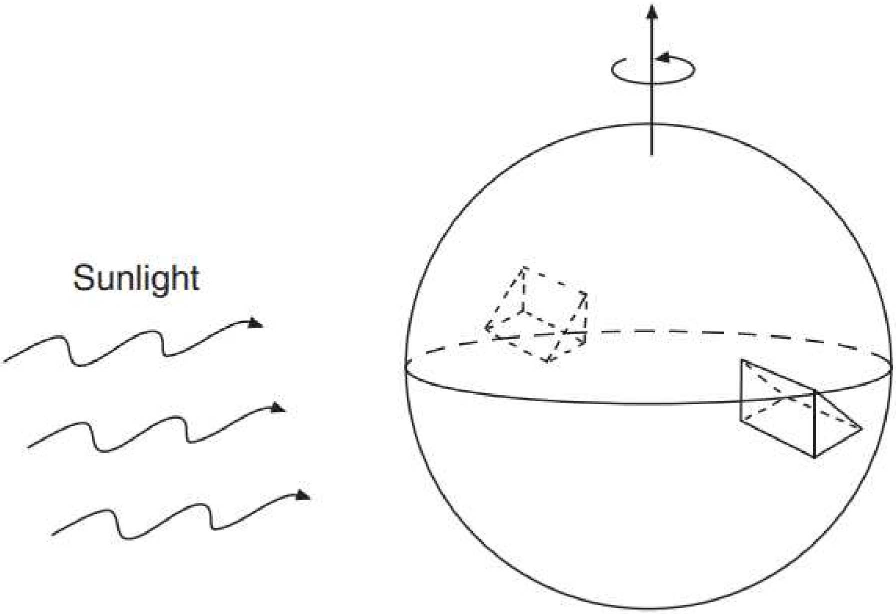

Figure 1.5: the asteroid is represented as a spherical object with two wedges attached to its equator. Treating the asteroid as a black body means that it absorbs all incident sunlight and then emits the absorbed energy in the form of infrared heat radiation. As the photons emitted from the wedges impart kicks in different directions, a resultant torque is generated, driving the asteroid into a state of increased rotation. Figure taken from Bottke (2002) [11].

1.2.3 Overview of NEOs

NEOs (for example Bennu, in figure 1.6) are asteroids and comets whose trajectory can pass within 1.3 AU of the Sun. It is important to note that this does not mean that NEOs are continuously close to the Earth, but rather that their motion occasionally brings them close to the Sun and potentially close to the Earth. As the Earth has a heliocentric distance of 1 AU, these objects can move within 0.3 AU from the Earth. The population of NEOs includes extinct short-period cometary nuclei, meteoroid streams with perihelion distances of less than 1.3 AU, and well-known asteroid-meteoroid complexes consisting of related streams and Near-Earth Asteroids (NEAs). However, there are long-period comets that do not belong to the NEO population, even though they pass within 1.3 AU due to their long revolution. Typically, NEOs constitute asteroids that originated in the Main Belt, while only a small ratio consists of comets and their tiny fragments or disintegration products commonly known as "meteroids" [71]. Comets constitute approximately 5 - 15% of the NEO population [1]. The asteroid and comets in this group are called NEAs and Near-Earth Comets (NECs)[28]. Asteroids and comets have impacted the Earth-Moon system since the formation of the Solar System. The Moon's craters resulted from interactions with these celestial objects, not from volcanism. Studying NEOs is crucial also considering the potential danger they represent to the Earth's population. Studying their orbits and sizes is fundamental in order to calculate the probability of a collision with our planet [38].

Moreover, these bodies are remnants of planetary formation and are known as planetesimals. After the completion of planetary accretion, numerous planetesimals persisted in orbit around

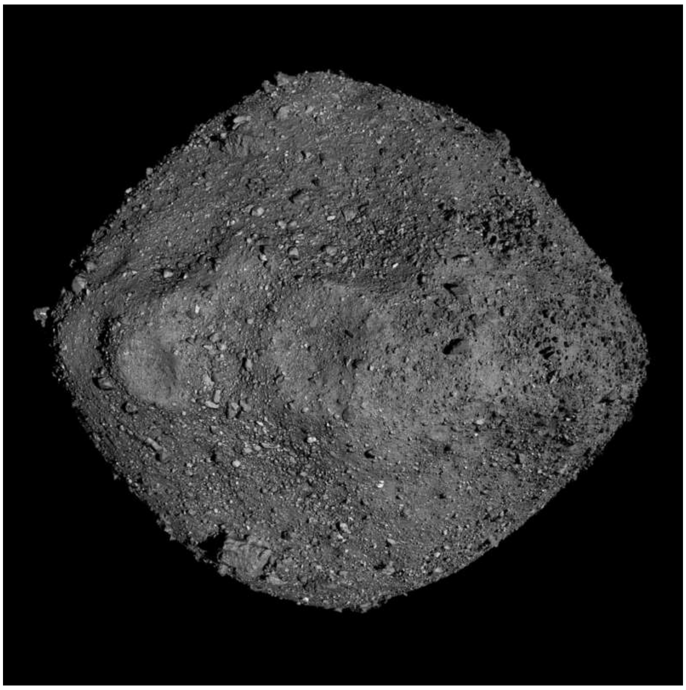

Figure 1.6: a photograph capturing the asteroid Bennu, obtained during the NASA OSIRIS-REx mission, providing invaluable insights into its geological composition and celestial dynamics. Figure taken from apod.nasa.gov

the Sun. During this period, the planets underwent intense bombardment. Although the bombardment rate decreased after 3.8 Gy ago, a small fraction of them were trapped inside the Solar System, preventing it from reaching zero.
It is essential to study the physical properties, size, composition, and structure of NEAs to establish the damage they can do to Earth and pontentially prevent it. Multiple techniques can be employed to determine the size of asteroids, including photometry, polarimetry, radar measurements, speckle interferometry, transit measurements, and thermal radiometry [28]. All these methods allow moves advantages and disadvantages to be determined with a certain level of precision. For example, in radar observations, the size of asteroids can be calculated using the observed Doppler echo power spectra. The diameter of the target is a function of the Doppler bandwidth. Radar observations are typically used to determine the diameter first and then measure the albedo based on the obtained dimensions. Instead, by using optical observations, the diameter of NEAs can be calculated using the absolute magnitude H described in the next section (1.2.8). The prediction of NEO distributions is challenging because of the existence of many unobservable NEOs. The detection of NEOs depends on both their size and orbit. Large NEOs are easier to detect than small ones because the latter are only visible when they pass close to Earth. Additionally, NEOs with moderately eccentric orbits and low inclination orbits with a period greater than one year are more easily detectable than NEOs on orbits with short periods, high inclinations or large eccentricities. The first ones pass near the opposition point in the sky, where the largest NEO surveys are concentrated, while the others remain for a longer period at a small solar elongation or far from the ecliptic. However, theoretical models allow us to estimate their distribution, due to the growing number of NEO observations [71].

1.2.4 Near-Earth Comets

NECs have a perihelion distance of less than 1.3 AU; they are a short-period comets (P less than 200 years) and they cross very close the orbit of Earth. Currently, around 120 NECs are known, including comets such as 1P/Halley, 2P/Hencke, 21P/Giacobini-Zinner and 67P/ChuryumovGerasimenko [28].

1.2.5 Number of NEAs

Nowadays (as of 12 March 2024), 34490 NEAs were discovered. NEAs have been distributed according to their size in the Figure 1.7 (https://cneos.jpl.nasa.gov/). Among them, there are 9712 NEAs less than 30 m in diameter, 11579 with diameters ranging from 30 to 100 m, 7459 with a diameter between 100 and 300 m, 4879 with a diameter between 300 and 1000 m, and 861 NEAs with a diameter greater than 1 km.

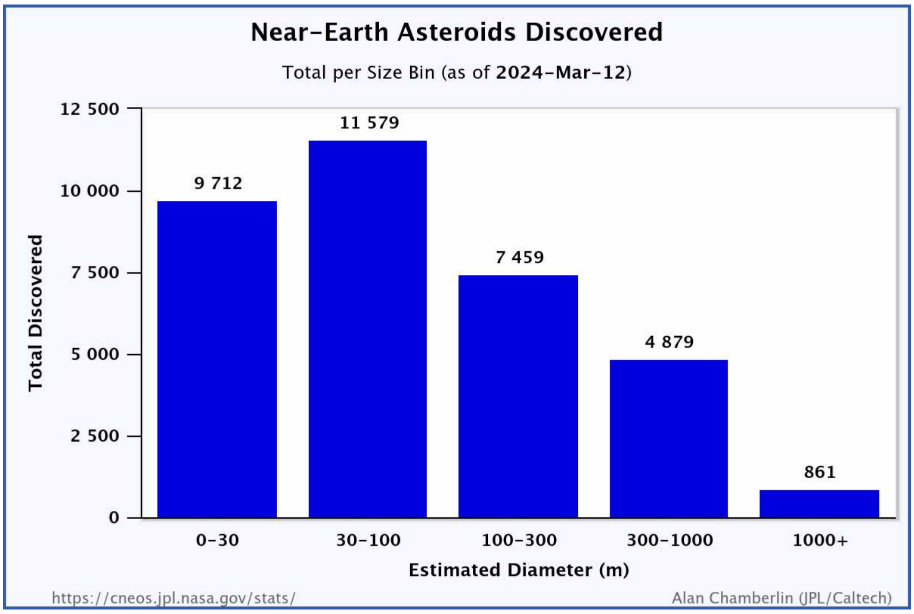

Figure 1.7: histogram showing the total number of asteroids discovered as a function of their estimated diameter. Figure taken from (https://cneos.jpl.nasa.gov/)

1.2.6 Groups of NEAs

NEAs are classified into four main subpopulations: Apollos, Amors, Atiras, and Atens (see fig. 1.8).

The **Apollos** are the largest group in number of asteroids, named after their member (1862) Apollo. They consist of the main objects orbiting close to Earth with a semimajor axis $a > 1$ AU and a perihelion distance $q \leq 1.017$ AU [1]. These asteroids have an orbital period greater than one year, and (1620) Geographos [28] is a typical example of this class.

The **Amor** asteroids, named after the asteroid (1221) Amor, are the second largest group orbiting the outer part of the Earth's orbit. Their distance from the Sun at perihelion is within the range of $1.017 < q < 1.3$ AU [1]. Although they could cross the orbit of Mars, they do not reach the Earth orbit. An example of a typical Amor asteroid is (433) Eros [28].

Atens refer to objects with a semimajor axis of less than 1 AU and an aphelion distance of $Q > 0.983$ AU. They orbit within the inner orbit of Earth but cross it. Asteroids classified as Atens have an orbital period of less than one year. A common asteroid of this class is Ra-Salom [28].
The smallest group in number of asteroids is **Atiras**, named after the asteroid (163693) Atira. Atiras asteroids orbit inside the Earth with an aphelion of $Q <= 0.983$ AU [1]. They consist of objects with orbits that are mainly inside the orbit of the Earth, but cross the orbit of the Earth. It is difficult to identify them, as they can only be observed during morning or evening at elongations from the Sun not exceeding 90 degrees [28].
In June 2023, the Apollos comprise 51.2%, the Amors 40.8%, the Atens 7.8%, and the Atiras 0.2% of the NEO subpopulations [1]. Fig. 1.9 illustrates the region on the semimajor axis versus the eccentricity space of the four NEO subpopulations [1].

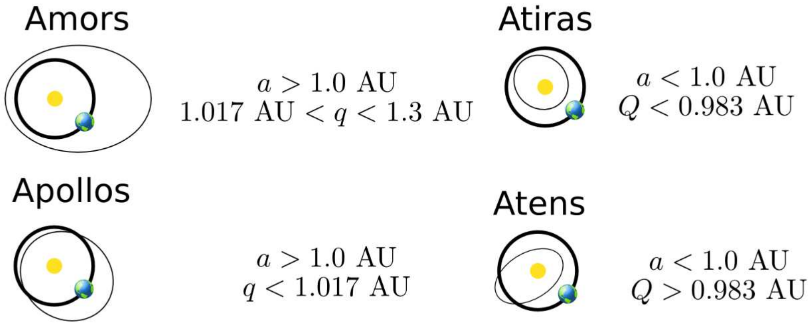

Figure 1.8: representation of the 4 NEA groups, where q is the perihelion, Q is the aphelion, and a is the semimajor axis of the orbit.Figure taken from nasa.gov

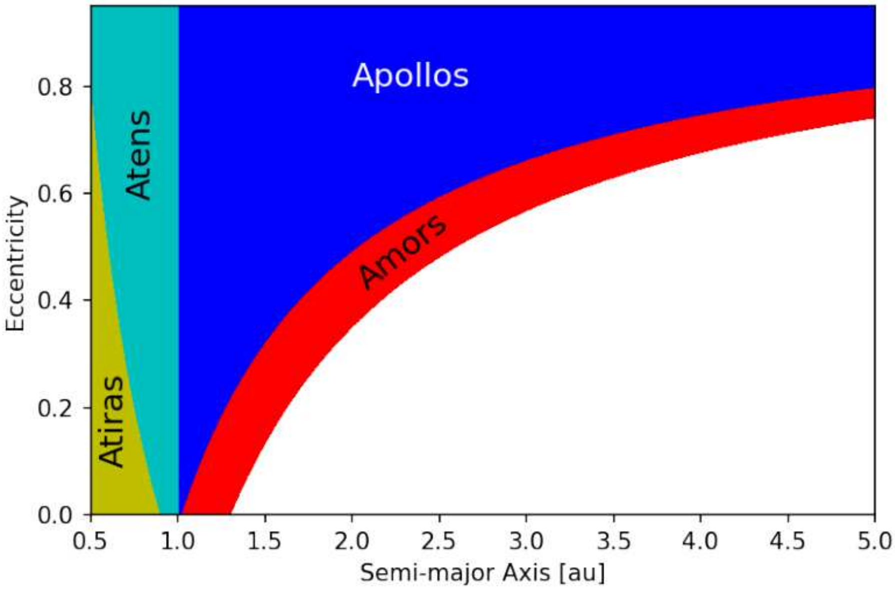

Figure 1.9: the distribution of the four subpopulations of NEAs in the region is dependent on the semimajor axis eccentricity. Figure taken from Grav (2023) [1].

1.2.7 Potentially Hazardous Asteroids

Potentially Hazardous Objects (PHOs) are a subgroup of NEOs, but their orbits are close to Earth's orbit and have the potential to collide with it. Potentially hazardous asteroids (PHAs) are those that cross a minimum distance of 0.05 AU (which constitutes about 7.5 million km) from Earth and have an absolute magnitude H not exceeding 22 mag (the figure 1.10 shows the orbits of 1000 PHAs). Between the limit of 0.05 AU there can be imprecisions in the calculation of the minimum orbital distance as determined by the MOID (Minimum Orbit Intersection Distance) parameter, for a newly asteroid discovered, as well as potential variations may occur due to various disturbances in the near future. The condition on the absolute magnitude is imposed because an asteroid with an albedo of 0.14 and a magnitude greater than 22 mag has a size of less than 140 meters [1]. PHAs are estimated to constitute around 20% of NEAs, and as of March 2024, there are 2419 known PHAs. A well-known PHA is the Aten-type (99942) Apophis, which is scheduled to cross the Earth orbit on 13 April 2029 at a distance of 0.00025 AU [28]. The Apophis passage will be important because, with its diameter of approximately 350m, it will be the first asteroid visible to the naked eye.

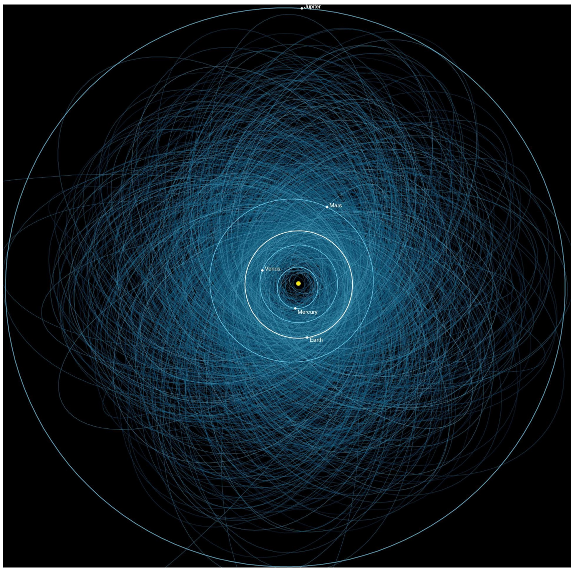

Figure 1.10: this picture is the map of the orbits of the over 1000 known PHAs. These documented tumbling boulders of rock and ice are over 140 meters across and will pass within 7.5 million kilometers of Earth (about 20 times the distance to the Moon). Figure taken from https://apod.nasa.gov/apod/ap230630.html

1.2.8 Absolute magnitudine and size

Absolute magnitude H is defined as the theoretical visible magnitude that an object would have if it was at 1 AU from the Sun and Earth at zero phase angle (the angle between the light incident onto an observed object and the light reflected from the object) [1]. The absolute magnitude H is derived from the apparent magnitude measured while the asteroid is observed at different distances from the Sun and Earth and at different phase angles when there is no geometrical data available [28]. To measure the albedo of asteroid, it is assumed that the geometry of asteroids is spherical. The albedo of asteroids is determined by their taxonomic class, and each class has its own albedo. This method is applied to asteroids of the Main Belt, but NEAs of unknown taxonomic class are excluded [72]. The diameter of NEAs can be obtained through the absolute magnitude H of an asteroid in optical observations if we know the asteroid's albedo or reflectivity. We currently have data on the largest NEA, (1036) Ganymede, with a diameter of 41 km, followed by (433) Eros and (3552) Don Quixote, which have a diameter of 20 km. In 2005, the smallest NEA, measuring 9 meters in size, was identified as the 1991 BA. NEAs smaller than 1 m are known today [28].

Most of the asteroids have an irregular shape due to their small dimensions and a weak gravitational field that it is not sufficient to give them a round shape. The size of an asteroid depends on its rotational velocity. NEAs exhibit a rotation period similar to that of asteroids in the Main Belt [28]. With some differences asteroids greater than 30-40 km exhibit a Maxwellian distribution for their rotation period [73], [68]. The distribution of rotational periods among asteroids between 10 and 40 km in size and those smaller than 10 km does not follow this distribution [68]. Slow and fast rotators were identified: approximately 0.8 revolution/day for slow and $>$ 7 rev / day for fast. Pravec [74] concluded that asteroids ranging in size from a few hundred meters to 10 km have periods longer period than 2.2 h, while those smaller than 100 m have a period of 10 minutes or less. The rotation of NEAs differs from that of a main-belt asteroid for two primary reasons. First, asteroids smaller than 10 m have shorter rotation periods, lasting between 1-20 minutes, which is significantly less than those of MBAs. The second reason is that some NEAs exhibit a complex rotation, they do not rotate around the main axis of inertia (the shorter axis), keeping the momentum at a maximum and the energy at a minimum. These are known as "tumbling" asteroids [75] and their tumbling motion is thought to be caused by collisions with other asteroids.

1.2.9 Composition and physical properties

The surfaces of NEAs are rougher than those of the main belt asteroids [76] and are covered by a layer of regolith, i.e. a fragmented material with dimensions of one micron to one centimeter with low thermal conductivity. The thermal inertia of NEAs is greater by a factor of 11 than that of the lunar surface. Thus, the regolith of NEAs is coarser-grained than the lunar regolith and, than the regolith of larger-size MBA [28]. From a cratering point of view, they are similar to those of the Main Belt [28]: several asteroids have craters, but there are asteroids with no craters. From a chemical perspective, their population represents all types of main-belt asteroids. Asteroids are taxonomically classified by their albedo and mineralogical composition obtained from spectra. They can be categorized into three main groups [28]:

- **C-type** (carbonaceous) asteroids have a very dark appearance with an albedo of 0.03-0.09 and constitute 75% of known asteroids, dominating the outer portion of the Main Belt [28].
- **S-type** (siliceous) have an albedo ranging from 0.10-0.22, accounting for approximately 17% of the population, and are located in the inner region.
- **M-type** (metallic) have an albedo between 0.10-0.18 and consist of magnesian-ferruginous silicates with nickel iron inclusions. They are situated in the middle part of the Main Belt.

In addition, S-type asteroids are characterized by a low abundance of iron, and their meteorite analogues are usually made of a low abundance of metals. The most prevalent asteroids are relate to ordinary chondrites meteorites, consisting of rock particles that have remained unchanged since the formation of the Solar System, whereas metallic asteroids originate from the disintegration of larger celestial bodies [28].

An important physical characteristic of asteroid is the apparent density related to the mineralogical density of their meteorites: porosity. Bulk density measurements of asteroids, along with data on the mineral density of similar meteorites, provide information on the porosity and internal structure of asteroids. The bulk density of asteroids is lower than the mineralogical density of their analogous meteorites due to porosity. Therefore, this suggests that many asteroids have a significant porosity. If porosity is high, it weakens the impact propagation, greatly increasing the lifespan of asteroids during collisions. [77]. Asteroids can be divided into three groups:

- Hard asteroid.
- Asteroid with $\sim 20\%$ macroporosity (presence of large voids or empty spaces within their structure) that has many cracks. Examples include (433) Eros, (243) Ida, (1) Ceres, (2) Pallas, and (4) Vesta.
- Asteroids with a macroporosity greater than 30%, which are consolidated structures of piles of loose rubble with more empty space than solid material. Examples of such asteroids include (253) Matilda and (45) Eugenia. Porosity influences the formation of the crater and the strength of the impact.

1.2.10 Brief introduction to Planetary Defense

Measuring the diameter amd to a certain degree also the composition of asteroids is crucial for planetary defense research. Objects with a diameter of 1 kilometer have a rare probability of impact, but they can cause mass extinctions [78]. It has been estimated that these objects represent 90% of the risk of asteroid impact and the SpaceGuard ([79],[80]) goal of discovering 90% of asteroids in this size range was created to address this risk. This goal was achieved in 2010 [81], [82]. Thereafter, the mission's focus shifted to bodies larger than 140 meters that can cause local destruction. NASA aimed to identify and research 90% of these objects by 2020 [1]. One problem with SpaceGuard is determining the diameter of asteroids since the impact energy is proportional to the third power of the diameter ($\sim D^3$). If the visible geometric albedo of the object is known, the size of an object can be determined using this equation [83]:

$$D = \frac{1329}{\sqrt{\rho_V}} \times 10^{-0.2H} \tag{1.2}$$

where D is the diameter in kilometers, ρ_V is the geometrical albedo at visible wavelenghts, and H_V is the absolute magnitude.

Typically, an object of 140 m is assumed to have a magnitude of H=22 mag, while an object with a diameter of 1 km is assumed to have a magnitude of H=17.75 mag, given an albedo of 0.14 [1]. The study of these objects is continuously evolving, particularly with the construction of new telescopes such as the Vera Rubin Observatory [84]. This will result in the discovery of new and smaller NEOs and expand our understanding of these objects.

Of the roughly 30,000 NEAs that are known, more than 3,000 have been numbered, meaning that their orbits are well defined and no further observations are needed to maintain accurate positional predictions over the next century. An additional 2,000 NEAs have been observed for more than 10 years, with 10% of these having observations spanning more than 20 years. Most NEAs are observed only during their initial discovery, typically for less than 7 days. The Minor Planet Center (MPC) prioritizes the observation of Aten and Apollo asteroids because of their close proximity to Earth. Table 1.1 shows all the asteroids discovered between 2011 and 2023 according to their magnitude H.

Year	Total	$H \leq 17.75$		$17.75 < H \leq 23$		$H \geq 23$	
2011	897	19	2.1%	477	53.2%	401	44.7%
2012	991	15	1.5%	480	48.4%	496	50.1%
2013	1029	11	1.1%	500	48.6%	518	50.3%
2014	1480	8	0.5%	651	44.0%	821	55.5%
2015	1551	7	0.5%	688	44.4%	856	55.2%
2016	1874	7	0.4%	731	39.0%	1136	60.6%
2017	2039	7	0.3%	743	36.4%	1289	63.2%
2018	1825	5	0.3%	614	33.6%	1206	66.1%
2019	2438	6	0.3%	750	30.8%	1682	69.0%
2020	2958	3	0.1%	829	28.0%	2126	71.9%
2021	3093	5	0.2%	730	23.6%	2358	76.2%
2022	3189	4	0.1%	725	22.7%	2460	77.1%

Table 1.1: the yearly NEOs discovery statistics during the last decade. Table taken from Grave (2023) [1].

Chapter 2

Asteroid Spectroscopy

2.1 Introduction

Spectroscopy is a crucial tool in the study of asteroids. The color of an asteroid is a significant feature, and early studies focused mainly on color variations. These variations allowed differentiation between asteroids. The mineral grains on the surface of the asteroid absorb or scatter sunlight. The spectrum can have different slopes/features depending on the optical and chemical properties of these grains. Additionally, the color of an asteroid can change as it rotates; (4) Vesta is an example of such an asteroid. [2]; the non-homogeneity of asteroids' surfaces causes this phenomenon.

The study of asteroid colors began with the discovery of the first two asteroids (1) Ceres in 1801 and (2) Pallas in 1802 [85]. Herschel differentiated between the two by stating that (1) Ceres had a "ruddy, but not very deep" color, while (2) Pallas had a "dusky whitish color" [86]. Herschel's observations were made visually and in integrated light [85]. Vogel was the first using a prism and observe (4) Vesta [87]. Initial color measurements were conducted by Bobrovnikoff using microphotometry in 1929 [88]. Nevertheless, the photography technology of the era restricted his studies. In the mid-1950s, research of broadband UBV resulted in the categorization of asteroids into two groups based on their spectral reflectance properties: carbonaceous C-types and siliceous S-types. However, this classification was limited because of the small number of asteroids studied.

In the late 1960s, the first spectrophotometry programs of asteroids were developed on the basis of their spectral reflectance properties. These instruments had higher resolution than their predecessors. This program relied on narrow-band observations in the visible spectrum ranging from 0.3 to 1.1 μm [89][90]. These programs were based on the study of the strong absorption bands in the UV and near 1 μm, the development of taxonomy [91] and the identification of the chemical composition of their surfaces [92]. The Eight-Colour Asteroid Survey (ECAS) [93] was developed in the mid-1980s and is a survey based on spectrophotometric imaging of 600 asteroids: this was a key step in the formation of Tholen's taxonomy [85]. Successively, spectroscopy became a tool better than the traditional photometric filters thanks to different factors: the improvement of the spectroscopes, the invention of the charge-coupled device (CCD) cameras for the recording of the spectra, and the use of the long-slit spectrographs. CCDs were particularly useful because of their high sensitivity, stability, and two-dimensional format. These factors permitted to image much of the visible spectrum in a single exposure and to increase significantly the spectral resolution compared to the previous photometric techniques. Moreover, thanks to spectroscopy, the background is measured simultaneously along the slit of the spectrograph, allowing a much more precise background removal from the spectrum than previously.

The main aim of asteroid spectroscopy is to establish the ratio of light reflected from the surface of the asteroid to the light received from the Sun as a function of wavelength [2]. However, there are uncertainties in the final spectrum of asteroids due to several factors. One of the difficulties is that it is not possible to measure the spectrum of the Sun directly with a CCD spectrograph, but it is possible to use similar stars: the solar analogs. However, solar analogs are not perfectly identical to our Sun, which can introduce errors into the asteroid spectra.

The reflection of sunlight is attributed to grains present on the surface of asteroids. Consequently, the study of asteroid spectroscopy is not concerned with the internal chemical composition of these celestial bodies. Nevertheless, it is presumed that the surface composition can be taken to be similar to the internal composition, so spectroscopy is used to determine the chemical composition of asteroids. Some uncertainties are due to the Earth atmosphere, since light from the asteroid is scattered and absorbed by the atmosphere. Therefore, it is necessary to correct for these atmospheric effects and remove any additional instrumental offsets due to the characteristics of the CCD and spectrographs [2].

In addition to the factors mentioned above, the materials present on the surface of an asteroid can also change their optical properties due to varoius processes and can lead to a significant variations in the spectra:

- **Phase reddening:** the reflectance spectra changes with phase angle [2]. It is the angle formed between the Sun, the asteroid, and the observer, which affects the amount of sunlight reflected by the body.
- **Space weathering:** describes the darkening and reddening on the surface of an asteroid, altering its spectral slope due to different processes like quick melting and recrystallization of mafic materials, induced by short laser pulses, laser irradiation and the production of nanophase Fe on the surfaces of grains [2].
- **Particle size:** the presence of a particulate regolith on the asteroid surface affects the optical properties, the spectral slope and the band depths, which vary according to the size of the particles [2].
- **Temperature:** also plays a role, with a range of 120 K to 300 K observed for Trojan and near-Earth asteroids, respectively [94]. For example the spectral band shapes related to olivines and pyroxenes actually react to temperature and therefore alter the mineralogical composition of asteroids [95][96][97].

In the mid-1970s, asteroid classification relied on three fundamental characteristics:

– the presence or absence of UV absorption resulting from Fe^{2+} intervalence charge transitions;

– the slope of the spectrum longward of 0.55 μm, the magnitude of which depends of the presence or absence of reddening agents such as Fe-Ni metal or organics;

– the presence or absence of a silicate absorptions above 0.7 μm.

Fig. 2.1 illustrates twelve asteroids classified using these features. The image compares the ECAS colors (open squares) and the SMASSII spectra (closed dots) of certain taxonomic classes classified by Tholen [85],[2]. The absorption bands are identified because of the increased sensitivity and spectral resolution permitted by CCDs spectroscopy. To reveal the depth of these bands, it is necessary a spectra with an high S/N ratios. Absorption bands can only be distinguished from telluric water bands with the use of high-resolution instruments. The absorption bands of asteroids are explained by crystal field theory and charge-transfer mechanisms [98][99]. These bands help to understand the minerals that make up the asteroid rocks. Tholen [85] classified asteroids by utilizing these bands. For example:

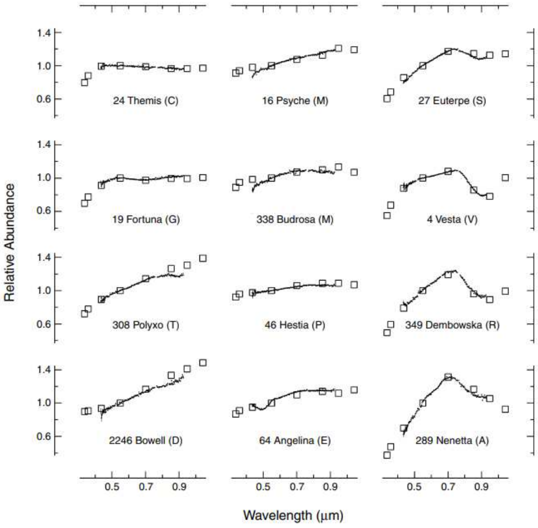

Figure 2.1: 12 spectra of asteroids in Tholen's classification. The y-axis shows Relative Abundance, while the x-axis represents the wavelength in μm. The empty squares represent data from the Eight-Colour Asteroid Survey (ECAS), and the black dots with relative errors represent the SMASSI spectra. Image taken from [2].

- A-type asteroids exhibit an absorption band centered at approximately 0.65 μm, as is evident in the spectra of (289) Nenetta. This feature is linked to the low ratios of forsterite:fayalite (Mg: Fe) [100].

- C-type asteroids show a characteristic centered at 0.7 μm due to the presence of phyllosilicates produced by aqueous alteration processes [101]. This feature can also be observed in the spectrum of (19) Fortuna. Weaker bands located at 0.43, 0.60-0.65 and 0.80-0.90 µm have been discovered and are related to Fe oxide minerals formed by aqueous alteration of anhydrous silicates [102],[103]. These asteroids also exhibit an absorption peak around 3 µm, which is associated with the presence of organic materials such as silicate hydrates and carbon compounds.

- S-type asteroids exhibit bands centered on 0.60-0.67 μm due to the oxidized Fe-Ni metal [104].

- V-type asteroids exhibit a weak absorption band located at 0.5 μm with the presence of augite (a high-Ca form of pyroxene) in freshly exposed surface materials [38]. V-type asteroids also exhibit two characteristic absorption bands positioned near 1 and 2 μm.

- X-type asteroids show an strong absorption band centered at 0.49 μm and a much weaker band located at 0.60 μm are observed in the spectrum of (64) Angelina. The origin of these bands can be attributed to the Fe-sulfide mineral troilite [16],[105].

Absorption bands have aided the classification of asteroids in previous methods. However, there have been recent changes in classification parameters and taxonomy, which are discussed in the next section.

2.2 Taxonomy

Taxonomy is the classification of objects that share common physical properties and characteristics. As the data increases, the identification of similarities and differences between these objects becomes more apparent. Biology was the first discipline to use taxonomy, followed by physics and now various branches of astronomy [85]. With the increasing number of known asteroids, classifying them into groups became necessary. In asteroids, taxonomy is based on a group of objects that share the same surface properties, such as absorption bands imprinted into their reflectance spectra or surface albedos.

Main belt asteroids are composed of various minerals. Mineralogical insights of the Main Belt facilitated the study of asteroid families [106], identification of the sources of meteors [107],[108], and comprehension of the dynamic evolution of the Solar System [109],[110],[111]. The Main Belt consists of both large and small minor bodies and originates from a later evolutionary phase of the Solar System's history [13]. The categorization of asteroids has undergone several revisions over time. In 1975, Chapman became the pioneer in classifying asteroids based on their reflectance spectra properties [91]. Advanced instrumentation has allowed many asteroids to be studied in detail and their physical characteristics, leading to a revised classification. Multivariate analysis techniques, such as cluster analysis, were used for taxonomic classification. To achieve the best possible classification, the targets to be classified must be clustered into groups that are well separated in some parameter space [13]. The initial four taxonomic classifications were obtained by combining data from the Eight-Color Asteroid Survey (ECAS) [93] and IRAS albedo [112]:

- Tholen [85], which was obtained using a clustering algorithm that uses the minimum spanning tree;
- Barucci [113], which was derived using G-mode analysis;
- Tedesco [112] three-parameter taxonomy was derived through objective visual identification of asteroid groupings in a parameter space defined by two asteroid colors and the IRAS albedos;
- Howell [114] used artificial neural networks to analyze the ECAS data and the combined data from ECAS and the 52-color asteroid survey [115].

The use of CCDs has resulted in a wealth of spectroscopic data for asteroids. Several data collection programs have been conducted, using standardized observational and data reduction techniques, enabling extensive data analysis. These programs include the low-albedo asteroids survey [101], which included 115 asteroids, and the Small Main-Belt Asteroid Spectroscopic Survey Phase I (SMASSI) [116], which included 316 asteroids observed. The Small Main-Belt Asteroid Spectroscopic Survey Phase II (SMASSII), consisting of 1447 asteroids observed, and the Small Solar System Objects Spectroscopic Survey (S^3OS^2), consisting of 800 asteroids observed. These surveys led to the creation of more precise taxonomic classifications and better understanding of Solar System minor bodies.

2.2.1 Tholen's taxonomy

Tholen's taxonomy [85] was created in 1984 and comprising of 589 asteroids observed included in the ECAS. It utilizes spectra within the range of 0.31-1.06 μm and albedo measurements that have been derived from thermal radiometric with NASA Infrared Telescope Facility (IRTF) on Mauna Kea in Hawaii. Classifies the asteroids into classes A, B, C, D, F, G, Q, R, S, T and V (see Fig. 2.3 which are obtained applying a Principal Component Analysis (PCA)). The B-types are asteroids that exhibit a visible albedo of 10% and are classified as 'bright-C' types. F-types have a flat slope in the UV spectra, while G-types show an absorption band in the UV range [13]. The Q, R, and V classes are composed of only one member each. The E-, M- and P-classes present degenerate spectra and can be separated using the albedos. In case this information is not available, the M-, E- and P- objects are grouped into a generic X- class. The Tholen classification has the advantage of relying on both visible albedo p_V and spectra in the UV range.

2.2.2 Bus and Binzel's taxonomy

Bus & Binzel's classification system [117] contains 1447 visible spectra included in SMASSII (see Table 2.1). This system uses five different methods, including the structure of Tholen's classification and the absorption bands of asteroids within the visible spectra. The system studies the reflectance of the spectral continuum and uses various analytical and multivariate analysis techniques to accurately parameterise the different spectral features [38]. The boundaries and sizes (scale-lengths) of the taxonomic classes were determined by observing the spectral variance observed in the natural asteroid groups, including dynamical families; another parameter is based on spectra that contain a silicate band at 1 μm. This taxonomy was built on the previous ones and includes 26 classes: three major groups (the S-, C- and X-complexes) and the classes A, B, C, D, K, L, O, R, S, T, V and X. Asteroids are named using a double-letter system, in which the first letter indicates the class to which the asteroid spectrum corresponds the most closely. The second letter represents the asteroid exhibiting an intermediate spectral characteristic. The three major S-, C- and X-complexes are further divided into Sa, Sk, Sl, S, Sq, Sr; Cb, Cg, Cgh, Ch; Xc, Xe, and Xk respectively. The Ch and Cgh have the spectral characteristic at 0.7 μm assumed to be indicative of hydration. The E-, M-, and P-classes are comprised of three spectral classes: Xe, Xc, and Xk. There is a new L-class where the spectra having a steep UV slope shortward of 0.75 μm but which are relatively flat longward of 0.75 μm. The classification of asteroids can be a challenging task, as it may depend on various observations. Moreover, with the growing number of taxonomies, an asteroid's classification may alter in time due to its heterogeneous surface. As a result, there is no definitive classification, and it is a product of our evolving understanding of the object.

Tholen Class	**SMASSII Class**	**Description**
B, F	B	Linear, featureless spectrum with bluish to neutral slope
	Cb	Similar to B spectrum with neutral to slight reddish slope
G	Cg	Strong absorption ($\lambda < 0.55\mu$m), and featureless with neutral to reddish slope ($\lambda > 0.55\mu$m)
	Cgh	Similar to Cg spectrum, with shallow absorption centered near 0.7 μm
C	C	Weak to medium absorption ($\lambda < 0.55\mu$m), neutral to slightly reddish and featureless ($\lambda > 0.55\mu$m)
	Ch	Similar to C spectrum, with shallow absorption centered near 0.7 μm
E, M, P	Xc	Slightly reddish spectrum, featureless except for broad convex curvature centered near 0.7 μm
	Xk	Similar to Xc spectrum, but redder slope ($\lambda < 0.7\mu$m), and generally flat ($\lambda > 0.7\mu$m)
	X	Generally featureless, linear spectrum with slight to moderate reddish slope
	Xe	Overall slope slight to moderately red, concave absorption feature centered near 0.5 μm, with occasional secondary absorption centered near 0.6 μm
T	T	Moderately reddish slope ($\lambda < 0.75\mu$m), and generally flat ($\lambda > 0.85\mu$m)
D	D	Relatively featureless spectrum with very steep red slope
S	K	Moderately steep red slope ($\lambda < 0.75\mu$m) and flat to slightly bluish ($\lambda > 0.75\mu$m)
	L	Very steep red slope ($\lambda < 0.75\mu$m) and flat to slightly bluish ($\lambda > 0.75\mu$m)
	Ld	Similar to L spectrum, but steeper red slope ($\lambda < 0.75\mu$m)
	Sa	Similar to S spectrum, but with steeper slope ($\lambda < 0.7\mu$m)
	Sl	Similar to S spectrum, but with steeper slope ($\lambda < 0.7\mu$m) and a shallower absorption ($\lambda > 0.75\mu$m)
	S	Moderately steep, reddish slope ($\lambda < 0.7\mu$m), and a moderate to deep absorption band ($\lambda > 0.75\mu$m)
	Sr	Similar to S spectrum, but with very steep red slope ($\lambda < 0.7\mu$m) and a deeper absorption ($\lambda > 0.75\mu$m)
	Sk	Similar to S spectrum, but with shallower reddish slope ($\lambda < 0.7\mu$m) and a shallower absorption ($\lambda > 0.75\mu$m)
	Sq	Similar to S spectrum, but with shallower reddish slope ($\lambda < 0.7\mu$m)
Q	Q	Moderately steep red slope ($\lambda < 0.7\mu$m) and a deep, very rounded absorption feature ($\lambda > 0.75\mu$m)
A	A	Very steep to extremely steep red slope ($\lambda < 0.75\mu$m) and a moderately deep absorption ($\lambda > 0.75\mu$m). Reflectance maximum or 1 μm feature usually more rounded than in S-type spectrum
R	R	Very steep red slope ($\lambda < 0.7\mu$m) and a deep absorption feature ($\lambda > 0.75\mu$m). Reflectance maximum more sharply peaked than in S-type spectra
V	V	Moderate to very steep red slope ($\lambda < 0.7\mu$m) with an extremely deep absorption band ($\lambda > 0.75\mu$m)
-	O	Moderately red slope ($\lambda < 0.55\mu$m), then less steep ($0.55 < \lambda < 0.7$ μm). Deep absorption ($\lambda > 0.75\mu$m)

Table 2.1: description of the Tholen and SMASSII classes. Table taken from Bus (2002) [2].

2.2.3 Bus and DeMeo's taxonomy

The taxonomic classification system proposed by Bus and DeMeo comprises 371 asteroids, as reported in their papers [117],[118]. Spectra and photometric observations were made in the visible and NIR ranges train 0.45 to 2.45 μm. The taxonomic classes are the same as those proposed by Bus and Binzel, except for three classes (Ld, Sk and Sl) which have been eliminated, and a new class (Sv) has been introduced. The C-complex was further divided into six subclasses (B, C, Ch, Cb, Cg and Cgh), each with different slopes. A "w" notation is added to the end of the marker to signify asteroids with a larger slope than other objects of the identical spectral category.

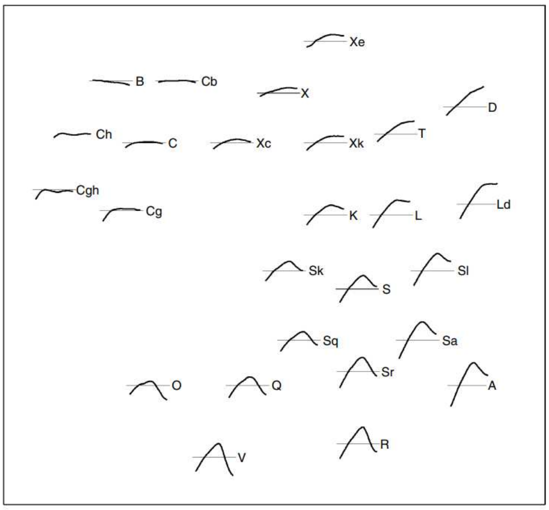

Figure 2.2: a diagram with all 26 taxonomic classes from Bus and Binzel [12]. The 26 possible spectra of the different classes are schematically represented in a pattern that approximates the location of each class in spectral component space. The spectral slope on average increases from left to right, while the absorption band depth of the 1 μm absorption band of the silicates generally increases from top to bottom. The spectral range is between 0.45 and 2.45 μm. Figure taken from Bus (2002) [2].

2.2.4 Mahkle's taxonomy

Mahkle's classification system [13] was recently developed to enhance existing classifications. It offers three advantages: it can classify complete and partial observations in the VisNIR region; it reintroduces the visual albedo p_V by resolving the degeneration of complex X; and finally, it uses a probabilistic model called Probabilistic PCA (PPCA) to determine the percentage of class membership. This method facilitates the classification of taxonomic outliers and transitional populations and is developed using 2983 spectra of 2125 asteroids obtained from different observatories, online and publications archives. These spectra source from the SMASS [116] and the MITHawaii Near-Earth Object Spectroscopic Survey (MITHNEOS) [119], [120]. Approximately 50% of the spectra are in the visible band, while the remainder are in VisNIR. Albedo measurements for 3543 asteroids are taken from the Solar System Open Database Network (SsODNet3) of the IMCCE (Institut de Mécanique Céleste et de Calcul des Éphémérides) [121]. The data used to measure the albedo comprise observations made by the Infrared Astronomical Satellite (IRAS) [122], the Wide Field Infrared Survey Explorer (WISE) [123], AKARI [124] and Spitzer Space Telescope [125]. This methodology involves combining the spectra and albedo observations for each asteroid. For a comprehensive understanding of the methodology, please refer to Mahlke's work [13]. The classification comprises 17 classes, three of which are C- ,M- , and S-complexes. Additionally, a new Z-class has been added compared to previous taxonomies, for extremely-red objects in the main belt. The presence of a second letter signifies specific absorption bands, which is described through h-, e-, and k- features. The h- feature corresponds to an absorption centered at 0.7 μm and is associated with phyllosilicates on the surface [126]. The e- and k- features are linked to a narrow absorption at 0.5 μm and a broad absorption within the range of 0.8 μm to 1.0 μm. In the following, we give a breakdown of the different categories which, for the most part, are similar to the previous classifications.

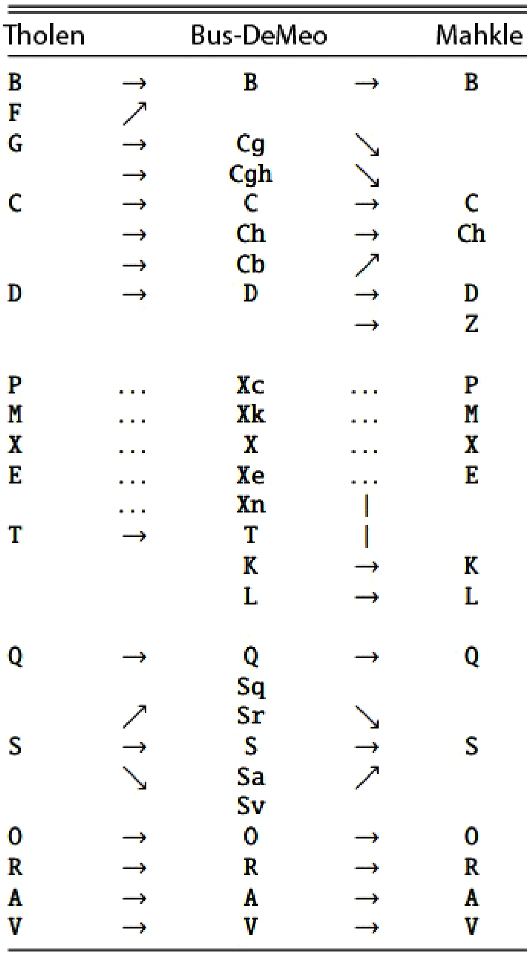

Tholen		Bus-DeMeo		Mahkle
B	→	B	→	B
F	↗			
G	→	Cg	↘	
	→	Cgh	↘	
C	→	C	→	C
	→	Ch	→	Ch
	→	Cb	↗	
D	→	D	→	D
			→	Z
P	...	Xc	...	P
M	...	Xk	...	M
X	...	X	...	X
E	...	Xe	...	E
	...	Xn	|	
T	→	T	|	
		K	→	K
		L	→	L
Q	→	Q	→	Q
		Sq		
	↗	Sr	↘	
S	→	S	→	S
	↘	Sa	↗	
		Sv		
O	→	O	→	O
R	→	R	→	R
A	→	A	→	A
V	→	V	→	V

Figure 2.3: representation of the taxonomic classes of Tholen, Bus-DeMeo and Mahlke. The arrows indicate the transformation of spectral type from Tholen taxonomy to Bus-DeMeo and finally to Mahkle. Figure taken from Mahlke (2022) [13].

2.2.4.1 C-complex

C-complex asteroids are dominant in the Main Belt and the regions beyond the 3:1 mean motion resonance in terms of number and mass [127], [128]. Their spectra are poor in features, but exhibit the h-feature at 0.7 μm, observed in one-third of their population. The C-complex is categorized into B-, C-, Ch-, and P- classes. These four classes are differentiated by their slope and shape of the spectra. The slope ranges from blue through neutral to red, whereas the spectral shape varies from linear to concave: these features are attributed to a carbonaceous surface composition that includes magnetite [91],[129]. Meteorites that are commonly associated with the C-complex population include carbonaceous chondrites such as CI, CK, CM and CO, which exhibit varying degrees of thermal metamorphism or aqueous alteration. Using a radiative transfer model, the spectral appearance of most C-complex asteroids is well matched with spectra of constituents of chondritic-porous interplanetary dust particles [130],[131],[132],[133]. In Mahkle's taxonomy there is not the X-complex: Xc, Xk, X and Xe become P-, M-, X- and E-type respectively. The D- and Z- types are referred to as endmembers because of some P-types showing intermediate spectra between the C- complex and these two classes.

- B-type: it is first introduced by Tholen [85], they have a slightly stronger UV absorption feature and the average albedo is higher compared to other classes of the C-complex. In Mahkle taxonomy compared to Tholen's, the F-types and B-types cannot be distinguished without the use of UV spectroscopy. B-type asteroids are brighter and bluer than C-type asteroids. The principal asteroids belonging to this class are (2) Pallas and the NEO (3200) Phaethon. 2.1% of Mahkle's asteroids sample falls under the B-type classification.

- C-type: the carbonaceous C-types show poor features, except for a broad feature at 1.3 μm, which gives a concave shape of the spectrum. The spectra slope ranges from neutral to slightly red. 10.4% of the asteroids in Mahkle's classification belong to the C-type. (1) Ceres, (10) Hygiea, (24) Thermis, (45) Eugenia, and (52) Europa belong to this class.

- Ch-type: have a spectra slope comparable to that of the B- and P-classes, but differ from them in the presence of the h-feature. They share similarities with asteroids of the C-class, exhibiting linear and slightly concave spectra. 5% of the taxonomy are comprised of these asteroids, with notable members such as (41) Daphne, (46) Pales, (121) Hermione, (144) Vibilia and (150) Elektra.

- P-type: are called 'pseudo-M' types and are spectrally degenerate with the E- and M-types in the visible wavelenght range [134]. They have a red linear slope in the NIR. There is ongoing spectral degeneracy between the P and M types in the NIR, but the E types exhibit neutral slopes. The P and M types are different for the value of the visible albedo that it is about 5% for P-types. Among the P-type asteroids, 19.2% have the h-feature, but they have not the k-feature, which it is commonly observed in M-types. The asteroids of P-type class account for 6.4% of the Mahkle's taxonomy.

- D-type: are dark asteroids have a strong red spectra slope in visible and near-infrared [118],[85]. They are predominantly in a region between the outer Main Belt and the Jupiter Trojan population, forming a homogeneous group in spectral and albedo space.

D-type asteroid spectra are characterized by the absence of absorption bands. D-types represent 3.9% of the asteroids in the Mahkle's classification, two examples are (911) Agamemnon and (1143) Odysseus.

- Z-type: these asteroids are similar to D-class asteroids, but they have steeper slopes and are extremely red due to the presence of organic matter. Their spectral shape becomes more convex as the slope increases. Z-class asteroids are dispersed throughout the main asteroid belt, located between the Jupiter Trojan population and Hilda asteroids. These asteroids have a relatively low albedo. Only 1% of these taxonomy are designated as Z-class. Some examples of asteroids in this classification include: (3283) Skorina, (15112) Arlenewolfe, (17906) 1999 FG32, (908) Buda, (203) Pompeja and (269) Justitia.

2.2.4.2 M-Complex

The spectra do not show evident features; some spectra show that weak absorption is observed around 0-9 μm or 1.9 μm, and the albedo is approximately 15%. The characteristics of the M-complex fall between those of the C- and S- complexes in terms of spectra and albedo. The M- complex is the most heterogeneous and is composed of three categories: K-, L-, and M- classes, and an endmember designated as E- class. Therefore, slight variations in the slope of the NIR are observed. Members of the M- complex do not share similar mineralogical compositions.

- K-type: K asteroids have a red spectra slope in the visible region with an absorption band at 1 μm associated with forsteric olivine [135] and a flat slope in the NIR spectra. They exhibit a visible albedo ranging between 10% and 15%. The Eos family is classified as K-type, comprising notable asteroids such as (402) Chloe, (1545) Thernoe, (221) Eos, (661) Cloelia, and (3028) Zhangguoxi. K-type asteroids account for 2% of the total classifications.

- L-type: these asteroids play an important role in studying the origin of the Solar System, particularly in relation to planetesimals [136]. The planetesimals and this type of asteroids shown a strong absorption at 2 μm due to spinelbearing calcium-aluminum-rich inclusions [137]. L-types demonstrate spectral heterogeneity in the slope and shape of the visible and 1 μm region, as well as in their albedo distribution [13].This heterogeneity indicates that the L-types parent bodies were the first planetesimals to form in the accretion disk. They represent 2.7% of this classification.

- M-type: these asteroids have spectra that are reddish and shown a linear, as well as a convex shape: this shape could potentially result in a blue trend beyond 1.5 μm. They exhibit an albedo distribution of 10-20%. Most of them have silicates features between 0.9 μm or 1.9 μm and 40% of these class present the K-feature. There are two distinct populations: a chondritic one with an archetype of (21) Lutetia and a metallic one with an archetype of (16) Psyche. Some asteroids belonging to this class are: (21) Lutetia, (771) Libera, (779) Nina, (16) Psyche, (55) Pandora, (129) Antigone and (201) Penelope, making up 6.7% of this classification.

- E-type: is composed of enstatite achondrites [138], with an albedo of more than 50% and a steep slope in the visible spectrum and flat in the near-infrared. They shows an absorption band of 0.5 μm, associated with the sulfide mineral oldhamite present in aubrietes [139] or with titanium-bearing pyroxene [140]. Some asteroids exhibit the k-feature, while others display the e-feature. They comprise 2.2% of the classification and examples include (64) Angelina, (434) Hungaria, and (214) Aschera.

2.2.4.3 S-Complex

The S-complex is by far the largest complex in terms of individual asteroids. The main type of the S-complex is S-type: they dominate all taxonomies and are mainly distributed within the inner Main Belt and near-Earth Space [119], [141], [127], with a high average albedo exceeding 20%, Their spectra and albedo show a larger homogeneity due to the abundance in number of S-Type asteroids. These asteroids usually exhibit a continuous trends in slope and the silicate features at 0.9, 1.0 and 1.9 μm due to the variation in mineral composition, especially olivines and pyroxenes. Specifically, this variation can be attributed to thermal alteration in ordinary chondrites [142], [143]. The S-complex is divided the S- and Q-classes along with the endmembers A-, R-, O-, and V-classes.

- S-type: they are formed by silicates and the pyroxene is their most common mineral. This classification does not include any subclasses due to the continuous distribution between the main S-complex and its subclasses. 42.3% of asteroids in this taxonomy are classified as S-class, including examples such as (3) Juno, (11) Parthenope, (43) Adriadne, (237) Coelestina, and (808) Merxia.

- Q-class: it predominantly consists of NEOs that represent 83.2% of the NEO population. Their spectral characteristics closely resemble those of chondrites, having a broad 1 μm band and a slope ranging from neutral to blue. The asteroids in this class exhibit a high albedo ranging from 20 to 35%, as predicted by the space weathering models [144], showing a darkening of the silicaceous asteroids with increasing surface age. Examples of asteroids in this class include (1862) Apollo and (54827) Kurpfalz. This classification encompasses 5% of the asteroids in the taxonomy.

- A-class: these asteroids exhibit a strong red slope and a deep olive imprint at 1 μm, attributable to brachinite achondrites [107], [145], [146]. These asteroids show an albedo variation ranging from 20 to 30%. The taxonomy comprises three asteroids: (246) Asporina, (354) Eleonora, and (446) Aeternitas with only 1.5% of the asteroids classified as such.

- O-class asteroids: the only asteroid in this category is (3628) Boznemcova, which is of ordinary chondritic type [147]. It exhibits winde round absorption at approximately 1 μm and has an estimated albedo of 25%. (7472) Kumakiri was also classified as type O within this classification, although it may also be classified as class V [148].

- R-class: it was established due to the discovery of (349) Dembowska. These asteroids exhibit 1 μm and 2 μm characteristics that are deeper than those found in S-types [13]. Their spectral signatures are derived from low-iron ordinary chondrites [149]. This classification comprises only 0.5% of the asteroids in the taxonomy.

- V-class: they have a characteristic deep 1 μm and 2 μm due to pyroxene and they are originating from the (4) Vesta asteroid. This classification comprises 6.7% of the asteroids in the taxonomy.

Taxonomic classification has been continuously evolving in recent years. For 50 years, there have been attempts to classify asteroids using spectroscopy and photometry. Owing to the advancement of increasingly new instruments and methods, ending up with the Mahlke classification. The S- complex is well understood in terms of mineralogy, meteorite material, and origin, whereas the other two complexes are still in doubt. On the basis of the characteristics explained previously, the three complexes have a total of 17 classes. Mahlke employs classy to categorize asteroids using the VisNIR spectrum and visual albedo. The UV data from Gaia may help clarify the uncertainties surrounding the C and M complexes.

The heterogeneity of an asteroid's surface may result in diverse taxonomic characteristics. Therefore, by obtaining spectra of a full rotation or at different phases, different classes can be found. The use of spectroscopy is crucial in studying NEOs, especially those smaller than 1 km, which cannot be observed in the MAB. It is crucial to determine its provenance within the main asteroid belt and comet population, as well as its chemical composition distribution [150], [151],[152]. Spectroscopic analysis is also essential in establishing a connection between meteorites and their original asteroidal parent body.

Furthermore, the study of visible spectroscopy together with NIR spectroscopy allows us to study the mineralogical composition of asteroids more comprehensively. The range between 0.7 and 2.5 μm is significant for the study of silicate minerals, such as pyroxenes, olivines and plagioclase, as they possess fundamental absorption bands centered approximately on 1 and 2 μm [99], [153], [154]. The 3 μm absorption bands correspond to the water and the OH structure discovered in hydrated silicates: they are used to map the spatial extent of aqueous alteration on the surfaces of asteroids [38].

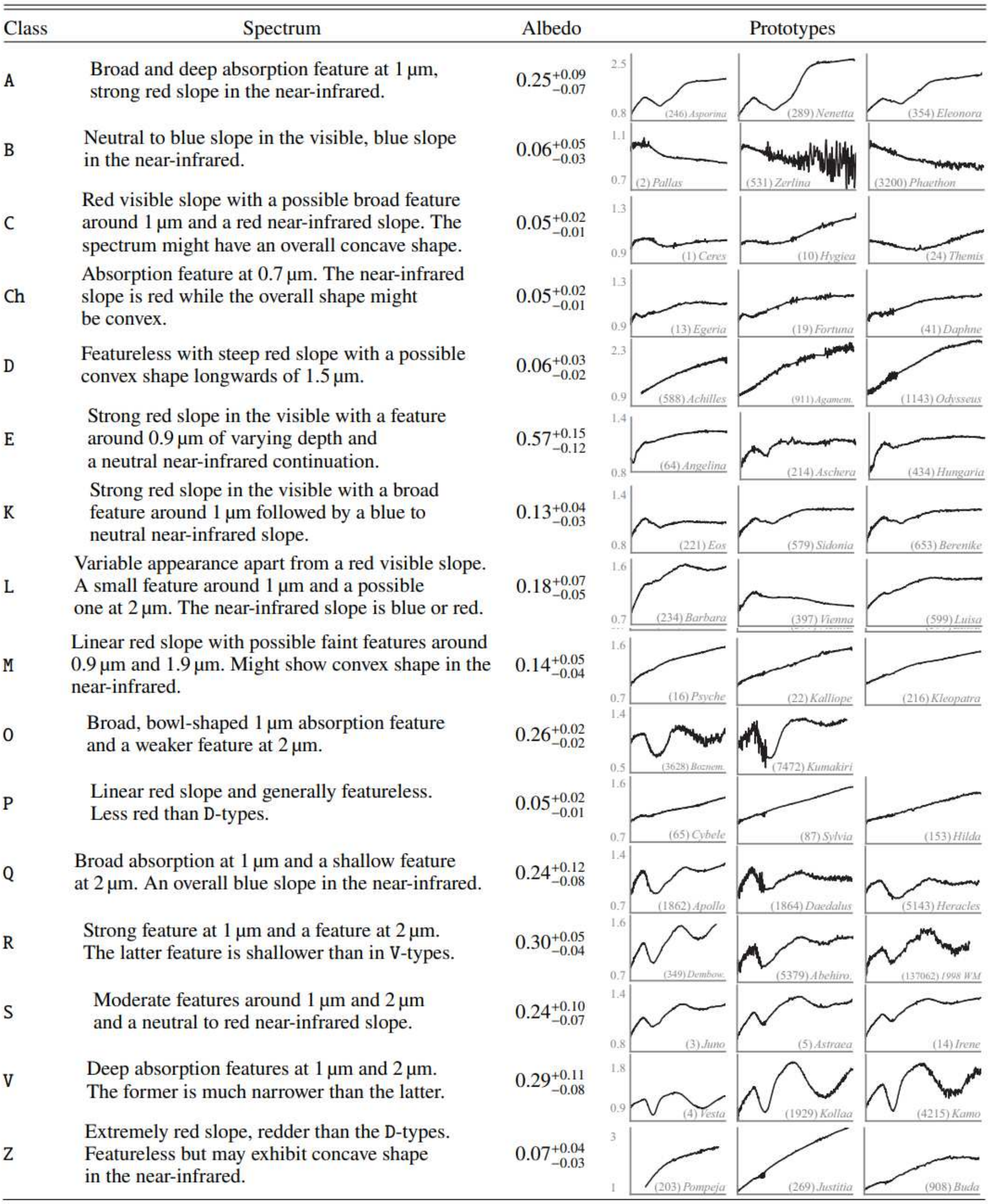

Class	Spectrum	Albedo	Prototypes
A	Broad and deep absorption feature at 1 µm, strong red slope in the near-infrared.	$0.25^{+0.09}_{-0.07}$	(246) *Asporina* (289) *Nenetta* (354) *Eleonora*
B	Neutral to blue slope in the visible, blue slope in the near-infrared.	$0.06^{+0.05}_{-0.03}$	(2) *Pallas* (531) *Zerlina* (3200) *Phaethon*
C	Red visible slope with a possible broad feature around 1 µm and a red near-infrared slope. The spectrum might have an overall concave shape.	$0.05^{+0.02}_{-0.01}$	(1) *Ceres* (10) *Hygiea* (24) *Themis*
Ch	Absorption feature at 0.7 µm. The near-infrared slope is red while the overall shape might be convex.	$0.05^{+0.02}_{-0.01}$	(13) *Egeria* (19) *Fortuna* (41) *Daphne*
D	Featureless with steep red slope with a possible convex shape longwards of 1.5 µm.	$0.06^{+0.03}_{-0.02}$	(588) *Achilles* (911) *Agamem.* (1143) *Odysseus*
E	Strong red slope in the visible with a feature around 0.9 µm of varying depth and a neutral near-infrared continuation.	$0.57^{+0.15}_{-0.12}$	(64) *Angelina* (214) *Aschera* (434) *Hungaria*
K	Strong red slope in the visible with a broad feature around 1 µm followed by a blue to neutral near-infrared slope.	$0.13^{+0.04}_{-0.03}$	(221) *Eos* (579) *Sidonia* (653) *Berenike*
L	Variable appearance apart from a red visible slope. A small feature around 1 µm and a possible one at 2 µm. The near-infrared slope is blue or red.	$0.18^{+0.07}_{-0.05}$	(234) *Barbara* (397) *Vienna* (599) *Luisa*
M	Linear red slope with possible faint features around 0.9 µm and 1.9 µm. Might show convex shape in the near-infrared.	$0.14^{+0.05}_{-0.04}$	(16) *Psyche* (22) *Kalliope* (216) *Kleopatra*
O	Broad, bowl-shaped 1 µm absorption feature and a weaker feature at 2 µm.	$0.26^{+0.02}_{-0.02}$	(3628) *Boznem.* (7472) *Kumakiri*
P	Linear red slope and generally featureless. Less red than D-types.	$0.05^{+0.02}_{-0.01}$	(65) *Cybele* (87) *Sylvia* (153) *Hilda*
Q	Broad absorption at 1 µm and a shallow feature at 2 µm. An overall blue slope in the near-infrared.	$0.24^{+0.12}_{-0.08}$	(1862) *Apollo* (1864) *Daedalus* (5143) *Heracles*
R	Strong feature at 1 µm and a feature at 2 µm. The latter feature is shallower than in V-types.	$0.30^{+0.05}_{-0.04}$	(349) *Dembow.* (5379) *Abehiro.* (137062) *1998 WM*
S	Moderate features around 1 µm and 2 µm and a neutral to red near-infrared slope.	$0.24^{+0.10}_{-0.07}$	(3) *Juno* (5) *Astraea* (14) *Irene*
V	Deep absorption features at 1 µm and 2 µm. The former is much narrower than the latter.	$0.29^{+0.11}_{-0.08}$	(4) *Vesta* (1929) *Kollaa* (4215) *Kamo*
Z	Extremely red slope, redder than the D-types. Featureless but may exhibit concave shape in the near-infrared.	$0.07^{+0.04}_{-0.03}$	(203) *Pompeja* (269) *Justitia* (908) *Buda*

Figure 2.4: list of Mahlke's 17 taxonomic classes, excluding X-types, with brief description, visual albedo mean value with relative standard deviation values, and three spectral examples for each class. The spectra range is between 0.45 and 2.45 μm. Table taken from Mahlke (2022) [13].

2.3 Asteroid Families

In 1918, Kiyotsugu Hirayama observed a number of asteroids orbiting around the Sun with very close unusually trajectories: he referred to them as "groups of asteroids probably of common origin" [155]. These groups, known as families, are composed of asteroids with similar orbital parameters (semimajor axes, orbital eccentricity and inclination) and similar physical properties. These asteroids were formed as a result of a collision between two minor celestial bodies within the Solar System. There are two types of asteroid families based on their origins: fragmentation and cratering families. In the former, the primordial body is completely destroyed, whereas in the latter, a parent body survives, as is the case of with (4) Vesta. Larger families may contain hundreds to thousands of asteroids, and it is estimated that 30-35% of the asteroids in the Main Belt belong to a family. Instead, groups of asteroids with similar orbital parameters but different origins are known as asteroid groups. These groups are composed of numerous small asteroids formed by primordial collisions of different magnitudes.

The study of asteroid families is crucial for various studies, including the NEO, in fact they bring some asteroids to the near-Earth region [156], [157]. In many cases, fragments of asteroids are brought into resonant orbits, such as the 3:1 or 5:2 mean motion with Jupiter, or the secular resonant v_6, or into the inner region of the Main Belt [158]. Within these areas, fragments can be swept towards the inner Solar System, indicating the continuous production of NEOs resulting from collisions within the inner part of the Main Asteroid Belt. Thus, the formation of families near the boundaries of the Asteroid Belt makes another contribution to the near-Earth region. Collisions between these families result in fragments being directed toward the orbits of the inner planets in a dynamic way [159].

Their research is significant in understanding the formation of the Solar System, modeling and studying the history of the collision that took place in the MAB [158], and dynamical evolution of the belt. The asteroid families represent an excellent example of low-energy collisional phenomena. Today, collisions are very rare, enabling the survival of organisms on the Earth. However, in the early stages of the Solar System, they were common and crucial for its evolution.

The parent bodies play a key role in determining the chemical composition of the family and their asteroids [160], [161], [162]. Moreover, such investigations can provide information on the heterogeneity of the proto-planetary disk, as well as the formation of planetesimals [163]. Additionally, examining families is crucial to better understanding the breakup events that led to the formation of these structures and how asteroids collide with each other at velocity of $5-6\ km/s$ [164], [58]. Families are employed to investigate the internal structure of asteroids, a key factor in the study of NEA impact hazards [158]. They are also linked to the size of asteroid fragments. The size is determined from the absolute magnitude and the albedo. In truth, families are distinguished by an even albedo distribution [165]. Furthermore, a correlation has been found between the dimensions of the fragments and their maximum ejection velocity [65]. The physical properties of families are studied based on three pieces of information: first, the coordinates of family members in the space of proper elements a', e', and i' (representing proper semimajor axis, eccentricity, and inclination, respectively); secondly, the size distributions of family members; and thirdly, spectrophotometric properties of the members [158]. Proper elements are obtained from instantaneously osculating orbital elements by removing periodic oscillations produced by gravitational perturbations of the planets [166].

Families are crucial for studying the effects caused by mean and secular orbital resonances as well as the non-gravitational Yarkovsky effect (see 1.2.2) [166],[167]. The orbital velocities of the fragments are linked to their ejection velocity, which varies based on the parent bodies. Furthermore, studying them can help us to understand the gravitational effects on the ejection velocities of the fragments. Finally, these findings help to understand the amount of water they brought to Earth, as some of the parent bodies contained water [163].

2.3.1 Families Spectroscopy

The study of the chemical composition and origin of asteroid families gave rise to spectroscopy of asteroids. The families originated from energetic collisional events. (4) Vesta was the first family with a collision origin to be found by spectroscopy. It belongs to the V taxonomic class and exhibits spectroscopic properties similar to those of basaltic achondrites. It is important to study the families for the properties and mineral composition in their inner layer and to detect random interlopers within the families. Interlopers share identical orbital characteristics with their respective families, but their taxonomic classification is different, they are not members of the family [15]. The number of interlopers and their identification can be determined through spectroscopic observations. This study is useful for measuring the size distribution of the fragments and for determining the overall properties of the original ejection velocity fields [168][158]. The spectroscopic observations conducted by Binzel and Yu reveled the existence of asteroids beyond the boundaries of their own family: they analyzed the Vesta family within the V taxonomic class. These objects were found in the region that separates the family from the 3:1 mean motion resonance with Jupiter. The Fig. 2.5 shows the members of the Vesta Family and the asteroids situated beyond its boundary.

The spectral properties of the families exhibit a high degree of homogeneity: it is advantageous to establish the mean reflectance characteristics and surface reflectivity of various groups [15]. Nevertheless, these members do not exhibit equal spectral reflectance. Variations can be very homogeneous or have small differences. The spectral properties of the groups are largely uniform, making it beneficial to determine the mean reflectivity and surface albedo values for each. However, there exist disparities between individual members' spectral

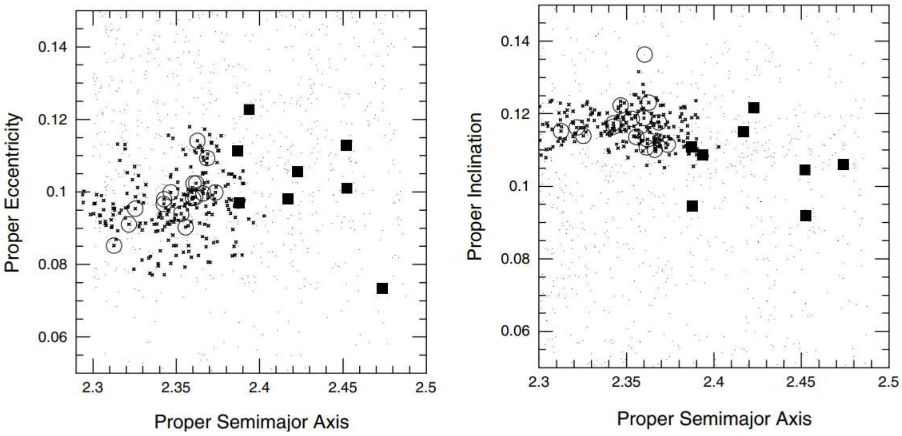

Figure 2.5: plot of asteroids located in the Vesta family in the space of the proper elements. The crosses indicate the elements of the family and the open circles indicate the basaltic asteroids found by Xu and Binzel [14]. Figure taken from Cellino (2002) [15].

reflectance; this range can be minimal or significant, reflecting differences in the mineralogical characteristics of their parent bodies and potential space weathering effects [169]. The Fig. 2.6 shows four families of asteroids: the Lydia family exhibits a considerable level of homogeneity, whereas the Agnia family demonstrates heterogeneity. These spectra were acquired and analyzed as part of the SMASSII spectroscopic survey by Bus (1999) [16]. Bus (1999) [16] plotted the proper inclination vs. semimajor axis for these asteroids in the Fig. 2.6. In this plot, the Hoffmeister families are in close proximity to each other, whereas the other groups are more dispersed: the results of these data are uncertain due to overlapping groups. Spectroscopy plays a crucial role in the physical properties of overlapping spectra. For instance, in this respect, the big Nysa family consists of two overlapping families of the taxonomic classes S and F [170].

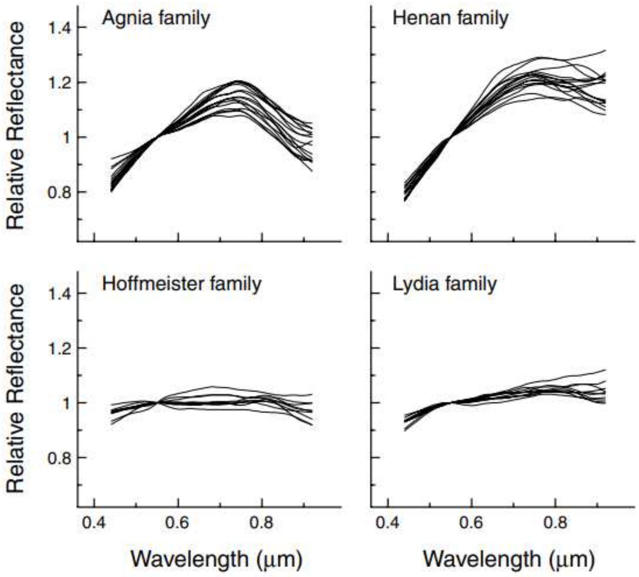

Figure 2.6: Bus (1999) [16] obtained spectra of four families. Some spectra show homogeneity in spectral properties, while others exhibit heterogeneity, such as those of the Agnia family. Figure taken from Cellino (2002) [15].

Bus [16] was the first to discover new families through spectroscopy, suggesting that they share a common collisional origin.

There are several families of asteroids, including Vesta, Eos, Polana, and Henan. The objects in Henan belong to the L taxonomic class [16], Polana belongs to the rare F taxonomic class [170], while Eos belongs to rare K-type characterized by the spectroscopic behavior between C- and S-class [171]. This fact led Zappala [172] to identify some asteroids in the 9:4 mean motion resonance band with Jupiter as members of Eos: they lie outside the family boundaries because they were moved away from the Main Belt during the early stages of the Solar System. As a result, these objects are perturbed by Mars and may cross Earth's orbit to become NEOs [15]. This indicates that families play a fundamental role in the production of the flux of NEAs and meteorites.

2.3.2 Identification of Families

There are various techniques available for identifying asteroid families, such as the Hierarchical Clustering Method (HCM), a Machine Learning-based (ML) method, a V-Shape method, and the Cladistic method. The most commonly used method to identify asteroids families is the HCM [173]. The methodology is based on a metric that quantifies the distances between different members of asteroids' family using three proper elements: semimajor axes, eccentricity, and inclination. The technique consists of clustering asteroids below a critical threshold distance. One significant advantage is that it is not based on an apriori any shape of the family. The disadvantage is the chaining effect (it is the first concentrations naturally tend to incorporate nearby groups, forming a chain [13]), if there are neighboring asteroids that are not part of the family, that is taken into account. However, asteroids within the same family share a homogeneous chemical composition [174] and surface reflectance characteristics (spectra, albedos, and colors). HCM cannot identify families that formed more than 3 Gyr ago because the dispersion of old group asteroids renders this method ineffective.
The Machine learning-based methodology is a reliable method for identifying asteroid families: Carruba [175] was the first to use it. This data analysis method uses algorithms to make predictions from input data sets. Various clustering algorithms are used in the PYTHON programming language to classify asteroids into families. Carruba utilized the distance acquired by Zappala [173] and analyzed the subpopulation of asteroids in the Main Belt through a high inclination orbit. The algorithm has the advantage of being able to identify groups in a very short time compared to the HCM method. However, its disadvantage is that the ratio of the number of correctly identified asteroids to the total number of asteroids in the family varies between 37 and 100%. Carruba [176] can accurately classify asteroids that do not belong to a family with 83-98% precision: the algorithms achieve better results when adding new members to existing families than when classification is done from scratch.
The V-shape method is an another tool to identify families. Identification of ancient asteroid families involves a clustering approach that takes advantage of the V-shaped data presented in the space occupied by the semimajor axis and the inverse of the diameter (or absolute magnitude) of the asteroids. An algorithm is employed to divide the data into two categories: the *border method* that utilizes a ratio between the number of objects just outside and inside the V-shape, and the *density method* that detects a peak of asteroids in a V-shape plane. These methods are used to identify primordial families. Walsh (2013) [177] was the first to use the V-shaped technique and identified the Polana family (group formed 2 Gyr ago) and the Eulalia family (group of 0.8-1 Gyr). Identification of families with an age range of 0.5-2.5 Gyr is easier and more efficient 80%, while those with more than 3 Gyr are more challenging.
The cladistic method proposed by Holt [178] is the last method to identify families: the methodology is built on the degree of parenthood, that is, the distance in time of the last common progenitor. An artificial neural network is used to analyze multiple parameters of the asteroid, including physical characteristics, orbital elements, and spectral features. This produces a phylogenetic tree that represents the evolutionary connections between asteroids. While it is advantageous to deal with missing data, it is time-consuming and does not always distinguish between independent and overlapping families.
In 2017, the creation of the Asteroid Families Portal (AFP) allowed access to a comprehensive database of all known asteroid families (http://asteroids.matf.bg.ac.rs/fam/). However, the immense volume of available data presents a formidable challenge in classifying these space

objects. It will be even more difficult in the future because the Vera Rubin telescope [84] will be expected to reveal millions of new asteroids in the Solar System, further compounds this issue. Due to its memory requirements, the HCM method will not suffice to manage the increasing number of objects. The newly available clustering methods will be used to address this challenge.

2.3.3 Dynamical Evolution

To study the dynamic evolution of families, it is necessary to examine the mechanisms that affect them. These can be categorized into gravitational and non-gravitational effects. When considering the former, it is impossible to take into account all the gravitational forces exerted by all objects in the Solar System. The eight planets of the Solar System and the most massive asteroids are responsible for the greatest gravitational influence. Non-gravitational effects include the YORP effects (see section 1.2.2). Additionally, the evolution of families is a result of collisional evolution. Collisional and dynamical evolution are interconnected, and it is essential to consider both when studying the evolutionary effects of families.
Novakovi's work [179] allows the study of the dynamics of small Solar System objects due to secular resonances. Indeed, by modifying the orbital inclination of family members, nodal secular resonances (the temporal evolution of the ascending node of an orbit resonantly interacts with other components of the dynamical system) indirectly modify the initial Ejection Velocity Field, in particular the velocity component out of the orbital plane. This fact can be analyzed to obtain the post-impact inertial velocity distribution [180]. For example, Carruba [180] used members of the Astrid family (with an unusual distribution of orbital inclination) to study constraints on parameters that describe the Yarkosky force, such as mass and surface density, and the thermal conductivity of the surface material.
Orbital element analysis is fundamental for studying the dynamic evolution of families in the long term. By studying the Yarkovsky effect, one can derive the age of families, as seen in the studies of Lowry [181]. Modeling the YORP effect presents a crucial and complex challenge in analyzing dynamic evolution. It modifies the spin axis orientation and spin rate of the asteroids, which affects the Yarkovsky effect, which depends on the rotation state of the asteroids. The YORP effect, however, depends on the shape and small scales topography (the presence of boulders and craters at the surface) of the asteroid. Therefore, to accurately model the Yarkovsky effect, it is necessary to model the combined effect of YORP and impacts. The YORP effect is made up of two components: stochastic and deterministic [57], [182], [183]. When considering only the deterministic component of the YORP effect, the evolution of the spin axis as a result of YORP reduces the magnitude of the Yarkovsky effect that is dependent on obliquity [183]. Thus, a decrease in the Yarkovsky effect is expected due to YORP, but this is not consistent with the observations obtained. For instance, the close approach of near-Earth asteroids is far too low to match the observations when the YORP effect is taken into account [184]. For this passage, adding both the stochastic component of the YORP effect and the spin evolution owing to impacts is necessary. However, it should be noted that different authors use varying models, which can yield varying results. Examples of these models include Bottke's [185] and Marzari's [186].

2.3.4 The age of families and the Ejection Velocity Field

Studying the long-term dynamic events of asteroid families requires the fundamental parameter of the initial ejection velocity field (EVF), that is the field of initial velocity arises from a collision. Its usefulness lies in understanding the physics of collisional events and studying the internal structure of asteroids. However, estimating the initial EVF of an asteroid family is a complex task; it involves two parallel studies: the evolutionary process and the age determination. Thus, by examining the family's evolution, one could obtain its age and EVF. Cellino [65] discovered a connection between size and ejection velocity among some family members: he observed an inverse relationship between ejection velocities and on the size defined by an exponent ranging with a power of -2/3 to -1.

Another crucial factor is the determination of the families' age, specifically the precise moment of the collision that brought about their formation. It is essential to know their age to understand the long-term development of the asteroid family. There are numerous dating approaches, and families are grouped into young or very young families formed less than ten million years ago and older families formed approximately fifty million years ago [163].

- **Old families:** families that are older than 50 million years can be dated using the Yarkovsky/YORP chronology and this method can be applied to nearly all older families. Family members evolve over time by changing positions away from the main body. The distance and velocity of the movement far away from the parent body can be calculated to determine the age of the family.
  The Yarkovsky effect is a non-gravitational perturbation caused by the thermal emission of thermal photons from the asteroid's surface [163] (see section 1.2.2). The effect depends on physical properties, including thermal inertia, albedo, and density, and is proportional to the inverse of the diameter of the asteroid. As a result, the effect is more pronounced in smaller bodies, causing significant changes in the semimajor axis over millions of years [187], [188]. As a result of this phenomenon, the smaller objects in the group move outward, creating the V-shape studied above. The V-shape occurs because of two processes: EVF and the secular evolution of the semimajor axis resulting from the Yarkovsky effect. Based on Michel's research [189], it is expected that the larger fragments initially have lower velocities than the smaller fragments, so that the smaller fragments are more widely spaced. Due to the Yarkovsky effect, smaller fragments drift farther from the larger body. As the current distribution ages, the initial EVF contribution decreases. Additionally, the probability of family formation suggests that families formed by larger bodies are older [190], and that the rate at which bodies are ejected increases with their size: more massive bodies release fragments at higher velocities. In conclusion, the Yarkovsky effect significantly restricts the method's calculation, as it relies on specific physical properties, including density, surface thermal properties, and spin state. Another limiting factor is the YORP effect, which alters the spin state of asteroids, leading to the Yarkovsky effect. Additionally, encounters with massive asteroids can alter the semimajor axis, resulting in a reduced observation of the V-shape. Ages have been calculated for more than 50 families in various studies [161], [191], [166] utilizing uniform methods, which is critical to determine age in the Main Belt.

- **Young families:** their age can only be determined through purely dynamic methods. The Veritas family was the first example when chaotic dynamics were used to determine

> the age of a family [192]. Following this, researchers began to use regular dynamics methods, such as the Backward Integration Method (BIM), which involves examining the convergent behavior of secular angles, to date families such as Karin [193]. The Karin and Veritas families have since become fundamental archetypes for establishing the age of young families.

In the future, more accurate age estimation are expected to be available. Additionally, with a greater number of asteroids and a better understanding of their physical properties, it will become easier to obtain more precise ages. The Gaia mission, led by the ESA, will aid in calculating ages accurately by studying the Yarkovsky effect on small objects' orbits. Gaia aims to obtain an age measurement for each family or alternatively for each spectral type. Such an effort would help to significantly reduce uncertainties surrounding age [163].

2.3.5 Family and their relationship with NEO

The investigation of families is closely related to NEO objects. Families provide a large number of asteroids that pass close to Earth orbit and produce a stream of meteorites to Earth [194], [14], [156]. As time progresses, some objects dissociate from their families and escape into near-Earth Space [195]. Although this phenomenon has fascinated many researchers, there are still many unanswered questions. All families contribute to the formation of NEOs, but only families located near the Main Belt transport routes to the near-Earth region are capable of carrying asteroids directly to these routes. Objects situated within these routes experience only a limited lifespan of a few million years due to their rapid transportation to the near-Earth region immediately following family formation (see Fig. 2.7) [82].
Some studies indicate that families formed with multiple members located near transport pathways cause the most cratering of terrestrial planets [196]. Therefore, families located inside strong orbital resonances are the main sources of NEAs. These fragments are directly injected and can be transported quickly, causing many objects to reach the near-Earth region in a short time after the family's formation. In contrast, families that do not eject their objects along the trajectories send a more stable number of fragments to the near-Earth region. Additionally, larger asteroid swarms towards Earth are caused by families located near powerful resonances. To maintain a stable population of objects that are close to Earth, Zappala [196] has explained that asteroid populations within powerful resonances are reformed by asteroid fragments. The Yarkovsky effect [197] later explained this mechanism.
To link clusters and families of asteroids, it is essential to consider various factors such as dynamic evolution, transport routes, the size of the progenitor body, EFV, and age of exposure to cosmic-ray exposure. The Gefion asteroid family is an example of a link between meteorites and asteroids, which serves as a source of L-type chondrite meteorites [198]. Another notable example is the Flora family, which is a significant source of NEO-type chondrite meteorites due to its close proximity to the ν_6 resonance. Bottke [199] studied five other families of the Main Belt, namely Erigone, Sulamitis, Clarissa, Eulalia, and New Polana. Additionally, Euphrosyne is an important family with some of the lowest known albedo values, and its members' large orbital inclinations cause them to cross the ν_6 resonance [106]. One last important family is the Karma family, located in the outer region of the 3:1 resonance with Jupiter, which has provided some asteroids in the near-Earth region [17]. The study remains open-ended, as virtually all families may contribute to NEO objects, and new correlations will be uncovered in the future.

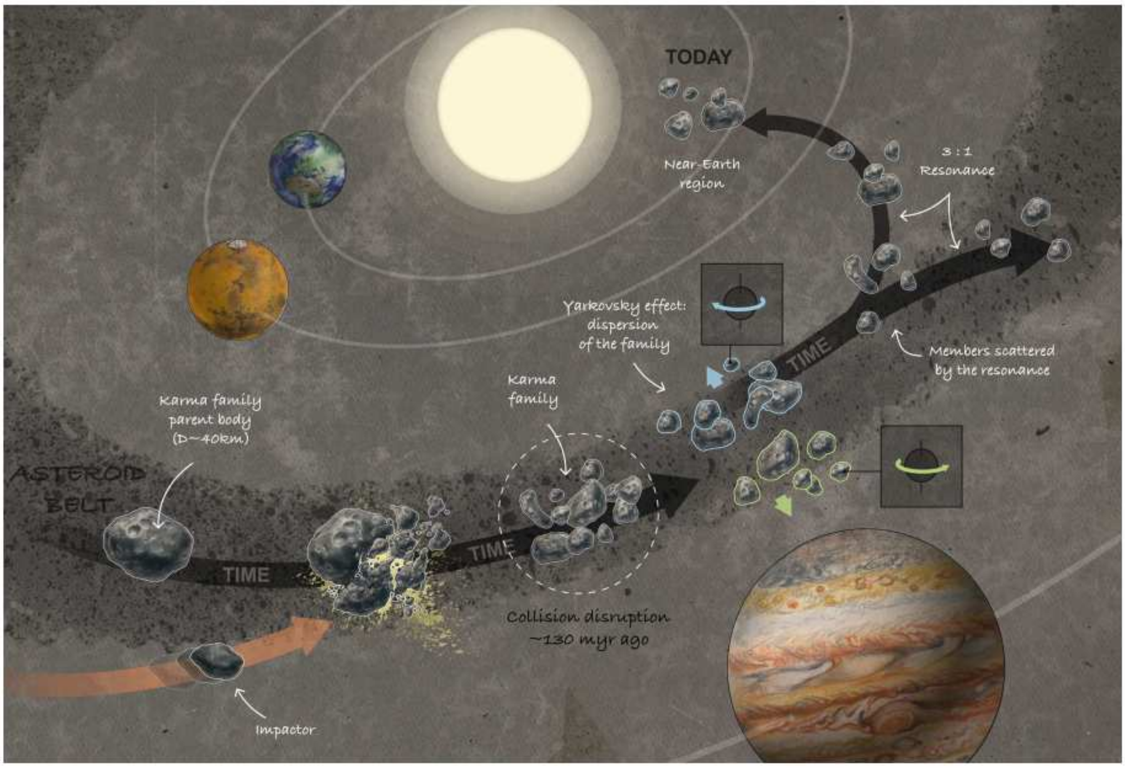

Figure 2.7: illustrates the various steps in the dynamic evolution of an asteroid family. It was created based on the work done on asteroid Karma by Pavela [17] and is taken from Mahlke (2002) [13].

Chapter 3

Didymos and DART

3.1 The binaries asteroids

The population of binary asteroids continues to increase. Specifically, between the great book Asteroid III [200] and Asteroid IV [201], the population increased from 33 to ~ 244: 49 NEAs, 19 Mars crossers, 93 MBAs and others not yet classified [202], [203]. Binaries and triples are gravitationally bound asteroids, while asteroid pairs are pairs of related but not gravitationally bound asteroids [18]. Paired binaries and triples are groups of two/three asteroids in which the primary NEA on a binary system is itself a binary or triple. The primary NEA, or primary asteroid, is the larger asteroid in the binary/triple system.

Radar is considered the primary tool used to detect multiple asteroid systems: it has played a crucial role in the discovery of most binary systems. According to radar observations, it is estimated that approximately one in six NEAs larger than 200 m in diameter is a multiple system [204], [205]. Radar can detect asteroidal satellites because it can resolve the components of the system both spatially (along the observer's line of sight) and in frequency (due to Doppler shifts in rotational and orbital line of sight velocities), resulting in a measurable separation between the two components. Additionally, the radar images provide valuable information about the shape of the primary body. A primary NEA typically exhibits a circular equatorial bulge, with uniformly sloped sides, and a spinning top-like polar flattening. The shape of smaller satellites cannot be resolved by radar, but radar images suggest that they are typically stretched [18]. Furthermore, it is important to note that radar has a limited range and can only reach about 0.2 AU from Earth.

Another method of detecting binary asteroids is to use the photometric curve: this technique involves examining the light curve of an asteroid. The components of the binary system can obscure or cast a shadow on each other, resulting in occultations or eclipses [18].

Multiple systems are considered important for studying the physical properties, composition, internal structure, formation, and evolutionary processes of minor planets [18]. Binary asteroids, in particular, are known to provide valuable information on the mass and density of objects, which is crucial to understanding their composition and internal structure. The formation mechanisms are different in multiple systems, depending on the different populations: NEA, MBA and TNO [206], [207]. This allows the study of various processes, such as accretional, collisional, tidal, and radiative processes that are important for the formation of planets. Furthermore, binary asteroids provide an opportunity to study the thermal and mechanical properties of asteroids. Spectroscopic observations of around 20 pairs of asteroids have shown similar spectra [18]. For some pairs, there are some small differences, which is attributed to a greater amount of eroded material on the surface of the primary [18].

3.1.1 Binary overview

In 1993, the Galileo spacecraft discovered the first binary asteroid, flying over (243) Ida and discovering its satellite Dactyl (see fig. 3.1) [208], [209]. All research programs prior to this mission had been unsuccessful, and it was difficult to imagine when asteroids could have satellites. Later on, many binary asteroids, such as (45) Eugenia [210], were discovered. According to research, MBA satellites are believed to have originated from subcatastrophic (capture through a three-body interaction in the near-Earth or Main Belt), or capture after a catastrophic impact, probably due to their small size [211], [212]. Furthermore, it has been observed that NEAs can exist as binary systems, and their formation is through rotational fission process [204]. Asteroid binaries are difficult to discover, but many asteroids have a satellite [18].

Figure 3.1: the Galileo spacecraft captured images of the asteroid Ida and its moon Dactyl as it traveled towards Jupiter in 1993. Figure taken from apod.nasa.gov

3.1.2 Binary Classification

The properties of binary systems depend mainly on their size. In the case of NEAs, the primary body is typically less than 10 km in size, whereas the secondary body ranges from 4 to 58% of the primary body's size. The distance between the two bodies can range from 2.5 to 7.2 primary radii and the system exhibits a fast-spinning primary with rotation period between 2.2 and 4.5 hours [213]. The binary asteroids in the small MBA population ($D < 15$ km) exhibit similar properties to the binary systems of the NEAs. However, it should be noted that binary asteroids in the large asteroid population ($D > 15$ km) have different characteristics. For instance, their satellites are smaller, but they orbit are larger [213].
Due to the increase in known binary systems between NEAs and MBAs, a classification has been made [202]:

- Group L: Large asteroids (diameter $D > 20$ km) with very small satellites (secondary to primary diameter ratio: $D_2/D_1 \leq 0.2$). Their rotational periods of the primary range from 4.1 to 7.0 hours.
- Group A: Small asteroids ($D < 20km$) with very small satellites ($0.1 \leq D_2/D_1 \leq 0.6$) in tight mutual orbits (semimajor axis, a, less than 9 primary radii, R_p).They have a rotational period of 2.2-4.4 hours.
- Group B: Small asteroids ($D < 20km$) with large satellites ($0.7 \leq D_2/D_1$) in tight mutual orbits ($a \leq 9R_p$).
- Group W: Small asteroids ($D < 20km$) with small satellites ($0.2 \leq D_2/D_1 \leq 0.7$) in wide mutual orbits ($a \geq 9R_p$).
- Three outliers: (90) Antiope and (617) Patroclus would be from group L with the characteristics of group B, but are much larger than those of group B ($D \sim 87-101km$) and (4951) Iwamoto has the characteristics of group B, but much wider mutual orbit ($a \sim 17R_p$).

NEA systems typically consist of a rapidly rotating primary asteroid and a smaller secondary asteroid, whose rotation is synchronized with the mutual orbit period [18]. The primary NEA usually completes a rotation in less than 2.8 hours, although this can vary from 2.2593 hours for (65803) Didymos [214] to 4.749 hours for 1998 QE2 [215]. Additionally, it is worth noting that the Didymos satellite has one of the shortest known orbital periods ($11.90^{+0.03}_{-0.02}$).

3.1.3 Formation of Binary

Binaries can be formed through three possible mechanisms: collisional breaking, rotational fission, and the splitting of unstable asteroid binaries [216]. The rotational fission mechanism can be explained by a correlation between the rotational periods of the primary asteroid and the mass ratio q between the secondary and primary asteroid. This correlation matches the Scheeres model [217], where the primary undergoes rotational fission with zero drag. It has been observed that pairs with low mass ratio pairs ($q < 0.05$) did not undergo a spin slowdown during the separation process. As a result, they are expected to rotate at a faster frequency, close to the fission spin rate. On the other hand, medium-high pairs with $q = 0.5$ experienced a spin slowdown due to the subtraction of angular momentum from the secondary. Finally, pairs with $q > 0.2$ should not exist because the energy released by the system formed by rotational fission would be negative and the main asteroid would not be able to split into two parts.

Asteroids in small systems move very fast and have very high angular momentum [202]. Thus, these properties are not consistent with subcatastrophic postimpact formation, capture by a three-body iteration, or capture after a catastrophic impact [18]. The most plausible hypothesis remains rotational fixation. According to the hypothesis, primary asteroids in a binary system can reach high speeds, which may cause centrifugal accelerations to exceed the gravitational accelerations that hold an asteroid together without drag [218]. In some cases, small asteroids have a cohesive or molecular drag, so centrifugal forces must overcome these forces [18]. As a result, the asteroid may split into two parts.

Finally, Bottke [11] proposed a YORP-induced rotational fixation hypothesis: the YORP effect drives the rotational acceleration of small asteroids and explains their period distribution [18]. The YORP effect increases the velocity of asteroids by taking them above the breaking point, i.e. by starting rotational fission. By assuming a spherical asteroid, its critical break-up velocity can be computed. In particular, in the case of two spherical components, one on top of the other, with mass ratio q, rotating about the axis of inertia, the breaking fission velocity is:

$$w_q = w_d \sqrt{\frac{1+q}{\left(1+\sqrt[3]{q}\right)^3}} \tag{3.1}$$

where w_q is the rotational breakup spin rate and w_d is the critical disruption spin limit ($w_d = \sqrt{4\pi\rho G/3}$). The formula demonstrates that a higher q ratio leads to a lower rotational break-up spin rate. The initial free energy (E_f) of the binary system is determined by its velocity, which in turn determines whether the objects will remain bound or separate. Negative energies indicate that the objects will remain bound, thus determining the system's stability. The energy can be calculated using the following formula:

$$E_f = \frac{2\pi\rho w_d^2 R_p^2}{15} \cdot f(q) \tag{3.2}$$

where R_p is the radius of the primary and $f(q)$ is an algebraic, monotonically decreasing function for $0 < q \leq 1$. The energy will be negative if $q > 0.2$ and vice versa. This formula is always applicable in the two-sphere approximation. As a result, binary systems with a $q > 0.2$ or $q < 0.2$ evolve differently [219],[220].

The distinction between high- and low-mass ratios allows for different rotational fixation scenarios [221]. The different scenarios are illustrated in Fig. 3.2. In the upper part ($q \geq 0.2$), the two binary objects synchronize tidally and then evolve according to the BYORP effect. However, in the case of a low mass ratio, the two bodies are not bound and often break apart to become asteroid pairs. The system can take on one of three scenarios: a reshaped asteroid, an asteroid pair, or a stable binary. It is important to note that as the system still has positive energy, it may be disrupted.

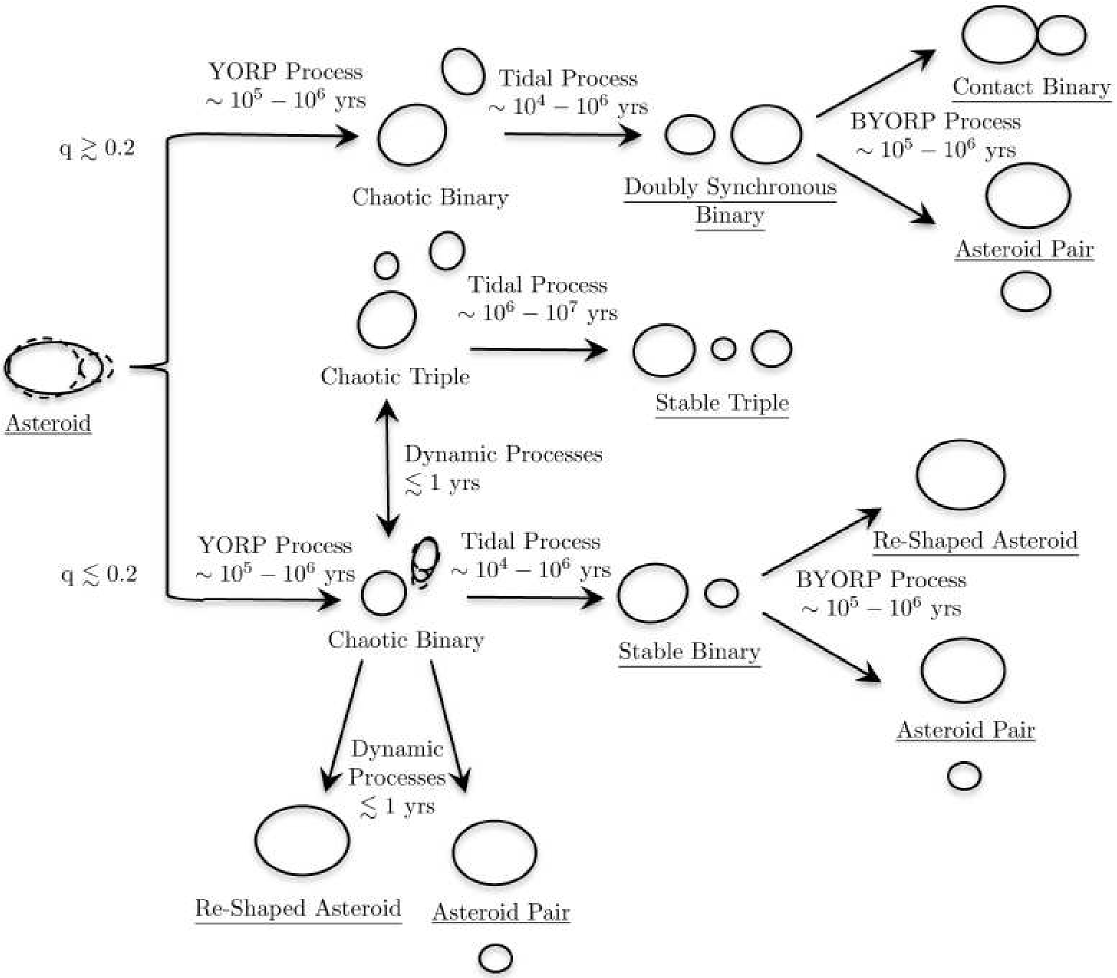

Figure 3.2: flowchart showing potential evolutionary trajectories for an asteroid following rotational fission. Each arrow is annotated with the predominant process and an estimated time frame for that process. The states underscored are nominally stable over the YORP effect timescale. Figure taken from Margot (2015) [18].

3.2 AIDA program

After the Don Quijote technique was abandoned [222], NASA and ESA began studying two independent but related missions to perform a deflection test using the kinetic impactor technique. These studies led to the creation of the international collaboration Asteroid Impact and Deflection Assessment (AIDA), supported by NASA and ESA [223][224]. The purpose of AIDA is to investigate the kinetic impactor technique for analyzing the orbit deflection of an asteroid, as well as to better understand momentum transfer and a possible impact crater formation [20]. AIDA will combine the results of two missions: Double Asteroid Redirection Test (DART) and Hera missions. The first mission was studied by ground telescopes before and after impact, as well as through LICIACUBE [225]. The second mission will study the binary system in detail after the impact of DART. Initially, the objective of Asteroid Impact Mission (AIM) was to reach the binary system with Hera before the impact of DART. However, due to a lack of funds, the mission was approved by the ESA Council at the Ministerial level in November 2019, which will result in Hera's arrival four years after the impact of DART.

3.2.1 DART

DART is a planetary defense demonstration mission managed by NASA's Planetary Defense Coordination Office (PDCO) [19]. DART mission has launched on 24^{th} November 2021 from Vandenberg Space Force Base in California, and the impact on Dimorphos occurred on 26^{th} September 2022 at 23.14 UT [21]. The main goal of the mission is the impact of DART on the satellite of (65803) Didymos: Didymos I Dimorphos (referred to exclusively as Dimorphos in the literature) in order to demonstrate that the "kinetic impactor" is a successful technique for planetary defence. This technique involves hitting an asteroid with a high-velocity mass to significantly change the orbit of the asteroid. It is one of several proposed methods for planetary defense in the future [19]. In addition, the Italian Space Agency (ASI) integrated DART with a 6U CubeSat named the Light Italian CubeSat for Imaging of Asteroids (LICIACube [225]). LICIACube provided documentation of the impact of DART and its immediate consequences. The data from LICIACube allowed the characterization of the Didymos system and the ejecta plume caused by DART, as well as the possible crater formed by DART [21]. DART had a narrow-angle imager called the Didymos Reconnaissance and Asteroid Camera for Optical navigation (DRACO). DRACO was used for optical navigation, terminal guidance, and asteroid characterization.

3.2.1.1 The goals of DART Mission

The DART project was based on ESA's Don Quijote mission concept [226]: a rendezvous spacecraft arrive at the asteroid for initial observations, and then a kinetic impactor arrive, while the rendezvous spacecraft remained nearby for observations. However, due to the high cost of two missions, it was decided to opt for a single spacecraft [19]. This was achieved by calculating the change in the orbit of Dimorphos before and after the kinetic impact. Orbit measurements are obtained by analyzing photometric curves captured from ground-based telescopes and by monitoring the timing of mutual events (such as occultation and eclipses), between the primary and secondary bodies before and after the experiment [214].
Before choosing Didymos as mission target, about 60 NEAs were identified as potential

targets. The accessibility of the mission target is measured in ΔV, which refers to the energy required to reach an object. Didymos had a ΔV that made it one of the most accessible among these 60 NEAs [19]. However, it is important to consider other factors as well. For instance, there were asteroids with a lower ΔV than Didymos, but with much larger satellites that could not be moved measurably by spacecraft masses, or that do not approach Earth for several decades, or that are not visible as non-eclipsing from Earth for large stretches of their orbit. However, Didymos is an excellent binary system with an orbit favorable for measuring changes in orbit through photometric measurements and will be visible for a long period [19]. Additionally, Didymos has another advantage: its visible-near-IR spectrum shows a composition consistent with L/LL chondrites, the chemical composition of meteoroids that commonly fall on our planet. During ground observations, it is not possible to study the primary asteroid's satellite, but previous studies have shown that the satellite is composed by material from the primary asteroid [18], [227]. Furthermore, studies of NEAs have shown that the albedos of a binary system are equal or similar within 20% [214]. Therefore, these results provide certainty that Dimorphos is likely an L / LL chondrite. This mission has an additional advantage: the diameters of Dimorphos is 165 m, very close to the minimum size (140 m) for an object to be defined as a potentially hazardous asteroid (PHA). Therefore, Dimorphos has the typical dimensions of common PHAs. The combination of these advantages means that the results of the DART mission will aid in planetary defense against a large number of possible asteroids [19].
Space missions have a set of Level 1 (L1) requirements that must be met to make the mission successful. Below are the five objectives of the Level 1 DART mission [19]:

- DART-1. DART shall intercept the secondary member of the binary asteroid (65803) Didymos as a kinetic impactor spacecraft during its 2022 September-October close approach to Earth.
- DART-2. The DART impact on the secondary member of the Didymos system shall cause at least a 73 s change in the binary orbital period.
- DART-3. The DART project shall characterize the binary orbit with sufficient accuracy by obtaining ground-based observations of the Didymos system before and after spacecraft impact to measure the change in the binary orbital period to within 7.3 s (1σ confidence).
- DART-4A. The DART project shall use the velocity change imparted to the target to obtain a measure of the momentum transfer enhancement parameter referred to as β (momentum transfer efficiency) using the best available estimate of the mass of Dimorphos.
- DART-4B. The DART project shall obtain data, in collaboration with ground-based observations and data from another spacecraft (if available), to constrain the location and surface characteristics of the spacecraft impact site and to allow the estimation of the dynamical changes in the Didymos system resulting from the DART impact and the coupling between the body rotation and the orbit.

It should be noted that modifying the orbital period of the binary system means changing the orbit of Dimorphos around Didymos, not modifying the orbit of the entire system around the Sun [19]. In addition to these objectives, there are other secondary objectives that are not less important: investigating the dynamic evolution of ejecta using ground-based telescopes, analyzing the dynamic effects of the DART impact, modeling the ejecta through nearby and distant fields, constraining the impact location, determining the physical properties of Didymos system, and characterizing the impact site [19].

DART-1 and DART-2

From 1st January 1996, Didymos reached its minimum distance from Earth (0.048 AU) since 2003. On 4th October 2022, it reached 0.071 AU and will only reach a closer distance on 20th October 2062 (see Figure 3.3). Therefore, it was chosen to impact in September 2022 because it allowed the best ground observation over the next 40 years. Furthermore, during the impact period of DART, there were the best opportunities to make high-quality radar measurements until 2062 [228]. DART-L1 indeed requires the best possible ground observations, when radar observations, although not mandatory, could provide useful information for the study of this system [19].

DART must impact Dimorphos and transfer enough momentum to cause the required period variation for DART-2. Dimorphos orbits Didymos in approximately 11.9 hours, or 42,840 seconds [214],[229],[228]. To achieve this goal, a 10% phase shift in the orbit must be obtained compared to the unperturbed case after one month. Therefore, Dimorphos completes approximately 59 orbits in 29 days, meaning that the variation in period must be 4284 seconds in 59 orbits, or 73 seconds per orbit. The spacecraft was designed to impact Dimorphos as close to the head as possible, specifically near the center of its leading hemisphere [19]. To study the system's orbit and assist DART's approach to the system, its properties must be determined (for example, using light curves or radar measurements). Therefore, ground observations were crucial in determining the position of Didymos relative to Dimorphos in order to properly organize the impact of DART. Additionally, it is important to consider the model binary system dynamics: Didymos and Dimorphos are not spherical and are very close to each other, approximately 730 meters apart (3.1 radii of Didymos). This makes the dynamics of the system more complex compared to a two-body Keplerian system [19].

DART-3

To obtain the required DART-3, astronomers must determine the property of the Didymos system and measure the variation of the orbital period. The former is similar to what is required for DART-1 and -2. Knowing the Didymos system before impact is necessary to determine changes in DART's orbital parameters [19]. Therefore, it is crucial to determine the position, orbit, rotation period, size, composition, and shape of Dimorphos. To calculate the change in orbit after impact, numerous collaborations around the world ensure highly precise measurements [19].

DART-4

The DART-4 requirement is divided into two parts: the threshold requirement (DART-4A) and the baseline requirement (DART-4B). DART-4A and DART-4B have different data requirements. DART-4A uses the same data as the other three requirements, while DART-4B uses additional data and analysis, such as that from LICIACube [19]. Both aim to calculate the momentum transfer efficiency factor β. To determine beta, the momentum of Dimorphos before and after impact must be compared, knowing the momentum carried along by DART itself. The initial hypothesis is that the momentum is not due to the momentum provided directly by DART, but rather to the momentum carried by the ejecta (see Figure 3.4). More details:

- **DART-4A:** aims to measure the parameter β. It does not directly calculate the mass of the body but rather calculates it from the determination of its shape (volume) and density calculations made previously. Additionally, β is a non-linear function of several input factors that are calculated by researchers to obtain very precise estimates [19].
- **DART-4B** its requirement is to accurately determine the β parameter and characterize the impact site, ejecta generated by the impact and dynamic changes in the Didymos system resulting from the impact of DART. LICIACube will model the ejecta on small and large spatial scales. Observations of the ejecta will also be attempted using space-based and ground-based telescopes. The impact site determination of Dimorphos and its characteristics will be based on the analysis of Didymos Reconnaissance and Asteroid Camera for Optical navigation (DRACO) onboard DART images, using LICIACube images. LICIACube will define the ejecta and the possible impact crater [19].

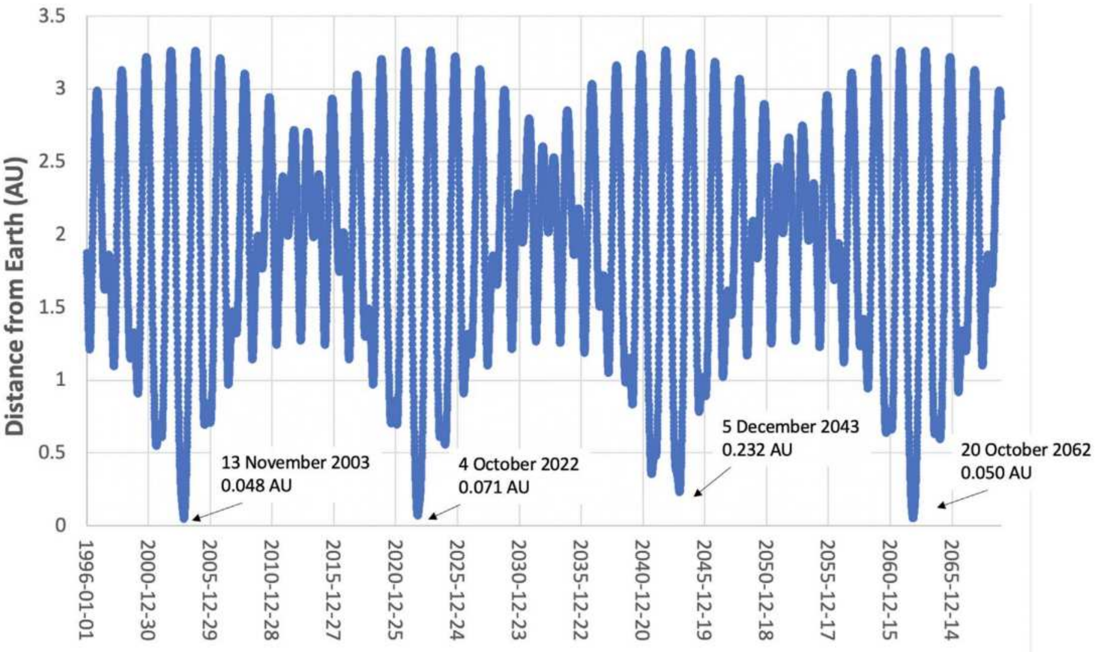

Figure 3.3: this graph shows the distance between Didymos and Earth from 01-01-1996 to 14-12-2065. Didymos will be very close to Earth ($< 0.1AU$) three times during this time period: on 13-11-2003, 4-10-2022, and 20-10-2062. Figure taken from Rivkin (2021)[19]

.

3.2.2 Hera mission

Hera will be the first mission designed to rendezvous with and characterize a binary asteroid. Previous missions to asteroids have revealed diversity in terms of geophysical and compositional properties, as well as the geophysical complexity of each asteroid taken separately.

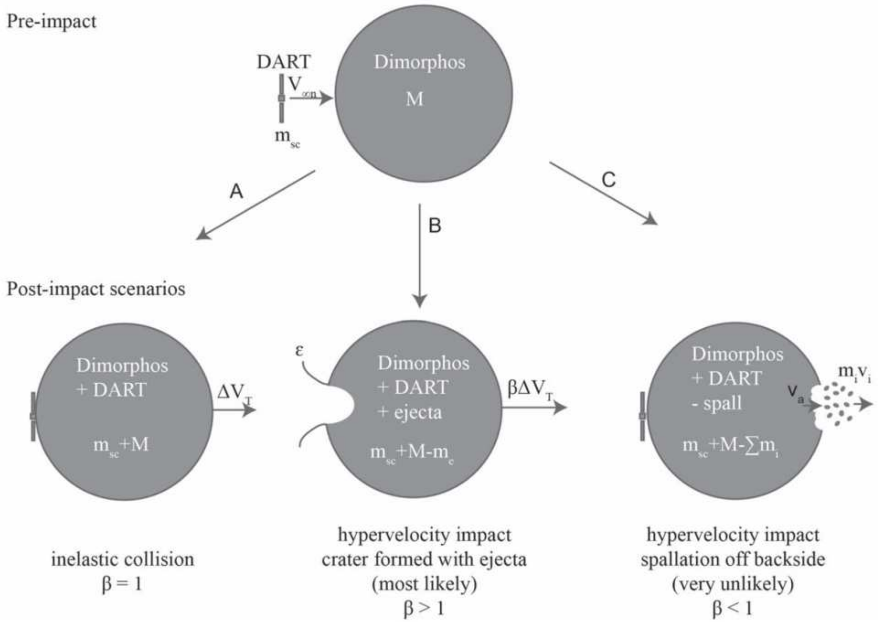

Figure 3.4: possible scenarios post DART impact. (A) Slow-velocity or inelastic collision adds DARTs momentum to the asteroid, $\beta = 1$. (B) Hypervelocity impact creates a crater and results in ejecta being thrown off asteroid, which acts to increase the momentum of the asteroid system, $\beta > 1$. (C) In a very unlikely case, spallation on the backside of the asteroid after the collision could act more than to counteract the enhancement of the momentum of the spacecraft, resulting in $\beta < 1$. Figure taken from Rivkin (2002) [19].

Hera will contribute to the geophysical understanding of small bodies and binary systems [20].

The Hera mission is currently under development as part of the European Space Agency's (ESA) Space Security Programme for launch in October 2024 with a launch schedule between 8^{th} and 25^{th} October 2024 [20]. The baseline launcher will be an Ariane 6.4 with a Falcon 9 launcher as backup. In summary, the Hera mission will arrive at the Didymos system and study their subsurface and interior properties. It will measure the result of the kinetic impactor test, providing valuable information for the development of techniques for planetary defense, mining extraction, and scientific purposes [230].

The following are the main objectives of the Hera mission, as written by Michel et al. [20]:

- Measure the mass of Dimorphos to fully determine the momentum transfer efficiency from DART impact.
- Investigate in detail the crater produced by DART to improve our understanding of the cratering process and the mechanisms by which the crater formation drives the momentum-transfer efficiency.
- Observe subtle dynamical effects (e.g., libration imparted by the impact, orbital, and spin excitation of Dimorphos) that are difficult to detect for remote observers.
- Characterize the surface and interior of Dimorphos, which have a great influence on

the impact response, to allow scaling of the momentum-transfer efficiency to different asteroids.

In addition to the DART-HERA joint objective, the HERA mission was also other specific objectives:

- Perform the first comprehensive characterization of a NEA, including for the first time its internal properties, allowing a precise comparison with theoretical models and assessment of the binary NEA production mechanism.
- Constrain the surface structure and regolith mobility on both Didymos and Dimorphos, thereby allowing a first insight into how material properties may affect asteroid satellite formation.
- Allow, for the first time, to measure the detailed surface and subsurface properties of an asteroid crater formed in an impact experiment at an impact speed ($\sim$ 6 km s^1) that is close to the average speed of interasteroid collisions [58].
- Provide a remarkable opportunity to study the surface geophysics of two objects of different size and surface gravity, probably formed from the same material.
- Obtain the first in situ measurements of the properties of an asteroid, Dimorphos, whose size ($\sim$ 160 m diameter) is at the frontier between gravity- and strength-dominated structures.
- Characterize a crater formed with known energy on a body 160 m in diameter for the first time, allowing us to verify whether strength or gravity is the most influential parameter in crater production on such a small asteroid.
- Observe native and post-DART surface activity and particle ejection events.
- Investigate the crater formed by the DART impact for the potential identification of fresh unweathered material on a silicate asteroid to understand possible space weathering processes.
- Test the conclusion that the crater produced by the Small Carry-on Impactor of the Japanese space mission Hayabusa2 on the top-shaped asteroid (162173) Ryugu formed in the gravity regime [231], comparing with the results of the DART impact on Dimorphos.
- Investigate an asteroid, Didymos, whose spin period of 2.26 h may place it at the limit of structural stability [232].

Hera is a small- to medium-sized planetary spacecraft with a mass of approximately 1280 kg. It will be equipped with 13 m^2 solar panels, a fixed high-gain antenna, and two low-gain antennas: communications with ground stations will use the X band [20]. To achieve its goals on planetary defense, Hera will bring several instruments, including two Asteroid Framing Cameras (AFCs), a spectral imager (Hyperscout-H), a microLIDAR (PALT), a Thermal Infrared Imager (TIRI), an X-band transponder referred to as X-DST, and a Hera-to-CubeSats Intersatellite Link (ISL) transceiver for the radio science experiment (RSE). Additionally, it has two CubeSats: Juventas and Milani (see fig. 3.5) [20]. After the launch

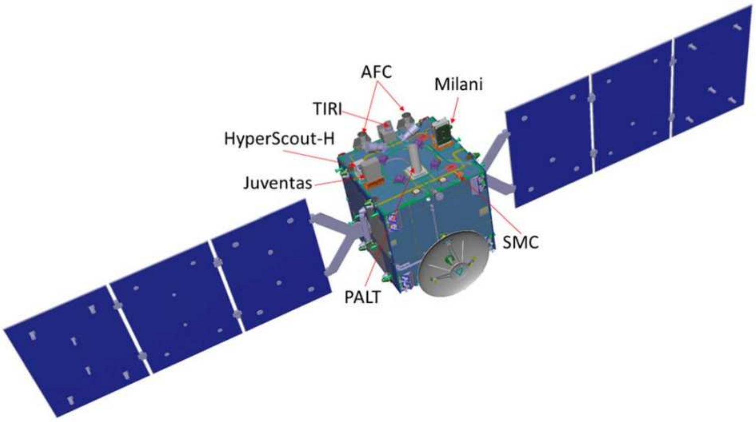

Figure 3.5: Hera spacecraft design. The locations of the different payload elements are indicated (AFC = Asteroid Framing Cameras; TIRI = Thermal InfraRed Imager; PALT = Planetary ALTimeter; SMC = Small Monitoring Cameras). Figure taken from Michel (2022) [20].

of Hera, a Deep-Space Maneuver (DSM) will occur 2-3 weeks later. It will pass within 5000-8000 km of Mars, and in January 2026, a second DSM will occur that will bring Hera towards Didymos. During the journey, it will pass close to Deimos, and a possible flyby of an other asteroid is also under consideration. On December 14th, 2026, five maneuvers will begin to enter orbit at the end of January or early February 2027 [20]. Once in orbit, there will be five phases (see fig. 3.6 and 3.7):

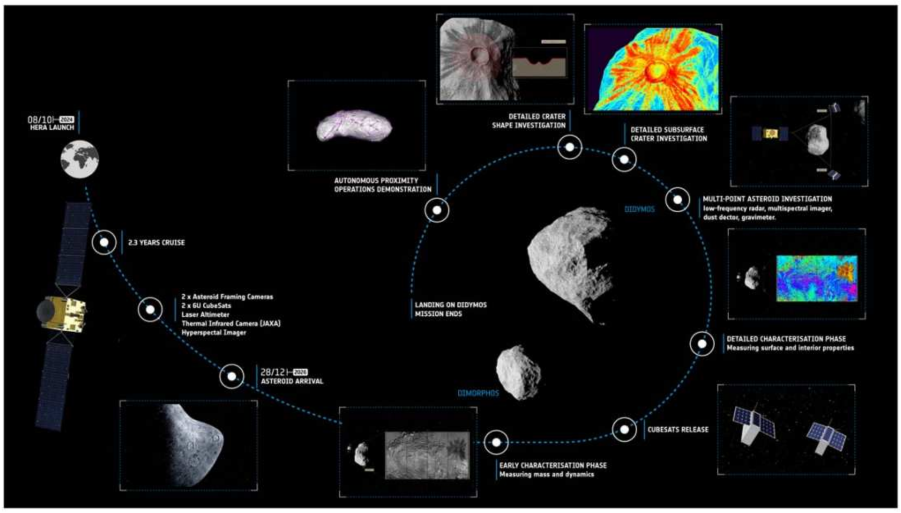

Figure 3.6: representative image of the HERA mission approaching the Didymos system. Figure taken from Michel (2002) [20].

- **early characterization phase (6 weeks):** the thermal and dynamic properties of the asteroids will be studies to determine the overall shape and mass/gravity of the system. This phase will begin when Hera will enter in orbit with the binary system and consists of arcs at a distance of 20-30 km. The interval is divided into short arcs of 3 days and long arcs of 4 days, creating a weekly cycle.

- **payload deployment phase (2 weeks):** it will be the release of the two CubeSats.

- **detailed characterization phase (4 weeks):** Hera will continue to move in hyperbolic arcs, but at a distance of 8-20 km. The purpose of this phase will be to map the asteroids at a meter scale and determine their thermal, spectral, and interior properties.

- **close observation phase (6 weeks):** the spacecraft will approach Didymos within 4 km following the same trajectory as the previous two phases. This phase will allow for high-resolution study of a large fraction of the Dimorphos surface, including the DART impact crater. Achievement of all mission objectives will be made possible through these phases.

- **experimental phase (6 weeks):** the spacecraft will reach lower altitudes, possibly as low as 1 km above Dimorphos. The main objective of this phase will be to achieve a resolution of decimeters in morphological, spectral, and thermal properties of Dimorphos. The Hera mission will conclude with the landing of the Hera spacecraft on Didymos, providing high-resolution data on the primary.

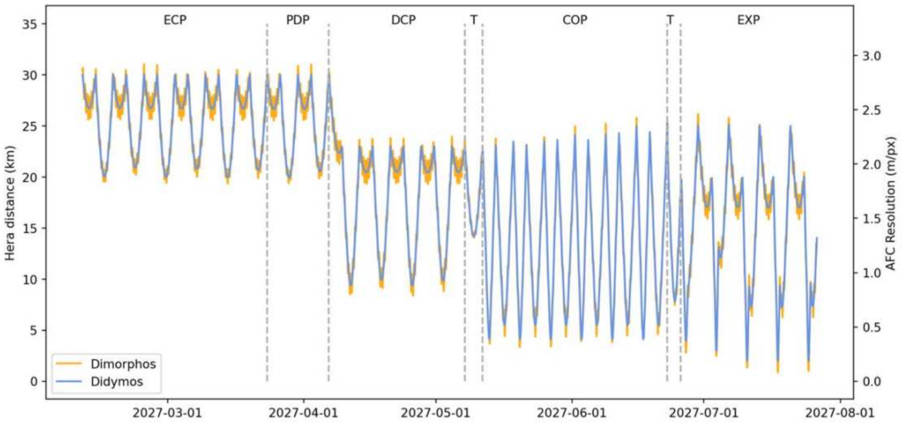

Figure 3.7: distance from Hera to Didymos/Dimorphos and AFC image resolution. ECP: Early Characterization Phase; PDP: Payload Deployment Phase; DCP: Detailed Characterization Phase; COP: Close Observation Phase; EXP: Experimental Phase; T: Transitions. Figure taken from Michel (2022) [20].

Hera will make a significant contribution to European planetary defense and aid in understanding the effects of a spacecraft impact on an asteroid. In addition, it will provide valuable information on the science of asteroids and the Solar System [20]. This mission will give more information on the internal and surface structure of small asteroids, the evolution of rubble-pile, the physics of impact craters in microgravity, the accretion of small bodies, and the evolution of terrestrial forms. It also provides information on the population of asteroids and planetesimals that joined together to form planets [20].

3.3 The Didymos-Dimorphos system

3.3.1 Before impact

The first detection by DRACO occurred 61 days before impact. On 27^{th} August 2022, DRACO began capturing images of the binary system every 5 hours. Four hours and five minutes before impact, the autonomous system Small-body Maneuvering Autonomous Real-Time Navigation (SMART Nav) took control of the spacecraft to impact Dimorphos in the best possible way (see Figure 3.8 [21]). From the beginning of the navigation until impact ($23{:}14{:}24.183 \pm 0.004$ UTC September 26^{th}), the probe continued to transmit images to Earth. The last complete image was captured 1.818 seconds before the impact, and the last partial image was captured 0.855 seconds after the impact. Before impact, little was known about the shape and surface of Dimorphos until DRACO obtained high-resolution images. A model of the asteroid's shape was used to describe Dimorphos: it is an oblate spheroid with a diameter equivalent to a volume of 151 ± 5 m. Furthermore, the albedo of Didymos was calculated more accurately as 0.15 ± 0.02 in the visible range (0.55 μm).

The images captured by DRACO reveal that Dimorphos has a surface scattered with rocks resembling some S-type NEAs such as (25143) Itokawa, C-type (101955) Bennu, and (162173) Ryugu, suggesting a rubble pile structure.

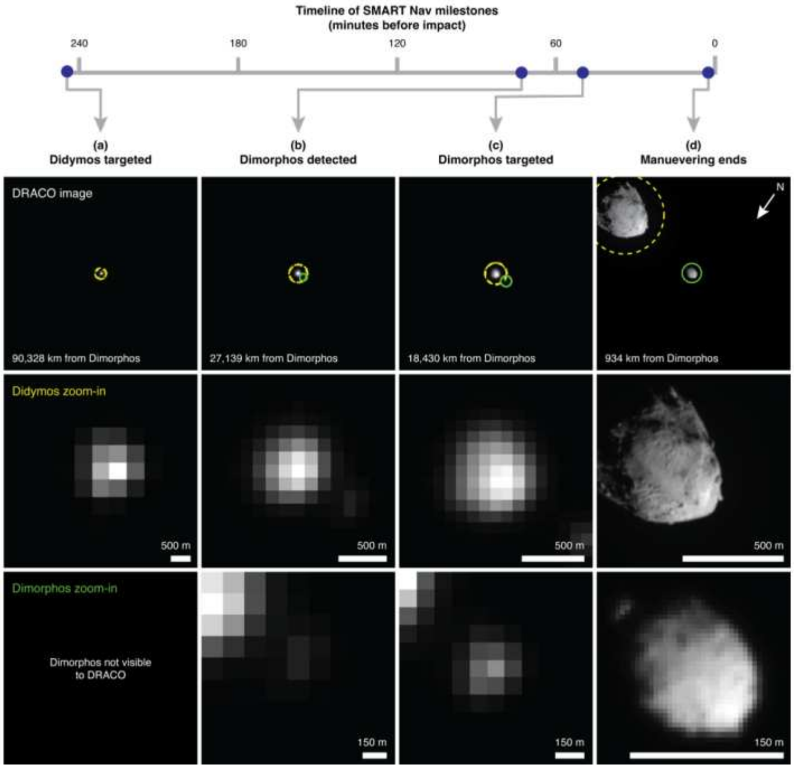

Figure 3.8: 12 images representing DART's approach towards Dimorphos since SMART Nav began targeting maneuvers are shown in a time sequence from left to right. Didymos is surrounded by dashed yellow circles and Dimorphos is surrounded by solid green circles. The images were taken by DRACO and used by the SMART Nav system to locate Dimorphos. Figure taken from Daly (2023)[21].

3.3.2 Impact

The trajectory and position of the impact was also calculated. DART impacted at 8.84±45° S, 264.30±0.47° E, with a 1 sigma uncertainty (68 cm) that is smaller than the size of DART (see Figure 3.9 [21]). The impact site was located between two large boulders: boulder 1 (6.5 m long and 2.2 m high) and boulder 2 (6. long and 1.6 m high). DART approached the asteroid with its solar antennas slightly tilted toward Dimrophos' surface. The first antenna hit boulder 1, followed by the second antenna that grazed boulder 2. Finally, DART affected Dimorphos between the two boulders (see Figure 3.10). Most of the momentum was transferred from the bulk of the DART, which constituted 88% of the spacecraft mass at the time of impact [21].

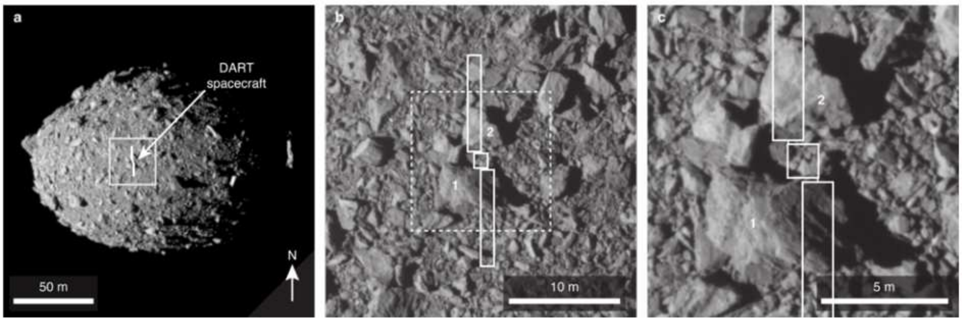

Figure 3.9: (a) shows Dimorphos with a correctly oriented outline of the DART spacecraft. (b) was taken 2,781 seconds before impact and shows Dimorphos with the two boulders 1 and 2 where the impact happened. (c) was taken 1,818 seconds before impact. The arrow on the lower left of panel (a) indicates the direction of the Dimorphos + Z (N) axis. The white box in image (a) indicates the position where image (b) was taken and the box in (b) shows the position where image (c) was taken. Figure taken from Daly (2023) [21].

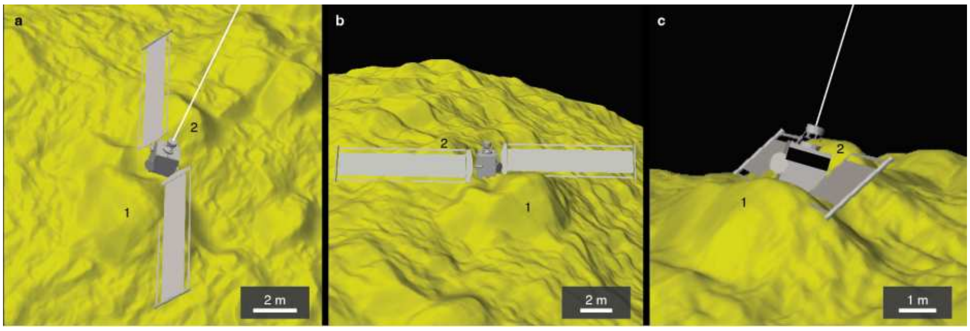

Figure 3.10: relationship between DART and the topography of the impact site. DART's position prior to impact with Dimorphos north is shown towards the top of the panel (a), to the right (b), and on page (c). Figure taken from Daly (2023) [21].

3.3.3 Earth-based observation after impact

On 26th September 2022 at 23:14 UT, DART impacted Dimorphos at a velocity of 6.6 km/s, giving it a large momentum (in a range between 2.2 and 4.9 [233]) [23]. The main objective was to change the orbital period of Dimorphos to demonstrate that a kinetic impactor is a valid method of deflecting asteroids. The DART spacecraft collided head-on with the leading hemisphere of Dimorphos [22]. This configuration was chosen to transfer the maximum possible momentum and reduce the semimajor axis of Dimorphos' orbit, thereby reducing the orbital period. In the simplest case, if DART crashed, the momentum of the impacting spacecraft was transferred to the asteroid target without any additional momentum enhancement and a change in orbital period of 7 minutes was expected [22]. However, depending on the strength of the material, impact conditions, and other properties, β could change and the value of the orbital period could reach up to 40 minutes. On 11st October 2022, NASA announced that the DART impact had reduced Dimorphos' orbit by 32 minutes, according to ground observations [22].

The orbital period before impact is 11.92148 ± 0.00013 h (3σ). The post-impact orbital period has been calculated by many researchers; as the results of Thomas et al. [22]. They calculated the orbital period using radar observations and light curves from the Didymos system. The observations began about 11 hours after impact using the Goldstone X-band (3.5 cm, 8560 MHz) and continued for 14 days. Radar echoes were received in a bistatic configuration with transmission from the Goldstone X-band using the Green Bank Telescope (see Fig. 3.11 [22]). The first observation of Dimorphos occurred approximately 12 hours after impact, resulting in an orbital value change of -36 ± 15 minutes. In conclusion, they determined a post-impact period of 11.372 ± 0.017 (3σ) hours with a period variation of -33.0 ± 1.0 (3σ) minutes. The rotation period of Didymos remained unchanged after impact, whereas the orbital period changed more than expected. The ejecta produced by the impact significantly contributed to the momentum carried by the DART spacecraft [22].

3.3.3.1 Photometry

There are numerous photometric data of Didymos system available in literature. For instance, observations obtained from the Lulin Observatory (National Central University, Taiwan) between September 21st, 2022, and January 5th, 2023, using an R-B-R-V-R-I-R observational sequence for color measurements in order to remove the effect of the magnitude variation that was due to the rotation of the asteroid [23]. The photometry of this study is shown in Figure 3.12. The values of m(1,1,α) have been reduced to a distance of 1 AU from both the heliocentric and geocentric perspectives using the following equation:

$$m(1,1,\alpha) = m - 5log(\Delta r_H) \tag{3.3}$$

where Δ and r_H are the geocentric and heliocentric distances of the asteroid in AU, respectively.

The first measurements of magnitude arrived 20 hours after the impact, showing an increase in brightness of around an order of magnitude. In the days following the impact, the magnitude decreased by 0.07 mag per day, indicating the movement of the ejecta away from the system due to the pressure of solar radiation [23]. Two weeks later, when the two twin tails disappeared, there was only a decrease in magnitude of 0.04 mag per night: this indicates that most of the ejecta were swept away from the system.

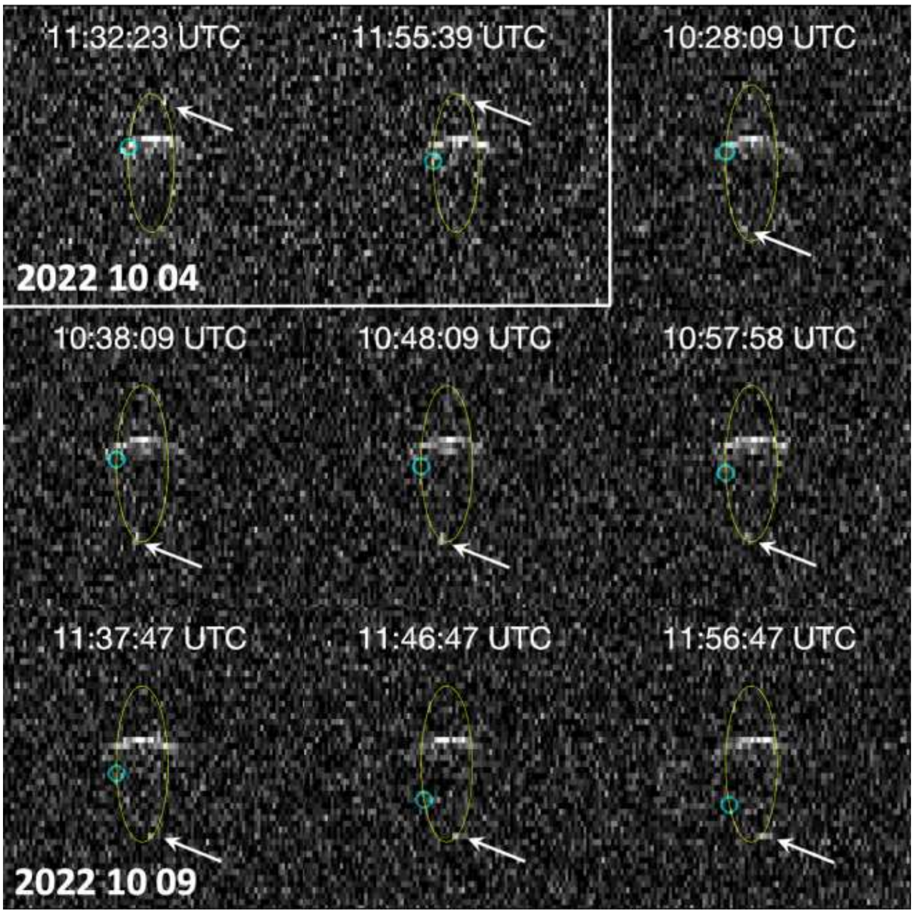

Figure 3.11: radar range-Doppler images acquired on 4^{th} October 2022 using Goldstone X-band and on October 9^{th} using Goldstone X-band for transmission and the Green Bank Telescope for reception, depict an increase in distance from Earth from top to bottom within each image, and a rise in Doppler frequency to the right. Consequently, both rotational and orbital motions appear counterclockwise. The broader echo originates from Didymos, while the smaller, fainter echo indicated by arrows corresponds to Dimorphos. Open circles represent predicted positions for Dimorphos based on the pre-impact orbit. The yellow ellipses illustrate the trajectory of Dimorphos. The prediction uncertainties are smaller than the image resolution. On 4^{th} October, the ellipse spans -870 m to +870 m along the y axis and -7 to +7 Hz along the x axis, corresponding to line-of-sight velocity of -12 cm/s to +12 cm/s. On 9^{th} October, the ellipse spans -980 m to +980 m along the y axis and -8 Hz to +8 Hz along the x axis, corresponding to line-of-sight velocity of -14 cm/s to +14 cm/s. The physical extents of the ellipse vary as a result of the viewing geometry. Figure taken from Thomas (2023) [22].

The V magnitude can be used to calculate the absolute magnitude H and the slope parameter G of an object based on the colour sequence of observations:

$$H(\alpha) = H - 2.5 \log \left[(1 - G)\Phi_1(\alpha) + G\Phi_2(\alpha)\right] \tag{3.4}$$

where H is the absolute magnitude observed at 1 AU from both the Sun and the Earth and at a zero phase angle, Φ_1 and Φ_2 are functions that describe single and multiple scattering from the asteroids surface, and G is the slope factor that describes the shape of the phase curve [23].
The H value before impact was 18.17 ± 0.48 mag with a slope parameter of G of 0.20 [234]. After impact, the calculated values were $H = 17.87 \pm 0.08$ and $G = 0.13 \pm 0.05$. As a result of contamination from the impact, there is significant uncertainty regarding the absolute magnitude values. The object is believed to have become slightly brighter than before as a result of the enhancement of the ejecta [23]. Using the average absolute magnitude before and after impact (18.02 ± 0.34) and the mean albedo for S-type (0.213 [235]), the effective diameter of Didymos was calculated, which is $0.72 \pm^{0.12}_{-0.0}$ km resulting in values lower than previous estimates (0.78 ± 0.03 km [23]). The difference may be due to the limited data available before the DART impact and contamination of the data by ejecta produced by the impact [23].
In addition, Polishook et al. [3] calculated the magnitude variation (ΔMag) dependent on the combined surface area of Didymos, Dimorphos, and the ejecta cloud (S_{index}):

$$\Delta \text{Mag} = -2.512 \log \left(\frac{S_{\text{Didymos}} + S_{\text{Dimorphos}} + S_{\text{ejecta}}}{S_{\text{Didymos}} + S_{\text{Dimorphos}}} \right) \tag{3.5}$$

The magnitude variation decreased from 64% on September 27^{th} to 23% on October 2^{nd} (see Table 3.1).

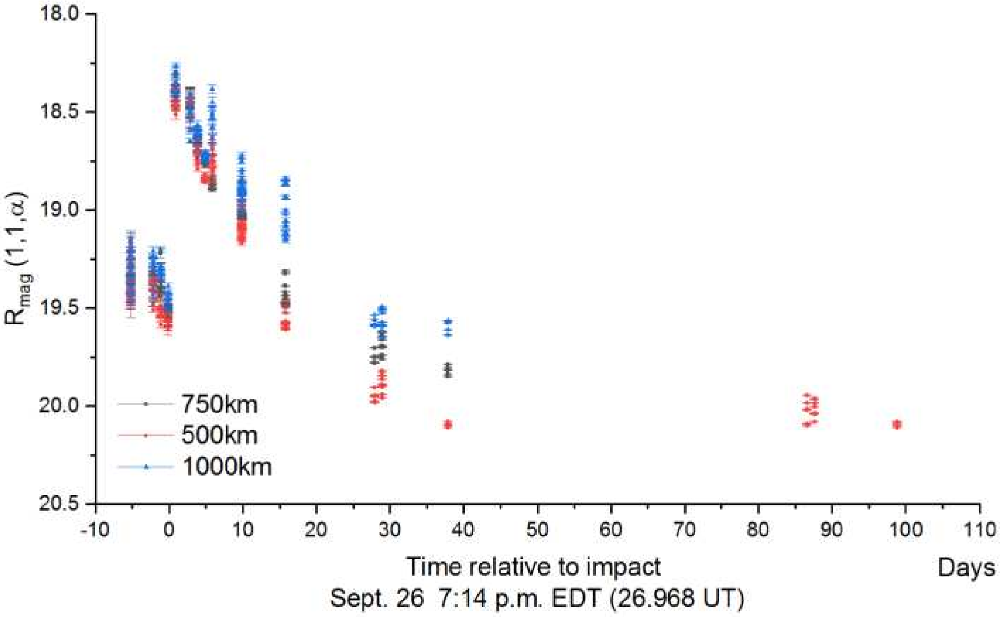

Figure 3.12: R-band magnitude $m(1, 1, \alpha)$ of the Didymos system. Magnitudes measured at three different apertures centered on the comet nucleus with diameters of 500 km (red), 750 km (black), and 1000 km (blue). Magnitudes are normalized to heliocentric and geocentric distance units as a function of time expressed in days since the impact with DART. Figure taken from Lin (2023) [23].

Night	T_{spec}	Δ Mag	$\Delta\text{Mag} = -2.512 \log\left(\frac{S_{\text{Didymos}}+S_{\text{Dimorphos}}+S_{\text{ejecta}}}{S_{\text{Didymos}}+S_{\text{Dimorphos}}}\right)$
2022 Sep 26	2459849.0833	0	0%
2022 Sep 27	2459850.0833	-1.12	64%
2022 Sep 28	2459851.0833	-0.95	58%
2022 Sep 29	2459852.0833	-0.78	51%
2022 Sep 30	2459853.0833	-0.62	43%
2022 Oct 1	2459854.0833	-0.45	34%
2022 Oct 2	2459855.0833	-0.28	23%

Table 3.1: brightness change of the Didymos system by the time of the spectral measurements compared to a preimpact baseline (20.1 mag) and ejecta cloud ratio based on photometric measurements collected by the Danish 1.54 m telescope at La Silla using an aperture of 1.5”. Table taken from Polishook (2023) [3].

3.3.3.2 Spectroscopy

In the literature, there are various taxonomic classifications of Didymos. The impact of DART on Dimorphos has allowed to study the internal composition of an asteroid and the spectral evolution of ejecta. Some studies suggested that the brightness of the ejecta exceeded that of Didymos for several tens of hours after impact [3], [236]. The brightness of the system increased due to two factors. First, a cloud of gaseous ejecta containing sodium and potassium was moving at a velocity of $1.5 - 1.7$ km s^{-1} in the direction opposite to DART for a few minutes [3]. Secondly, a slow and long-lasting cloud of ejecta formed around the body, creating a series of tails that changed in number, direction, and length in the months following the impact [3].

Some models suggest that asteroids with diameters smaller than a few tens of kilometers can break apart, and the expelled material goes into orbit, leading to the formation of a satellite [217], [237], [238], [214]. Therefore, it is believed that Didymos and Dimorphos were formed from a common origin, suggesting a similar composition for the two bodies and thus the same taxonomic classification [3]. Furthermore, the impact of DART causes the material to be lifted from layers tens or more centimeters thick, exposing the subsurface material [239]: Dimorphos is not subject to space weathering processes (impact of dust, solar particles and cosmic rays) [240], [241]. Most asteroid surfaces are exposed to these processes because the time of space weathering is short (10^6 years) [242], [243]. However, some asteroids have experienced uncommon events such as collisions, planetary encounters, and rotational breakup [244]. In the latter, material from the inner layers ('fresh material') has risen to the surface. To study this fresh material, the spectrum in the near-IR is examined, characterized by a shallow spectral slope and a wider and deeper 1 μm absorption band (Q-type spectral features, [3]). Due to DART, material has been extracted from the deeper layers and the ejecta can have a non-weathered surface [3]. Laboratory experiments suggest that the reduced spectral slopes are due to large boulders (> 100 μm) on the surface of Q-type asteroids [245]. This suggests that Q-type asteroids have a standard weathered surface dominated by large grains. Therefore, after the impact of DART, a variation in the Didymos spectrum due to various factors, including the material hidden by the surface can be expected [3].

Several spectral studies of the Didymos system have been published after the impact, some of which are reported below. Polishook et al. [3] utilized NASA's 3 m InfraRed Telescope Facility (IRTF) in Mauna kea, with a spectral range of 0.8-2.45 μm, suitable for characterizing bodies rich in silicates [3]. The results led to the measurement of different spectral slopes of the 70% from their spectra taken after the DART impact (between 26^{th} September 2022 and 2^{nd} October 2022). This variation is significative because Marsset et al. [120] analyzed the reflectance spectra of asteroids over the last 20 years and found a slope uncertainty of 4.2% μm^{-1}, which is significantly lower than the difference 70% reported by Polishook et al. [3]. They were unable to calculate the spectral slope of entire rotation in a single night, but by comparing the spectra collected during several nights, different slopes were obtained in the different rotational moments [3]. Their spectral classification coincides with type S, as shown in the figure 3.13. The other subgroups of the S complex (such as S1-, Q-, Sr-, Sv-, and Sa-types) do not match the spectra obtained from them due to significant differences in the depth and width of the 1μm band. Additionally, their PCA analysis indicates that no spectrum can correspond to the Q-type [3].

In conclusion, Polishook et al. [3] suggest that the variation in the spectrum may be due to three physical processes: compositional variation of the ejecta material, ejection of "fresh" non-weathered material, and ejected material with varied grain sizes. The shallow slope spectra of Didymos do not exhibit Q-type characteristics, leading to the conclusion that the surface material excavated by the impact of DART is not as fresh as that of Q-type asteroids [3].

Another taxonomic classification of Didymos has been carried out by researchers at the Lulin Observatory using B, V, R, and I filters to obtain the taxonomic type based on surface colours. They did not use the phase angle correction because it had little influence on their observations, which were made over a very short period of time [23]. They did not correct for phase reddening. Additionally, to unify the color measurements of the derived magnitude before and after impact, they used a circular aperture of 500 km, and normalized the relative reflectance to 0.55 μm (after subtracting the solar reflectance for each band). They classified Didymos as an S-type asteroid before impact with DART [23]. Previous studies before the impact, in 2004, Kitazato [234] reported that the asteroid was X-type from the spectral slope they had found. However, Kiersz (2021) [246] noticed that near-IR signatures are consistent with a S-type. To study its spectrum, as reported by Lin [23], Didymos showed characteristics of the C complex on 27^{th} September 2002 after the impact; on 29^{th} September, it became a Q-type asteroid. On 30^{th} September, it again showed the characteristics of the complete S-type asteroid (see fig.3.14). The spectral difference is due to the fact that on 27^{th} September Didymos was surrounded by a large amount of dust, while in the following days the amount of dust decreased, forming a long tail. They also compared color indices: an initial decrease in B-V, followed by an increase on 30^{th} September, while the R-I term increases after the DART impact and then remains constant until the first few days of October. The V-R index decreases from 27^{th} September to the beginning of October. The color varies over time, regardless of the aperture size, but they could not conclude whether these changes were due to the movement of the ejecta. However, this can be linked to the properties of the grains changing: the grains change from sub-micrometer to micrometer dimensions, which are associated with a cometary outburst [23]. Colour variation in comets is a common phenomenon caused by various factors, including differences in terminal velocities and radiation pressure efficiency due to variations in grain size [23].

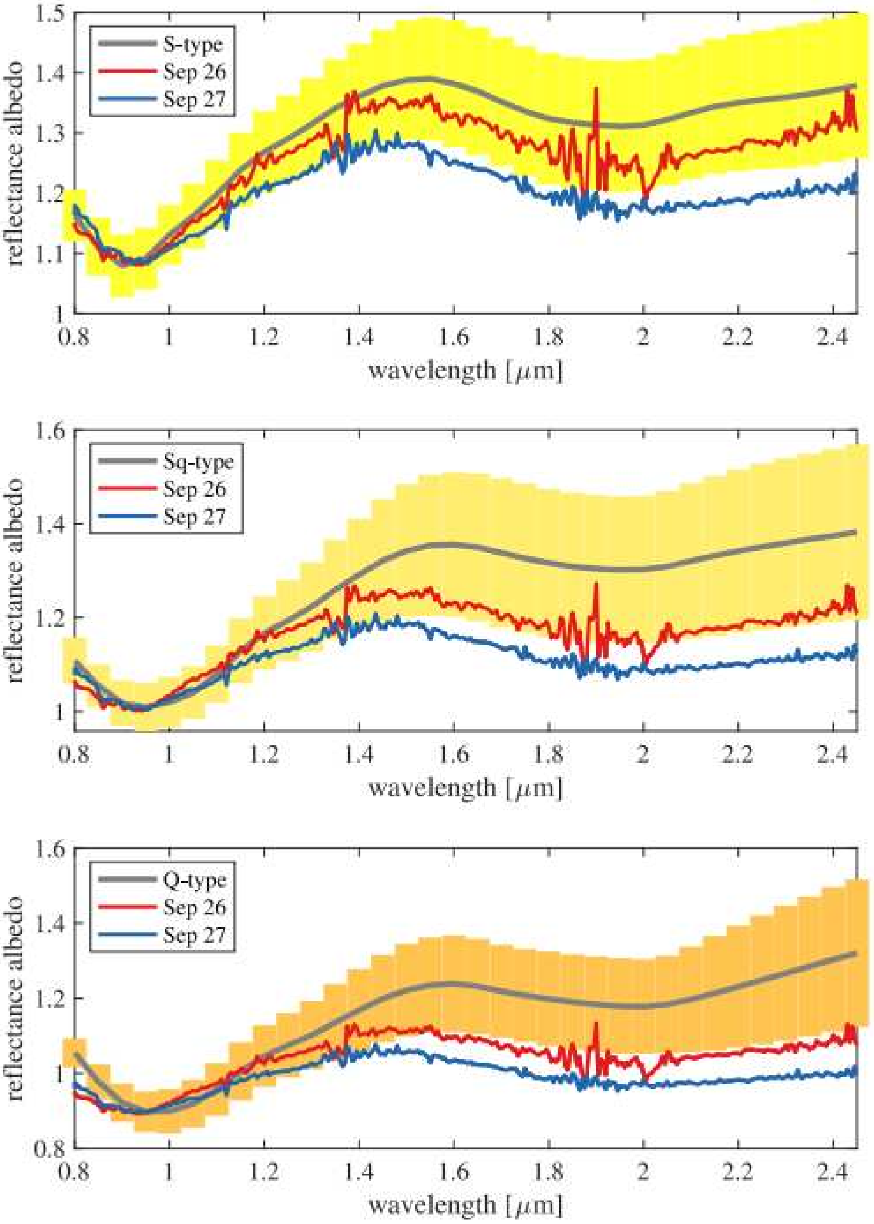

Figure 3.13: the spectra of Didymos before (red line) and after (blue line) the impact of DART (26th and 27th September 2022) are compared to the range of averaged taxonomies (gray lines) of S- (top), Sq (middle), and Q-types (bottom) within 1σ range (yellowish-orange bars). Both pre- and post-impact spectra match well with the S-type spectrum at the 1 m absorption band and do not fit the Q-type reflectance spectrum, rejecting the hypothesis of ejecta with fresh-looking material. The pre-impact spectrum's overall spectral slope matches the S-type spectrum well, and the post-impact spectrum's value also fits the S-type spectrum better than the Sq- and Q-types. Figure taken from Polishook [3].

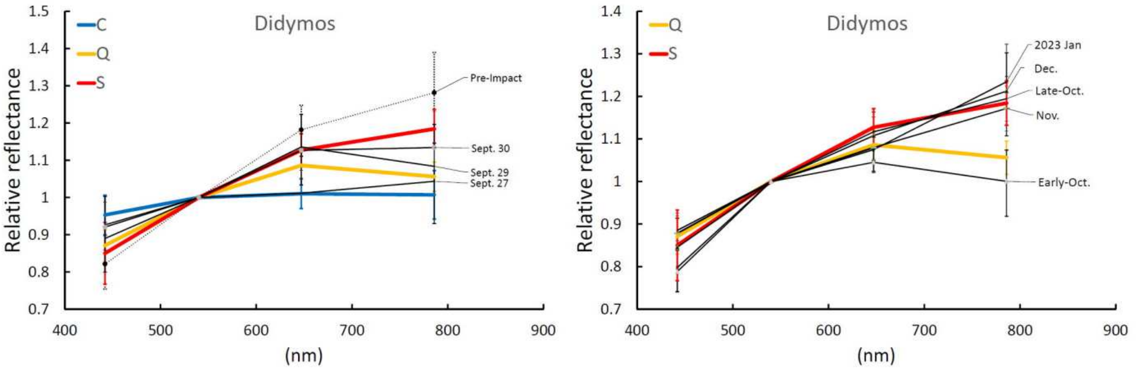

Figure 3.14: the relative reflectance of the Didymos-Dimorphos system was measured by the Lulin Observatory before impact, on 27th, 29th, and 30th September 2022 (left) and in early October, late October, November, December 2022, and January 2023 (right). The models of the relative reflectances of S, C, and Q are shown on the left and only S and Q on the right. Before impact, Didymos was classified as type S. On 27th September, it was reclassified as type C. From 29th September to early October, it was classified as type Q. The taxonomic classification returned to S-type after November. Figure taken from Lin (2023) [23].

3.3.3.3 Ejecta Studies

A comet tail is usually attributed to gas and dust. In the case of Dimorphos a long tail was formed which resembled that of comets but in this case all observed structures resulting from the impact were due to the ejected dust reflecting sunlight. After the impact, the dust from Didymos moved away from the point of impact. As shown in Figure 3.15, before impact, Didymos was a point-like object, whereas after impact, an antisunward-oriented tail (T) is visible. This element will be useful for estimating the intensity of impact and the velocity of particles projected away from the body. The projected expansion velocity of the dust corresponds to $\sim$ 31 m/s, as reported by Lin et al. [23] and studied through HST data. In addition to the tail, other independent dust structures were found on September 27th (labeled from A to E). On 29th September, two of these structures disappeared, and on 2nd October only the northern (A), sun-facing (D), and southern (E) ones remained (with E disappearing on 6th October). By 12nd October, the last two characteristics had disappeared and only the tail was detected. The signal-to-noise ratio of their observations is very good. Additionally, at some point the tail has split into two parts, but it is unclear when this occurred. Therefore, the disappearance of the dust structure is due to a real change in its properties, such as size, or changes in geometry, such as a variation in the phase angle [23].

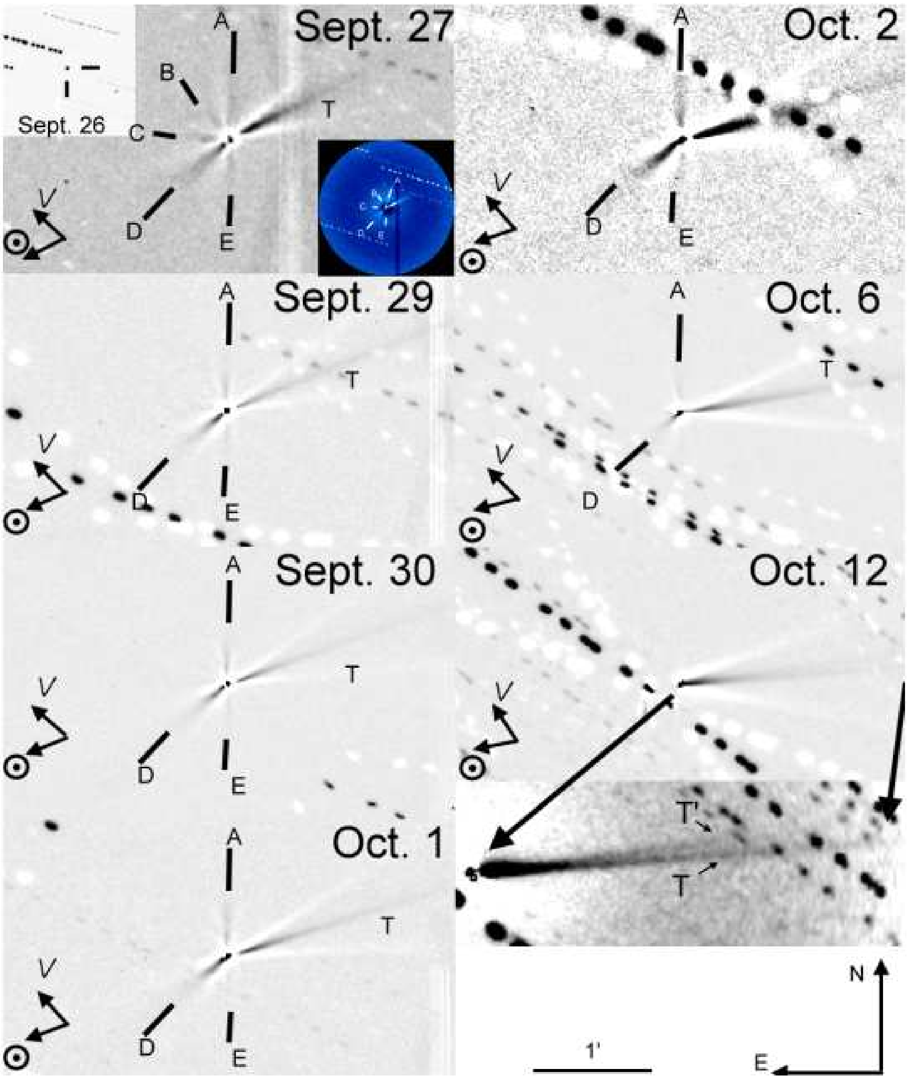

Figure 3.15: ejecta morphology from the Didymos-Dimorphos system after the collision at 23:14 UT on September 26^{th}, 2022. The small top-left panel shows a normal point-like source before the DART impact. It is showed the five components of the tails: A, B, C, D and E. Figure taken from Lin (2023) [23].

3.4 Observational campaign

In this thesis, the Didymos system was analysed using spectroscopic techniques after the DART impact. The results were compared to the spectra published in to the literature, characterized this system before and after impact. In addition, we studied the geometry of the system during the same time interval as my observations. Spectroscopic data were obtained using the 1.22 m Galileo and 1.82 m Copernico telescopes in Asiago (VI), Italy (see Section 3.4.1,3.4.2 for a description of the instrumentation). The nights for the observational campaign to study Didymos are October 19^{th} and 20^{th}, less than a month after the impact, and November 18^{th}, December 26^{th} and 27^{th} 2022. The covered spectral range is from 5000 to 9000 Å.

3.4.1 Copernico's Telescope

The Copernico 1.82 m telescope and its instruments are operated by the INAF Astronomical Observatory of Padova. The observatory situated atop Mount Ekar in Asiago (Italy) at coordinates 11°34′08.397" E 45°50′54.894" N, and altitude of 1376.2 m. The telescope's optical design is a classic Cassegrain with an equivalent focal number of f/9. The Asiago Faint Object Spectrograph and Camera (AFOSC), similar to the Danish Faint Object Spectrograph and Camera (DFOSC), works as a focal reducer type spectrograph/camera positioned at the Cassegrain focus of the Copernico 1.82 m telescope (see Figure 3.16). This instrument enables imaging, spectroscopy (resolution ranging from 240 to 3600), and polarimetry. Since 2015, the AFOSC has been equipped with the Andor iKon-L936 BEX2-DD-9HF (detector: E2V CCD42-40 back illuminated CCD 20482048 active pixels; 13.5 μm each).

3.4.1.1 AFOSC

The Asiago Faint Object Spectrograph and Camera (AFOSC) operates as a focal reducer instrument, allowing for a wide field (8.8 × 8.8 arcmin field of view) for imaging, low- and medium-resolution grism spectroscopy, polarimetry, and spectro-polarimetry observations. The instrument employs three wheels for selecting slits, filters, and grisms (see Figure 3.16). Briefly, the light coming from the telescope passes through the slit (spectrographic mode) or the hole (imaging mode) in the slits wheel, it is redirected by a total reflection prism and collected by the collimator. In the collimated beam, between the collimator and the camera, the light passes through the filter wheel and the prisms wheel, where the reimaged exit pupil of the telescope is positioned. Finally, the light is imaged by the camera on the detector. Table 3.2 lists the basic optical parameters of AFOSC.

AFOSC has been equipped with VPH grisms (#1 to #7), which offer higher resolution than classical grisms, and with a rather high efficiency (typically around 80%). For this observational campaign, two slits were used, one with a 1.69" aperture and the other with a pinhole (MF) for camera focus. The VPH6 grism (see Table 3.3) was used for scientific objects while calibrations, and the pyramid focus was used for the telescope focus. The pyramid focus device (PYFO) is fixed on the grism wheel, aiding in determining the telescope or AFOSC camera focus with a single exposure. The scientific images were taken with 2x2 binning and 50Hzx2 Hisens read-out modes.

Lambda calibration relies on two lamps: Neon (Ne) and Mercury-Cadmium (Hg-Cd).

The dome flats are acquired using available lamps (0.3, 1.0 kW) projected onto a white screen in the dome, along with a "Flat Low" lamp (~ 150 W) that produces diffused light.

Parameter	**Value**
Collimator Focal Length	234.27 mm
Collimator Linear Field	52.9x52.9 mm^2
Beam Diameter	27.4 mm
Camera Focal Length	159.35 mm
Camera Linear Field	24.58x24.58 mm
Reduction Ratio	0.68
Input f-number	f/8.97
Output f-number	f/6.10
Input Scale	12.64/mm
Output Scale	18.59/mm
Field of View	8.85x8.85'
CCD Pixel Scale	0.26/pixel
Wavelength Coverage	330 - 1100 nm
Limiting Spectral Resolution	7350

Table 3.2: AFOSC Technical Data

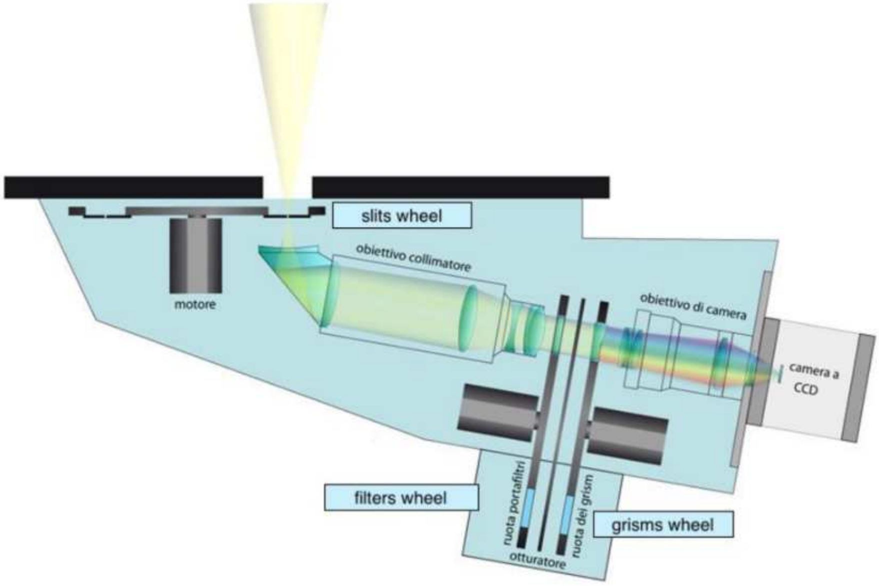

Figure 3.16: representation of the AFOSC spectroscope mounted on the Copernico telescope. Image by Sergio Dalle Ave.

3.4.2 Galileo Telescope

The Galileo telescope is located in Altopiano in Asiago (Italy), at coordinates 11°31′35" E +45°51′59" N, and altitude of 1045 m. It has a parabolic mirror with a diameter of 122 cm and a hyperbolic secondary mirror of 550 cm with an optical Cassegrain configuration

Grism	λ_{cen} (nm)	Wavelength Range (nm)	Dispersion (Å/mm)	Dispersion (Å/pixel)	RS	gr/mm
VPH#6	800	450-1000	261	2.95	500	285

Table 3.3: features of VPH6 grism.

f/16. The telescope is equipped with a Boller & Chivens spectrograph, complemented by an ANDOR iDus 440 camera featuring a back-illuminated EEV 42-10BU sensor with dimensions of 2048x512 pixels (pixel size: 13.5 x 13.5 microns). See Tables 3.4 and 3.5 for camera and CCD data. For these observations a 300 line/mm grating was adopted (see Table 3.6). The configuration of the spectrograph is detailed in Figure 3.17.

Specification	**Value**
Sensor	E2V 42-10 Back Illuminated
Active Pixels	2048 x 512
Pixel Size (μm)	13.5 x 13.5
Image Area (mm)	27.6 x 6.9
Readout Noise	3 e- rms
Gain	1.4 e-/ADU
Dark Current (@ 203 K)	0.004 e-/px/sec

Table 3.4: ANDOR iDus DU440A sensor specifications

Specification	**Value**
Camera Model	ANDOR iXon DV885
Technology	EMCCD
Active Pixels	1004 x 1002
Pixel Size (μm)	8 x 8
Image Area (mm)	8 x 8
Useful Field of View	8.2' x 5.5'
Resolution	0.68 arcsec/px
Dark Current (@ 203 K)	0.004 e-/px/sec

Table 3.5: ANDOR iXon DV885 guide samera specifications

Gratings	**Blaze Angle**	λ_{Blaze} (Å)	**Dispersion**	**Resolution at** λ_{Blaze}	**Resolution at** λ_{Blaze}	
(tr/mm)		**(Å)**	**(Å/mm)**	**(Å/px)**	**150**μ	**250**μ
300	4 18’	5000	166.8	2.25	960	555

Table 3.6: features of 300 tr/mm gratings.

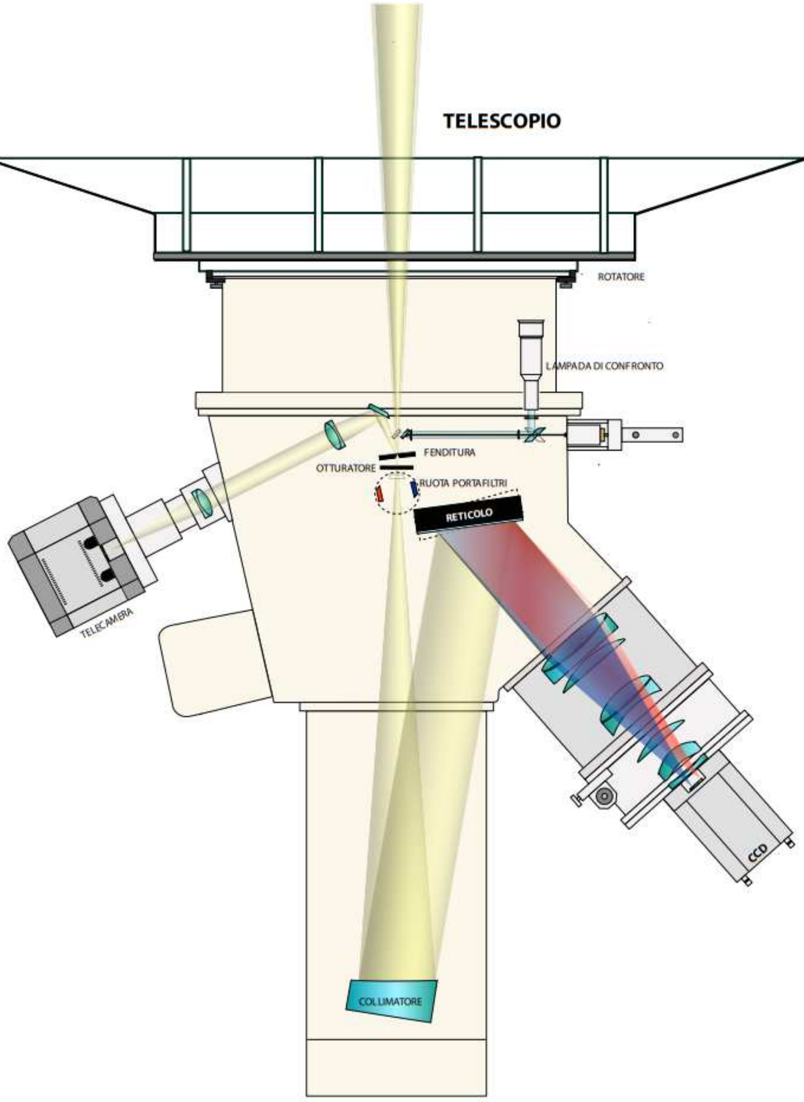

Figure 3.17: representation of the Boller & Chivens spectrograph mounted at the Galileo telescope. Image by Sergio Dalle Ave.

3.4.3 Data Observations

Didymos was observed with the Galileo and Copernico telescopes at the Astrophysics Asiago Observatory, both before and after the impact of the DART spacecraft. Unfortunately, the data acquired before the impact of the DART spacecraft could not be used because of the low signal-to-noise (S/N) ratio of the spectra. In fact, in August 2022, six Didymos spectra were acquired at a maximum altitude of 22° above the horizon and an airmass of around 2.65, which are very challenging conditions for observing any object. Additionally, the differential tracking of the Copernico telescope was not working well, and this has led to a different observation strategy from that of the "normal" one: the slit was not oriented along the direction of atmospheric refraction of the target (along the parallactic angle (PA)) to prevent the target from leaving the slit in very short times (less than 5 minutes). This technical issue is related to the guide camera probe. The Copernico telescope's guide camera has a probe that allows it to position itself on a star near the target field, allowing the telescope to track it. However, when differential tracking was initiated, sometimes due to a hardware problem, the probe would get stuck and the telescope would stop moving at the velocity set by the differential tracking. This minor technical issue was resolved after the observational campaign of Didymos in October 2022. This fact introduced a significant error in the spectral slope of the spectra (see 3.4.5.2 for details). Therefore, the six spectra obtained in August are not reported in this work, and there were no other nights available before the impact to observe Didymos due to adverse weather conditions.
After the impact, forty-five spectra were taken on different nights: forty using the 1.82 m Copernico Telescope and five using the 1.22 m Galileo Telescope at the Astrophysics Asiago Observatory in Italy (see Table 3.7). The goal was to obtain enough spectra to cover one rotation of the primary Didymos. The post-impact observational campaign consisted of six nights.

- Night 1: seven spectra taken on October 18^{th} between 1:52 UT and 3:50 UT, covered rotation: 2.13 h (94% of the entire rotation). The exposure time is 900 seconds per spectrum and the solar analog used is Land 98-978. The range in altitude above the horizon reached by Didymos of the Asiago observatory was between 27.8° and 36.4° with a variation of airmass between 2.13 and 1.681.

- Night 2: five spectra taken on October 19^{th} between 1:44 UT and 3:27 UT using the Galileo telescope, and six spectra taken between 1:05 UT and 3:54 UT with the Copernico telescope, covered rotation: 2.05 h (91% of the entire rotation) and 1.45 h (64% of the entire rotation). Respectivetely the exposure time for spectra obtained with the Galileo telescope is 1200 s, and those obtained with the Copernico telescope are 720 s. The solar analog used for the division is Land 98-978. The range of altitude above the horizon reached by Didymos of the Asiago Observatory was between 22.6° and 37.6° with a variation of airmass between 2.583 and 1.633.

- Night 3: eight spectra taken on October 20^{th} between 1:45 UT and 3:49 UT, covered rotation: 2.26 h (100% of the entire rotation). The exposure time is 720 s for six spectra and 900 s for two spectra, and the solar analogue used for division is Hyades 64. The range in altitude above the horizon reached by Didymos at the Asiago Observatory was between 28.6° and 38.6° with a variation of airmass between 2.080 and 1.599.

- Night 4: five spectra were taken between 18^{th} and 19^{th} November from 23:24 UT to

1:32 UT, covered rotation: 2.46 h (109 % for the entire rotation). The exposure time for each spectrum is 1200 s, and the solar analogue used for division is Hyades 64. The range of altitude above the horizon reached by Didymos of the Asiago observatory was between 28.7° and 49.3° with a variation of airmass between 1.964 and 1.316.

- Night 5: eleven spectra were taken between 26^{th} and 27^{th} December 2022, from 22:09 UT to 3:35 UT, covering a rotation of 5.93 h (262% for the entire rotation). The exposure time for each spectrum is 1800 seconds, and the solar analogue used for division is Hyades 64. The range in altitude above the horizon reached by Didymos of the Asiago observatory was between 52.7° and 72.6° with a variation of airmass between 1.261 and 1.048.

- Night 6: three spectra taken on December 27^{th} between 21:39 UT and 22:44 UT, covered rotation: 1.58 h (70% for the entire rotation). The exposure time for each spectrum is 1800 s, and the solar analogue used for the division is Hyades 64. The range in altitude above the horizon reached by Didymos at the Asiago Observatory was between 50.7° and 61.6° with a variation of airmass between 1.261 and 1.139.

Table 3.7 contains all data for the forty-five spectra, including image name, acquisition start date and time, exposure time, S/N, spectral slope and its error, and the solar analog used. Images starting with $AF\_number.fits$ were taken with the Copernico telescope, while those starting with $IMA\_number.fits$ were taken with the Galileo telescope. For nights 2, 3, and 4, the slit was not oriented along the object's required parallactic angle because of differential tracking issues with the Copernico telescope. This was done to keep Didymos within the slit for a longer time with respect to the case when the slit is oriented along the direction of the atmospheric refraction of the target. An analysis of the data was carried out to understand the importance of the slit orientation, which will be described in section 3.4.5.2. During these observations, Didymos had an apparent magnitude ranging from 15.4 to 16.4 mag in the V band. Observations with the Copernico telescope were made using the long-slit at a 132-micron aperture (1.69 arcsec) and the VPH6 grism of 285 lines/mm, which yields a dispersion of 3.5 Å/pixel with low resolution, R=500, in the spectral range of 0.4-1 micron. The exposure time varies from 720 to 1800 seconds depending on the object's magnitude and based on the workings of the differential tracking. The spectra obtained with the Galileo telescope were acquired using a long slit with a 250 micron aperture (3 arcsec) and a grating of 300 lines/mm in the spectral range of 0.35-0.8 microns.

3.4.4 Data Reduction

The spectra were reduced using the Image Reduction and Analysis Facility (IRAF) astronomical package, following standard reduction procedures. The images undergo trimming, bias subtraction, and flat field division before being calibrated in wavelength using the appropriate lamp (HeFeAr for the Galileo telescope and HgCd for the Copernico telescope). The dark correction was not made because the CCD reaches a temperature of -95° and the dark noise is negligible. Finally, the spectra are extracted and corrected for atmospheric extinction. Each spectrum is then divided by the appropriate solar analog taken during the same night with a similar airmass because the asteroid reflects the light of Sun. Therefore, when observing an asteroid, my spectrum is composed of the asteroid's spectrum and that of the Sun. To obtain the spectrum of the asteroid, we divide the obtained spectrum by

N	Image	Date	Epoch (UT)	Exp time (s)	S/N	Spectal Slope (%/1000A)	Solar Analog
1st night, 1.82 m Telescope							
1	AF784958*	18 Oct	01:52:25.0	900	25.6	7.45 ± 5.47	Land 98-978
2	AF784959*	18 Oct	02:11:11.9	900	18.9	0.39 ± 4.03	Land 98-978
3	AF784960*	18 Oct	02:32:31.9	900	20.1	5.68 ± 6.16	Land 98-978
4	AF784961*	18 Oct	02:50:44.5	900	27.1	8.45 ± 1.69	Land 98-978
5	AF784962*	18 Oct	03:11:28.7	900	23.0	5.00 ± 6.27	Land 98-978
6	AF784963*	18 Oct	03:29:23.0	900	27.8	8.07 ± 3.27	Land 98-978
7	AF784964*	18 Oct	03:50:28.6	900	37.3	5.36 ± 3.22	Land 98-978
2nd night, 1.22 m Telescope							
8	IMA108103	19 Oct	01:44:44.1	1800	10.8	31.89 ± 4.56	Land 98-978
9	IMA108104	19 Oct	02:19:29.7	1200	13.2	2.58 ± 12.80	Land 98-978
10	IMA108105	19 Oct	02:34:44.9	1200	4.9	17.93 ± 18.27	Land 98-978
11	IMA108106	19 Oct	03:05:47.7	1200	5.2	17.90 ± 16.36	Land 98-978
12	IMA108107	19 Oct	03:27:10.9	1200	2.7	19.80 ± 31.92	Land 98-978
2nd night, 1.82 m Telescope							
13	AF785029*	19 Oct	01:05:35.2	720	12.6	11.35 ± 11.09	Land 98-978
14	AF785030	19 Oct	01:36:41.0	720	29.6	35.05 ± 2.55	Land 98-978
15	AF785031	19 Oct	01:52:39.7	720	20.2	-6.23 ± 4.81	Land 98-978
16	AF785032	19 Oct	02:12:02.3	720	3.56	21.09 ± 45.84	Land 98-978
17	AF785033	19 Oct	02:30:31.3	720	7.39	-16.58 ± 9.95	Land 98-978
18	AF785041	19 Oct	03:54:54.2	720	6.20	27.67 ± 10.88	Land 98-978
3rd night, 1.82 m Telescope							
19	AF785103	20 Oct	01:45:13.1	720	14.9	-40.33 ± 4.15	Hyades 64
20	AF785104	20 Oct	02:00:13.4	720	17.6	6.67 ± 7.19	Hyades 64
21	AF785105	20 Oct	02:15:35.7	720	24.5	25.35 ± 8.79	Hyades 64
22	AF785106	20 Oct	02:29:27.0	720	22.0	25.03 ± 0.18	Hyades 64
23	AF785108	20 Oct	02:59:01.2	720	27.9	23.40 ± 6.54	Hyades 64
24	AF785109	20 Oct	03:12:59.9	900	26.0	15.78 ± 2.32	Hyades 64
25	AF785110	20 Oct	03:32:04.0	900	24.6	18.26 ± 4.37	Hyades 64
26	AF785111	20 Oct	03:49:30.4	720	26.5	22.48 ± 3.33	Hyades 64
4th night, 1.82 m Telescope							
27	AF792178	18-nov	23:24:26.8	1200	69.6	11.02 ± 1.24	Hyades 64
28	AF792179	18-nov	23:58:30.7	1200	18.9	18.79 ± 5.62	Hyades 64
29	AF792180	19-nov	00:22:10.3	1200	19.7	14.47 ± 6.79	Hyades 64
30	AF792181	19-nov	00:45:49.5	1200	22.5	13.89 ± 2.38	Hyades 64
31	AF792183*	19-nov	01:32:22.7	1200	19.2	10.31 ± 7.34	Hyades 64
5th night, 1.82 m Telescope							
32	AF800545*	26 Dec	22:09:36.0	1200	39.8	4.03 ± 2.54	Hyades 64
33	AF800546*	26 Dec	22:33:36.6	1500	51.1	5.39 ± 1.29	Hyades 64
34	AF800547*	26 Dec	23:03:28.2	1800	48.7	5.14 ± 3.20	Hyades 64
35	AF800548*	26 Dec	23:36:27.2	1800	48.8	8.55 ± 2.62	Hyades 64
36	AF800549*	27 Dec	00:10:14.7	1800	48.4	5.64 ± 3.33	Hyades 64
37	AF800550*	27 Dec	00:50:16.5	1800	59.6	3.69 ± 1.12	Hyades 64
38	AF800551*	27 Dec	01:23:27.7	1800	63.4	2.14 ± 1.08	Hyades 64
39	AF800552*	27 Dec	01:56:24.7	1800	62.5	4.16 ± 1.61	Hyades 64
40	AF800553*	27 Dec	02:30:01.4	1800	49.7	2.86 ± 2.47	Hyades 64
41	AF800554*	27 Dec	03:02:53.4	1800	45.6	9.50 ± 2.19	Hyades 64
42	AF800555*	27 Dec	03:35:58.2	1800	34.9	4.69 ± 2.20	Hyades 64
6th night, 1.82 m Telescope							
43	AF800625*	27 Dec	21:39:48.6	1800	52.8	3.99 ± 1.70	Hyades 64
44	AF800626*	27 Dec	22:11:41.3	1800	45.8	14.79 ± 1.03	Hyades 64
45	AF800627*	27 Dec	22:44:10.0	1800	41.0	11.79 ± 2.02	Hyades 64

Table 3.7: table with the 45 spectra of Didymos acquired after the DART impact between 18^{th} October and 27^{th} December 2022. The columns show the start date of spectrum acquisition, exposure time, S/N, Spectral Slope calculated in %/1000 Å, and the corresponding solar analogs. Spectra marked with an asterisk (*) after the name were used to study the rotation of Didymos.

that of a solar analog, which is a star similar to the Sun. The solar analog spectrum should be acquired under similar airmass conditions as the asteroid spectrum to introduce minimal error into the final asteroid spectrum. A median filter with a box of 100 pixels and 3 sigma was applied to remove cosmic rays and spurious features.
The ratio between the signal S and the noise N is the so-called S/N, and represents a measure of the presence of useful signal compared to the level of noise present within the signal itself. There are many methods to calculate the S/N ratio. In this thesis, it was calculated using three different methods:

- **method 1:** to calculate the signal S, intervals of 15 Å were considered starting from the beginning of the spectrum and calculated the median value of the flux in each interval. The sum of the values of all intervals is the signal S. To calculate the noise N, the standard deviation is calculated for each interval of 15 Å: the sum of the standard deviations is the noise N. In this case, the error of measurement of each point of the spectrum is standard deviation;
- **method 2:** the S/N is computed in the range between 5700 and 7700 Å using the previous method. The error is the standard deviation calculated for each interval of 15 Å: the sum of the standard deviations is the noise N;
- **method 3:** the third method, the signal is the sum of the flux of each points of spectrum in Å. The noise is $\sqrt{S+B}$, where S is the signal and B is the background. In this case, measurement errors of the points in the spectrum is the propagation of errors between the errors of the solar analogue and the errors of the asteroid without division for the solar analog.

The spectral range between 5700 and 7700 Å has less noise, resulting in a higher S/N ratio with the second method compared to the first. For the following analysis the first method was adopted, as it considers the total spectrum. If the S/N value obtained using method 1 is greater than 10, the spectrum is considered acceptable for the measurements. A comparison between the third and second methods shows a very similar S/N. The S/N value reported in table 3.7 are calculated using the first method. Furthermore, the spectra were normalized to 5500 Å. Normalization is calculated by taking the median value of the flux between 5400 and 5600 Å and dividing all points of the spectra by the median value found. The spectral slope is calculated using the least squares method in the spectral range between 6000-7000 Å. The spectral slope is calculated as follows:

$$\frac{f(\lambda_2) - f(\lambda_1)}{\lambda_2 - \lambda_1} \tag{3.6}$$

where f(λ_1) and f(λ_2) are the values in y of the line in 6000 and 7000 Å. The value found in formula 3.6 was calculated as a percentage and then multiplied by 1000: the spectral slope is calculated in %/1000 Å.

3.4.5 Results

The data analysis of Didymos can be divided into two parts:

1. study of the spectral slope and taxonomy of Didymos after the impact of DART;
2. instrumental analysis of differential tracking and slit orientation.

3.4.5.1 Spectral Slope

To describe the rotation of Didymos, we will only consider a few spectra (the spectra used have a '*' next to the name in table 2): seven spectra from October 18^{th}, 2022 (number 1, 2, 3, 4, 5, 6 and 7), one spectrum from October 19^{th}, 2022 (number 13), one spectrum from November 19^{th}, 2022 (number 31), and eleven spectra from December $26^{th}/27^{th}$ (number 32, 33, 34, 35, 36, 37, 38, 39, 40, 41 and 42). On the first night, almost a complete rotation of Didymos (2.13 hours compared to the 2.26 hours rotation) occurred, and on the fifth night, Didymos performed more than two complete rotations (5.93 hours). Figure 3.18 shows the spectra obtained on the night of October 18^{th}, 2022 (night 1): the derived spectra S/N is (18.9<S/N< 37.3), which is good for these measurements being the major value of 10, although some small fluctuations can be observed in the spectrum due to Didymos remaining in the slit for less than 15 minutes (in a range between 8 and 12 minutes depending on the spectrum, 15 minutes is the exposure time), due to problems with the differential tracking of the Copernico telescope. Figure 3.19 shows the AF800555 spectrum acquired on December 27^{th}, 2022, along with its errors, and the S spectral type curve from Bus-DeMeo taxonomy with its errors (this curve is taken form the site http://smass.mit.edu/busdemeoclass.html). Figure 3.20 shows the spectra of the two Didymos rotations during the night of December $26^{th}/27^{th}$, 2022.

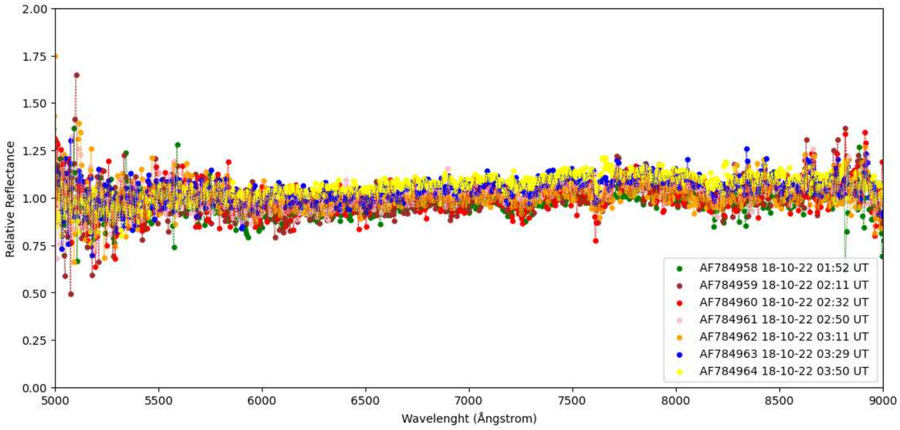

Figure 3.18: 7 spectra of Didymos acquired using the Copernicos telescope on 18^{th} October 2022, from 1:52 UT to 3:50 UT.

At the beginning Didymos was classified as Xk-type by Binzel [247] on the basis of visible spectroscopy. However, a few years later, De Leon [248],[249] classified Didymos as S-type based on NIR data, and this classification is confirmed by Dunn [250]. Didymos and Dimorphos are expected to have the same chemical composition because the small binary systems are formed through mass shedding from a progenitor. Furthermore, even if Dimorphos had a different surface composition, it would not be observable because its contribution before impact is only 5% of the reflected light from the system. Polishook [3] and Lin [23] found a variation in spectral slope in the first 4 days after the impact of DART. Despite the observed variation, Polishook [3] consistently classified Didymos as S-type during all of its observations, while Lin [23] classified Didymos as C-type on 27^{th} September 2022, Q-type on 29^{th} September 2022, and S-type on 30^{th} September 2022. Lin explained the change in slope and spectral type due to the dense dust cloud formed by the impact in front

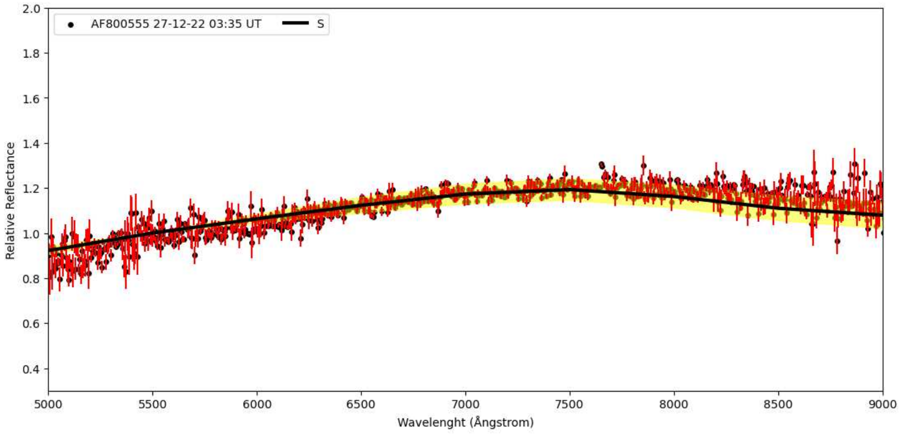

Figure 3.19: 1 spectrum of Didymos (blue points) acquired using the Copernico's telescope on 27^{th} December 2022 at the 3:50 UT. It plots the measurement errors in flux of each point of the spectrum (red bars) on each spectrum point and the curve of the S-type classification taxonomy (black line) with its errors (yellow bars).

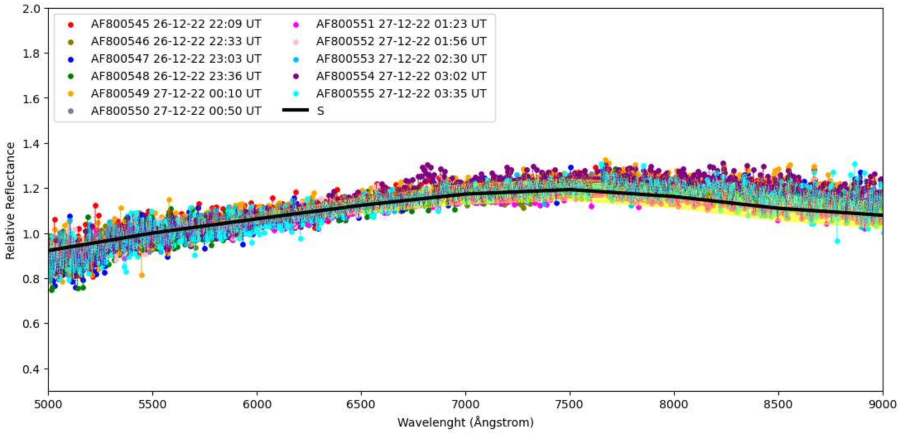

Figure 3.20: 11 spectra of Didymos acquired using the Copernicos telescope from 26^{th} December 2022 at 22:09 UT to 27^{th} December at 3:55 UT. It plots the curve of S-type Bus and DeMeo taxonomy classification (black line) with its errors (yellow bars).

of the binary system. The dust cloud decreased in the following days, forming a long tail (see fig. 3.21, and Didymos returned to show the S-type. Polishook [3] observed a difference in spectral slope, but maintained the S-type spectral classification even days after impact. According to Polishook [3], the spectral variation may be due to three physical processes: compositional variation of the ejecta material (ejection of 'fresh'), non-weathered material, and ejected material with varied grain sizes. The shallow slope spectra of Didymos do not exhibit Q-type characteristics. This suggests that the surface material excavated by the impact of DART is not as fresh as that of Q-type asteroids.

The observational strategy adopted in this thesis was based on studying a possible spectral variation of the system before and after the impact, which could be related to intrinsic surface properties of Didymos or the presence of ejecta dust developed during DART impact. My observations confirm that the taxonomic type S was present in both October and December.

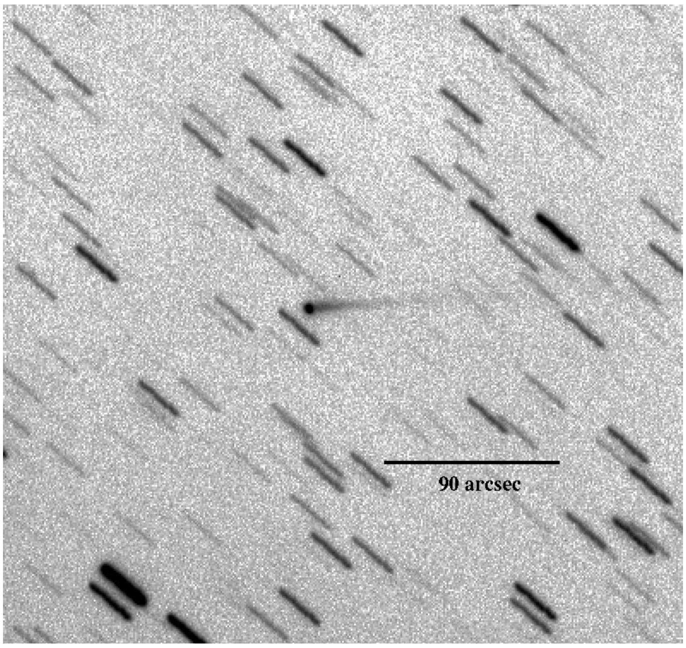

Figure 3.21: image of Didymos' tail captured by the Schmidt telescope at the Asiago Astrophysical Observatory (INAF) on October 16, 2022.

Approximately nineteen days after impact, the spectrum of Didymos showed a taxonomic class of type S. This indicates that the dust cloud was not dense enough to be observed in the Didymos spectrum. Additionally, I studied the variation of the spectral slope from October to December. Figure 3.22 shows the values of the spectral slope with their respective errors. The red line is the best fits of my data that intercepts the values of the spectral slope within a 3 sigma error range. The only three spectra (AF784959, AF785029 and AF792183) that have a different value of the spectral slope are those with a low S/N ratio (18.9, 12.6, and 19.2). However, the measurement error of the spectral slope of these last spectra is very high, making their measurements fall within 1 sigma of error.

My observations severally agree with other observation published in literature regarding the taxonomic classification, but I am disagree with the changed in spectral slope as shown in the figure 3.22. In the first few days after the impact, a dense cloud of dust was observed in front of the binary system, which in the following days appeared as a long tail opposite to the motion of Didymos. In the following days, additional tails with different directions from the main tail emerged: the dust environment surrounding the system is non-uniform, as demonstrated by both ground-based [251] and space-based [252] measurements. The evolution of ejecta is complex: immediately after the impact, the distribution is more uniform compared to the following days. The tail is composed of grains of different sizes, ranging from finer to larger. Finer grains are dispersed faster during the first few hours/days [251]. Therefore, I expected that a change in slope could be due to the presence of larger grains. However, my observations show that even the larger grains have dispersed into the long tail as early as nineteen days after impact, as no variation in spectral slope has been observed. Therefore, after nineteen days from impact, the dense dust cloud observed in the first few days has diluted and become less dense, forming a long tail in the opposite direction of Didymos' motion.

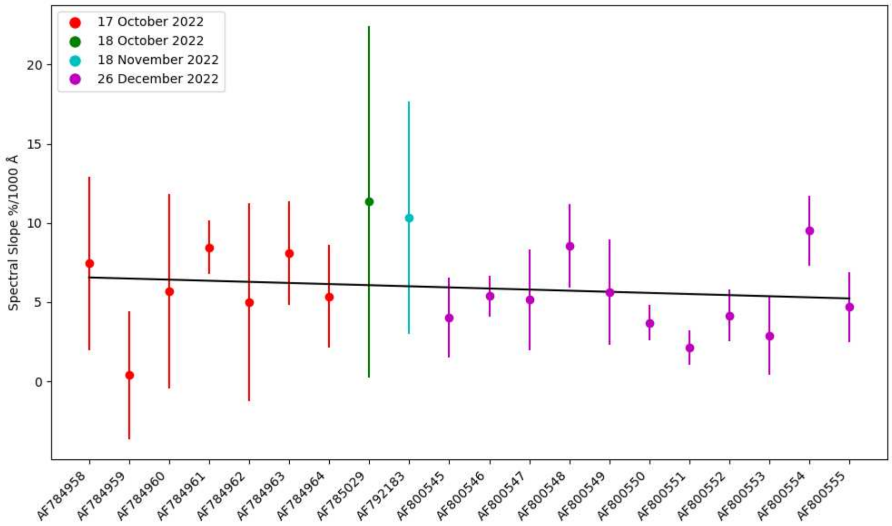

Figure 3.22: all values of the spectral slope in %/1000 Å, calculated between 6000 and 7000 Å. The values plotted are those used for the rotation/taxonomic study of the Didymos system in order of data acquisition from left to right. The red line is the best fit line for my data within a 3σ error.

Figure 3.23 compares 4 spectra: AF784963 from October 18th, 2022, AF785029 from October 19th, 2022, AF792183 from November 19th, 2022, and AF800547 from December 26th, 2022. The spectral slope remained unchanged during the three months after the impact, and Didymos has consistently shown a taxonomic classification of S-type since the beginning of my observations.

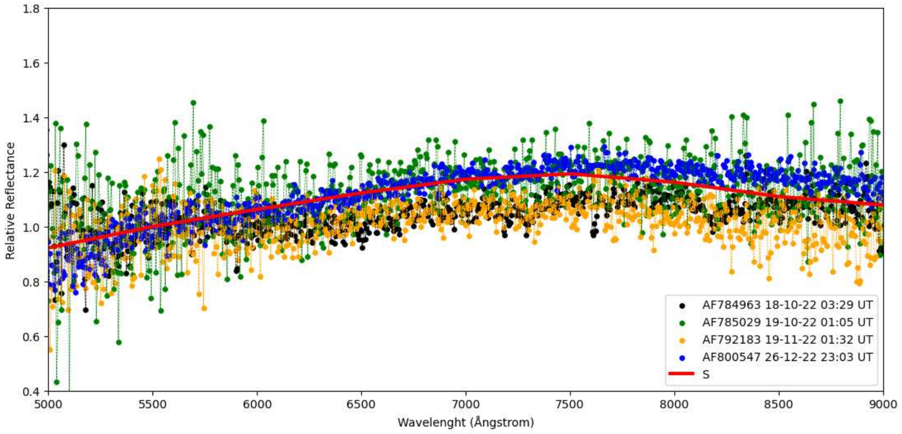

Figure 3.23: comparison of four spectra of Didymos: AF784963 from 18th October 2022, AF785029 from 19th October 2022, AF792183 from 19th November 2022, and AF800547 from 26th December 2022. The red curve represents the S-type curve of the Bus and DeMeo taxonomic classification.

3.4.5.2 Slit orientation

Some spectra (those without * next to their name in tab. 3.7) were not used in the analysis of Didymos' rotation due to technical and observational strategy issues during observations after the DART impact. During the Didymos observations, differential tracking of the Copernico telescope did not work well. Between October 17^{th} and 20^{th} 2020, Didymos had an apparent velocity ranging from 220 to 180 arcsec/hour in d(RA)×cos(DEC) and from 185 to 165 arcsec/hour in d(DEC)/dt. These are apparent velocities that can be considered "slow", but they are sufficient to get Didymos out of the slit in a few minutes, given the problem with the probe of the guide camera. Therefore, the observational strategy to keep Didymos in the slit for longer time was not to orient the slit along the direction of the atmospheric refraction so that Didymos could move vertically along the slit and remain in the slit for a few more minutes. However, tracking issues and incorrect slit orientation resulted in a significant error in the spectral slope of my spectra,lead to exclude these spectra from the analysis of Didymos rotation data. The 'discarded' data were instead used to study the effects of atmospheric refraction on my spectra.

The parallactic angle q is the spherical angle that indicates the inclination at which a celestial body appears to us with respect to the zenith position in its apparent motion on the celestial sphere. Figure 3.24 shows a spherical body in a small section of its apparent motion. Point Z is the point at the end of the disk that is turned towards the zenit and point N is the point turned towards the north celestial pole. The parallactic angle is the angle between these two directions and is conventionally positive when the object has passed its meridian. When the object is in the meridian, $q = 0°$. The following formula give the tangent of the parallactic angle:

$$\tan(q) = \frac{\sin(H)}{\tan(\phi)\cdot\cos(\delta) - \sin(\delta)\cdot\cos(H)} \tag{3.7}$$

where q is the parallactic angle, ϕ the latitude of the observatory, δ the declination of the target and H the hour angle.

The atmosphere plays a fundamental role in observing celestial objects. The light from a celestial object passes through the atmosphere of Earth and undergoes the phenomenon of refraction. When observing a celestial object with terrestrial telescopes, a small spectrum of the observed object is observed wider at greater distances from the zenith of the observatory. Atmospheric differential refraction affects the results of many measurement techniques in astronomy [253]. In spectroscopy, more light is lost at large zenith angles when an object is recorded at a wavelength that differs from the convolution of its energy distribution and the spectral response of the human eye. Therefore, if we consider a spectrum from the blue to the red wavelength and the spectrum is centered in the spectrograph's slit, more light can be lost in the outer regions compared to the central ones. This leads to errors in calculating the spectral energy distribution if the considered spectral range is very wide. These errors are smaller at low airmasses, but they are not negligible [253]. To minimize errors caused by atmospheric refraction, the slit should be rotated along the direction of atmospheric refraction, as well as rotated by the same value as the parallactic angle. Atmospheric dispersion can be influenced by several factors: indeed, it increases with increasing zenith angle and decreasing wavelength. Furthermore, the amount of atmospheric dispersion depends on the refractive index of the air, which in turn is affected by temperature, altitude, and location. A detaildanalysis of the atmospheric dispersion is out of this thesis; the mathematical/physical explanation was provided in the Filippenko's paper [253]. However, in this work, calculations

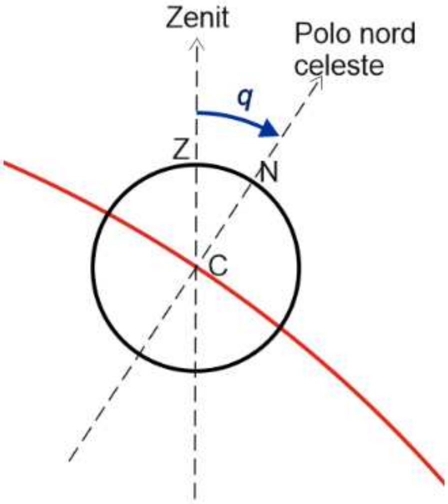

Figure 3.24: a spherical body in a small section of its apparent motion. Point Z is the point at the end of the disk that is turned towards the zenith, and point N is the point turned towards the north celestial pole. The parallactic angle is the angle between these two directions. Figure taken from https://eratostene.vialattea.net/wpe/glossario/angolo-parallattico

of the effects of atmospheric dispersion for the Asiago observatory were not conducted. According to calculations done by different observatories, it has been concluded that at small airmass (typically in the range 1.05-1.20) corresponding to small distances from to zenith, the spectral distance between red and blue wavelengths is less than 1", but the same width can even exceed 2" at airmass greater than 1.5. Figure 3.25 shows the values in arcsec of the width of the spectrum resulting from atmospheric refraction at different wavelengths for the Mauna Kea observatory. In figures 3.25 and 3.26, the effect of atmospheric refraction can be observed. Figure 3.26 is very similar to figure 3.25, but takes into account the angular distance from the zenith. Table 3.8 shows the parallactic angle values used during the observations and those predicted by the direction of the atmospheric refraction. Upon analysing my spectra, I observed a 12.09% difference in slope in the spectra obtained with the Galileo telescope on night 2 (see fig. 3.28). The spectral slope is always calculated with the same method described in 3.4.3 The spectral slope of these spectra is very different from that observed in the observations of December or of night 1 with the correct slit orientation. During night 2, I measured a difference in slope greater than 50% in the spectra obtained with the Copernico telescope (see fig. 3.29). On night 3, I observed a slope difference very similar to that of night 2 (see fig. 3.30). However, on night 4, I observed an 8.48% difference in the spectra obtained with the Copernico telescope (see fig. 3.31). Furthermore, in the spectra obtained in August 2022, the difference in slopes is much greater than the slopes calculated in October 2022. As Didymos rose in altitude relative to the horizon, the difference in slope decreased. This result is predicted by Filippenko's work [253] because the difference in distance between the red and blue wavelengths decreases with increasing altitude. After each exposure, Didymos was not in the slit, so it had to be repositioned between each acquisition. If the spectrum given by atmospheric refraction is wide, a different part of the spectrum is placed in the slit each time. This is why on the night of 18^{th} November 2022, the percentage difference in spectral slope is lower compared to October and August

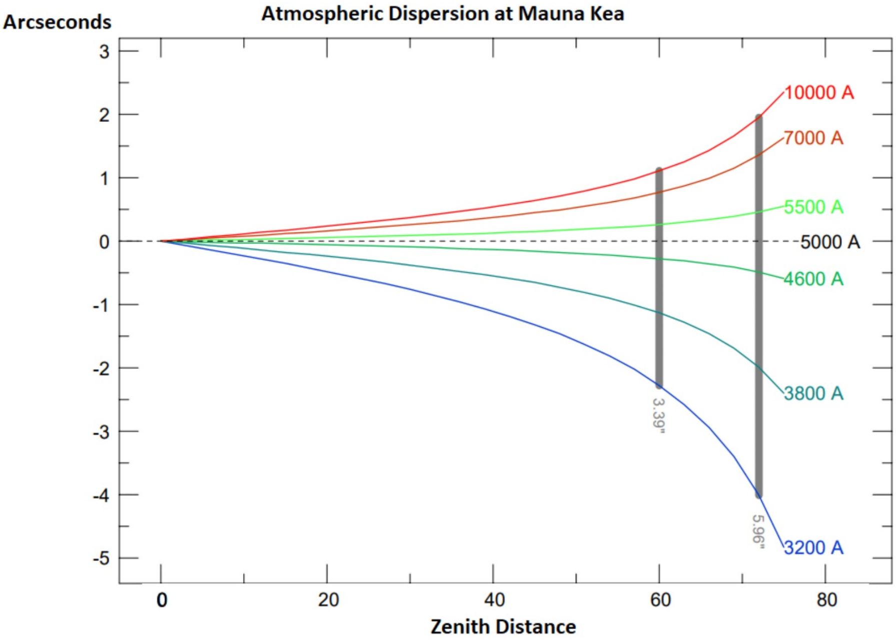

Figure 3.25: the graph shows the effect of atmospheric refraction on wavelengths of 3200, 3800, 4600, 5500, 7000, and 10000 Åat the Mauna Kea observatory. The x-axis represents the distance from the zenith in degrees, and the y-axis represents the distance of the wavelengths from 5000 Åin arcsec. Figure taken from Rakich (2021) [24].

2022. In the spectra obtained in December 2022, it was not necessary to orient the slit along the direction of atmospheric refraction because the difference between the blue and red parts is much smaller than the width of the slit. In fact, at an altitude greater than 60°, the orientation of the slit does not affect the spectral slope. After this analysis, starting from December 2022, the differential tracking of the Copernico telescope works well and it can be possible to observe objects with maximum apparent velocities up of 830 arcsec/hour in d(RA)×cos(DEC) and 1700 arcsec/hour in d(DEC)/dt defining the slit with parallactic without the risk that the object goes out of the slit.

N	Image	Date	Epoch (UT)	S/N	Alt (deg)	Airmass	PA (deg)	PA prev. (deg)
1st night, 1.82 m Telescope								
1	AF784958	18 Oct	01:52:25.0	25.6	27.79	2.133	-27.0	-27.3
2	AF784959	18 Oct	02:11:11.9	18.9	29.86	2.001	-27.0	-24.4
3	AF784960	18 Oct	02:32:31.9	20.1	31.88	1.886	-7.0	-20.7
4	AF784961	18 Oct	02:50:44.5	27.1	33.37	1.811	-14.0	-17.4
5	AF784962	18 Oct	03:11:28.7	23.0	34.78	1.748	-14.0	-13.4
6	AF784963	18 Oct	03:29:23.0	27.8	35.70	1.710	-7.0	-9.7
7	AF784964	18 Oct	03:50:28.6	37.3	36.41	1.681	-3.0	-5.3
2nd night, 1.22 m telescope								
8	IMA108103	19 Oct	01:44:44.1	10.8	27.67	2.142	-0.1	-29.0
9	IMA108104	19 Oct	02:19:29.7	13.2	31.57	1.907	-0.1	-23.7
10	IMA108105	19 Oct	02:34:44.9	4.9	33.01	1.790	-0.1	-19.2
11	IMA108106	19 Oct	03:05:47.7	5.2	35.44	1.720	-0.1	-15.2
12	IMA108107	19 Oct	03:27:10.9	2.7	36.70	1.671	-0.1	-10.8
2nd night, 1.82 m Telescope								
13	AF785029	19 Oct	01:05:35.2	12.6	22.56	2.583	-30.0	-34.0
14	AF785030	19 Oct	01:36:41.0	29.6	26.68	2.111	0.0	-30.1
15	AF785031	19 Oct	01:52:39.7	20.2	28.63	2.075	0.0	-27.8
16	AF785032	19 Oct	02:12:02.3	3.56	30.85	1.944	0.0	-24.8
17	AF785033	19 Oct	02:30:31.3	7.39	32.64	1.847	0.0	-21.7
18	AF785041	19 Oct	03:54:54.2	6.20	37.64	1.633	0.0	-4.8
3rd night, 1.82 m Telescope								
19	AF785103	20 Oct	01:45:13.1	14.9	28.60	2.080	0.0	-29.4
20	AF785104	20 Oct	02:00:13.4	17.6	30.38	1.970	0.0	-27.2
21	AF785105	20 Oct	02:15:35.7	24.5	32.04	1.877	0.0	-24.8
22	AF785106	20 Oct	02:29:27.0	22.0	33.45	1.808	0.0	-22.5
23	AF785108	20 Oct	02:59:01.2	27.9	36.01	1.697	0.0	-17.0
24	AF785109	20 Oct	03:12:59.9	26.0	36.89	1.660	0.0	-14.2
25	AF785110	20 Oct	03:32:04.0	24.6	37.98	1.622	0.0	-10.2
26	AF785111	20 Oct	03:49:30.4	26.5	38.62	1.599	0.0	-6.5
4th night, 1.82 m Telescope								
27	AF792178	18-nov	23:24:26.8	69.6	28.70	1.964	0.0	-45.5
28	AF792179	18-nov	23:58:30.7	18.9	34.54	1.756	0.0	-44.5
29	AF792180	19-nov	00:22:10.3	19.7	38.56	1.600	0.0	-43.0
30	AF792181	19-nov	00:45:49.5	22.5	42.29	1.480	0.0	-41.0
31	AF792183	19-nov	01:32:22.7	19.2	49.33	1.316	0.0	-38.4
5th night, 1.82 m Telescope								
32	AF800545	26 Dec	22:09:36.0	39.8	54.63	1.225	0.0	-49.7
33	AF800546	26 Dec	22:33:36.6	51.1	58.05	1.171	0.0	-47.2
34	AF800547	26 Dec	23:03:28.2	48.7	62.78	1.119	0.0	-42.3
35	AF800548	26 Dec	23:36:27.2	48.8	67.54	1.080	0.0	-33.6
36	AF800549	27 Dec	00:10:14.7	48.4	71.17	1.056	0.0	-19.7
37	AF800550	27 Dec	00:50:16.5	59.6	72.55	1.048	0.0	2.5
38	AF800551	27 Dec	01:23:27.7	63.4	71.32	1.057	0.0	20.5
39	AF800552	27 Dec	01:56:24.7	62.5	67.83	1.080	0.0	33.9
40	AF800553	27 Dec	02:30:01.4	49.7	63.07	1.121	0.0	42.6
41	AF800554	27 Dec	03:02:53.4	45.6	58.37	1.179	0.0	47.8
42	AF800555	27 Dec	03:35:58.2	34.9	52.65	1.261	0.0	50.7
6th night, 1.82 m Telescope								
43	AF800625	27 Dec	21:39:48.6	52.8	50.72	1.262	0.0	-51.4
44	AF800626	27 Dec	22:11:41.3	45.8	55.82	1.204	0.0	-49.2
45	AF800627	27 Dec	22:44:10.0	41.0	61.64	1.139	0.0	-45.1

Table 3.8: with the 45 spectra of Didymos acquired after the DART impact between 18th October and 27th December 2022. The columns show the start date of spectrum acquisition, S/N, altitude, airmass, the orientation of slit of Didymos at the starting of acquisition (PA) and the expected parallel angle (PA prev.).

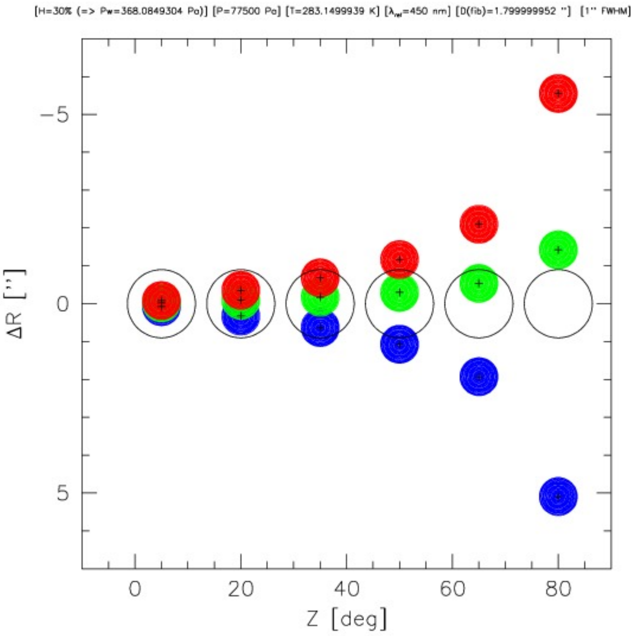

Figure 3.26: illustrates the effect of atmospheric refraction at different distances from the zenith. The red, green, and blue dots represent the wavelengths in the red, green, and blue. As the distance from the zenith increases, the red and blue wavelengths are further separated from the green wavelength. The x-axis represents the distance from the zenith in degrees, and the y-axis represents the width in arcsec of the spectrum formed by atmospheric refraction. Figure taken from https://stargazerslounge.com/topic/308032-atmospheric-dispersion-corrector-omegon-v-zwo/page/2

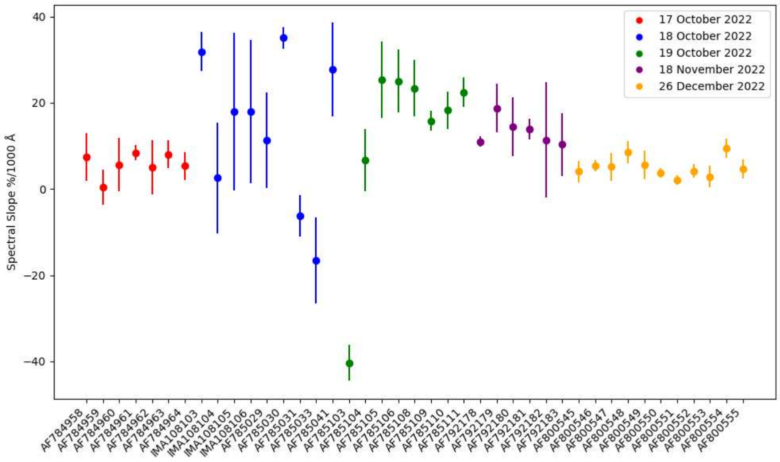

Figure 3.27: graphic with all the values of the spectral slope in %/1000 Å, calculated between 6000 and 7000 Å. The values plotted are the values of all spectra of the Didymos system in order of data acquisition from right to left.

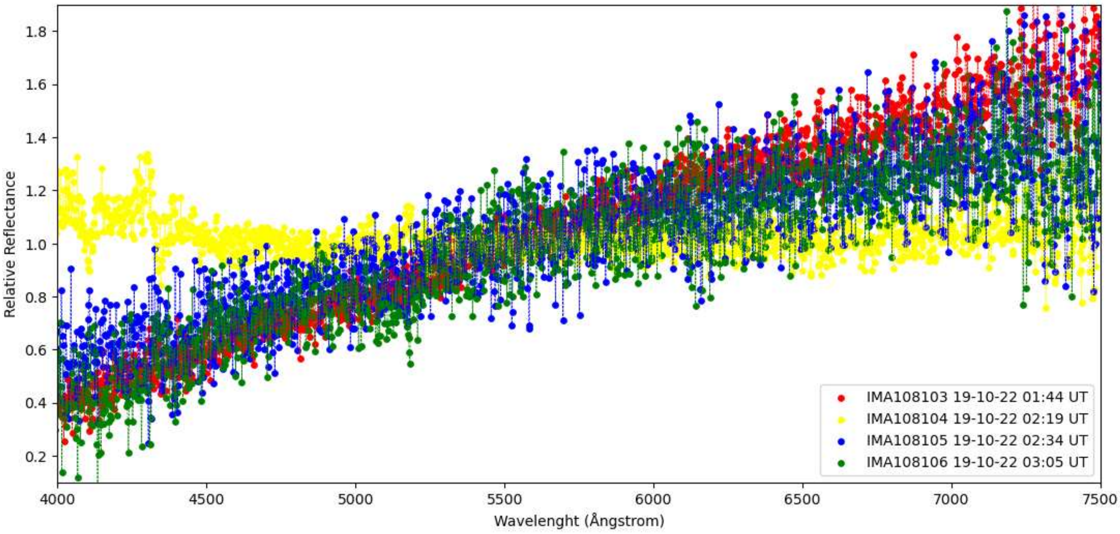

Figure 3.28: 4 spectra of Didymos acquired using the Galileos telescope on 19^{th} October 2022 from 1:44 UT to 3:05 UT.

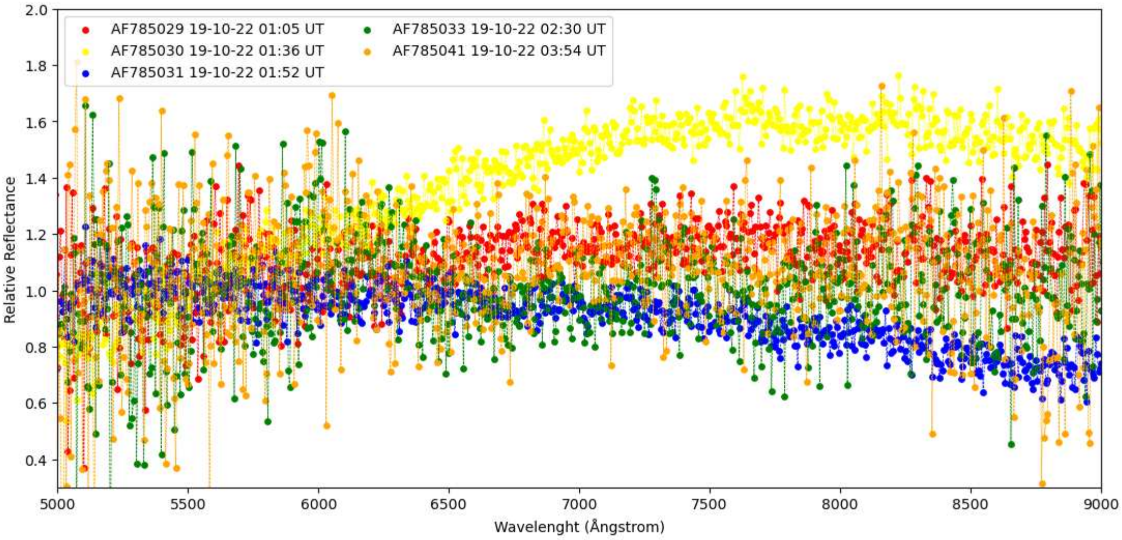

Figure 3.29: 5 spectra of Didymos acquired using the Copernicos telescope on 19^{th} October 2022 from 1:05 UT to 3:54 UT.

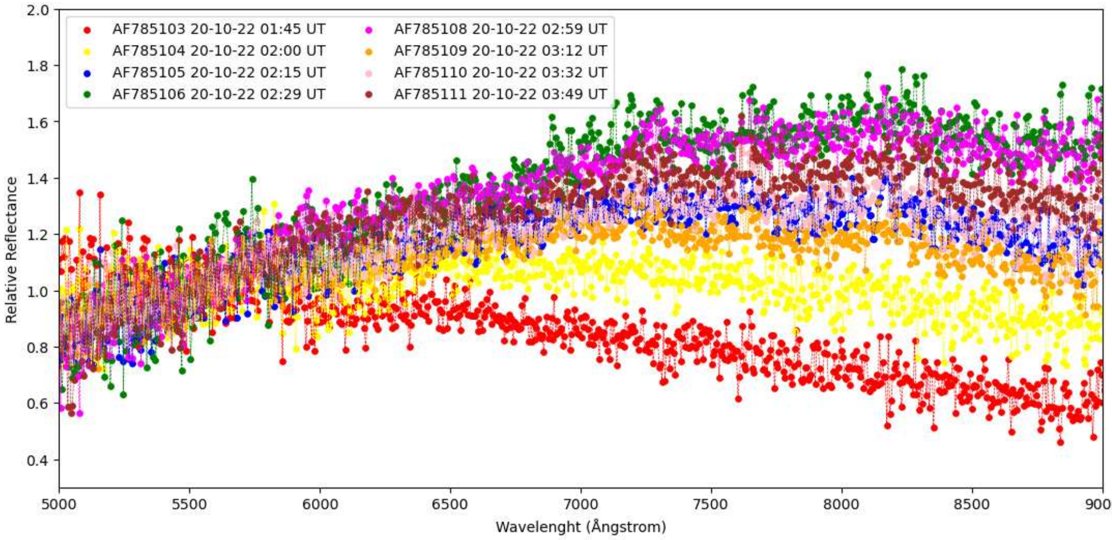

Figure 3.30: 8 spectra of Didymos acquired using the Copernicos telescope on 20th October 2022 from 1:45 UT to 3:49 UT.

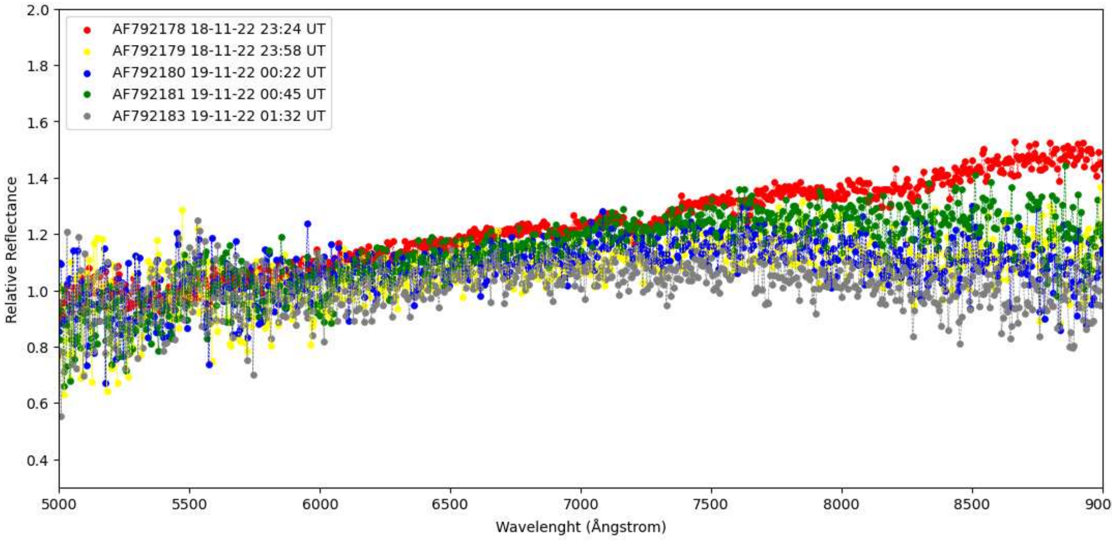

Figure 3.31: 5 spectra of Didymos acquired using the Copernicos telescope from 18th November 2022 at 23:45 UT to 19th November at 1:32 UT.

Chapter 4

The NEOROCKS Project

4.1 Summery of NEOs properties

This paragraph summarizes several properties of NEOs, selected on the basis of their fundamental role in the data analysis carried out in my thesis. NEOs are asteroids that come from the Main Belt or the comet population and are studied for various reasons [254]:

- some NEOs are remnants of planetesimals that led to the formation of planets, making them crucial for studying the origin and evolution of the Solar System [254];
- due to their proximity to Earth, NEOs are important to understand the amount of water and organic-rich material that they have brought to early Earth, and the description of the formation of life on our planet [255],[256];
- the dynamic and physical investigation of NEOs allowed to assess the orbital evolution of small bodies in the context of gravitational perturbations from major planets and YORP, Yarkovsky, and space weathering effects [254];
- being planetary defence the main focus of NEOs, it is crucial to determine their orbit to assess the probability of impact on our planet, their chemical composition, and their physical properties in order to predict whether they impact on Earth, and which damages can produce (e.g., wind, fires, earthquake, tsunami) in addition to the creation of the crater itself [9];
- in the near future, the chemical composition of NEOs will be useful in identifying the 'richest' NEOs to extract their materials for transportation to Earth.

In particolar, some NEAs are classified as PHAs, which means that they are potentially hazardous objects for our planet ($H \leq 22$ and with a $MOID \leq 0.05$ AU). These objects can represent a long-term risk for collisions with our planet and can cause extensive damage. Currently, only 10% of the NEAs population are classified as PHAs [254]. Additionally, the small asteroids in the Main Belt are challenging to observe: NEO population includes objects that are approximately three orders of magnitude smaller than those observable in the Main Belt [254]. To study NEOs, photometry and spectroscopy are fundamental techniques for investigating their main physical properties, such as size, shape, taxonomy, and morphology. The largest spectroscopic survey of asteroids is provided by the SMASS program (http://smass.mit.edu/smass.html) and its continuation: MIT-UH_IRTF NEO Reconnaissance (http://smass.mit.edu/minus.html) [116][117][107]. The spectra obtained are mainly in the visible and near-infrared (NIR) wavelengths. There are several programs that aim to sample NEOs and study their physical properties[254]. For instance, the Spectroscopic Investigation of Near Earth Objects (SINEO) used the ESO New Technology Telescope and the Italian Telescopio Nazionale Galileo (TNG) [257], while the Near-Earth and Mars-Crosser Asteroids Spectroscopic Survey (NEMCASS) employed the Nordic Optical Telescope and the TNG [249].

4.2 NEOROCKS

Due to new ground-based telescopes, a large amount of data on NEOs have been collected, leading to the need of different programs/projects to be developed to study the physical properties of NEOs. These programs must ensure access to their archives, as well as maintenance and uploading of the data products on the long-term [258]. The NEO Rapid Observation, Characterization and Key Simulations (NEOROCKS) Collaborative Research Project is an EU-funded project that started in January 2020 to address the topic "Improvement of our knowledge of the physical characteristics of the NEO population" of the call SU-SPACE-23-SEC-2019 from the Horizon 2020 - Work Programme 2018-2020 Leadership in Enabling and Industrial Technologies - Space [259].
NEOROCKs aims to improve our understanding of the physical characteristics, origin, and evolution of NEOs for planetary defense [225].
In more details, the NEOROCKS objectiving are:

- to develop and validate advanced mathematical methods and innovative algorithms for NEO orbit determination and impact monitoring [259];
- to organize follow-up astronomical observations of NEOs efficiently, in order to obtain high-quality data needed to derive their physical properties, giving priority to timely addressing potentially hazardous objects [259];
- to improve dramatically statistical analysis, modelling and computer simulations aimed to understand the physical nature of NEOs, focussing on small size objects, which are of uttermost importance for designing effective impact mitigation measures in space and on the ground [259];
- to ensure maximum visibility and dissemination of the data beyond the timeline of the project, by hosting it in an existing astronomical data center facility [259];
- to foster European and international cooperation on NEO physical characterization, providing scenarios and roadmaps with the potential to scale-up at a global level the experience gained during the project [259];
- to apply and guarantee continuity of educational and public outreach activities needed to improve significantly public understanding and perception of the asteroid hazard, counteracting the spreading of fake news and unjustified alarms [259];
- building a team of European expert astronomers able to grant access to large aperture telescopes equipped with state of the art instrumentation in order to perform high-quality physical observations and foster the related data reduction process [225];

- investigating the strong relationship between the orbit determination of newly discovered objects and the quick execution of follow-up observations in order to provide enabling SW technologies for facing the threat posed by the imminent impactors [225];
- profiting of the European industrial expertise in on-going SSA (Space Situational Awareness) initiatives to plan and execute breakthrough experiments foreseeing the remote tasking of highly automatized robotic telescopes in order to provide a proof-of-concept rapid response system [225];
- guarantee extremely high standards in the data dissemination through the involvement at agency level of a data centre facility already operating in a European and international context, thus scaling up at a global level the visibility of the results achieved during the project [225].

The NEOROCKs project ended in June 2023. The data collected during its three-year activity is now available on the web portal and database, which will be migrated to the Space Science Data Center of the Italian Space Agency (ASI-SSDC: https://www.ssdc.asi.it/) in order to be hosted in a permanent space data management infrastructure [260]. In conclusion, NEOROCKs aims to attract the scientific community by describing the physical characteristics of NEOs and offering the possibility to manage their data in a shared context, allowing for long-term data storage and access.

4.3 NEOROCKS observation at Asiago telescopes

The observation program in Asiago began on 5^{th} December, 2019 and is still ongoing as of 12^{th} March, 2024 (for NEOROCKS it is valid until June 2023 and now NEO monitoring is conducted independently). For the first two years (until January 2022), the program was based on specific Target of Opportunity (ToO) or service observations at the Asiago telescopes, with only one NEO being observed per night. Since January 2022, a proposal was submitted and accepted for the Copernico telescope in Astrophysics Observatory in Asiago, which provided the opportunity to observe three nights per month, for nine months per year. During this period, I observed the majority of the NEOs analysed for our study. In January 2024, a second proposal was accepted for the Copernico telescope in Asiago, allowing our group to continue observing NEOs for another two years. This section will describe the data analysis and results obtained after five years of observation with the Galileo and Copernico telescopes in Asiago. The first two years of observations were carried out by other researchers in the research group to which I belong, as well as by observers in service at the Copernico/Galileo telescope. I conducted the observational nights since January 2022. Other researchers in the group performed data reduction for the first three years of observation, while I did it for the last two. Data analysis was carried out by the entire research group during the five years of the observational campaign.
The observational strategy used for this project is similar to that adopted for Didymos (see section 3.4.3). Observations with the Copernico telescope were made using the long-slit at a 132-micron aperture (1.69 arcsec) and the VPH6 grism of 285 lines/mm, which yields a dispersion of 3.5 Å/pixel with low resolution, R=500, in the spectral range of 0.4-1 μm. The spectra obtained with the Galileo telescope were acquired using a long slit with a 250 μm aperture (3 arcsec) and a grating of 300 lines/mm in the spectral range of 0.45-0.9 μm. The exposure time varied from 1200 s to 1800 s depending on the observatory's weather

conditions and the target’s magnitude. The apparent magnitude in the V band did not exceed 18.5 mag for the Copernico telescope and 16 mag for the Galileo telescope.
The observations were conducted by orienting the slit along the atmospheric refraction for objects below 60° altitude relative to the horizon. The observation strategy relied on selecting objects very close to the zenith to minimize the effects of atmospheric differential refraction. Additionally, a G2V solar analog has a similar airmass with the observed asteroid was chosen. There was a choice of 10 solar analogs available, summarized in table 4.1. The objects to be observed were selected based on the search for NEOs from the site

solar analog	RA	Dec	Mag V
Land (SA) 93-101	01h 53m 18.0s	+00° 22’ 25”	9.7
Hyades 64	04h 26m 40.1s	+16° 44’ 49”	8.1
Land (SA) 98-978	06h 51m 34.0s	-00° 11’ 33”	10.5
Land (SA) 102-1081	10h 57m 04.4s	-00° 13’ 12”	9.9
Landolt (SA) 107-684	15h 37m 18.1s	-00° 09’ 50”	8.4
Land (SA) 107-998	15h 38m 16.4s	+00° 15’ 23”	10.4
16 Cyg B	19h 41m 52.0s	+50° 31’ 03”	6.2
Land (SA) 112-1333	20h 43m 11.8s	+00° 26’ 15”	10.0
Land (SA) 115-271	23h 42m 41.8s	+00° 45’ 14”	9.7

Table 4.1: solar analogs used during my observations. The table shows the name, right ascension, declination and V-band magnitude of the star.

https://ssd.jpl.nasa.gov/tools (by entering the parameters described above, magnitude less than 18.5 and altitude greater than 30°). Priority was given to PHAs, which were identified according to the database out $https : //ssd.jpl.nasa.gov/tools/sbdb_lookup.html$. I chose targets with an absolute magnitude H between 16 and 23 mag, because smaller NEOs are more likely to impact Earth than larger ones. However, during the 5-year observation period, only six NEOs with a magnitude H<16 (including Eros with a magnitude of approximately 10) and two very small NEOs (16 and 24 m, H>24) were observed (see fig. 4.1). The site https://neo.ssa.esa.int was used to check if an asteroid had already been taxonomically classified: priority was given to NEOs that had not yet been classified. Objects far from the galactic plane were selected to avoid a crowded field of stars, ensuring that the asteroid did not appear to move above them. During the observation, the https://asteroid.lowell.edu/astfinder/ site was used to track the asteroid’s path in the following hours. This allowed for the identification of the asteroid and ensured that it did not pass over a star during the observations. Two spectra were acquired for each NEO and then compared after data reduction to be sure that there were no issues during the observation. Different slopes would have made us consider discarding data due to varying weather conditions or the asteroid’s exit from the slit. The spectra were reduced using the astronomical package Image Reduction and Analysis Facility (IRAF), following standard reduction procedures. I normalized the spectrum at 5500 Å and calculated the S/N for each spectra (see section 3.4.3).

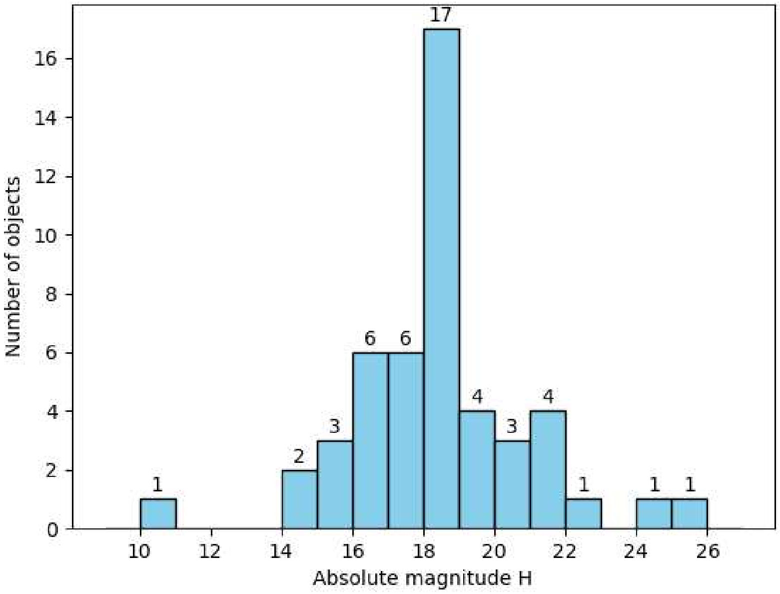

Figure 4.1: histogram showing the absolute magnitude H of the 49 NEOs analyzed. The x-axis represents the absolute magnitude, while the y-axis represents the number of counts.

4.4 Data Analysis

Spectral data in the visible region provides information on the surface composition of NEOs. My data analysis is divided into several parts, with the main objective being the taxonomic classification of the observed NEOs. Over the 5-year observation period, a total of ninety-eight NEOs were observed, although some of were subsequently discarded for the analysis on the basis of:

- low S/N ration of the spectrum;
- NEO exited from the slit due to its high velocity, which exceeded the correct functioning limits of Asiago's telescopic differential tracking;
- the slit was not oriented along the direction of atmospheric refraction.

This thesis reports the data analysis of 49 NEOs. It should be noted that some of the observed NEOs still require analysis. To describe the taxonomic classification procedure, I will explain the process using a single NEO as an example. If the spectral slope calculation (see section 3.4.3) was within 3σ of error, the spectra were considered good. The classification was performed using the Bus-DeMeo and Mahkle taxonomy framework. Bus-DeMeo's taxonomy consists of 25 classes covering a spectral range of 0.45-2.45 μm, while Mahkle's taxonomy comprises 17 classes in the spectral range of 0.45-2.45 μm. To classify according to Bus and DeMeo taxonomy, I compared my spectrum with the curve of each taxonomic type and its errors (downloadable from the sitehttp://smass.mit.edu/busdemeoclass.html). Figure 4.2 shows the spectrum of NEO 1999 AP10 with all the taxonomic types curves of the Bus and DeMeo classification. Figure 4.3 shows the spectrum of 1999 AP10 with its corresponding

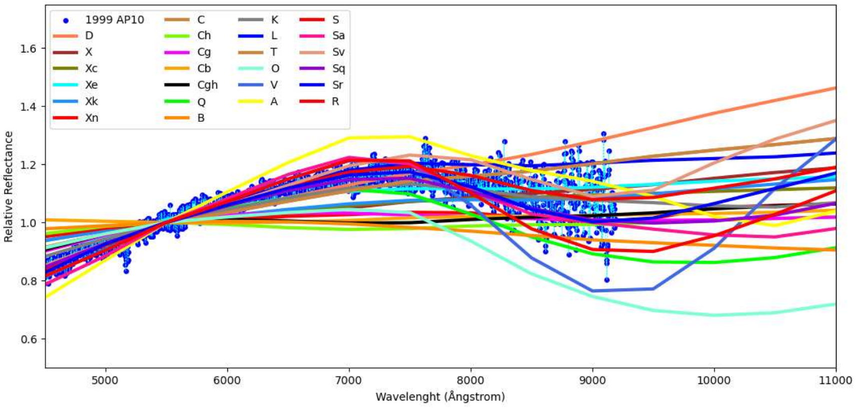

Figure 4.2: the spectrum of NEO 1999 AP10 was obtained using the Galileo telescope at the Asiago Astrophysical Observatory. The spectral types from the Bus and DeMeo classification are plotted in different colours.

errors. Measurement errors were calculated as described in section 3.4.3: the error is the standard deviation of the signal measured in the 15 $\mathring{A}$ interval. Additionally, Figure 4.3 shows the Bus and DeMeo S-type taxonomic curve. The S curve model data was interpolated using a CubicSpline polynomial function to match the same number of data points in my spectrum. Figure 4.4 shows the spectrum of 1999AP10, with the S-type taxonomic curve and its errors (yellow bar). Bus and DeMeo classification identifies 25 taxonomic types (see Figure 4.3) and to determine which curve best fits the data, I used the reduced χ^2 method.

The χ^2 method allows us to determine the probability of whether a hypothesized distribution

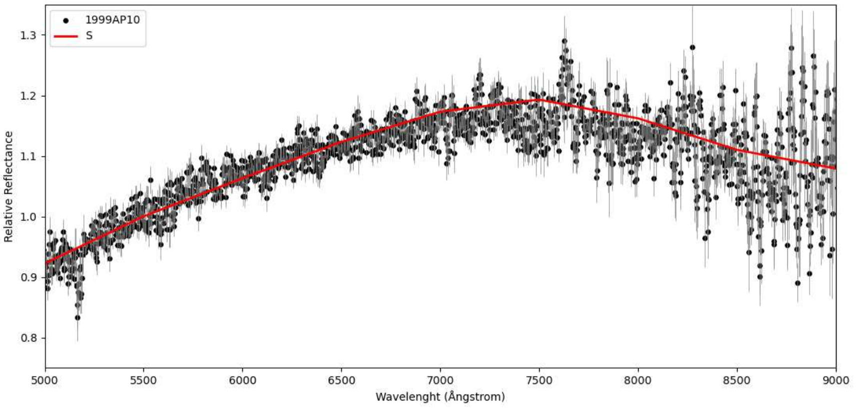

Figure 4.3: the spectrum of NEO 1999 AP10 was obtained using the Galileo telescope at the Asiago Astrophysical Observatory. The flux errors of individual points in the spectrum are plotted in grey. The red curve represents the S-type taxonomy classification by Bus and DeMeo.

can be accepted or rejected. If the χ^2 value is zero, then the consistency between the experimental and the expected data is perfect. If it is grater than 0, then the consistency

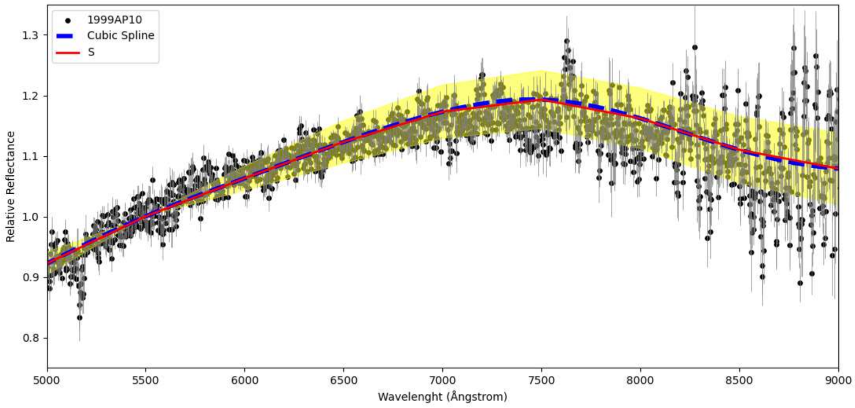

Figure 4.4: the spectrum of NEO 1999 AP10 was obtained using the Galileo telescope at the Asiago Astrophysical Observatory. The flux errors of individual spectrum points are plotted in grey. The red curve represents the S-type taxonomy classification by Bus and DeMeo, while the yellow bar indicates the errors of the curve. The blue dashed curve is the CubicSpline polynomial interpolation of the S spectral type curve by Bus and DeMeo.

cannot be "perfect" and the distribution of the expected data can be accepted for certain significant levels of probability. The χ^2 method was computed in three different ways:

- **Method 1:** the reduced χ^2 method was calculated taking into account both the measurement errors on the spectrum flux and those of the Bus and DeMeo taxonomic type model (in my example of S-type). The sigma was calculated by error propagation. The equation is:

  $$\chi^2 = \frac{1}{\nu}\sum_{i=1}^{n}\frac{(o_i - e_i)^2}{\sigma_i^2}$$

  where o_i is the number of times the variable value is observed within a certain class, e_i is the expected value of the frequency, σ is the error calcuted with the error propagation, ν is given by the number into which the dispersion interval of the variable has been divided minus the number of parameters calculated from the sample and again minus one unit for the constraint formed by the summation of o_i and n is the total number of my data;

- **Method 2:** the reduced χ^2 method was derived by considering only measurement errors on the spectral flux;

- **Method 3:** the χ^2 method was obtained without considering measurement errors; therefore, the division was calculated using the expected value from the cubic spline function, using the following equation:

  $$\chi^2 = \frac{1}{\nu}\sum_{i=1}^{n}\frac{(o_i - e_i)^2}{e_i}$$

The choice of which method to use depends on the type of spectrum available. All three methods have been applied to the available data. The best method to use is based on the

S/N ratio of each individual spectrum. Method 1 appears to be the most "appropriate" because it considers both the error of measurements, but it was not always applicable due to the S/N ratio of the spectrum. In fact, if the spectra have an $S/N > 10$, method 1 is the ideal method for the taxonomic classification of my spectra. If S/N< 10, it is difficult to determine the taxonomic type of an asteroid. Method 1 does not work well in this case because the data have large errors. However, there should only be one curve of the Bus and DeMeo's classification that interpolates my data well. If the spectrum has too many errors, many curves of taxonomic types interpolate my spectrum well. In this case, I cannot determine with certainty the taxonomic type of NEOs, but I can determine the taxonomy curve that is closest. Therefore, I used method 3 which disregards measurement errors and only considers the points in my spectrum. However, in this case, I cannot confirm my classification but only provide an estimate of the taxonomic type that best matches my data. Histograms 4.5, 4.6, 4.7, 4.10, 4.11, 4.12 provide a good description of this process. Histograms 4.5, 4.6, and 4.7 represent the probability calculated through χ^2 for each taxonomic type for asteroid 1999 AP10. This asteroid has an S/N ratio of 43.5, which is greater than the limit value of 10 that I consider for using method 1 (see Figs 4.3 and 4.4 for the spectrum of 1999 AP10). Histogram 4.5 shows that the probability calculated based on χ^2 method of asteroid 1999AP10 being an S-type is 95.42%, while the other spectral types have a lower probability. The spectral types with a high probability percentage are only those of the S-complex, such as Sq and Sr. After considering both measurement errors, it can be observed that other taxonomic types have a high percentage value, such as D, K, and L, because these last three taxonomy curves have very high measurement errors, but lower than the probability of the S-type curve. If we consider histograms 4.6 and 4.7, it is noticeable how the percentages decrease drastically. This is due to the fact that the χ^2 method will have given high values and consequently low probability values. Considering data with a high S/N ratio, the points are more compact and further away from the curves of the taxonomic types to which the asteroid does not belong. However, since the S/N ratio is high, the highest percentage value of the two histograms always refers to type S. This asteroid has been classified as S-type, but these two methods are not always in agreement with method 1 even if the S/N ratio is high because many taxonomic types have very similar curves.

Figure 4.8 and 4.9 shows the spectrum of 1999 AW1, which has a very low S/N ratio (5.8). The red curve represents the asteroid's spectrum, with the errors of curve (yellow bars) and the dashed line is the CubicSpline. The asteroid's spectral type that best fits the data is Q-type. Histogram 4.10 shows the χ^2 probability calculated using method 1. Compared to histogram 4.5, we can observe that the probabilities are lower than 50% due to a higher chi-square value, and almost all taxonomic types interpolate the spectrum of 1999 AW1 with a similar percentage. This is because, considering the spectrum error (which is much higher in this case than in the case of 1999 AP10), many taxonomic types interpolate my spectrum well. Therefore, neither method 1 nor method 2 can be used in this case. As expected, in method 2 there are fewer taxonomic types with a similar probability because I am considering only one error, but there are still too many to use this method. Similarly, method 2 is also not applicable as it takes into account errors on the spectrum. Histogram 4.11 shows the probability of the χ^2 measured by method 2. In this case, I used method 3, although in histogram 4.12 I can see that the probability percentage is very low (23.28% for Q-type). In this case, I note that a few taxonomic types have a "high" percentage (compared to the percentage for Q-type) because I am only considering points on the spectrum, without errors. This classification cannot be confirmed due to the low S/N, but can be confirmed

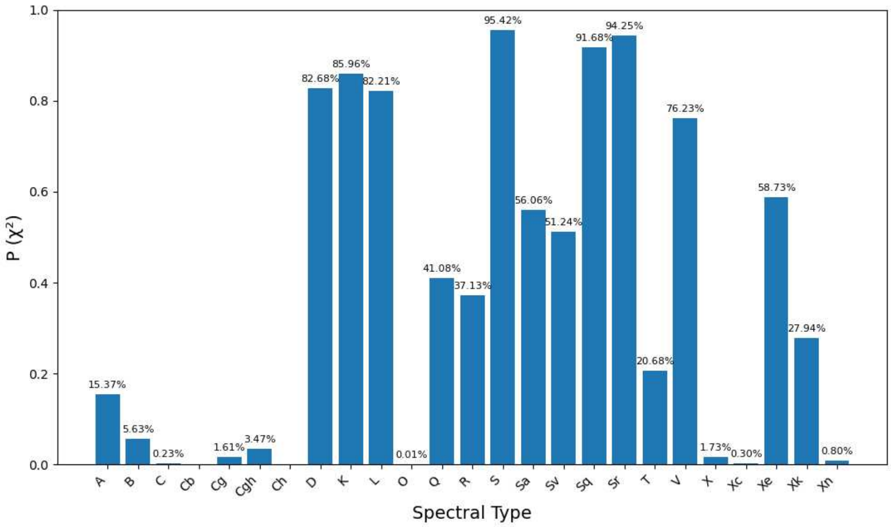

Figure 4.5: the chi-square probability for NEO 1999 AP10 belonging to each spectral type. The y-axis shows the probability calculated for each spectral type of the Bus and DeMeo classification, while the x-axis shows all spectral types of this taxonomy. The chi-square was calculated using method 1.

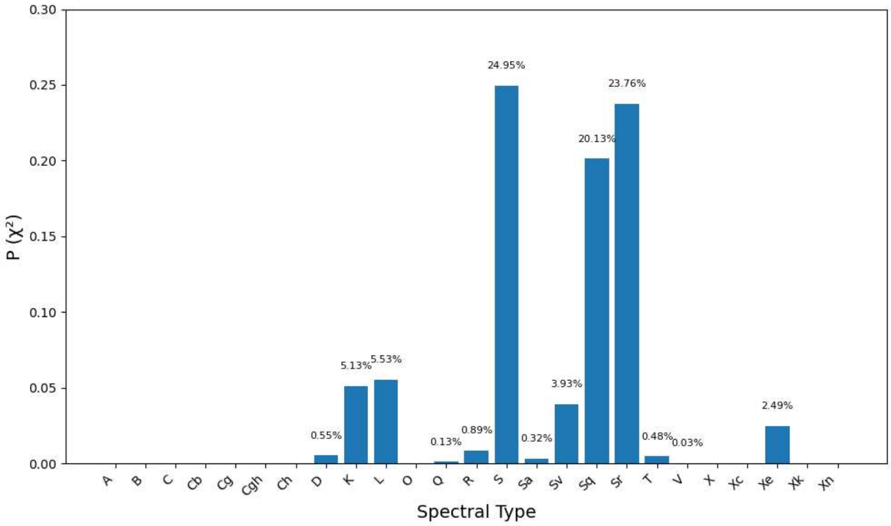

Figure 4.6: the chi-square probability for NEO 1999 AP10 belonging to each spectral type. The y-axis shows the probability calculated for each spectral type of the Bus and DeMeo classification, while the x-axis shows all spectral types of this taxonomy. The chi-square was calculated using method 2.

or modified during the next observation: the asteroid need follow up observation for a more definitive classification.

As stated at the beginning of this chapter, this procedure was carried out for the 49 NEOs analysed in this thesis. The spectra for all 49 NEOs are shown in Figures 4.13, 4.14, and 4.15. Additionally, the Mahkle taxonomy was calculated using a Python pro-

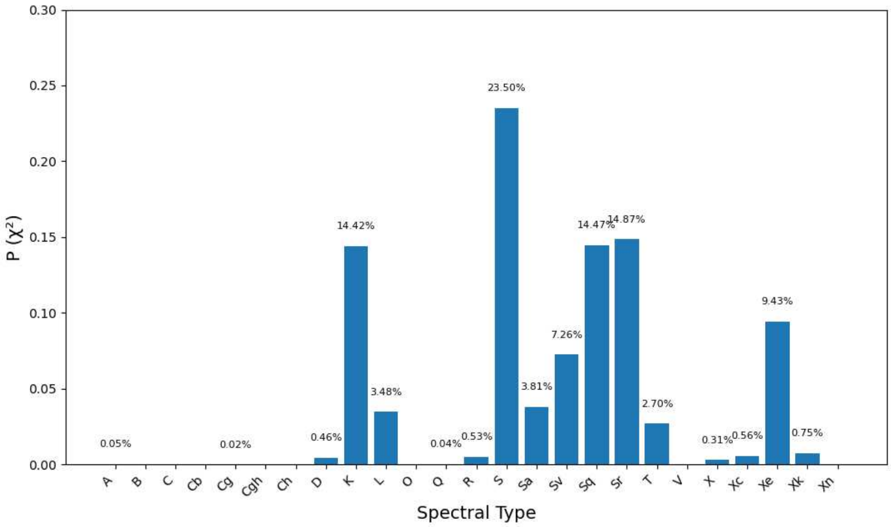

Figure 4.7: the chi-square probability for NEO 1999 AP10 belonging to each spectral type. The y-axis shows the probability calculated for each spectral type of the Bus and DeMeo classification, while the x-axis shows all spectral types of this taxonomy. The chi-square was calculated using method 3.

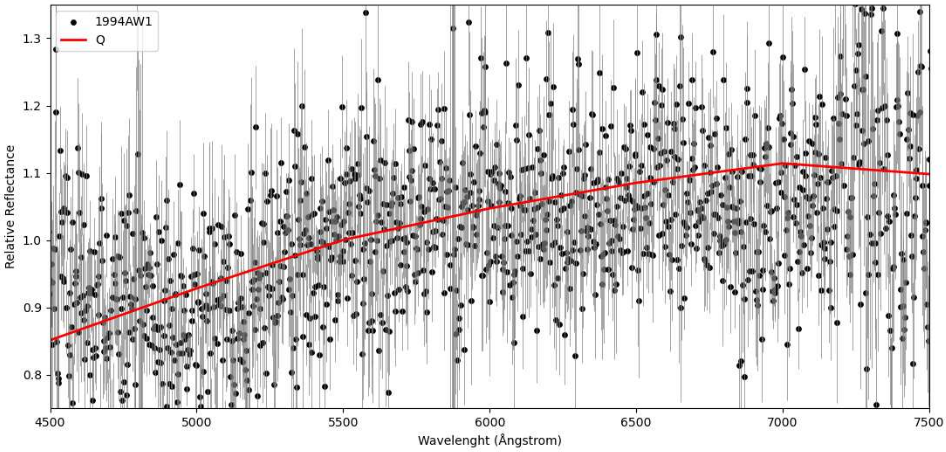

Figure 4.8: the spectrum of NEO 1999 AW1 was obtained using the Galileo telescope at the Asiago Astrophysical Observatory. The flux errors of individual points in the spectrum are plotted in grey. The red curve represents the Q-type taxonomy classification by Bus and DeMeo.

gram with the ROCKS and CLASSY libraries, which allow for the taxonomic classification of spectra. Both classifications are presented in Table 4.3. This table shows the asteroid number (when available), name, type (NEO or PHA), S/N ratio calculated using methods 1 and 2 (see section 3.4.3), Mahkle and Bus-DeMeo classification, taxonomic classification reported in literature (obtained from the site https://neo.ssa.esa.int/search-for-asteroids), and the telescope used to acquire the spectra ('C' = Copernico, 'G' = Galileo). Table

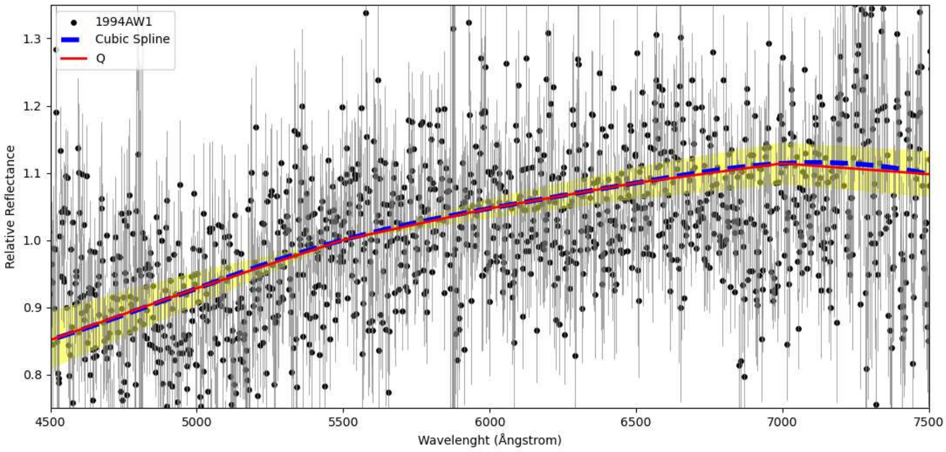

Figure 4.9: the spectrum of NEO 1999 AW1 was obtained using the Galileo telescope at the Asiago Astrophysical Observatory. The flux errors of individual spectrum points are plotted in grey. The red curve represents the Q-type taxonomy classification by Bus and DeMeo, while the yellow bar indicates its errors. The blue dashed curve is the CubicSpline polynomial interpolation of the Q spectral type curve by Bus and DeMeo.

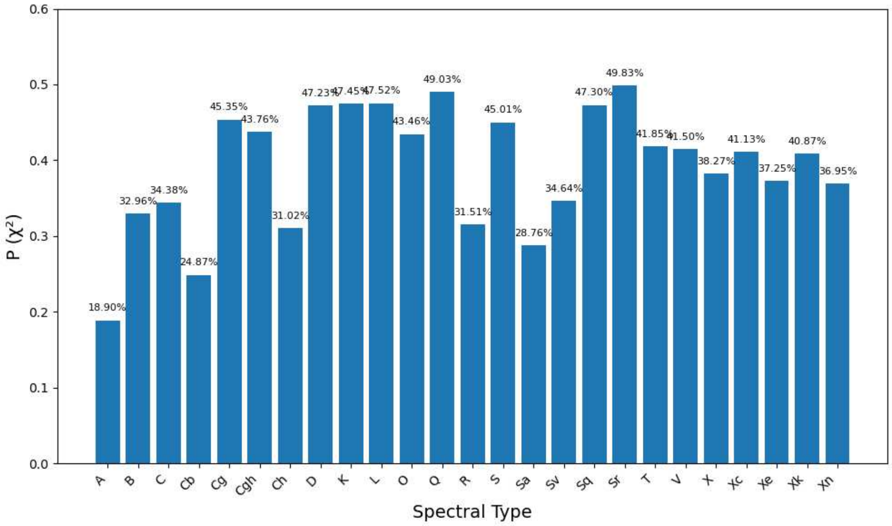

Figure 4.10: the chi-square probability for NEO 1999 AW1 belonging to each spectral type. The y-axis shows the probability calculated for each spectral type of the Bus and DeMeo classification, while the x-axis shows all spectral types of this taxonomy. The chi-square was calculated using method 1.

4.2 shows the eccentricity, inclination, orbital period P, absolute magnitude H, rotation period T (when known), and family membership (Apollo, Aten, Amor) taken from the site https://neo.ssa.esa.int/search-for-asteroids. Additionally, it includes the expected diameter (provided at the site https://neo.ssa.esa.int/search-for-asteroids) and the diameter calcu-

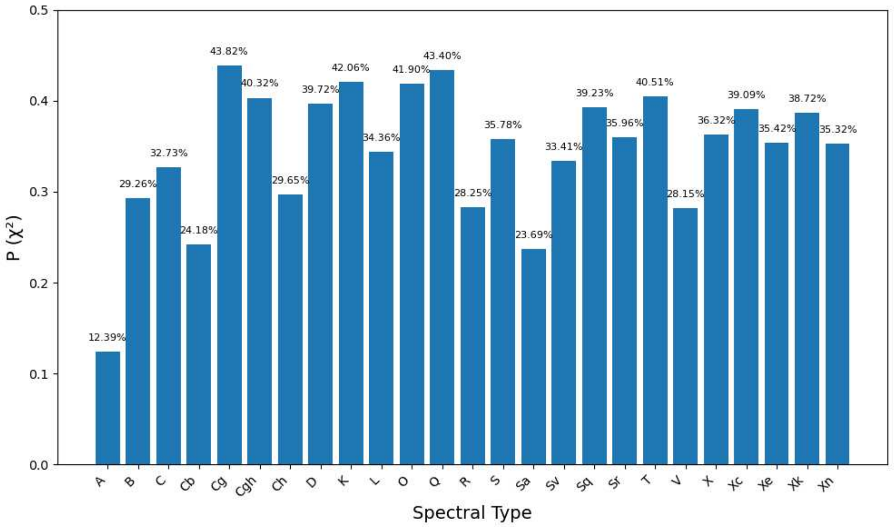

Figure 4.11: the chi-square probability for NEO 1999 AW1 belonging to each spectral type. The y-axis shows the probability calculated for each spectral type of the Bus and DeMeo classification, while the x-axis shows all spectral types of this taxonomy. The chi-square was calculated using method 2.

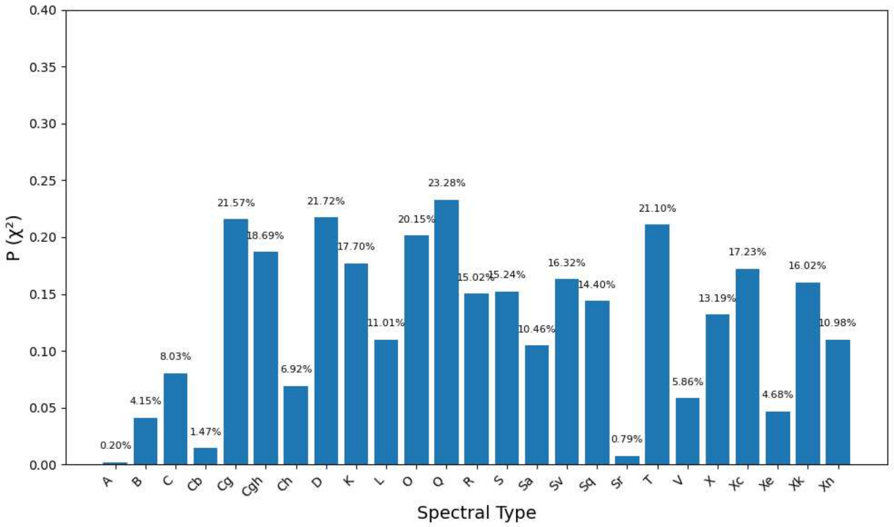

Figure 4.12: the chi-square probability for NEO 1999 AW1 belonging to each spectral type. The y-axis shows the probability calculated for each spectral type of the Bus and DeMeo classification, while the x-axis shows all spectral types of this taxonomy. The chi-square was calculated using method 3.

lated for this thesis by using the equation [26]:

$$D = 1329 \cdot (\rho_V)^{-0.5} \times 10^{-0.2H} \tag{4.1}$$

where ρ_V represents the literature albedo (if calculated) or the predicted albedo of the taxonomic class (if not yet calculated), and H is the absolute magnitude.

N	Id	Name	Type	S/N	S/N**	Mahkle	Bus-DeMeo	Tax. Prev.	Telescope
1	\	2019WO2	NEO	12.3	21.5	S	Sr	\	C
2	\	2019WR3	NEO	39.7	68.7	M	Xk	\	C
3	35107	1991VH	PHA	7.2	29.3	E	Xe	Sq	G
4	52768	1998OR2	PHA	22.7	49.6	M	Xk	Xn	C
5	163373	2002PZ39	PHA	7.3	14.2	M	Xk	Scomp	G
6	40267	1999GJ4	NEO	6.1	13.4	Q	Q	Sq	G
7	65690	1991DG	PHA	15.7	19.1	E	Xe	U	C
8	373428	1999TC5	NEO	16.6	21.9	L	L	U	C
9	137170	1999HF1	NEO	35.9	68.5	C	Cgh	X	C
10	388945	2008TZ3	PHA	15.7	24.9	Ch	Ch	B	G
11	539940	2017HW1	NEO	17.4	27.6	Ch	Ch	\	G
12	136900	1998HL49	NEO	20.1	34.1	R	R	V	C
13	411165	2010DF1	NEO	12.1	19.9	L	L	Xk	C
14	500094	2012BC20	NEO	20.9	30.2	S	Sq	\	C
15	\	2020RF	NEO	12.6	24.3	K	K	S	C
16	159402	1999AP10	NEO	43.5	69.3	S	S	Scomp	G
17	\	2020ST1	PHA	12.1	18.4	K	K	S	G
18	\	2013PY6	NEO	22.0	34.7	D	D	C	C
19	275714	2000YH4	NEO	16.4	27.8	A	A	\	C
20	163902	2003SW222	NEO	19.8	34.8	A	A	Scomp	C
21	\	2003AF23	PHA	12.9	17.5	C	Cg	C	G
22	332446	2008AF4	PHA	14.6	22.1	O	O	S/Sr	G
23	\	2015NU13	PHA	15.6	24.7	O	O	Sq	G
24	\	2020WU5	PHA	15.9	24.6	C	Cg	L	G
25	99942	Apophis	PHA	9.4	17.7	S	Sq	Scomp	C
26	612050	1997GL3	PHA	30.5	52.1	V	V	V	C
27	5189	1990UQ	PHA	24.5	37.9	Q	Q	Q	G
28	\	2011YQ10	NEO	7.0	14.6	A	A	U	C
29	\	2021LQ24	NEO	10.4	18.4	S	Sa	\	C
30	385186	1994AW1	PHA	5.8	12.8	Q	Q	L	G
31	215188	2000NM	NEO	6.9	15.7	A	A	V	G
32	\	2015HH	NEO	6.0	14.5	A	A	\	G
33	422787	2001WS1	PHA	12.9	30.5	Ch	Ch	U	C
34	199003	2005WJ56	PHA	23.4	51.1	Ch	Ch	\	C
35	138971	2001CB21	PHA	19.2	44.1	S	S	B	C
36	\	2016UT80	NEO	19.8	43.7	E	Xe	\	C
37	37638	1993VB	PHA	31.6	72.7	M	Xk	\	C
38	\	2004BE86	NEO	9.04	26.9	D	D	V	C
39	\	2004GA	NEO	19.3	36.4	L	T	\	C
40	\	2023BE10	NEO	6.5	16.4	S	S	\	C
41	3752	Camillo	NEO	11.1	30.6	S	Sv	S	C
42	349507	2008QY	PHA	12.2	29.8	Ch	Ch	\	C
43	518635	2008HO3	NEO	45.6	136.6	M	Xk	U	C
44	\	2015VL142	NEO	12.1	26.6	A	A	\	C
45	363505	2003UC20	PHA	7.9	25.2	B	B	\	C
46	\	2023QE11	NEO	21.6	50.7	B	B	\	C
47	433	Eros	NEO	47.8	124.3	S	Sv	S	C
48	326683	2002WP	NEO	9.0	22.0	S	S	Scomp	C
49	65803	Didymos	PHA	59.6	98.7	S	S	S	C

Table 4.2: shows data for 49 NEOs observed from December 2019 to March 2024. It includes the ID number, name, S/N calculated using method 1 (see section 3.4.3), S/N** calculated using method 2 (see section 3.4.3), our taxonomy using Mahkle and Bus and DeMeo classification, the expected taxonomy from literature, and the telescope used (C = Copernico and G = Galileo).

N (-)	Id (-)	Name (-)	e (-)	i (deg)	D (m)	D2 (m)	P (d)	H (mag)	Perielio (au)	MOID (au)	T (h)	Type (-)
1	\	2019WO2	0.481	7.4	24-50	24	970.1	25.2	0.995	0.01370	\	Apollo
2	\	2019WR3	0.237	12.6	80-180	107	561.0	22.6	1.016	0.03554	\	Apollo
3	35107	1991VH	0.144	13.9	1010	1238	443.0	16.9	0.973	0.02567	2.624	Apollo
4	52768	1998OR2	0.576	5.9	2510	2195	1341.3	15.9	1.010	0.00801	4.110	Apollo
5	163373	2002PZ39	0.547	1.7	400-1000	562	650.3	19	0.666	0.00272	\	Apollo
6	40267	1999GJ4	0.808	34.5	1940	2057	565.5	15.6	0.256	0.15634	4.957	Apollo
7	65690	1991DG	0.363	11.1	510	278	623.1	19	0.909	0.03884	\	Apollo
8	373428	1999TC5	0.546	29.1	500-1100	596	1045.6	18.6	0.914	0.18743	\	Apollo
9	137170	1999HF1	0.463	25.7	4400	3994	270.8	14.6	0.440	0.17357	2.312	Aten
10	388945	2008TZ3	0.392	8.7	220-500	451	733.3	20.4	0.968	0.01635	44.20	Apollo
11	539940	2017HW1	0.459	34.0	950	1563	1140.8	17.9	1.155	0.15381	\	Amor
12	136900	1998HL49	0.637	11.0	900-2000	803	843.9	17.4	0.635	0.08370	\	Apollo
13	411165	2010DF1	0.503	20.1	100	152	738.0	22	0.794	0.04333	\	Apollo
14	500094	2012BC20	0.279	23.8	470	493	588.2	18.7	0.991	0.14661	\	Apollo
15	\	2020RF	0.612	18.3	100-220	133	1527.9	22.2	1.008	0.03589	\	Apollo
16	159402	1999AP10	0.572	7.6	1200	650	1340.7	16.5	1.018	0.07650	7.908	Amor
17	\	2020ST1	0.578	8.0	110-240	68	1402.5	21.9	1.036	0.04721	\	Amor
18	\	2013PY6	0.465	3.4	400-800	748	1259.2	19.3	1.222	0.22842	\	Amor
19	275714	2000YH4	0.459	18.0	500-1000	461	664.0	18.8	0.807	0.08571	\	Apollo
20	163902	2003SW222	0.248	16.1	1000-2100	1031	781.8	17.1	1.249	0.27133	\	Amor
21	\	2003AF23	0.426	23.2	680	592	298.7	21	0.502	0.03302	\	Aten
22	332446	2008AF4	0.410	8.9	300-700	299	592.2	19.7	0.814	0.00199	\	Apollo
23	\	2015NU13	0.749	4.2	400-800	343	903.9	19.4	0.749	0.01047	\	Apollo
24	\	2020WU5	0.102	41.5	590	570	397.8	18.7	0.951	0.04102	\	Apollo
25	99942	Apophis	0.191	3.3	375	409	323.7	18.9	0.746	0.00012	30.56	Aten
26	612050	1997GL3	0.784	6.7	400-900	373	1249.1	19.1	0.489	0.00381	\	Apollo
27	5189	1990UQ	0.478	3.6	550	521	706.0	17.9	0.810	0.04466	6.640	Apollo
28	\	2011YQ10	0.521	2.4	400-900	402	1226.7	19.1	1.073	0.07974	\	Apollo
29	\	2021LQ24	0.640	11.2	260-600	259	1914.5	20.1	1.085	0.09060	17.10	Amor
30	385186	1994AW1	0.076	24.1	800-1800	819	424.3	17.6	1.022	0.01971	\	Amor
31	215188	2000NM	0.663	22.3	2470	2111	1607.9	15.5	0.904	0.13302	9.24	Apollo
32	\	2015HH	0.102	11.5	16-40	16	402.9	26	0.959	0.02850	\	Apollo
33	422787	2001WS1	0.619	13.2	3510	2477	1523.5	16.9	0.988	0.01249	\	Apollo
34	199003	2005WJ56	0.152	21.6	710	1361	343.0	18.2	0.813	0.02338	4.379	Aten
35	138971	2001CB21	0.333	7.9	500-1200	541	383.8	18.5	0.689	0.02378	\	Apollo
36	\	2016UT80	0.418	8.3	400-900	266	1067.3	19.1	1.189	0.21696	\	Amor
37	37638	1993VB	0.520	5.1	400-800	490	966.6	19.3	0.919	0.00053	\	Apollo
38	\	2004BE86	0.238	3.8	160-400	326	631.8	21.1	1.099	0.10708	2.284	Amor
39	\	2004GA	0.631	10.6	250-600	299	1737.6	20.1	1.042	0.06589	\	Amor
40	\	2023BE10	0.638	4.3	120-260	118	1769.1	21.8	1.037	0.05813	\	Amor
41	3752	Camillo	0.302	55.6	2480	2474	613.9	15.2	0.987	0.07881	\	Apollo
42	349507	2008QY	0.582	13.6	500-1200	1185	461.1	18.5	0.489	0.03040	\	Apollo
43	518635	2008HO3	0.651	14.1	1030	813	1820.0	18.2	1.019	0.11710	13.41	Amor
44	\	2015VL142	0.596	0.596	1200-2700	1214	1492.3	16.7	1.033	0.31293	\	Amor
45	363505	2003UC20	0.337	3.8	1900	1082	252.2	18.5	0.518	0.03493	\	Aten
46	\	2023QE11	0.548	6.5	190-400	393	1318.7	20.7	1.064	0.11258	\	Amor
47	433	Eros	0.233	10.8	23300	17923	643.2	10.9	1.133	0.14956	5.270	Amor
48	326683	2002WP	0.216	19.2	518	541	637.7	18.5	1.137	0.15275	6.262	Amor
49	65803	Didymos	0.383	3.4	700-1500	769	769.0	18.0	1.013	0.04029	2.259	Apollo

Table 4.3: contains data on 49 NEOs observed from December 2019 to March 2024. It includes the Id number, name, eccentricity, inclination, expected diameter based on literature, diameter calculated by us, orbital period, absolute magnitude H, perihelion, MOID, rotation period T, and orbit type.

4.5 Results

In this work, 49 NEOs have been classified, including 21 PHAs. 28 belong to the Apollo group, 16 to the Amor group, and 5 to the Aten group. Although statistical analysis cannot be performed with such a small number of NEOs compared to their total number of discovered NEOs, as expected the number of Apollos is greater than that of Amors, which is greater than that of Atens. My main goal for the thesis is to classify NEOs taxonomically to contribute to the NEOROCKs project. Additionally, I have completed other minor tasks as described in the following sections.

4.5.1 Taxonomy classification

In my taxonomic classification, 20 NEOs have not yet been classified in literature, while 29 have already been classified. The latter have been classified after my observations, and my data is useful for confirming or refuting the classification of other authors. The taxonomic classification is shown in the three figures that represent all the plots of all the observed NEOs (see Figure 4.16, 4.17, 4.18). Histogram 4.19 shows the frequencies of the taxonomic types in my classification according to the Bus and DeMeo taxonomy. The S-complex appeared in 32.7%, the C-complex in 20.4%, the X-complex in 16.3%, the A-type in 6.1%, the D-type in 4.1%, the L-type in 4.1%, the K-type in 4.1%, T in 2%, and R in 2%.

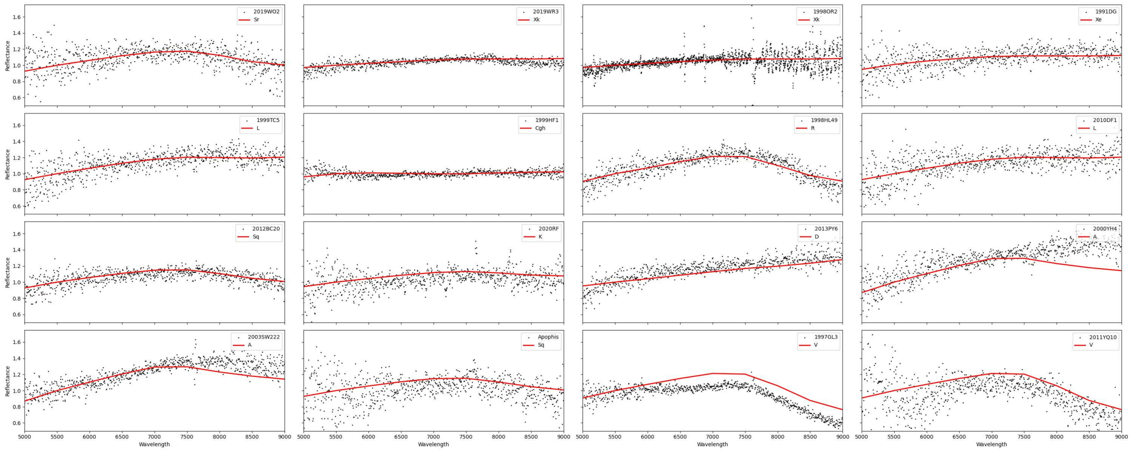

Figure 4.13: 16 spectra of the 49 NEOs observed with the Copernico telescope at the Asiago Astrophysical Observatory. The spectral range is from 5000 to 9000 Å and the reflectance varies from 0.5 and 1.7. The red curve represents the taxonomic type according to the Bus and DeMeo classification.

The taxonomic classification according to Mahkle was also carried out, and the results are shown in histogram 4.20. The percentages of the various taxonomic types in the entire classification by Makhle [13] are described in section 2.2.4. My work does not involve comparing the frequency percentages of my taxonomic types with those of Makhle. This statistic cannot provide a consistent result because the number of observed NEOs is much smaller compared to the survey used by Makhle, which includes data from 2125 asteroids. However, the percentages were calculated to compare whether the distribution of 49 NEOs

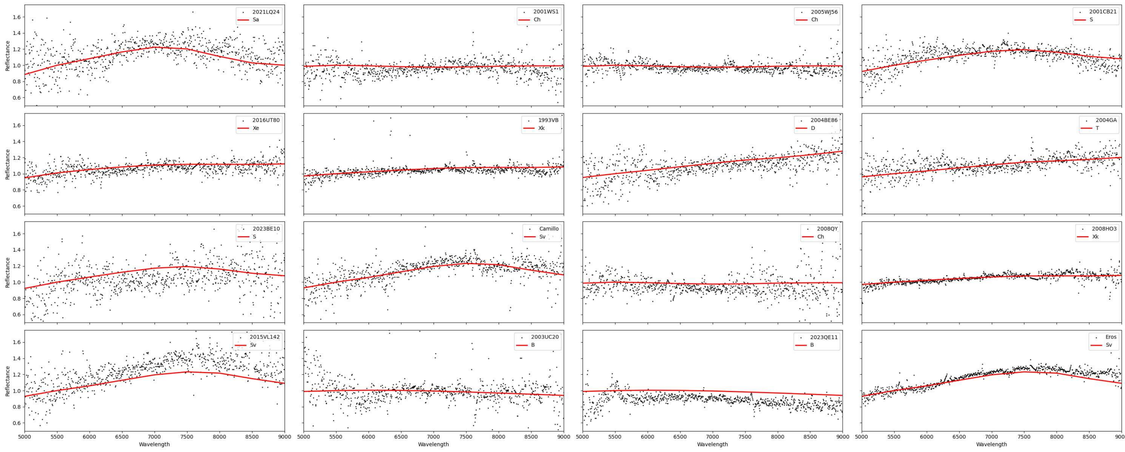

Figure 4.14: 16 spectra of the 49 NEOs observed with the Copernico telescope at the Asiago Astrophysical Observatory. The spectral range is from 5000 to 9000 Å and the reflectance varies from 0.5 and 1.7. The red curve represents the taxonomic type according to the Bus and DeMeo classification.

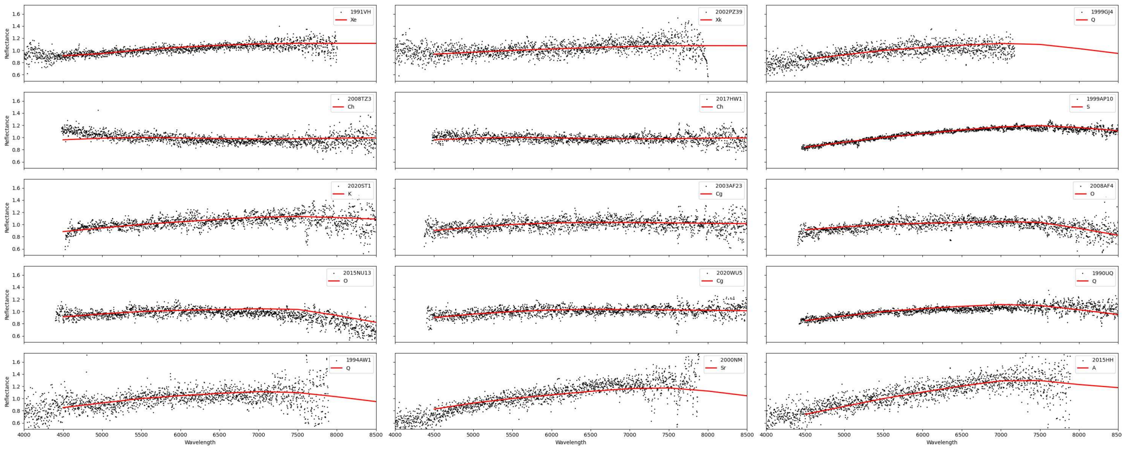

Figure 4.15: 15 spectra of the 49 NEOs observed with the Galileo telescope at the Asiago Astrophysical Observatory. The spectral range is from 3500 to 9000 Å and the reflectance varies from 0.5 and 1.7. The red curve represents the taxonomic type according to the Bus and DeMeo classification.

is similar to the one found by Makhle. The purple bars represent the count number of my classification, while the grey bar represents that expected by Makhle's survey. As we can see, some types are not present in my classification such as P- and Z-types. Although the percentages do not match, the frequency distribution is consistent with what was found by Makhle: S-types are much more numerous than the others.

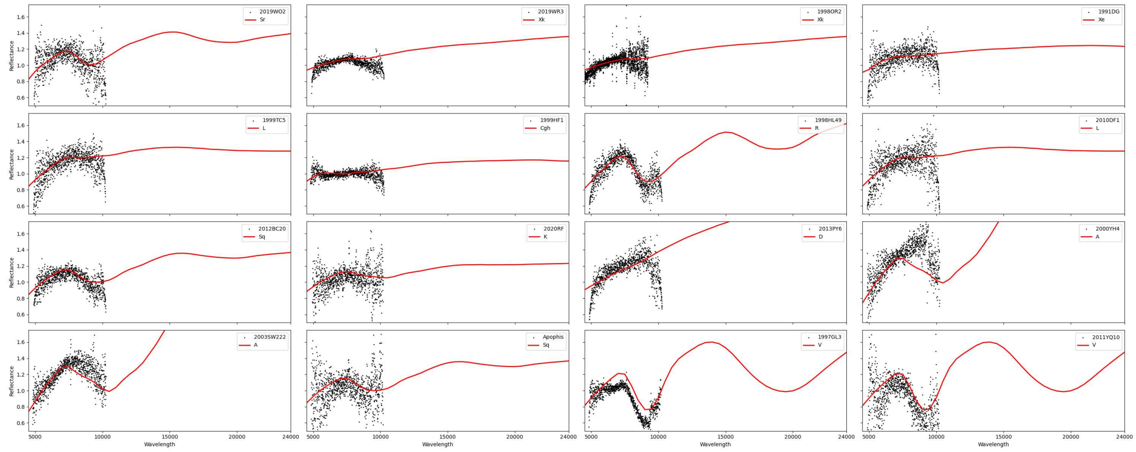

Figure 4.16: the same 16 spectra reported in 4.13 of the 49 NEOs observed with the Copernico telescope at the Asiago Astrophysical Observatory. The spectral range is from 5000 to 9000 Åand the red curve represents the taxonomic type according to the Bus and DeMeo classification. The red curve has a spectral range from 5000 to 24000 Å.

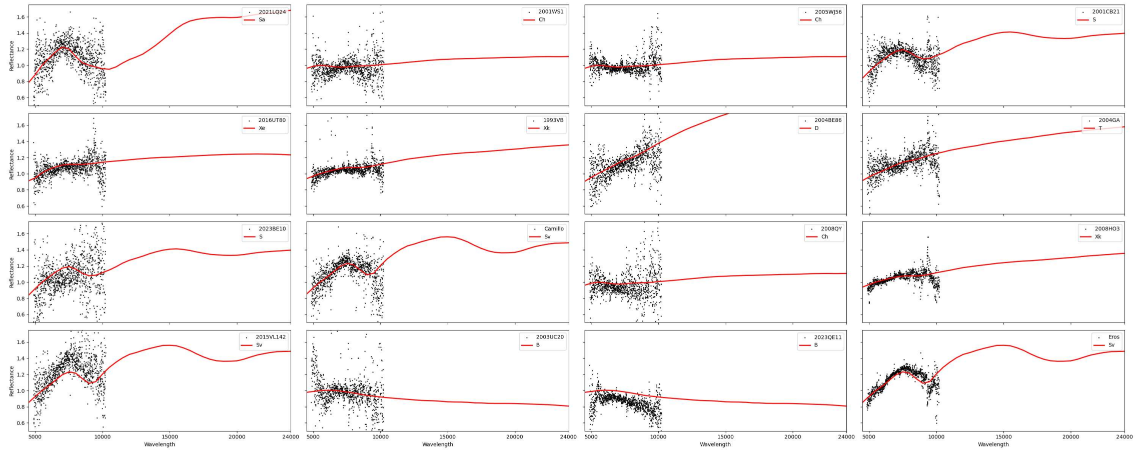

Figure 4.17: the same 16 spectra reported in 4.14 of the 49 NEOs observed with the Copernico telescope at the Asiago Astrophysical Observatory. The spectral range is from 5000 to 9000 Åand the red curve represents the taxonomic type according to the Bus and DeMeo classification. The red curve has a spectral range from 5000 to 24000 Å.

4.5.2 Comparison with other physical classification

4.5.2.1 Hromakina et al.

Hromakina et al. [25] analysed and classified 42 NEOs and combined their data with that already existing in the NEOROCKs database, analysing a total of 92 NEOs. In Hromakina et al.'s study, 46% of the NEOs belonged to the S-complex, 18% to the C-complex, 18% to the X-complex, 13% to the D-type, 3% to the A-type and 3% to the V-type [25]. These values are consistent with those found in my analysis, as shown in histogram 4.23. As expected, half of the NEOs fall within the S-complex: S-complexes are the predominant among all NEOs classified in all surveys. The S-type asteroids among NEOs can be affected by an observa-

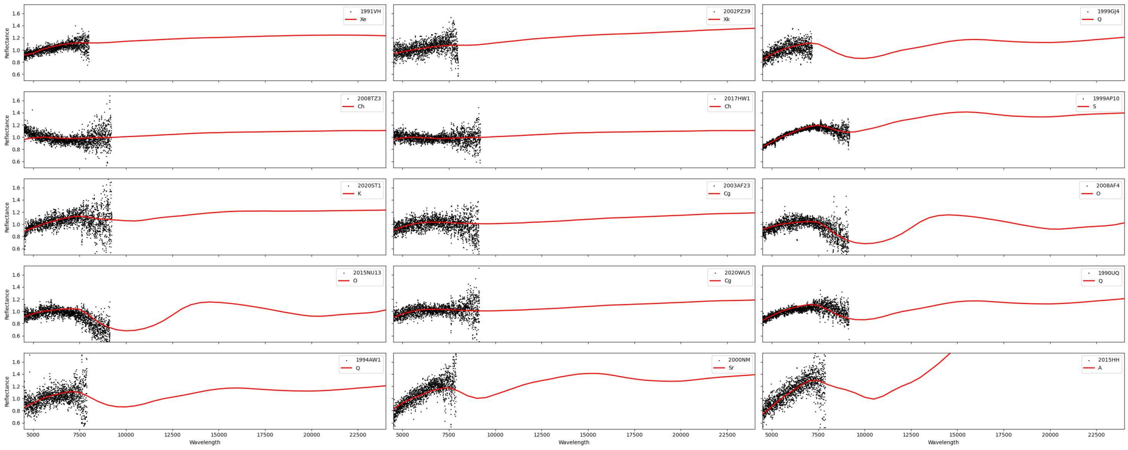

Figure 4.18: the same 16 spectra reported in 4.15 of the 49 NEOs observed with the Galileo telescope at the Asiago Astrophysical Observatory. The spectral range is from 3500 to 9000 Åand the red curve represents the taxonomic type according to the Bus and DeMeo classification. The red curve has a spectral range from 5000 to 24000 Å.

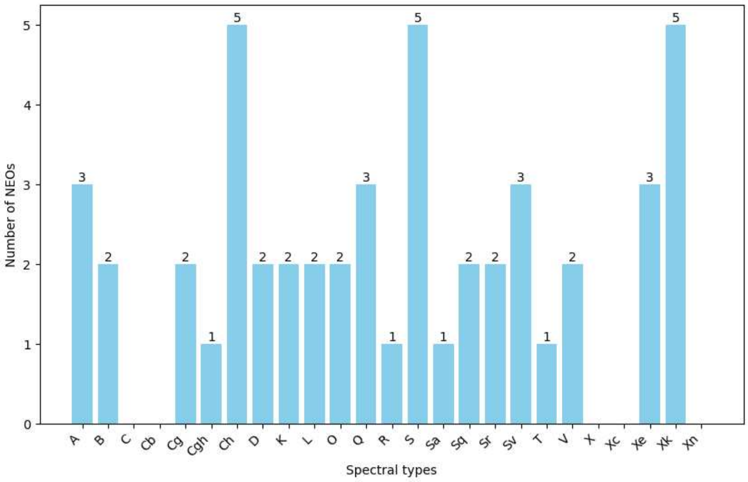

Figure 4.19: histogram showing all my 49 NEOs classified according to the Bus and DeMeo taxonomy. The x-axis represents all 25 spectral types and the y-axis represents the frequency of the number of NEOs for each spectral type.

tional bias towards objects with higher albedo. Therefore, a debiasing technique is necessary to determine the actual chemical composition of S-type asteroids [25]. However, a very large sample size is required to perform this debiasing technique, which has not been achieved by either us or Hromakina et al. Hromakina et al. divided the NEOs into three groups: the silicate group, which includes the S-complex, Q-, A-, and V-types; the carbonaceous group, which includes the C-complex, D-, and Xc; and the miscellaneous group, which includes all other taxonomic types [25].

In my study, I analysed NEOs ranging from 16 m to 4 km (excluding (433) Eros). Histogram 4.21 shows the number of NEOs related to their approximate diameter value (calculated in

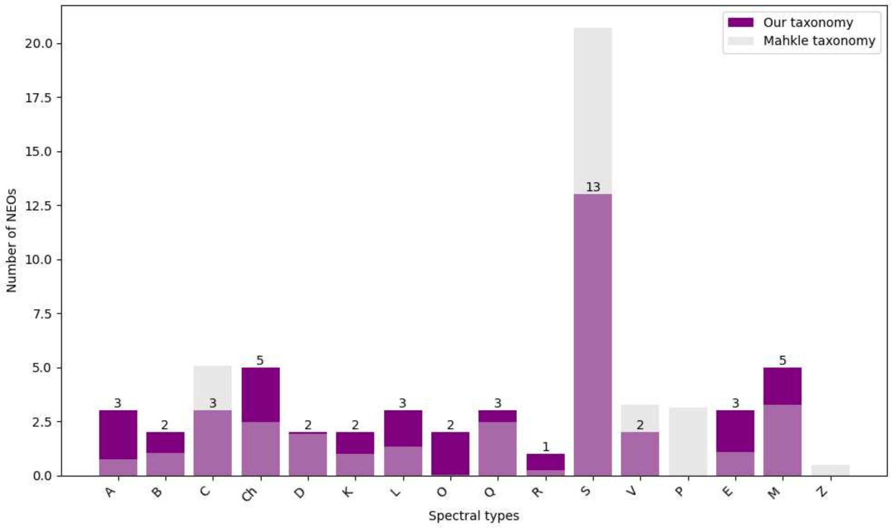

Figure 4.20: histogram showing the my 49 NEOs classified according to the Mahkle taxonomy. The purple bars represent my data, while the gray bar represents the probability of each spectral type in Mahkle's database. The x-axis represents all 17 spectral types and the y-axis represents the frequency of NEOs for each spectral type.

section 4.3), divided into 250 m intervals: most NEOs have a diameter of $D < 1$ km (19 NEOs have D < 500 m and 17 NEOs have 500 m < D < 1000 m), 8 NEOs are in the range of $1 < D < 2$ km and only 6 NEOs have a diameter $D > 2000$ m. These numbers are in agreement with Hromakina et al.'s study: most of the NEOs studied in their work have a size smaller than 1 km. Hromakina et al. plotted the number of NEOs in a histogram (see Figure 4.22 [25]) divided into three groups based on size intervals of 500 m [25]. In their studies found that the number of carbonaceous objects decreases steadily with size, while the number of silicate objects is more prevalent in smaller objects and decreases rapidly when the diameter is greater than 1 km. In their work, the ratio of carbonaceous to silicate objects with a diameter D < 500 m is 28-72%, while for objects with a diameter D>500 m, the ratio is 46-54%. I replicated the work done by Hromakina et al. by dividing my NEOs into three groups (see Figure 4.23). Histogram 4.23 is consistent with the data found by Hromakina et al., as I observe a decrease in the number of silicate objects with increasing diameter, which drops sharply above 1 km. Furthermore, my carbonaceous to silicate ratio for D < 500m is 25-72% and 46-54% for D > 500 m. This confirms the ratio found by Hromakina et al., who also found 28-72% and 46-54% [25]. Such distribution is most probabably caused by the bias towards higher albedo objects. In the histogram 4.23, there are more NEOs in the miscellaneous group, the difference with Hromakine may be due to several factors. Firstly, I are considering only half of the number of NEOs studied by Hromakina et al. Additionally, my observations are based on a random selection of visible NEOs during my observation nights, and some of my NEOs have a low S/N ratio, which leads to errors in taxonomic classification. In fact, 11 of my NEOs have an S/N < 10, meaning their classification is uncertain and the number of miscellaneous objects may be lower, resulting in an increase in the number of the other two groups.

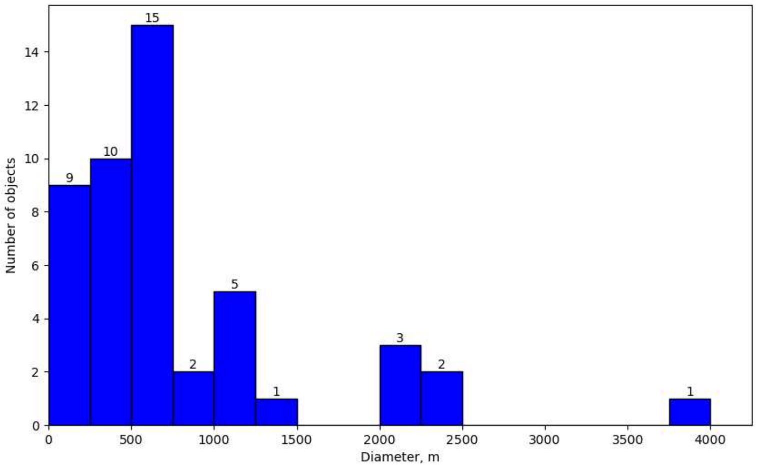

Figure 4.21: histogram showing the diameter of my 48 NEOs (excluding Eros). The x-axis is divided into intervals of 250 meters.

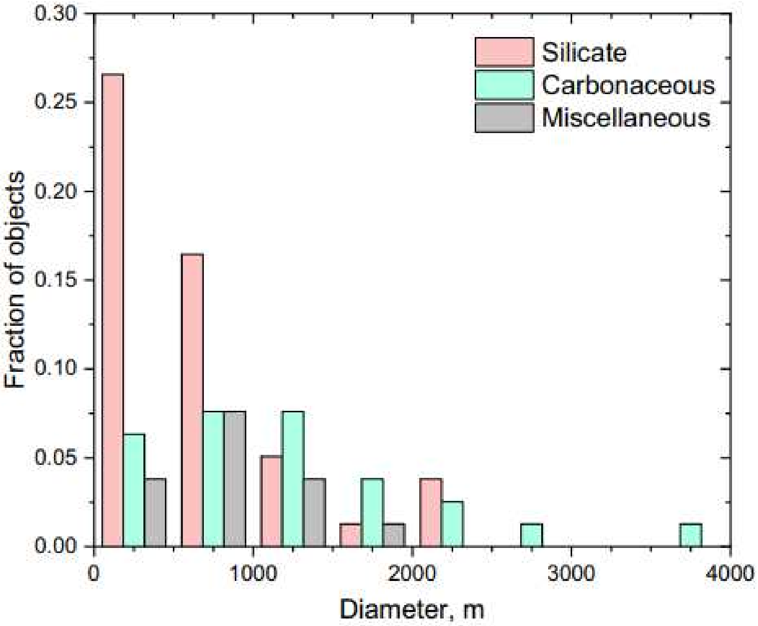

Figure 4.22: distribution in size of the 92 NEOs studied by Hromakina et al. The histogram is divided into 500-meter ranges on the x-axis and shows the diameter values for the three groups: silicates, carbonaceous, and miscellaneous. Figure taken from Hromakina (2023) [25].

4.5.2.2 Popescu et al.

Popescu et al. [26] classified 76 NEAs for NEOROCKs using the Isaac Newton Group (ING) telescope, similar to Hromakina et al.'s work. ING is located at an altitude of 2336 m at Observatorio del Roque de los Muchachos in La Palma (Canary Islands, Spain). In

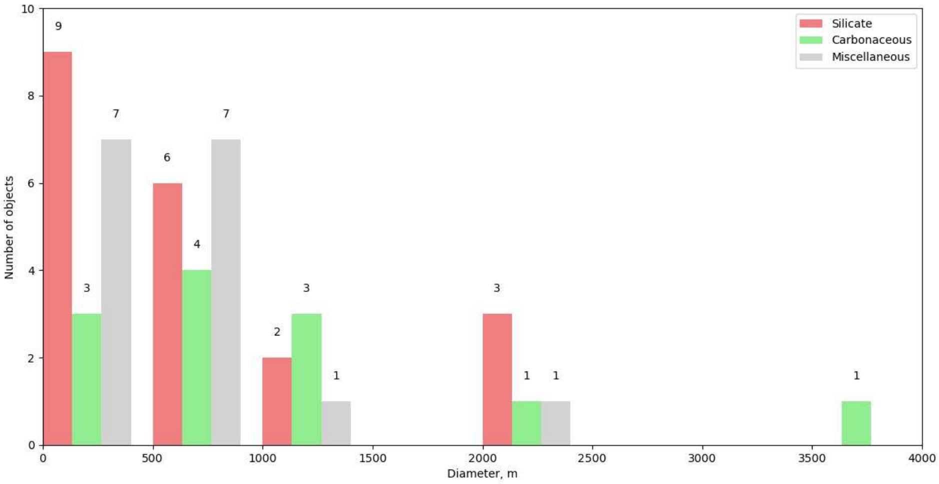

Figure 4.23: the distribution in size of 48 NEOs analysed in my study is shown in the histogram. The x-axis is divided into 500-meter ranges and displays the diameter values for three groups: silicates, carbonaceous, and miscellaneous.

their work they divided the NEOs into four groups: 16 objects in the B/C-complex and low albedo X-complex, D- and T- types, 44 objects in the Q/S-complex, which includes the S-complex, the end-members Q-types, and the peculiar A-types, 8 basaltic-like objects (V-types) and 6 NEOs in a miscellaneous group classified as X-complex (which can represent various compositions depending on their albedo), as well as the two rare L- and O-types. Therefore, 58% belongs to the Q/S complex group, 21% to the B/C complex group, and 10% is part of the miscellaneous group. In my work, I found 40.8% of the Q/S-complex and 26.5% of the B/C-complex, in agreement with the values found by both Popescu et al. [254] and Binzel et al. [261], [119] in the literature (>50% for Q/S-complex, 15% for B/C-complex, and 10% for miscellaneous). I did not consider the miscellaneous group for the reasons described on the section 4.5.2.1. These broad proportions of spectral types match the taxonomic class distribution of inner main-belt asteroids as reported by Gradie [262] e DeMeo [127]. In my study, I have identified several rare classifications, including 3 A-types (rich in olivine), 2 K-types, 2 L-types, 2 O-types, and 1 R-type. Additionally, the B/C-complex group is more challenging to observe than the Q/S-complex due to its low albedo. My observations confirm that the B/C-complex is a minority compared to the Q/S-complex.

- **B/C-complex group:** in my classification, this group comprises 2 NEOs B-type, 2 Cg-type, 1 Cgh-type, 5 Ch-type, 2 D-type, and 1 T-type. No NEOs of the low albedo Xc-type was found. This group, charaterized by low albedo (≤ 0.1), exhibits spectral characteristics similar to those of carbonaceous chondrite meteorites [131], [132] and interplanetary dust particles [263][264]. Similarly to the NEOs studied by Popescu et al. [26], also my sample of NEOs has a diameter ranging from 0.4 to 4 km. B-types were mainly found in the middle and outer parts of the Main Belt. However, a recent study by De Leon et al. [265] was shown a significant number in the inner Main Belt families. More information on this class has been provided by NASA's OSIRIS-Rex mission [266], which explored the B-type target near-Earth asteroid Bennu. On the other hand, D-types and T-types asteroids are rare and have an organic and volatile-rich composition. Carbonaceous asteroids are generally fragile and porous. It is expected that these bodies are gravity-dominated aggregates with negligible tensile strength due to their chemical composition. Most of them have a very high rotation period, greater than 2.5 hours. This limit is known as the cohesionless spin-barrier [26]. If an NEO in this group has a very low rotation period, it means that its chemical composition is heterogeneous and formed from a different material such as metals.

- **Q/S-complex:** most of the NEOs found belong to this group and their size ranges mainly from 16 m to 2300 m. There are 5 S-types, 1 Sa-, 2 Sq-, 2 Sr-, 3 Sv, 3 Q- and 3 A-types. Popescu et al. [26] studied the diameter distribution as a function of the perihelion of Q, Sq, and S/Sa/Sr/Sv types to investigate their physical properties. However, I can confirm that all objects with a perihelion less than 0.6 AU are larger than 450 m (5 NEAs). This explains the thermal fracturing of asteroids. For this thesis, I do not have enough data to replicate the entire study conducted by Popescu et al., but I made a comparison with my data to note if there is a correlation (see figure 4.24, 4.25). Thermal fatigue causes fragmentation, which is a rock weathering process that leads to regolith generation. The thermal fatigue fragmentation that produces fresh regolith is an important process for rejuvenating NEA surfaces [254]. My data confirms Popescu et al.'s results, which suggest that this process is more efficient for objects with a low perihelion. This is consistent with the prediction that small NEAs can be eroded by thermal fragmentation and radiation pressure sweeping on timescales shorter than their dynamical lifetime.

- **Basaltic like group:** 2 NEOs are the V-type, with a composition similar to (4) Vesta, which is considered their parent body. No further analysis has been conducted on this group.

- **Miscellaneous types:** I found 2 NEOs of L-type, 2 of O-type, and 8 of X-complex. The X complex exhibits both high and low albedo, resulting in different compositions.

4.5.3 Orbital Classification

An analysis was also conducted on the orbital type, comparing my results with the literature. Histograms 4.26, 4.27, and 4.28 show the number of spectral types for the three groups. For the Apollo group, I found 35.7% and 14.3% for the Q/S-complex and B/C-complex groups, respectively. Carry et al. [180] found 38% and 31%, while Popescu et al. found 50% and 25%. My results are more in line with Carry's than Popescu et al.'s, but I are still considering a small taxonomic sample. For Amor asteroids, I found percentages of 43.8% and 31.2% for Carry and 51% and 20% for Popescu et al. Atens are challenging to observe due to their proximity to the Sun, making statistics even more difficult. My results for Atens are 20% and 80% for Carry, and 50% and 12% for Popescu et al.

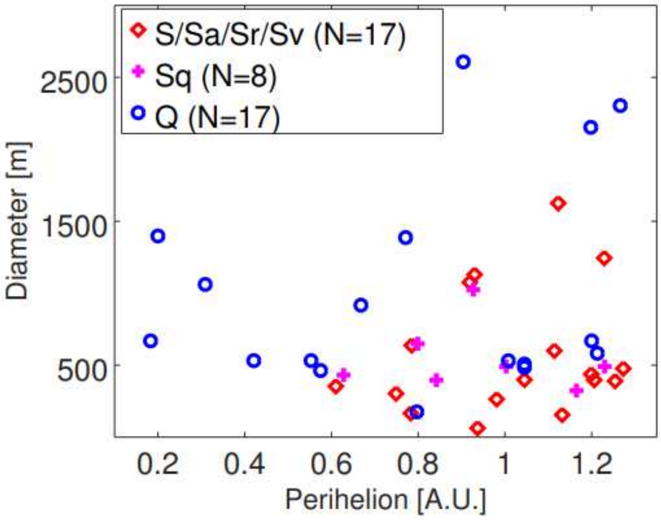

Figure 4.24: the distribution of Q/S-complex group asteroids in the perihelion (q) versus diameter space. Blue dots represent Q-type asteroids, which are believed to have fresh surfaces, while red dots represent S/Sr/Sv/Sa-types, which have surfaces affected by space-weathering. Magenta dots represent Sq-type asteroids, which are an intermediate class between S-types and Q-types. These are the data from Popescu et al.'s work. Figure taken form Popescu (2019) [26]

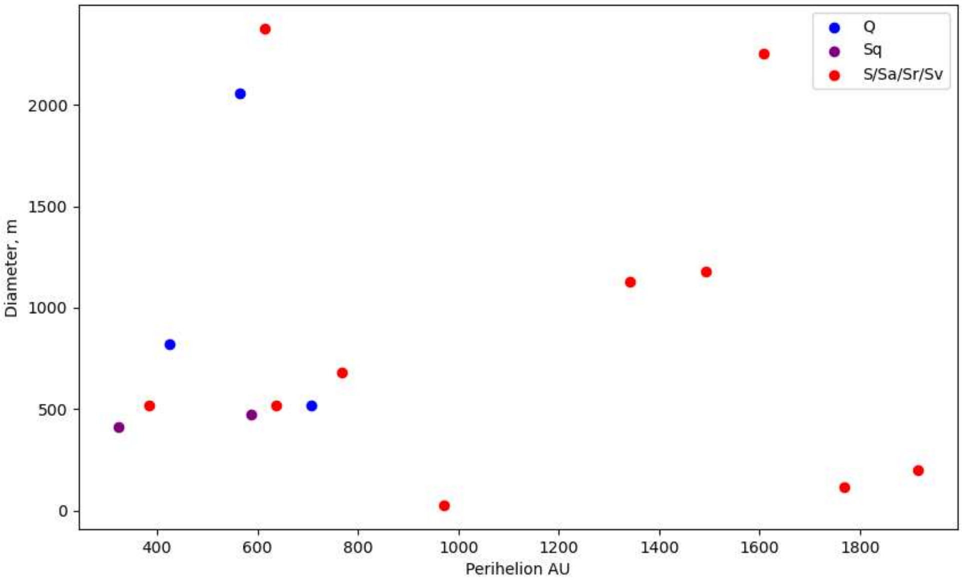

Figure 4.25: the distribution of Q/S-complex group asteroids in the perihelion (q) versus diameter space of my data. Blue dots represent Q-type asteroids, which are believed to have fresh surfaces, while red dots represent S/Sr/Sv/Sa-types, which have surfaces affected by space-weathering. Magenta dots represent Sq-type asteroids, which are an intermediate class between S-types and Q-types.

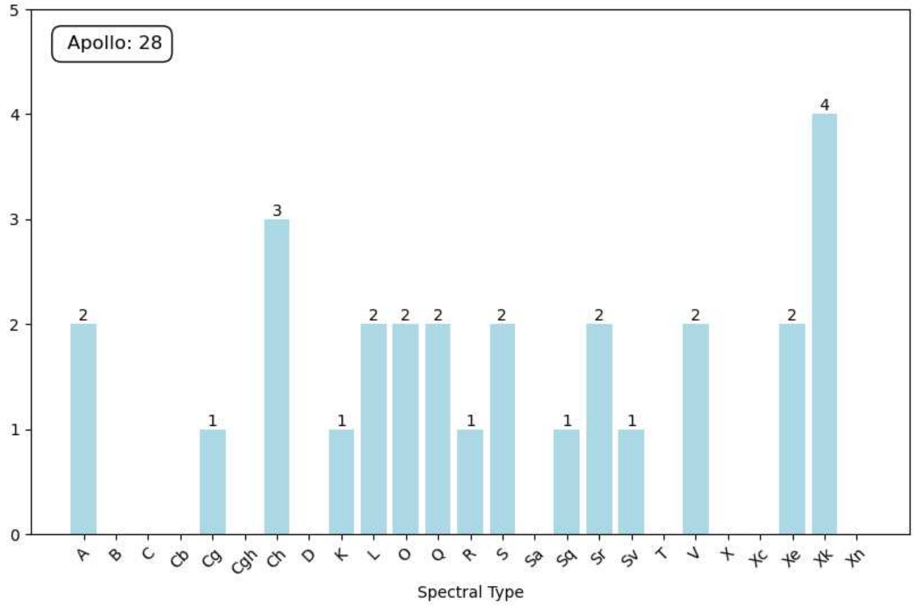

Figure 4.26: the histogram shows the spectral type according to the Bus and DeMeo classification of 28 Apollo NEOs studied in my work.

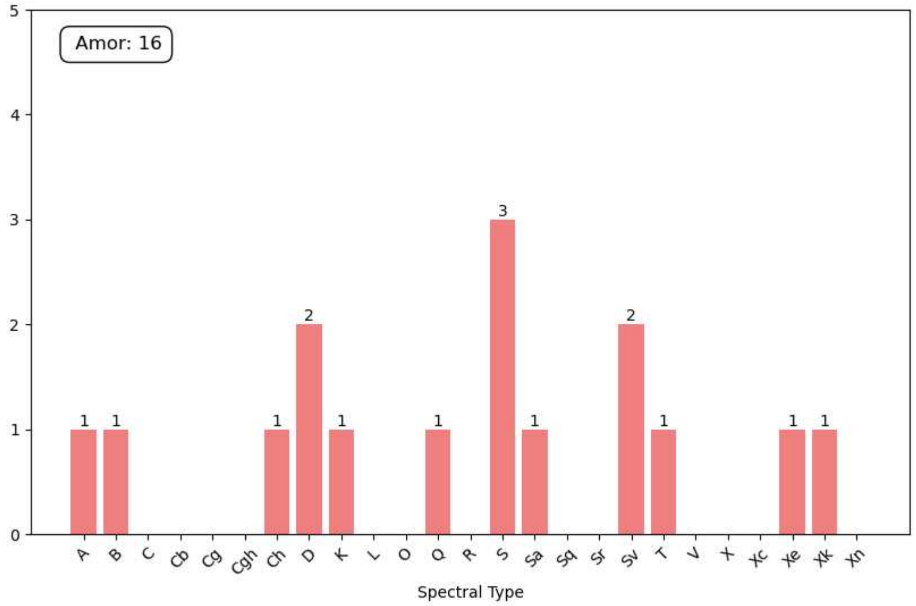

Figure 4.27: the histogram shows the spectral type according to the Bus and DeMeo classification of my 28 Amor NEOs studied in my work.

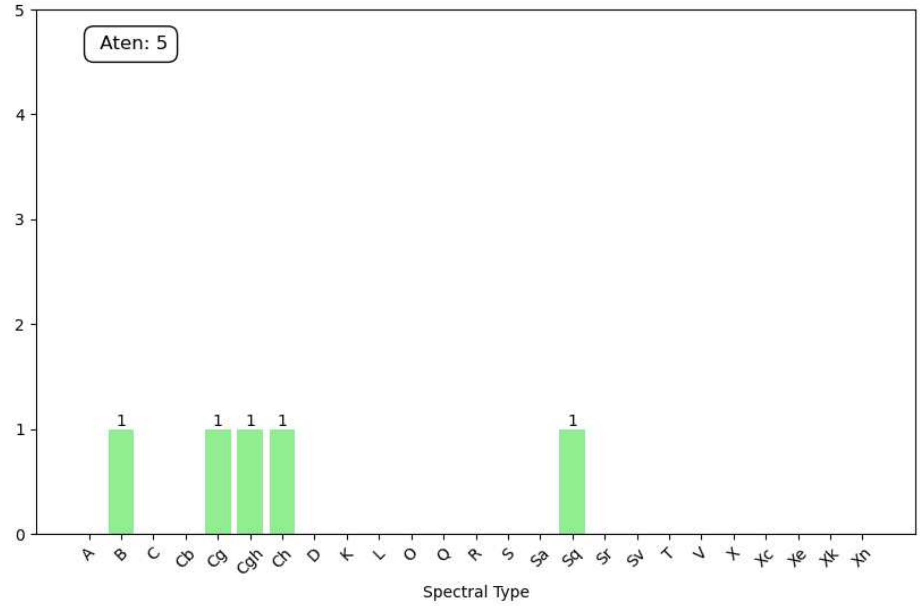

Figure 4.28: the histogram shows the spectral type according to the Bus and DeMeo classification of my 28 Aten NEOs studied in my work.

Conclusion

This thesis focuses on the spectroscopic study of NEAs to better understand their surface composition. Nowadays (March 12^{nd}, 2024), there are approximately 35,000 known NEAs, and this number is continuously increasing. Providing a taxonomic classification will aid in a better understanding of these small celestial bodies and provide important information to future researchers in the event of their impact on our planet. In this thesis, I observed several NEAs through the Copernico and Galileo telescopes located in Asiago. The data was then reduced and analysed for 49 NEAs as part of the NEOROCKS project. Additionally, I studied the Didymos-Dimorphos system simultaneously with NASA's DART mission. Both studies provide a better understanding of the surface and structure of asteroids, aiding in planetary defense against potential impacts with these objects.

For the study of Didymos system, my main goal were twofold: to taxonomically classify the binary system after the impact of the DART probe on Dimorphos and to analyze the slope of the spectra of the Didymos system during a complete rotation on itself. In fact, the impact of DART on Dimorphos allows for the study of the asteroid's internal composition and the spectral evolution of ejecta.

Before the impact with the DART spacecraft, there were several taxonomic classifications of the Didymos binary system. The initial classifications identified it as Xk- and C-type, which later changed to S-type thanks to observations in NIR. The taxonomy of Didymos is the same as that of Dimorphos because asteroids with a diameter smaller than a few tens of kilometers can break apart, and the expelled material goes into orbit, leading to the formation of a satellite. Therefore, it is believed that Didymos and Dimorphos were formed from a common origin, suggesting the same chemical composition between the two bodies. Additionally, the contribution of reflected light from Dimorphos during spectroscopic observations from the ground is only 5% compared to the entire binary system and therefore negligible: it cannot be confirmed that Dimorphos has the same chemical composition as Didymos.

After the impact, the magnitude of the binary system increased by approximately one order of magnitude. The system's brightness increased due to two factors. First, a cloud of gaseous ejecta containing sodium and potassium moved at a velocity of 1.5 - 1.7 km/s in the opposite direction to DART for a few minutes. Secondly, a slow and long-lasting cloud of ejecta formed around the body, creating a series of tails that changed in number. My initial spectra were taken approximately 19 days after impact and cover 94% of a complete rotation. From these spectra, it can be deduced that the taxonomic class of Didymos is compatible with S-type, confirming the pre-impact literature taxonomy. This taxonomic classification confirms two other taxonomic classifications of Didymos system observed in the first days after impact. My spectra are within 3σ of error compared to the S-type taxonomic curve of the Bus and DeMeo classification. Polishook et al.'s spectral observations on September 26^{th} and 27^{th}, 2022 confirm the pre-impact S-type taxonomic class, although a slope variation was observed in its spectra. Lin et al.'s also observed a change in slope in Didymos' spectra, but interpreted it differently from Polishook et al.: on September 27th, 2022, the binary system shows a C-type spectrum, on September 29th, 2022, it becomes a Q-type, and on September 30th, 2022, it returns to showing S-type characteristics. Despite the discrepancy between the two authors, both confirm the taxonomic classification of S-type after September 30th, 2022. This classification was also confirmed by my observations in October, November, and December 2022. The difference in slope during the initial days is also related to the increase in brightness caused by the impact of DART on Dimorphos and the raise of ejecta. In the days following the impact, the magnitude decreased by 0.07 mag per day, indicating the movement of the ejecta away from the system due to the pressure of solar radiation. Additionally, Polishook et al. suggests that the variation in the spectrum may be due to three physical processes: compositional variation of the ejecta material, ejection of 'fresh' non weathered material, and ejected material with varied grain sizes. The shallow slope spectra of Didymos do not exhibit Q-type characteristics, leading to the conclusion that the surface material excavated by the impact of DART is not as fresh as that of Q-type asteroids. Instead, after approximately 19 days, I did not observe any changes in slope in the spectra obtained from the rotation on October 18th, 2022. All spectral slope values are within 3σ of error. The same values remain unchanged for the spectra obtained on the following night (October 19th) and on November 18th, 2022.

In the days following the impact, a long tail was formed due to the radiation pressure and the movement of the binary system, along with other minor tails in different directions, indicating that the dust environment surrounding the system is non-uniform. From a photometric point of view, it is evident that two weeks later, when the twin tails had disappeared, there was only a decrease in magnitude of 0.04 mag per night: this indicates that most of the ejecta were swept away from the system. To confirm this fact, on the night of December 26th, 2022, more than two complete rotations of Didymos were observed. The binary system consistently showed the same slope within a 3σ error, which is consistent with the values found in October 2022. The change in slope in the spectra after the initial impact may be due to the dense dust cloud formed by the impact in front of the binary system. The evolution of ejecta is complex: immediately after the impact, the distribution is more uniform compared to the following days. The tail is composed of grains of different sizes, ranging from finer to larger ones. Finer grains are dispersed faster during the first few hours/days. I expected that a change in slope could be due to the presence of larger grains. However, the observations show that even the larger grains have dispersed into the long tail as early as 19 days after impact, as no variation in spectral slope has been observed. Therefore, in about three weeks, the dense dust cloud observed in the first few days has diluted and become less dense, forming a long tail in the opposite direction of Didymos' motion. Furthermore, based on the albedo calculated in literature and the absolute magnitude H, I estimated the diameter of Didymos to be approximately 769 m, which is consistent to the value 780 m, obtained before impact and available in literature [267], and represents a better estimates that the value of 720 mderived by Polishook et al. [3].

During the study of Didymos' rotation, the importance of the slit orientation with the direction of atmospheric refraction of the observed object was investigated. A hardware issue with the Copernico telescope's guide camera probe caused differential tracking to malfunction, resulting in Didymos exiting the slit. For this reason, I was chosen to not orient the slit along the direction of the atmospheric refraction of the object so that Didymos would remain in the slit for a longer time to obtain spectra with a higher S/N ratio. The atmosphere plays a fundamental role in the spectroscopic observation of any celestial object. From the literature and my obtained spectra, it is evident that the greater the airmass, the wider the spectrum due to atmospheric refraction. Therefore, the spectrum width between red and blue wavelengths is much greater at high airmass than at low airmass. My results show that there is a variation in the spectra slope of the spectra acquired in August, October, and November 2022. The lower value of the slope was achived in October. This difference in slope is due to Didymos reaching a maximum altitude of 22° in August 2022, between 26° and 28° in October, and between 28° and 49° in November. Therefore, a higher altitude means a smaller airmass and consequently a narrower spectrum width due to atmospheric refraction between blue and red wavelengths. In general, during the same evening, a lower variation is expected because of the incorrect orientation of the slit along the direction of the atmospheric refraction of the object. The slope variation I found was very high because Didymos exited the slit after each exposure, requiring a reposition of the binary system in the slit. The new position in which it was placed inside the slit was different from the previous one because of the inevitable human error. Therefre, for each position, a different portion of the spectrum was placed in the slit because of atmospheric refraction of the target: at each spectrum acquisition, randomly put either the reddest or the bluest part of the spectrum in the slit. Due to this fact, the spectral slope obtained was much higher than expected. Additionally, in the spectra obtained in December 2022, Didymos had an altitude between 52° and 72°, with a very low airmass (about 1.0 - 1.2). The spectral slope of these spectra remains unchanged because the effects of atmospheric refraction are negligible. Previous literature shows that at an altitude greater than 50°, the width of the spectrum due to atmospheric refraction is less than or approximately equal to 1", which is smaller than the values of seeing during those observations (1" - 2") and the width of the slit (1.69"). Therefore, no effect of slope change due to atmospheric refraction is observed. In conclusion, the incorrect orientation of the slit, combined with the issue of the differential tracking, forced to reposition Didymos after each acquisition, resulting in a high variation of slope in our spectra. Additional analysis of the effects of atmospheric refraction at the Asiago Observatory will be done after submission of this thesis. Furthermore, after the differential tracking issues encountered in October 2022, they were resolved in December 2022, improving all future observations.

The DART mission has demonstrated the effectiveness of the 'kinetic impactor' technique for deflecting a small asteroid approaching Earth. The DART spacecraft collided with the leading hemisphere of Dimorphos, changing its revolution period from -33 ± 1.0 minutes to a new period of 11.372 ± 0.017 hours. The upcoming Hera mission will study the binary system after impact, including measuring the mass of Dimorphos, characterizing its external and internal surface, and examining the possible crater formed by the impact.

NEOROCKS is a project aimed at improving our understanding of the physical characteristics, origin, and evolution of NEOs for planetary defense. For this second project, I observed 98 NEAs and, 49 of which were selected for investigation. To classify them, I compared the spectral data with the curve of the respective taxonomic type using the χ^2 method. Their taxonomic classification is based on the Bus and DeMeo and Mahkle taxonomy. The χ^2 method allowed to classify the selected NEAs with $S/N > 10$, while it was not possible to classify those with $S/N < 10$. The S/N was obtained using different methods. The first method considered the signals and noises across the entire spectral range used, deriving a S/N ratio that is much loer in respect to the other two methods, which take into account the spectral range between 5700 and 7700 Å. Method 2 considers the one-dimensional spectrum after division by the solar analog, while method 3 considers it before division. Comparing the

S/N ratio of these two methods shows very similar results. From the 49 NEAs analysed, 12 of them have a spectrum with an S/N < 10, which means that their taxonomic classification cannot be confirmed, affecting the statistical analysis in this work. As expected, most of the observed NEAs belong to the orbital type of Apollo, followed by Amors. Observing Atens is challenging due to their proximity to the Sun, making statistics even more negligible. Mw NEA database does not include Atiras. This is due to the challenging in their observation, since they can only be oberved at the morning or evening at elongations from the Sun not exceeding 90°. Mahkle's taxonomic classification for our NEOs does not match the percentages obtained in their study. This is because I analyzed only 49 NEAs, while their database contains data on 2125 asteroids. In my study, I compared the percentages of asteroids in a certain taxonomic group and found them to be very similar to those of Hromakina. As expected, half of the NEOs belong to the S-complex, which is the most common among all NEOs in all surveys. My research shows that the number of carbonaceous objects decreases as their size increases, while the number of silicate objects is more common in smaller objects and decreases rapidly for objects with a diameter greater than 1 km, as confirmed by Hromakina et al. Such distribution is most probably caused by the bias towards higher albedo objects. Our taxonomic percentages are consistent with those found by Popescu et al. Additionally, I have identified several rare types, including 3 A-types, 2 K-types, 2 L-types, 2 O-types, and 1 R-type. Additionally, the B/C-complex group is more challenging to observe than the Q/S-complex due to its low albedo. My observations confirm that the B/C-complex is a minority compared to the Q/S-complex.

In conclusion, my main goal is to taxonomically classify NEOs to contribute to the NEOROCKs project and understand the chemical composition and physical parameters of NEAs. Nowadays, new NEAs are discovered thanks to sophisticated astronomical tools. Studying NEAs provides a better understanding of the formation of the Solar System and their contribution to the amount of water and organic-rich material brought to early Earth. It is important to study them to understand how to prevent them from falling on our planet and causing a global disaster like the one that occurred approximately 66 million years ago responsible of the dinosaur mass extinction. the comprehesive characterization of NEOs would thus prevent a key element for planetary defence programs. Therefore, it is crucial to determine the orbit of a NEO to assess the probability of impact on our planet, its chemical composition and its physical properties in order to predict the impact on Earth and the possible crater it could form.

Bibliography

[1] T. Grav, A. K. Mainzer, J. R. Masiero, D. W. Dahlen, T. Spahr, W. F. Bottke, and F. J. Masci, arXiv e-prints , arXiv:2310.20149 (2023), arXiv:2310.20149 [astro-ph.EP] .

[2] S. J. Bus, F. Vilas, and M. A. Barucci, in *Asteroids III* (a, 2002) pp. 169–182.

[3] D. Polishook, F. E. DeMeo, B. J. Burt, C. A. Thomas, A. S. Rivkin, J. A. Sanchez, and V. Reddy, Planetary Science Journal **4**, 229 (2023), arXiv:2311.00421 [astro-ph.EP] .

[4] P. Brown, R. E. Spalding, D. O. ReVelle, E. Tagliaferri, and S. P. Worden, Nature **420**, 294 (2002).

[5] H. A. Boslough M., Brown P., 2015 IEEE Aerospace Conference (2015).

[6] E. A. Silber, D. O. ReVelle, P. G. Brown, and W. N. Edwards, Journal of Geophysical Research (Planets) **114**, E08006 (2009).

[7] B. W. Stokes G.H, Barbee B.W, Report of the Near-Earth Object Science Defnition Team NASA (2017).

[8] P. Tricarico, Icarus **284**, 416 (2017), arXiv:1604.06328 [astro-ph.EP] .

[9] E. A. Silber, M. Boslough, W. K. Hocking, M. Gritsevich, and R. W. Whitaker, Advances in Space Research **62**, 489 (2018), arXiv:1805.07842 [astro-ph.EP] .

[10] A. Morbidelli, J. Bottke, W. F., C. Froeschlé, and P. Michel, in *Asteroids III* (a, 2002) pp. 409–422.

[11] J. Bottke, W. F., D. Vokrouhlický, D. P. Rubincam, and M. Broz, in *Asteroids III* (a, 2002) pp. 395–408.

[12] S. J. Bus and R. P. Binzel, Icarus **158**, 146 (2002).

[13] M. Mahlke, B. Carry, and P. A. Mattei, Astronomy & Astrophysics **665**, A26 (2022), arXiv:2203.11229 [astro-ph.EP] .

[14] R. P. Binzel and S. Xu, Science **260**, 186 (1993), https://www.science.org/doi/pdf/10.1126/science.260.5105.186 .

[15] A. Cellino, S. J. Bus, A. Doressoundiram, and D. Lazzaro, in *Asteroids III* (a, 2002) pp. 633–643.

[16] S. J. Bus, *Compositional structure in the asteroid belt: Results of a spectroscopic survey*, Ph.D. thesis, Massachusetts Institute of Technology (1999).

[17] D. Pavela, B. Novakovi, V. Carruba, and V. Radovi, Monthly Notices of the Royal Astronomical Society **501**, 356 (2020).

[18] J. L. Margot, P. Pravec, P. Taylor, B. Carry, and S. Jacobson, in *Asteroids IV* (a, 2015) pp. 355–374.

[19] A. S. Rivkin, N. L. Chabot, A. M. Stickle, C. A. Thomas, D. C. Richardson, O. Barnouin, E. G. Fahnestock, C. M. Ernst, A. F. Cheng, S. Chesley, S. Naidu, T. S. Statler, B. Barbee, H. Agrusa, N. Moskovitz, R. Terik Daly, P. Pravec, P. Scheirich, E. Dotto, V. Della Corte, P. Michel, M. Küppers, J. Atchison, and M. Hirabayashi, Planetary Science Journal **2**, 173 (2021).

[20] P. Michel, M. Küppers, A. C. Bagatin, B. Carry, S. Charnoz, J. de Leon, A. Fitzsimmons, P. Gordo, S. F. Green, A. Hérique, M. Juzi, Ö. Karatekin, T. Kohout, M. Lazzarin, N. Murdoch, T. Okada, E. Palomba, P. Pravec, C. Snodgrass, P. Tortora, K. Tsiganis, S. Ulamec, J.-B. Vincent, K. Wünnemann, Y. Zhang, S. D. Raducan, E. Dotto, N. Chabot, A. F. Cheng, A. Rivkin, O. Barnouin, C. Ernst, A. Stickle, D. C. Richardson, C. Thomas, M. Arakawa, H. Miyamoto, A. Nakamura, S. Sugita, M. Yoshikawa, P. Abell, E. Asphaug, R.-L. Ballouz, W. F. Bottke, D. S. Lauretta, K. J. Walsh, P. Martino, and I. Carnelli, Planetary Science Journal **3**, 160 (2022).

[21] R. T. Daly, C. M. Ernst, O. S. Barnouin, N. L. Chabot, A. S. Rivkin, A. F. Cheng, E. Y. Adams, H. F. Agrusa, E. D. Abel, A. L. Alford, E. I. Asphaug, J. A. Atchison, A. R. Badger, P. Baki, R.-L. Ballouz, D. L. Bekker, J. Bellerose, S. Bhaskaran, B. J. Buratti, S. Cambioni, M. H. Chen, S. R. Chesley, G. Chiu, G. S. Collins, M. W. Cox, M. E. DeCoster, P. S. Ericksen, R. C. Espiritu, A. S. Faber, T. L. Farnham, F. Ferrari, Z. J. Fletcher, R. W. Gaskell, D. M. Graninger, M. A. Haque, P. A. Harrington-Duff, S. Hefter, I. Herreros, M. Hirabayashi, P. M. Huang, S.-Y. W. Hsieh, S. A. Jacobson, S. N. Jenkins, M. A. Jensenius, J. W. John, M. Jutzi, T. Kohout, T. O. Krueger, F. E. Laipert, N. R. Lopez, R. Luther, A. Lucchetti, D. M. Mages, S. Marchi, A. C. Martin, M. E. McQuaide, P. Michel, N. A. Moskovitz, I. W. Murphy, N. Murdoch, S. P. Naidu, H. Nair, M. C. Nolan, J. Ormö, M. Pajola, E. E. Palmer, J. M. Peachey, P. Pravec, S. D. Raducan, K. T. Ramesh, J. R. Ramirez, E. L. Reynolds, J. E. Richman, C. Q. Robin, L. M. Rodriguez, L. M. Roufberg, B. P. Rush, C. A. Sawyer, D. J. Scheeres, P. Scheirich, S. R. Schwartz, M. P. Shannon, B. N. Shapiro, C. E. Shearer, E. J. Smith, R. J. Steele, J. K. Steckloff, A. M. Stickle, J. M. Sunshine, E. A. Superfin, Z. B. Tarzi, C. A. Thomas, J. R. Thomas, J. M. Trigo-Rodríguez, B. T. Tropf, A. T. Vaughan, D. Velez, C. D. Waller, D. S. Wilson, K. A. Wortman, and Y. Zhang, Nature **616**, 443 (2023), arXiv:2303.02248 [astro-ph.EP] .

[22] C. A. Thomas, S. P. Naidu, P. Scheirich, N. A. Moskovitz, P. Pravec, S. R. Chesley, A. S. Rivkin, D. J. Osip, T. A. Lister, L. A. M. Benner, M. Brozović, C. Contreras, N. Morrell, A. RoŻek, P. Kušnirák, K. Hornoch, D. Mages, P. A. Taylor, A. D. Seymour, C. Snodgrass, U. G. Jørgensen, M. Dominik, B. Skiff, T. Polakis, M. M. Knight, T. L. Farnham, J. D. Giorgini, B. Rush, J. Bellerose, P. Salas, W. P. Armentrout, G. Watts, M. W. Busch, J. Chatelain, E. Gomez, S. Greenstreet, L. Phillips,

M. Bonavita, M. J. Burgdorf, E. Khalouei, P. Longa-Peña, M. Rabus, S. Sajadian, N. L. Chabot, A. F. Cheng, W. H. Ryan, E. V. Ryan, C. E. Holt, and H. F. Agrusa, Nature **616**, 448 (2023), arXiv:2303.02077 [astro-ph.EP] .

[23] Z.-Y. Lin, J.-B. Vincent, and W.-H. Ip, Astronomy & Astrophysics **676**, A116 (2023).

[24] A. Rakich, Applied Sciences **11** (2021), 10.3390/app11146261.

[25] T. Hromakina, M. Birlan, M. A. Barucci, M. Fulchignoni, F. Colas, S. Fornasier, F. Merlin, A. Sonka, S. Anghel, G. Poggiali, I. Belskaya, D. Perna, E. Dotto, E. Dotto, M. Banaszkiewicz, S. Banchi, M. A. Barucci, F. Bernardi, M. Birlan, B. Carry, A. Cellino, J. de Leon, M. Lazzarin, E. Mazzotta Epifani, A. Mediavilla, J. Nomen Torres, D. Perna, E. Perozzi, P. Pravec, C. Snodgrass, C. Teodorescu, S. Anghel, A. Bertolucci, F. Calderini, F. Colas, A. Del Vigna, A. Dell'Oro, A. di Cecco, L. Dimare, P. Fatka, S. Fornasier, E. Frattin, P. Frosini, M. Fulchignoni, R. Gabryszewski, M. Giardino, A. Giunta, T. Hromakina, J. Huntingford, S. Ieva, J. P. Kotlarz, F. La Forgia, J. Licandro, H. Medeiros, F. Merlin, F. Pinna, G. Polenta, M. Popescu, A. Rozek, P. Scheirich, A. Sergeyev, A. Sonka, G. B. Valsecchi, P. Wajer, A. Zinzi, and NEOROCKS Team, Monthly Notices of the Royal Astronomical Society **520**, 3143 (2023), arXiv:2302.01165 [astro-ph.EP] .

[26] M. Popescu, O. Vaduvescu, J. de León, R. M. Gherase, J. Licandro, I. L. Boacă, A. B. Şonka, R. P. Ashley, T. Močnik, D. Morate, M. Predatu, M. De Prá, C. Fariña, H. Stoev, M. Díaz Alfaro, I. Ordonez-Etxeberria, F. López-Martínez, and R. Errmann, Astronomy & Astrophysics **627**, A124 (2019), arXiv:1905.12997 [astro-ph.EP] .

[27] D. A. Kring, L. Zurcher, and O. Abramov, in *AGU Spring Meeting Abstracts*, Vol. 2007 (2007) pp. U33A–08.

[28] G. I. Kokhirova and P. B. Babadzhanov, Solar System Research **57**, 467 (2023).

[29] J. Borovička, WGN, Journal of the International Meteor Organization **44**, 31 (2016).

[30] M. Ćuk, B. J. Gladman, and D. Nesvorný, Icarus **239**, 154 (2014), arXiv:1406.0825 [astro-ph.EP] .

[31] A. Alvarez-Candal, R. Duffard, D. Lazzaro, and T. Michtchenko, Astronomy & Astrophysics **459**, 969 (2006).

[32] V. Carruba, D. Nesvorný, S. Aljbaae, and M. E. Huaman, Monthly Notices of the Royal Astronomical Society **451**, 244 (2015), arXiv:1505.03745 [astro-ph.EP] .

[33] M. N. De Prá, N. Pinilla-Alonso, J. M. Carvano, J. Licandro, H. Campins, T. Mothé-Diniz, J. De León, and V. Alí-Lagoa, Icarus **311**, 35 (2018), arXiv:1711.02071 [astro-ph.EP] .

[34] M. Connors, in *American Astronomical Society Meeting Abstracts*, American Astronomical Society Meeting Abstracts, Vol. 55 (2023) p. 147.01.

[35] L. Dones and M. Womack, in *European Planetary Science Congress* (2020) pp. EPSC2020–515.

[36] A. Morbidelli and D. Nesvorný, in *The Trans-Neptunian Solar System*, edited by D. Prialnik, M. A. Barucci, and L. Young (a, 2020) pp. 25–59.

[37] G. W. Wetherill, Geochimica et Cosmochimica Acta **40**, 1297 (1976).

[38] T. Gehrels, *Asteroids III* (University of Arizona Press, 2002).

[39] G. W. Wetherill, Icarus **37**, 96 (1979).

[40] J. Wisdom, Meteoritics **18**, 422 (1983).

[41] S. J. Peale, "Orbital Resonances in the Solar System," Reports of Accomplishments of Planetology Programs, 1975-1976. NASA Technical Memorandum, NASA TM X-3364. Office of Space Science. Washington, DC: National Aeronautics and Space Administration, 1976., p.15 (1976).

[42] B. J. Gladman, F. Migliorini, A. Morbidelli, V. Zappala, P. Michel, A. Cellino, C. Froeschle, H. F. Levison, M. Bailey, and M. Duncan, Science **277**, 197 (1997).

[43] A. Morbidelli and B. Gladman, Meteoritics & Planetary Science **33**, 999 (1998).

[44] A. Morbidelli, *Modern celestial mechanics : aspects of solar system dynamics* (a, 2002).

[45] A. Morbidelli and M. Moons, a **102**, 316 (1993).

[46] N. Murray and M. Holman, Astronomical Journal **114**, 1246 (1997).

[47] A. Morbidelli and D. Nesvorný, Icarus **139**, 295 (1999).

[48] P. Michel, F. Migliorini, A. Morbidelli, and V. Zappalà, Icarus **145**, 332 (2000).

[49] W. F. Bottke, A. Morbidelli, R. Jedicke, J. M. Petit, and H. F. Levison, in *AAS/Division of Dynamical Astronomy Meeting #32*, AAS/Division of Dynamical Astronomy Meeting, Vol. 32 (2001) p. 07.05.

[50] P. Michel, F. Migliorini, A. Morbidelli, and V. Zappalà, Icarus **145**, 332 (2000).

[51] P. Michel, C. Froeschlé, and P. Farinella, Earth Moon and Planets **72**, 151 (1996).

[52] G. Beekman, Journal for the History of Astronomy **37**, 71 (2006).

[53] E. J. Opik, Proc. R. Irish Acad. Sect. A **54**, 165 (1951).

[54] V. V. Radzievskii, azh **29**, 162 (1952).

[55] V. P. Vinogradova and V. V. Radzievskii, Soviet Astronomy **9**, 334 (1965).

[56] M. Ćuk and J. A. Burns, Icarus **176**, 418 (2005).

[57] D. Vokrouhlický, W. F. Bottke, S. R. Chesley, D. J. Scheeres, and T. S. Statler, in *Asteroids IV* (a, 2015) pp. 509–531.

[58] W. F. Bottke, M. C. Nolan, R. Greenberg, and R. A. Kolvoord, Icarus **107**, 255 (1994).

[59] V. Zappala and A. Cellino, in *Completing the Inventory of the Solar System*, Astronomical Society of the Pacific Conference Series, Vol. 107, edited by T. Rettig and J. M. Hahn (1996) pp. 29–44.

[60] P. Farinella, C. Froeschle, and R. Gonczi, Celestial Mechanics and Dynamical Astronomy **56**, 287 (1993).

[61] M. W. Caffee, J. N. Goswami, C. M. Hohenberg, K. Marti, and R. C. Reedy, in *Meteorites and the Early Solar System*, edited by J. F. Kerridge and M. S. Matthews (a, 1988) pp. 205–245.

[62] T. Graf and K. Marti, Meteoritics **27**, 227 (1992).

[63] W. F. Bottke, D. Vokrouhlický, M. Broz, D. Nesvorný, and A. Morbidelli, Science **294**, 1693 (2001).

[64] W. F. Bottke, R. Jedicke, A. Morbidelli, J.-M. Petit, and B. Gladman, Science **288**, 2190 (2000).

[65] A. Cellino, P. Michel, P. Tanga, V. Zappalà, P. Paolicchi, and A. Dell'Oro, Icarus **141**, 79 (1999).

[66] R. P. Binzel, P. Farinella, V. Zappala, and A. Cellino, in *Asteroids II*, edited by R. P. Binzel, T. Gehrels, and M. S. Matthews (1989) pp. 416–441.

[67] P. Paolicchi, A. Cellino, D. Davis, P. Farinella, and V. Zappald, in *Lunar and Planetary Science Conference*, Lunar and Planetary Science Conference, Vol. 20 (1989) p. 816.

[68] P. Pravec and A. W. Harris, Icarus **148**, 12 (2000).

[69] P. Pravec, A. W. Harris, and T. Michalowski, in *Asteroids III* (a, 2002) pp. 113–122.

[70] D. P. Rubincam, Icarus **148**, 2 (2000).

[71] I. Bekey, *Dealing with the THREAT TO EARTH From ASTEROIDES and COMETS*, EAN (International Academy of Astronautics (IAA), 2009).

[72] P. Pravec, A. W. Harris, P. Kusnirak, A. Galad, and K. Hornoch, in *Asteroids, Comets, Meteors 2012*, LPI Contributions, Vol. 1667, edited by LPI Editorial Board (2012) p. 6089.

[73] A. W. Harris and J. A. Burns, Icarus **40**, 115 (1979).

[74] P. Pravec, A. W. Harris, and B. D. Warner, in *Near Earth Objects, our Celestial Neighbors: Opportunity and Risk*, Vol. 236, edited by G. B. Valsecchi, D. Vokrouhlický, and A. Milani (2007) pp. 167–176.

[75] P. Pravec, A. W. Harris, P. Scheirich, P. Kušnirák, L. Šarounová, C. W. Hergenrother, S. Mottola, M. D. Hicks, G. Masi, Y. N. Krugly, V. G. Shevchenko, M. C. Nolan, E. S. Howell, M. Kaasalainen, A. Galád, P. Brown, D. R. DeGraff, J. V. Lambert, W. R. Cooney, and S. Foglia, Icarus **173**, 108 (2005).

[76] B. Rozitis, S. F. Green, E. MacLennan, and J. P. Emery, Monthly Notices of the Royal Astronomical Society **477**, 1782 (2018).

[77] D. T. Britt and G. J. Consolmagno, in *AAS/Division for Planetary Sciences Meeting Abstracts #32*, AAS/Division for Planetary Sciences Meeting Abstracts, Vol. 32 (2000) p. 07.02.

[78] L. W. Alvarez, W. Alvarez, F. Asaro, and H. V. Michel, Science **208**, 1095 (1980), https://www.science.org/doi/pdf/10.1126/science.208.4448.1095 .

[79] A. Milani, M. Carpino, and F. Marzari, Icarus **88**, 292 (1990).

[80] D. Morrison, Mercury **21**, 103 (1992).

[81] A. Mainzer, J. Bauer, T. Grav, J. Masiero, R. M. Cutri, J. Dailey, P. Eisenhardt, R. S. McMillan, E. Wright, R. Walker, R. Jedicke, T. Spahr, D. Tholen, R. Alles, R. Beck, H. Brandenburg, T. Conrow, T. Evans, J. Fowler, T. Jarrett, K. Marsh, F. Masci, H. McCallon, S. Wheelock, M. Wittman, P. Wyatt, E. DeBaun, G. Elliott, D. Elsbury, T. Gautier, S. Gomillion, D. Leisawitz, C. Maleszewski, M. Micheli, and A. Wilkins, The Astrophysical Journal **731**, 53 (2011).

[82] M. Granvik, A. Morbidelli, R. Jedicke, B. Bolin, W. F. Bottke, E. Beshore, D. Vokrouhlick, D. Nesvorn, and P. Michel, Icarus **312**, 181 (2018).

[83] E. F. Tedesco, G. J. Veeder, J. W. Fowler, and J. R. Chillemi, "The IRAS Minor Planet Survey," The IRAS Minor Planet Survey, Final Report by E.R. Tedesco, G.J. Veeder, J.W. Fowler, and J.R. Chillemi. Philliips Laboratory, Hanscom Air Force Base, MA, December 1992. PL-TR-92-2049. (1992).

[84] V. C. R. O. L. S. S. S. Collaboration, R. L. Jones, M. T. Bannister, B. T. Bolin, C. O. Chandler, S. R. Chesley, S. Eggl, S. Greenstreet, T. R. Holt, H. H. Hsieh, Z. Ivezic, M. Juric, M. S. P. Kelley, M. M. Knight, R. Malhotra, W. J. Oldroyd, G. Sarid, M. E. Schwamb, C. Snodgrass, M. Solontoi, and D. E. Trilling, Bulletin of the AAS **53** (2021), https://baas.aas.org/pub/2021n4i236.

[85] D. J. Tholen, *Asteroid Taxonomy from Cluster Analysis of Photometry.*, Ph.D. thesis, University of Arizona (1984).

[86] W. Herschel, Philosophical Transactions of the Royal Society of London Series I **92**, 213 (1802).

[87] H. C. Vogel, Annalen der Physik **234**, 461 (1876).

[88] N. T. Bobrovnikoff, Lick Observatory Bulletin **407**, 18 (1929).

[89] T. B. McCord, J. B. Adams, and T. V. Johnson, Science **168**, 1445 (1970).

[90] C. R. Chapman, T. V. Johnson, and T. B. McCord, in *NASA Special Publication*, Vol. 267, edited by T. Gehrels (a, 1971) p. 51.

[91] C. R. Chapman, D. Morrison, and B. Zellner, Icarus **25**, 104 (1975).

[92] M. J. Gaffey and T. B. McCord, in *Asteroids*, edited by T. Gehrels and M. S. Matthews (a, 1979) pp. 688–723.

[93] B. Zellner, D. J. Tholen, and E. F. Tedesco, Icarus **61**, 355 (1985).

[94] J. L. Hinrichs, P. G. Lucey, M. S. Robinson, A. Meibom, and A. N. Krot, Geophysical Research Letters **26**, 1661 (1999).

[95] R. B. Singer and T. L. Roush, Journal of Geophysical Research **90**, 12,434 (1985).

[96] P. G. Lucey, K. Keil, and R. Whitely, Journal of Geophysical Research **103**, 5865 (1998).

[97] F. Adamian, A. Aganiants, Y. Borzunov, S. Chumakov, N. Demekhina, G. Frangulian, L. Golovanov, V. Grabski, A. Hairapetian, H. Hakobyan, I. Keropian, I. Lebedev, Z. Manukian, N. Moroz, G. Movsesian, E. Muradian, A. Oganesian, R. Oganezov, Y. Panebratsev, M. Rekalo, S. Shimanski, A. Sirunian, H. Torosian, A. Tsvenev, H. Vartapetian, and V. Volchinski, European Physical Journal A **8**, 423 (2000).

[98] R. G. Burns, Annual Review of Earth and Planetary Sciences **9**, 345 (1981).

[99] R. G. Burns, *Mineralogical Applications of Crystal Field Theory* (a, 1993).

[100] J. M. Sunshine, R. P. Binzel, T. H. Burbine, and S. J. Bus, in *Lunar and Planetary Science Conference*, Lunar and Planetary Science Conference (1998) p. 1430.

[101] S. R. Sawyer, in *Bulletin of the American Astronomical Society*, Vol. 23 (1991) p. 1235.

[102] F. Vilas, S. M. Larson, E. C. Hatch, and K. S. Jarvis, Icarus **105**, 67 (1993).

[103] F. Vilas, K. S. Jarvis, and M. J. Gaffey, Icarus **109**, 274 (1994).

[104] T. Hiroi, F. Vilas, and J. M. Sunshine, Icarus **119**, 202 (1996).

[105] T. H. Burbine, E. A. Cloutis, S. J. Bus, A. Meibom, and R. P. Binzel, in *Bulletin of the American Astronomical Society*, Vol. 30 (1998) p. 1025.

[106] J. R. Masiero, F. E. DeMeo, T. Kasuga, and A. H. Parker, in *Asteroids IV* (a, 2015) pp. 323–340.

[107] T. H. Burbine, T. J. McCoy, A. Meibom, B. Gladman, and K. Keil, in *Asteroids III* (a, 2002) pp. 653–667.

[108] M. Granvik and P. Brown, Icarus **311**, 271 (2018), arXiv:1804.07229 [astro-ph.EP] .

[109] R. Gomes, H. F. Levison, K. Tsiganis, and A. Morbidelli, Nature **435**, 466 (2005).

[110] A. Morbidelli, H. F. Levison, K. Tsiganis, and R. Gomes, Nature **435**, 462 (2005).

[111] K. Tsiganis, R. Gomes, A. Morbidelli, and H. F. Levison, Nature **435**, 459 (2005).

[112] E. F. Tedesco, J. G. Williams, D. L. Matson, G. J. Veeder, J. C. Gradie, and L. A. Lebofsky, in *Asteroids II*, edited by R. P. Binzel, T. Gehrels, and M. S. Matthews (1989) pp. 1151–1161.

[113] M. A. Barucci, M. T. Capria, A. Coradini, and M. Fulchignoni, Icarus **72**, 304 (1987).

[114] E. S. Howell, E. Merenyi, and L. A. Lebofsky, Journal of Geophysical Research **99**, 10847 (1994).

[115] J. F. Bell, P. D. Owensby, B. R. Hawke, and M. J. Gaffey, in *Lunar and Planetary Science Conference*, Lunar and Planetary Science Conference, Vol. 19 (1988) p. 57.

[116] S. Xu, R. P. Binzel, T. H. Burbine, and S. J. Bus, Icarus **115**, 1 (1995).

[117] S. J. Bus and R. P. Binzel, Icarus **158**, 106 (2002).

[118] F. E. DeMeo, R. P. Binzel, S. M. Slivan, and S. J. Bus, Icarus **202**, 160 (2009).

[119] R. P. Binzel, F. E. DeMeo, E. V. Turtelboom, S. J. Bus, A. Tokunaga, T. H. Burbine, C. Lantz, D. Polishook, B. Carry, A. Morbidelli, M. Birlan, P. Vernazza, B. J. Burt, N. Moskovitz, S. M. Slivan, C. A. Thomas, A. S. Rivkin, M. D. Hicks, T. Dunn, V. Reddy, J. A. Sanchez, M. Granvik, and T. Kohout, Icarus **324**, 41 (2019), arXiv:2004.05090 [astro-ph.EP] .

[120] M. Marsset, F. E. DeMeo, B. Burt, D. Polishook, R. P. Binzel, M. Granvik, P. Vernazza, B. Carry, S. J. Bus, S. M. Slivan, C. A. Thomas, N. A. Moskovitz, and A. S. Rivkin, VizieR Online Data Catalog , J/AJ/163/165 (2022).

[121] J. Berthier, B. Carry, M. Mahlke, and J. Normand, Astronomy & Astrophysics **671**, A151 (2023), arXiv:2209.10697 [astro-ph.EP] .

[122] E. F. Tedesco, P. V. Noah, M. Noah, and S. D. Price, Astronomical Journal **123**, 1056 (2002).

[123] J. R. Masiero, A. K. Mainzer, T. Grav, J. M. Bauer, R. M. Cutri, C. Nugent, and M. S. Cabrera, Astrophysical Journal Letters **759**, L8 (2012), arXiv:1209.5794 [astro-ph.EP] .

[124] F. Usui, D. Kuroda, T. G. Müller, S. Hasegawa, M. Ishiguro, T. Ootsubo, D. Ishihara, H. Kataza, S. Takita, S. Oyabu, M. Ueno, H. Matsuhara, and T. Onaka, Publications of the Astronomical Society of Journal **63**, 1117 (2011).

[125] D. E. Trilling, M. Mommert, J. Hora, S. Chesley, J. Emery, G. Fazio, A. Harris, M. Mueller, and H. Smith, Astronomical Journal **152**, 172 (2016), arXiv:1608.03673 [astro-ph.EP] .

[126] A. S. Rivkin, Icarus **221**, 744 (2012).

[127] F. E. DeMeo and B. Carry, Nature **505**, 629 (2014), arXiv:1408.2787 [astro-ph.EP] .

[128] P. Vernazza, J. Castillo-Rogez, P. Beck, J. Emery, R. Brunetto, M. Delbo, M. Marsset, F. Marchis, O. Groussin, B. Zanda, P. Lamy, L. Jorda, O. Mousis, A. Delsanti, Z. Djouadi, Z. Dionnet, F. Borondics, and B. Carry, Astronomical Journal **153**, 72 (2017), arXiv:1701.06603 [astro-ph.EP] .

[129] M. J. Gaffey and T. B. McCord, in *Asteroids*, edited by T. Gehrels and M. S. Matthews (a, 1979) pp. 688–723.

[130] B. E. Clark, J. Ziffer, D. Nesvorny, H. Campins, A. S. Rivkin, T. Hiroi, M. A. Barucci, M. Fulchignoni, R. P. Binzel, S. Fornasier, F. DeMeo, M. E. Ockert-Bell, J. Licandro, and T. Mothé-Diniz, Journal of Geophysical Research (Planets) **115**, E06005 (2010).

[131] E. A. Cloutis, T. Hiroi, M. J. Gaffey, C. M. O. D. Alexander, and P. Mann, Icarus **212**, 180 (2011).

[132] J. de León, N. Pinilla-Alonso, H. Campins, J. Licandro, and G. A. Marzo, Icarus **218**, 196 (2012).

[133] T. Hiroi, M. E. Zolensky, C. M. Pieters, and M. E. Lipschutz, Meteoritics & Planetary Science **31**, 321 (1996).

[134] J. Gradie and E. Tedesco, Science **216**, 1405 (1982).

[135] T. Mothé-Diniz, J. M. Carvano, S. J. Bus, R. Duffard, and T. H. Burbine, Icarus **195**, 277 (2008).

[136] M. Devogèle, P. Tanga, A. Cellino, P. Bendjoya, J. P. Rivet, J. Surdej, D. Vernet, J. M. Sunshine, S. J. Bus, L. Abe, S. Bagnulo, G. Borisov, H. Campins, B. Carry, J. Licandro, W. McLean, and N. Pinilla-Alonso, Icarus **304**, 31 (2018), arXiv:1802.06975 [astro-ph.EP] .

[137] J. M. Sunshine, H. C. Connolly, T. J. McCoy, S. J. Bus, and L. M. La Croix, Science **320**, 514 (2008).

[138] M. J. Gaffey, K. L. Reed, and M. S. Kelley, Icarus **100**, 95 (1992).

[139] Watters, in *Geodetic Symposium on Satellite Doppler Positioning*, Vol. 1 (1979) p. 1083.

[140] D. I. Shestopalov, L. F. Golubeva, L. A. McFadden, S. Fornasier, and M. N. Taran, Planetary and Space Science **58**, 1400 (2010).

[141] F. E. DeMeo and B. Carry, Icarus **226**, 723 (2013), arXiv:1307.2424 [astro-ph.EP] .

[142] J. Eschrig, L. Bonal, M. Mahlke, B. Carry, P. Beck, and J. Gattacceca, Icarus **381**, 115012 (2022), arXiv:2206.10172 [astro-ph.EP] .

[143] P. Vernazza, B. Zanda, R. P. Binzel, T. Hiroi, F. E. DeMeo, M. Birlan, R. Hewins, L. Ricci, P. Barge, and M. Lockhart, The Astrophysical Journal **791**, 120 (2014), arXiv:1405.6850 [astro-ph.EP] .

[144] R. Brunetto, P. Vernazza, S. Marchi, M. Birlan, M. Fulchignoni, V. Orofino, and G. Strazzulla, Icarus **184**, 327 (2006).

[145] D. P. Cruikshank and W. K. Hartmann, Science **223**, 281 (1984).

[146] F. E. DeMeo, D. Polishook, B. Carry, B. J. Burt, H. H. Hsieh, R. P. Binzel, N. A. Moskovitz, and T. H. Burbine, Icarus **322**, 13 (2019), arXiv:1901.02797 [astro-ph.EP] .

[147] R. P. Binzel, S. Xu, S. J. Bus, M. F. Skrutskie, M. R. Meyer, P. Knezek, and E. S. Barker, Science **262**, 1541 (1993).

[148] M. R. Solontoi, M. Hammergren, G. Gyuk, and A. Puckett, Icarus **220**, 577 (2012), arXiv:1202.4424 [astro-ph.EP] .

[149] B. Zellner and J. Gradie, Astronomical Journal **81**, 262 (1976).

[150] R. P. Binzel, S. J. Bus, T. H. Burbine, and J. M. Sunshine, Science **273**, 946 (1996).

[151] M. Hammergren, *The Composition of Near-Earth Objects*, Ph.D. thesis, University of Washington, Seattle (1998).

[152] M. D. Hicks, U. Fink, and W. M. Grundy, Icarus **133**, 69 (1998).

[153] J. B. Adams, Journal of Geophysical Research **79**, 4829 (1974).

[154] E. A. Cloutis, M. J. Gaffey, T. L. Jackowski, and K. L. Reed, Journal of Geophysical Research **91**, 11,641 (1986).

[155] K. Hirayama, Astronomical Journal **31**, 185 (1918).

[156] A. Morbidelli, V. Zappala, M. Moons, A. Cellino, and R. Gonczi, Icarus **118**, 132 (1995).

[157] P. R. Heck, B. Schmitz, W. F. Bottke, S. S. Rout, N. T. Kita, A. Cronholm, C. Defouilloy, A. Dronov, and F. Terfelt, Nature Astronomy **1**, 0035 (2017).

[158] V. Zappalà, A. Cellino, A. dell'Oro, and P. Paolicchi, in *Asteroids III* (a, 2002) pp. 619–631.

[159] V. Zappalà and A. Cellino, in *Astrophysics and Space Science Library*, Astrophysics and Space Science Library, Vol. 261, edited by M. Y. Marov and H. Rickman (2001) pp. 303–321.

[160] W. F. Bottke, M. Brož, D. P. O'Brien, A. Campo Bagatin, A. Morbidelli, and S. Marchi, in *Asteroids IV* (a, 2015) pp. 701–724.

[161] F. Spoto, A. Milani, and Z. Kneevi, Icarus **257**, 275 (2015).

[162] J. R. Masiero, F. E. DeMeo, T. Kasuga, and A. H. Parker, in *Asteroids IV* (a, 2015) pp. 323–340.

[163] B. Novaković, D. Vokrouhlický, F. Spoto, and D. Nesvorný, Celestial Mechanics and Dynamical Astronomy **134**, 34 (2022), arXiv:2205.06340 [astro-ph.EP] .

[164] P. Farinella and D. R. Davis, Icarus **97**, 111 (1992).

[165] V. Zappalà, A. Cellino, A. Dell'oro, F. Migliorini, and P. Paolicchi, Icarus **124**, 156 (1996).

[166] D. Nesvorný, M. Brož, and V. Carruba, in *Asteroids IV* (a, 2015) pp. 297–321.

[167] V. Carruba, D. Vokrouhlick, and B. Novakovi, Planetary and Space Science **157**, 72 (2018).

[168] F. Migliorini, V. Zappalà, R. Vio, and A. Cellino, Icarus **118**, 271 (1995).

[169] D. Lazzaro, T. Mothé-Diniz, J. M. Carvano, C. A. Angeli, A. S. Betzler, M. Florczak, A. Cellino, M. Di Martino, A. Doressoundiram, M. A. Barucci, E. Dotto, and P. Bendjoya, Icarus **142**, 445 (1999).

[170] A. Cellino, Space Science Reviews **92**, 397 (2000).

[171] M. J. Gaffey, T. H. Burbine, and R. P. Binzel, Meteoritics **28**, 161 (1993).

[172] V. Zappalà, P. Bendjoya, A. Cellino, M. Di Martino, A. Doressoundiram, A. Manara, and F. Migliorini, Icarus **145**, 4 (2000).

[173] V. Zappala, A. Cellino, P. Farinella, and Z. Knezevic, Astronomical Journal **100**, 2030 (1990).

[174] A. Parker, . Ivezi, M. Juri, R. Lupton, M. Sekora, and A. Kowalski, Icarus **198**, 138 (2008).

[175] V. Carruba, S. Aljbaae, and A. Lucchini, Monthly Notices of the Royal Astronomical Society **488**, 1377 (2019).

[176] V. Carruba, S. Aljbaae, R. C. Domingos, A. Lucchini, and P. Furlaneto, Monthly Notices of the Royal Astronomical Society **496**, 540 (2020), https://academic.oup.com/mnras/article-pdf/496/1/540/33396415/staa1463.pdf .

[177] K. J. Walsh, M. Delb, W. F. Bottke, D. Vokrouhlick, and D. S. Lauretta, Icarus **225**, 283 (2013).

[178] T. R. Holt, J. Horner, D. Nesvorn, R. King, M. Popescu, B. D. Carter, and C. C. E. Tylor, Monthly Notices of the Royal Astronomical Society **504**, 1571 (2021), https://academic.oup.com/mnras/article-pdf/504/2/1571/37412619/stab894.pdf .

[179] B. Novakovi, C. Maurel, G. Tsirvoulis, and Z. Kneevi, The Astrophysical Journal Letters **807**, L5 (2015).

[180] V. Carruba and D. Nesvorn, Monthly Notices of the Royal Astronomical Society **457**, 1332 (2016), https://academic.oup.com/mnras/article-pdf/457/2/1332/2907110/stw043.pdf .

[181] V. C. Lowry, D. Vokrouhlick, D. Nesvorn, and H. Campins, The Astronomical Journal **160**, 127 (2020).

[182] O. Golubov and D. J. Scheeres, The Astronomical Journal **157**, 105 (2019).

[183] O. Golubov, V. Unukovych, and D. J. Scheeres, The Astronomical Journal **162**, 8 (2021).

[184] M. Granvik, A. Morbidelli, D. Vokrouhlický, W. F. Bottke, D. Nesvorný, and R. Jedicke, Astronomy & Astrophysics **598**, A52 (2017).

[185] W. F. Bottke, D. D. Durda, D. Nesvorn, R. Jedicke, A. Morbidelli, D. Vokrouhlick, and H. F. Levison, Icarus **179**, 63 (2005).

[186] F. Marzari, A. Rossi, O. Golubov, and D. J. Scheeres, The Astronomical Journal **160**, 128 (2020).

[187] Vokrouhlicky, Icarus **148**, 118 (2000).

[188] D. Farnocchia, S. Chesley, D. Vokrouhlick, A. Milani, F. Spoto, and W. Bottke, Icarus **224**, 1 (2013).

[189] P. Michel, D. C. Richardson, D. D. Durda, M. Jutzi, and E. Asphaug, in *Asteroids IV* (a, 2015) pp. 341–354.

[190] W. F. Bottke, M. Brož, D. P. O'Brien, A. Campo Bagatin, A. Morbidelli, and S. Marchi, in *Asteroids IV* (a, 2015) pp. 701–724.

[191] A. Milani, Z. Kneevi, F. Spoto, A. Cellino, B. Novakovi, and G. Tsirvoulis, Icarus **288**, 240 (2017).

[192] A. Milani and P. Farinella, Nature **370**, 40 (1994).

[193] D. Nesvorný, J. Bottke, William F., L. Dones, and H. F. Levison, Nature **417**, 720 (2002).

[194] V. Zappala and A. Cellino, Celestial Mechanics and Dynamical Astronomy **54**, 207 (1992).

[195] Novaković and B. , Nature Astronomy **2**, 528 (2018).

[196] V. Zappal, A. Cellino, B. Gladman, S. Manley, and F. Migliorini, Icarus **134**, 176 (1998).

[197] P. Farinella and D. Vokrouhlick, Science **283**, 1507 (1999), https://www.science.org/doi/pdf/10.1126/science.283.5407.1507 .

[198] D. Nesvorn, D. Vokrouhlick, A. Morbidelli, and W. F. Bottke, Icarus **200**, 698 (2009).

[199] W. F. Bottke, D. Vokrouhlick, K. J. Walsh, M. Delbo, P. Michel, D. S. Lauretta, H. Campins, H. C. Connolly, D. J. Scheeres, and S. R. Chelsey, Icarus **247**, 191 (2015).

[200] T. Gehrels, *Asteroids III* (University of Arizona Press, 2002).

[201] T. Gehrels, *Asteroids III* (University of Arizona Press, 2002).

[202] P. Pravec and A. W. Harris, Icarus **190**, 250 (2007).

[203] W. R. Johnston, NASA Planetary Data System , EAR-A-COMPIL-5-BINMP-V7.0 (2014).

[204] J. L. Margot, M. C. Nolan, L. A. M. Benner, S. J. Ostro, R. F. Jurgens, J. D. Giorgini, M. A. Slade, and D. B. Campbell, Science **296**, 1445 (2002).

[205] P. A. Taylor, E. S. Howell, M. C. Nolan, and A. A. Thane, in *AAS/Division for Planetary Sciences Meeting Abstracts #44*, AAS/Division for Planetary Sciences Meeting Abstracts, Vol. 44 (2012) p. 302.07.

[206] W. J. Merline, S. J. Weidenschilling, D. D. Durda, J. L. Margot, P. Pravec, and A. D. Storrs, in *Asteroids III* (a, 2002) pp. 289–312.

[207] K. S. Noll, W. M. Grundy, E. I. Chiang, J. L. Margot, and S. D. Kern, in *The Solar System Beyond Neptune*, edited by M. A. Barucci, H. Boehnhardt, D. P. Cruikshank, A. Morbidelli, and R. Dotson (a, 2008) pp. 345–363.

[208] C. R. Chapman, J. Veverka, P. C. Thomas, K. Klaasen, M. J. S. Belton, A. Harch, A. McEwen, T. V. Johnson, P. Helfenstein, M. E. Davies, W. J. Merline, and T. Denk, Nature **374**, 783 (1995).

[209] M. J. S. Belton, C. R. Chapman, P. C. Thomas, M. E. Davies, R. Greenberg, K. Klaasen, D. Byrnes, L. D'Amario, S. Synnott, T. V. Johnson, A. McEwen, W. J. Merline, D. R. Davis, J. M. Petit, A. Storrs, J. Veverka, and B. Zellner, Nature **374**, 785 (1995).

[210] W. J. Merline, L. M. Close, C. Dumas, C. R. Chapman, F. Roddier, F. Menard, D. C. Slater, G. Duvert, C. Shelton, and T. Morgan, Nature **401**, 565 (1999).

[211] D. D. Durda, Icarus **120**, 212 (1996).

[212] A. Doressoundiram, P. Paolicchi, A. Verlicchi, and A. Cellino, Planetary and Space Science **45**, 757 (1997).

[213] K. J. Walsh and S. A. Jacobson, in *Asteroids IV* (a, 2015) pp. 375–393.

[214] P. Pravec, P. Scheirich, P. Kušnirák, L. Šarounová, S. Mottola, G. Hahn, P. Brown, G. Esquerdo, N. Kaiser, Z. Krzeminski, D. P. Pray, B. D. Warner, A. W. Harris, M. C. Nolan, E. S. Howell, L. A. M. Benner, J. L. Margot, A. Galád, W. Holliday, M. D. Hicks, Y. N. Krugly, D. Tholen, R. Whiteley, F. Marchis, D. R. DeGraff, A. Grauer, S. Larson, F. P. Velichko, W. R. Cooney, R. Stephens, J. Zhu, K. Kirsch, R. Dyvig, L. Snyder, V. Reddy, S. Moore, Š. Gajdoš, J. Világi, G. Masi, D. Higgins, G. Funkhouser, B. Knight, S. Slivan, R. Behrend, M. Grenon, G. Burki, R. Roy, C. Demeautis, D. Matter, N. Waelchli, Y. Revaz, A. Klotz, M. Rieugné, P. Thierry, V. Cotrez, L. Brunetto, and G. Kober, Icarus **181**, 63 (2006).

[215] P. Pravec, P. Kusnirak, K. Hornoch, A. Galad, Y. N. Krugly, V. Chiorny, R. Inasaridze, O. Kvaratskhelia, V. Ayvazian, O. Parmonov, J. Pollock, S. Mottola, J. Oey, D. Pray, J. Zizka, J. Vrastil, I. Molotov, D. E. Reichart, K. M. Ivarsen, J. B. Haislip, and A. LaCluyze, IAU Circ. **9268**, 1 (2013).

[216] D. Vokrouhlický and D. Nesvorný, in *Asteroids, Comets, Meteors 2008*, LPI Contributions, Vol. 1405, edited by LPI Editorial Board (2008) p. 8157.

[217] D. J. Scheeres, Icarus **189**, 370 (2007).

[218] S. J. Weidenschilling, Icarus **44**, 807 (1980).

[219] D. J. Scheeres, Celestial Mechanics and Dynamical Astronomy **104**, 103 (2009).

[220] S. A. Jacobson and D. J. Scheeres, Astrophysical Journal Letters **736**, L19 (2011), arXiv:1104.4671 [astro-ph.EP] .

[221] S. A. Jacobson and D. J. Scheeres, Icarus **214**, 161 (2011), arXiv:1404.0801 [astro-ph.EP] .

[222] A. W. Harris, A. Galvez, W. Benz, A. Fitzsimmons, S. F. Green, P. Michel, G. Valsecchi, M. Paetzold, B. Haeusler, and I. Carnelli, in *36th COSPAR Scientific Assembly*, Vol. 36 (2006) p. 2002.

[223] A. F. Cheng, C. Reed, I. Carnelli, P. Michel, and S. Ulamec, in *46th Annual Lunar and Planetary Science Conference*, Lunar and Planetary Science Conference (2015) p. 1386.

[224] P. Michel, A. Cheng, M. Kppers, P. Pravec, J. Blum, M. Delbo, S. Green, P. Rosenblatt, K. Tsiganis, J. Vincent, J. Biele, V. Ciarletti, A. Hrique, S. Ulamec, I. Carnelli, A. Galvez, L. Benner, S. Naidu, O. Barnouin, D. Richardson, A. Rivkin, P. Scheirich, N. Moskovitz, A. Thirouin, S. Schwartz, A. Campo Bagatin, and Y. Yu, Advances in Space Research **57**, 2529 (2016).

[225] E. Dotto, V. Della Corte, M. Amoroso, I. Bertini, J. Brucato, A. Capannolo, B. Cotugno, G. Cremonese, V. Di Tana, I. Gai, S. Ieva, G. Impresario, S. Ivanovski, M. Lavagna, A. Lucchetti, E. Mazzotta Epifani, A. Meneghin, F. Miglioretti, D. Modenini, M. Pajola, P. Palumbo, D. Perna, S. Pirrotta, G. Poggiali, A. Rossi, E. Simioni, S. Simonetti, P. Tortora, M. Zannoni, G. Zanotti, A. Zinzi, A. Cheng, A. Rivkin, E. Adams, E. Reynolds, and K. Fretz, Planetary and Space Science **199**, 105185 (2021).

[226] S. D. Wolters, A. J. Ball, N. Wells, C. Saunders, and N. McBride, Planetary and Space Science **59**, 1506 (2011), arXiv:1107.4229 [astro-ph.EP] .

[227] K. J. Walsh and S. A. Jacobson, in *Asteroids IV* (a, 2015) pp. 375–393.

[228] S. Naidu, L. Benner, M. Brozovic, M. Nolan, S. Ostro, J. Margot, J. Giorgini, T. Hirabayashi, D. Scheeres, P. Pravec, P. Scheirich, C. Magri, and J. Jao, Icarus **348**, 113777 (2020).

[229] P. Scheirich and P. Pravec, Icarus **200**, 531 (2009).

[230] P. Michel, M. Kueppers, H. Sierks, I. Carnelli, A. F. Cheng, K. Mellab, M. Granvik, A. Kestil, T. Kohout, K. Muinonen, A. Nsil, A. Penttila, T. Tikka, P. Tortora, V. Ciarletti, A. Hrique, N. Murdoch, E. Asphaug, A. Rivkin, O. Barnouin, A. C. Bagatin, P. Pravec, D. C. Richardson, S. R. Schwartz, K. Tsiganis, S. Ulamec, and O. Karatekin, Advances in Space Research **62**, 2261 (2018), past, Present and Future of Small Body Science and Exploration.

[231] M. Arakawa, T. Saiki, K. Wada, K. Ogawa, T. Kadono, K. Shirai, H. Sawada, K. Ishibashi, R. Honda, N. Sakatani, Y. Iijima, C. Okamoto, H. Yano, Y. Takagi, M. Hayakawa, P. Michel, M. Jutzi, Y. Shimaki, S. Kimura, Y. Mimasu, T. Toda, H. Imamura, S. Nakazawa, H. Hayakawa, S. Sugita, T. Morota, S. Kameda, E. Tatsumi, Y. Cho, K. Yoshioka, Y. Yokota, M. Matsuoka, M. Yamada, T. Kouyama, C. Honda, Y. Tsuda, S. Watanabe, M. Yoshikawa, S. Tanaka, F. Terui, S. Kikuchi, T. Yamaguchi, N. Ogawa, G. Ono, K. Yoshikawa, T. Takahashi, Y. Takei, A. Fujii, H. Takeuchi, Y. Yamamoto, T. Okada, C. Hirose, S. Hosoda, O. Mori, T. Shimada, S. Soldini, R. Tsukizaki, T. Iwata, M. Ozaki, M. Abe, N. Namiki, K. Kitazato, S. Tachibana, H. Ikeda, N. Hirata, N. Hirata, R. Noguchi, and A. Miura, Science **368**, 67 (2020), https://www.science.org/doi/pdf/10.1126/science.aaz1701 .

[232] Y. Zhang, P. Michel, D. C. Richardson, O. S. Barnouin, H. F. Agrusa, K. Tsiganis, C. Manzoni, and B. H. May, Icarus **362**, 114433 (2021).

[233] A. F. Cheng, H. F. Agrusa, B. W. Barbee, A. J. Meyer, T. L. Farnham, S. D. Raducan, D. C. Richardson, E. Dotto, A. Zinzi, V. Della Corte, T. S. Statler, S. Chesley, S. P. Naidu, M. Hirabayashi, J.-Y. Li, S. Eggl, O. S. Barnouin, N. L. Chabot, S. Chocron, G. S. Collins, R. T. Daly, T. M. Davison, M. E. DeCoster, C. M. Ernst, F. Ferrari, D. M. Graninger, S. A. Jacobson, M. Jutzi, K. M. Kumamoto, R. Luther, J. R. Lyzhoft, P. Michel, N. Murdoch, R. Nakano, E. Palmer, A. S. Rivkin, D. J. Scheeres, A. M. Stickle, J. M. Sunshine, J. M. Trigo-Rodriguez, J.-B. Vincent, J. D. Walker, K. Wünnemann, Y. Zhang, M. Amoroso, I. Bertini, J. R. Brucato, A. Capannolo, G. Cremonese, M. Dall'Ora, P. J. D. Deshapriya, I. Gai, P. H. Hasselmann, S. Ieva, G. Impresario, S. L. Ivanovski, M. Lavagna, A. Lucchetti, E. M. Epifani, D. Modenini, M. Pajola, P. Palumbo, D. Perna, S. Pirrotta, G. Poggiali, A. Rossi, P. Tortora, M. Zannoni, and G. Zanotti, Nature **616**, 457 (2023), arXiv:2303.03464 [astro-ph.EP] .

[234] K. Kitazato, M. Abe, H. Mito, K. Tarusawa, T. Soyano, S. Nishihara, and Y. Sarugaku, in *Lunar and Planetary Science Conference*, Lunar and Planetary Science Conference, edited by S. Mackwell and E. Stansbery (2004) p. 1623.

[235] F. Usui, T. Kasuga, S. Hasegawa, M. Ishiguro, D. Kuroda, T. G. Müller, T. Ootsubo, and H. Matsuhara, The Astrophysical Journal **762**, 56 (2013), arXiv:1211.2889 [astro-ph.EP] .

[236] E. G. Fahnestock, A. F. Cheng, S. Ivanovski, P. Michel, S. D. Raducan, A. Rossi, P. A. Abell, S. Chesley, E. Dotto, F. Ferrari, L. Kolokolova, E. Kramer, J.-Y. Li, S. R. Schwartz, S. Soldini, G. Tancredi, A. C. Bagatin, and Y. Zhang, The Planetary Science Journal **3**, 206 (2022).

[237] K. J. Walsh, D. C. Richardson, and P. Michel, in *Asteroids, Comets, Meteors 2008*, LPI Contributions, Vol. 1405, edited by LPI Editorial Board (2008) p. 8138.

[238] P. Snchez and D. J. Scheeres, The Astrophysical Journal **727**, 120 (2011).

[239] M. Hirabayashi, F. Ferrari, M. Jutzi, R. Nakano, S. D. Raducan, P. Snchez, S. Soldini, Y. Zhang, O. S. Barnouin, D. C. Richardson, P. Michel, E. Dotto, A. Rossi, and A. R. Rivkin, The Planetary Science Journal **3**, 140 (2022).

[240] B. E. Clark, B. Hapke, C. Pieters, and D. Britt, in *Asteroids III* (a, 2002) pp. 585–599.

[241] C. R. Chapman, Annual Review of Earth and Planetary Sciences **32**, 539 (2004).

[242] P. Vernazza, R. P. Binzel, A. Rossi, M. Fulchignoni, and M. Birlan, Nature **458**, 993 (2009).

[243] D. Nesvorn, W. F. Bottke, D. Vokrouhlick, C. R. Chapman, and S. Rafkin, Icarus **209**, 510 (2010).

[244] F. E. DeMeo, M. Marsset, D. Polishook, B. J. Burt, R. P. Binzel, S. Hasegawa, M. Granvik, N. A. Moskovitz, A. Earle, S. J. Bus, C. A. Thomas, A. S. Rivkin, and S. M. Slivan, Icarus **389**, 115264 (2023).

[245] S. Hasegawa, T. Hiroi, K. Ohtsuka, M. Ishiguro, D. Kuroda, T. Ito, and S. Sasaki, Publications of the Astronomical Society of Japan **71**, 103 (2019), https://academic.oup.com/pasj/article-pdf/71/5/103/54667662/pasj_71_5_103.pdf .

[246] D. A. Kiersz, S. F. Green, A. S. Rivkin, A. Fitzsimmons, and T. Seccull, in *7th IAA Planetary Defense Conference* (2021) p. 194.

[247] R. P. Binzel, A. S. Rivkin, J. S. Stuart, A. W. Harris, S. J. Bus, and T. H. Burbine, Icarus **170**, 259 (2004).

[248] J. de León, J. Licandro, R. Duffard, and M. Serra-Ricart, Advances in Space Research **37**, 178 (2006).

[249] J. de León, J. Licandro, M. Serra-Ricart, N. Pinilla-Alonso, and H. Campins, Astronomy & Astrophysics **517**, A23 (2010).

[250] T. L. Dunn, T. H. Burbine, W. F. Bottke, and J. P. Clark, in *44th Annual Lunar and Planetary Science Conference*, Lunar and Planetary Science Conference (2013) p. 1197.

[251] J.-Y. Li, M. Hirabayashi, T. L. Farnham, J. M. Sunshine, M. M. Knight, G. Tancredi, F. Moreno, B. Murphy, C. Opitom, S. Chesley, D. J. Scheeres, C. A. Thomas, E. G. Fahnestock, A. F. Cheng, L. Dressel, C. M. Ernst, F. Ferrari, A. Fitzsimmons, S. Ieva, S. L. Ivanovski, T. Kareta, L. Kolokolova, T. Lister, S. D. Raducan, A. S. Rivkin, A. Rossi, S. Soldini, A. M. Stickle, A. Vick, J.-B. Vincent, H. A. Weaver, S. Bagnulo, M. T. Bannister, S. Cambioni, A. Campo Bagatin, N. L. Chabot, G. Cremonese, R. T. Daly, E. Dotto, D. A. Glenar, M. Granvik, P. H. Hasselmann, I. Herreros, S. Jacobson, M. Jutzi, T. Kohout, F. La Forgia, M. Lazzarin, Z.-Y. Lin, R. Lolachi, A. Lucchetti, R. Makadia, E. Mazzotta Epifani, P. Michel, A. Migliorini, N. A. Moskovitz, J. Ormö, M. Pajola, P. Sánchez, S. R. Schwartz, C. Snodgrass, J. Steckloff, T. J. Stubbs, and J. M. Trigo-Rodríguez, Nature **616**, 452 (2023), arXiv:2303.01700 [astro-ph.EP] .

[252] T. Kareta, C. Thomas, J.-Y. Li, M. M. Knight, N. Moskovitz, A. Rożek, M. T. Bannister, S. Ieva, C. Snodgrass, P. Pravec, E. V. Ryan, W. H. Ryan, E. G. Fahnestock, A. S. Rivkin, N. Chabot, A. Fitzsimmons, D. Osip, T. Lister, G. Sarid, M. Hirabayashi, T. Farnham, G. Tancredi, P. Michel, R. Wainscoat, R. Weryk, B. Burrati, J. Pittichová, R. Ridden-Harper, N. J. Tan, P. Tristram, T. Brown, M. Bonavita, M. Burgdorf, E. Khalouei, P. Longa, M. Rabus, S. Sajadian, U. G. Jorgensen, M. Dominik, J.-B. Kikwaya, E. Mazzotta Epifani, E. Dotto, P. Deshapriya, P. Hasselmann, M. Dall'Ora, L. Abe, T. Guillot, D. Mékarnia, A. Agabi, P. Bendjoya, O. Suarez, A. Triaud, T. Gasparetto, M. N. Günther, M. Kueppers, B. Merin, J. Chatelain, E. Gomez, H. Usher, C. Stoddard-Jones, M. Bartnik, M. Bellaver, B. Chetan, E. Dugan, T. Fallon, J. Fedewa, C. Gerhard, S. A. Jacobson, S. Painter, D.-M. Peterson, J. E. Rodriguez, C. Smith, K. V. Sokolovsky, H. Sullivan, K. Townley, S. Watson, L. Webb, J. M. Trigo-Rodríguez, J. M. Llenas, I. Pérez-García, A. J. Castro-Tirado, J.-B. Vincent, A. Migliorini, M. Lazzarin, F. La Forgia, F. Ferrari, T. Polakis, and B. Skiff, Astrophysical Journal Letters **959**, L12 (2023), arXiv:2310.12089 [astro-ph.EP] .

[253] A. V. Filippenko, Publications of the Astronomical Society of the Pacific **94**, 715 (1982).

[254] M. Popescu, O. Vaduvescu, J. de León, R. M. Gherase, J. Licandro, I. L. Boacă, A. B. Şonka, R. P. Ashley, T. Močnik, D. Morate, M. Predatu, M. De Prá, C. Fariña, H. Stoev, M. Díaz Alfaro, I. Ordonez-Etxeberria, F. López-Martínez, and R. Errmann, Astronomy & Astrophysics **627**, A124 (2019), arXiv:1905.12997 [astro-ph.EP] .

[255] A. Izidoro, K. de Souza Torres, O. C. Winter, and N. Haghighipour, The Astrophysical Journal **767**, 54 (2013), arXiv:1302.1233 [astro-ph.EP] .

[256] B. Marty, G. Avice, Y. Sano, K. Altwegg, H. Balsiger, M. Hässig, A. Morbidelli, O. Mousis, and M. Rubin, Earth and Planetary Science Letters **441**, 91 (2016).

[257] M. Lazzarin, S. Marchi, S. Magrin, and J. Licandro, Monthly Notices of the Royal Astronomical Society **359**, 1575 (2005).

[258] A. Giunta, M. Giardino, E. Perozzi, G. Polenta, and A. Zinzi, in *European Planetary Science Congress* (2020) pp. EPSC2020–1047.

[259] E. Dotto, M. Banaszkiewicz, S. Banchi, M. A. Barucci, F. Bernardi, M. Birlan, B. Carry, A. Cellino, J. De Leon, M. Lazzarin, E. Mazzotta Epifani, J. Nomen Torres, D. Perna, E. Perozzi, P. Pravec, N. Sánchez Ortiz, C. Snodgrass, and C. Teodorescu, in *European Planetary Science Congress* (2020) pp. EPSC2020–949.

[260] A. Zinzi, A. Mediavilla, E. Dotto, E. Perozzi, M. Giardino, A. Giunta, B. Teodorescu, A. Flores-Garcia, D. Perna, V. Petropoulou, E. M. Epifani, and I. Di Pietro, in *2nd NEO and Debris Detection Conference* (2023) p. 83.

[261] T. Hromakina, M. Birlan, M. A. Barucci, M. Fulchignoni, F. Colas, S. Fornasier, F. Merlin, A. Sonka, S. Anghel, G. Poggiali, I. Belskaya, D. Perna, E. Dotto, E. Dotto, M. Banaszkiewicz, S. Banchi, M. A. Barucci, F. Bernardi, M. Birlan, B. Carry, A. Cellino, J. de Leon, M. Lazzarin, E. Mazzotta Epifani, A. Mediavilla, J. Nomen Torres, D. Perna, E. Perozzi, P. Pravec, C. Snodgrass, C. Teodorescu, S. Anghel, A. Bertolucci, F. Calderini, F. Colas, A. Del Vigna, A. Dell'Oro, A. di Cecco, L. Dimare, P. Fatka, S. Fornasier, E. Frattin, P. Frosini, M. Fulchignoni, R. Gabryszewski, M. Giardino, A. Giunta, T. Hromakina, J. Huntingford, S. Ieva, J. P. Kotlarz, F. La Forgia, J. Licandro, H. Medeiros, F. Merlin, F. Pinna, G. Polenta, M. Popescu, A. Rozek, P. Scheirich, A. Sergeyev, A. Sonka, G. B. Valsecchi, P. Wajer, A. Zinzi, and NEOROCKS Team, Monthly Notices of the Royal Astronomical Society **520**, 3143 (2023), arXiv:2302.01165 [astro-ph.EP] .

[262] J. Gradie and E. Tedesco, Science **216**, 1405 (1982).

[263] P. Vernazza, M. Marsset, P. Beck, R. P. Binzel, M. Birlan, R. Brunetto, F. E. Demeo, Z. Djouadi, C. Dumas, S. Merouane, O. Mousis, and B. Zanda, The Astrophysical Journal **806**, 204 (2015).

[264] M. Marsset, P. Vernazza, M. Birlan, F. DeMeo, R. P. Binzel, C. Dumas, J. Milli, and M. Popescu, Astronomy & Astrophysics **586**, A15 (2016), arXiv:1601.02405 [astro-ph.EP] .

[265] J. de León, N. Pinilla-Alonso, M. Delbo, H. Campins, A. Cabrera-Lavers, P. Tanga, A. Cellino, P. Bendjoya, J. Gayon-Markt, J. Licandro, V. Lorenzi, D. Morate, K. J. Walsh, F. DeMeo, Z. Landsman, and V. Alí-Lagoa, Icarus **266**, 57 (2016).

[266] D. S. Lauretta, S. S. Balram-Knutson, E. Beshore, W. V. Boynton, C. Drouet d'Aubigny, D. N. DellaGiustina, H. L. Enos, D. R. Golish, C. W. Hergenrother, E. S. Howell, C. A. Bennett, E. T. Morton, M. C. Nolan, B. Rizk, H. L. Roper, A. E. Bartels, B. J. Bos, J. P. Dworkin, D. E. Highsmith, D. A. Lorenz, L. F. Lim, R. Mink, M. C. Moreau, J. A. Nuth, D. C. Reuter, A. A. Simon, E. B. Bierhaus, B. H. Bryan, R. Ballouz, O. S. Barnouin, R. P. Binzel, W. F. Bottke, V. E. Hamilton, K. J. Walsh, S. R. Chesley, P. R. Christensen, B. E. Clark, H. C. Connolly, M. K. Crombie, M. G. Daly, J. P. Emery, T. J. McCoy, J. W. McMahon, D. J. Scheeres, S. Messenger, K. Nakamura-Messenger, K. Righter, and S. A. Sandford, Space Science Reviews **212**, 925 (2017), arXiv:1702.06981 [astro-ph.EP] .

[267] P. Scheirich and P. Pravec, The Planetary Science Journal **3**, 163 (2022).

Acknowledgments

Vorrei ringraziare tantissime persone, tutte le persone che hanno fatto parte di questo mio percorso, ormai concluso. Prima di ringraziare tutti, vorrei dire il "grazie" piú grande alle due persone che mi hanno permesso di essere qua, che mi hanno reso la persona che sono e ogni giorno non hanno mai smesso di essere qua con me. Mi hanno cresciuto, educato e insegnato a vivere la vita, facendomi credere che tutto é possibile, facendo vivere una parte di me con i piedi per terra e una parte volando in giro per il mondo. Negli ultimi anni, sono loro che sono stati vicino a me durante ogni mio momento della vita ed io continuo a volare per l'Universo sapendo che loro sono li che volano con me. Un grazie a mio nonno Favaro Orazio e a mia nonna Pierangela Cassanmagnago che avrebbero tanto voluto vedermi uscire da quell'aula con la corona d'alloro in testa, anche se in qualche modo sapevano giá che questo giorno sarebbe successo.

Ringrazio tutte le persone che mi hanno seguito durante la stesura della mia tesi. Un grazie alla mia relatrice Monica Lazzarin che mi ha seguito durante tutto il mio percorso di tesi e mi ha concesso tante opportunitá come osservare ad Asiago con il telescopio Copernico, la partecipazione a congressi fondamentali e l'osservazione al TNG delle Canarie. Ringrazio la mia correlatrice Fiorangela La Forgia che mi ha pure lei seguito durante la stesura della mia tesi e concesso l'opportunitá di partecipare ad eventi di divulgazione insieme. Un grande grazie al mio correlatore (per la seconda volta consecutiva) Paolo Ochner che in questi ultimi tre anni mi ha insegnato a usare i telescopi di Asiago, mi ha seguito durante le notti osservative, mi ha dato l'opportunitá di conoscere tantissime persone e aiutato in tantissimi progetti di divulgazione. Inoltre, lo ringrazio per tutte le esperienze che abbiamo passato assieme e per avermi seguito per la seconda volta alla stesura di una tesi. Ringrazio il mio relatore della triennale, Stefano Ciroi che mi ha presentato a Monica Lazzarin dandomi l'opportunitá di osservare per il loro gruppo, lo ringrazio anche per tutti gli insegnamenti dati durante i suoi corsi, nell'utilizzo dei telecopi di Asiago, nella riduzione dati, e per tutti i suoi consigli ricevuti. Ringrazio Andrea Reguitti per avermi seguito durante le osservazioni, per tutti i suoi insegnamenti sull'analisi dati, per le varie classificazione sulle Supernove e i consigli che mi ha dato durante il mio percorso universitario. Ringrazio Elisa Frattin e Alessandra Migliorini per i consigli ricevuti all'interno del gruppo di ricerca della mia tesi. Ringrazio Alessandro Siviero e Lina Tomasella per avermi permesso di osservare ad Asiago e avermi fatto partecipare nei loro progetti di divulgazione. Ringrazio Irene Albanese, Luca Cortese, Vittorio Andreoli e Stefano Fiscale per il supporto che mi hanno dato in questi 3 anni di osservazioni ad Asiago. Ringrazio Simone Zaggia per l'immagine della coda di Didymos, ma in particolare per avermi dato opportunitá nel campo della divulgazione astronomica. Ringrazio tutto il gruppo delle escape room "AsteroidAlert" per le belle esperienze passate insieme. Ringrazio Federico Manzini per l'aiuto nella stesura dell'atlante delle comete e le sue conoscenze. Ringrazio tutto il personale di Asiago, tecnici, custode, organizzatori e tutte le persone dell'universitá di Padova che mi hanno seguito e permesso di vivere questa bellissima esperienza, in atto ancora oggi.

Quando ho iniziato l'universitá, pensavo di intraprendere un percorso accademico, ma man mano che andavo avanti, mi sono reso conto che tutti gli esami, le conoscenze che apprendevo non erano la cosa piú importante. La bellezza di tutti questi sei anni, sono state le persone che ho conosciuto, le esperienze che ho fatto con loro; devo dire che ho avuto la

fortuna di conoscerne tante e vivere tantissime emozioni differenti. Mi piacerebbe ringraziarle tutte e dirgli ogni giorno grazie. Diamo sempre troppa importanza a quello che dobbiamo fare, a tutte le scadenze che gli altri ci danno e ci dimentichiamo di vivere e ringraziare le persone che sono state importanti e quelle che saranno importanti nella nostra vita. Vorrei partire dal principio perché li tutto é iniziato e io sono cosí grazie a tutte le persone che ho incontrato, e sono arrivato fino qui grazie a tutte loro che mi hanno permesso di conoscere chi sono e ogni giorno mi permettono di mostrarmi per quello che sono.

Un grazie enorme a tutta la mia famiglia, a mia mamma Patrizia Favaro e mio padre Loris Farina che mi hanno cresciuto e permesso di essere qua a Padova a vivere un'esperienza che sará indimenticabile per la mia vita. Vorrei anche ringraziarli per i loro insegnamenti e per l'educazione che mi hanno dato. Non dev'essere facile vedere un figlio partire, ma quando ti danno l'opportunitá di andare lontano da casa é perché sanno che hai un sogno, credono in te e che tu quel sogno possa realizzarlo. Prima pensavo che il mio sogno fosse questo: arrivare qua a scrivere i ringraziamenti e uscire da quell'aula, ma poi ho scoperto che la mia vita é un sogno e quando ho iniziato a vivere il mio sogno ogni giorno, tutto é diventato piú bello. Grazie a mio fratello Matteo Farina che mi ha accompagnato durante il mio cammino di vita. Nonostante, le nostre litigate di quando eravamo bambini, nulla puó togliere l'amore che lega due fratelli, un fratello che si mette a piangere e che mi abbraccia dopo non avermi visto per 5 mesi di quarantena covid. Ringrazio anche Giulia, la fidanzata di mio fratello, ormai parte della famiglia. Un grazie ai miei zii Stefania Farina, Gigi e Alessandro Frigerio per tutte le esperienze che abbiamo fatto insieme, per avermi accompagnato e creduto nel mio cammino. Un grazie a mia nonna Zemira Bellini e mio nonno Oscar Farina per avermi sostenuto nel mio percorso. Un grazie molto importante a Maurizio e Maurizia per essere entrati nella nostra famiglia ed essere vicini ai miei genitori. Un grazie davvero per essere diventate due persone importanti anche per la mia vita. Un grazie anche a mio cugino Matteo Colombo per tutte le risate che ci siamo fatti da bambini e poi avermi seguito durante le scuole medie. Un grazie a Marco, Graziella e a tutta la mia famiglia che mi ha seguito nel mio percorso.

Un grazie a tutti i miei amici d'infanzia, in particolare a Stefano Miotto. Dopo 18 anni di amicizia, Stefano é ancora qua vicino a me nel mio percorso, come da vero amico. Ringrazio tutte le mie maestre, professori ed educatori della mia infanzia che ancora oggi, ogni tanto, ricordo alcuni dei loro insegnamenti. Riporto solo un piccolo ricordo della mia maestra delle elementari Cristina che un giorno ci ha fatto pescare delle frasi motivazionali da un barattolo, a me era uscito: "non arrenderti mai" e da quel giorno non mi sono mai arreso, e ho portato sempre a termine le cose. Da quel giorno, mi sono detto: "per me l'impossibile sará possibile" e non smetteró mai di credere a queste parole. Anche se sono parole forti, non si puó mai dire a un bambino di smettere di credere alle sue idee.

Il prossimo grazie non é per una persona, ma per il luogo piú importante della mia vita: Santo Stefano Al Mare, un piccolissimo paese vicino a San Remo. Ogni anno ti ringrazio, ogni anno sono sempre tuo debitore, ogni anno mi fai scrivere e pensare tantissimo. Si dice che siano le persone a rendere speciale un luogo, e le persone che ho conosciuto a Santos sono sicuramente spettacolari, ma in questo caso anche il posto fa tanto e l'anno scorso ho verificato che questo posto é veramente speciale. Non ho ancora capito cosa sia cosí speciale, forse é perché da 13 anni lascio una parte di me e quando torno mi ritrovo, questo posto merita di essere ringraziato in questa tesi. Ringrazio Santo Stefano che ogni anno mi sopporta, mi fa vivere emozioni indimenticabili e soprattutto, mi fa essere completamente me stesso, una sensazione che auguro a tutti. Ringrazio tutte le persone che ho conosciuto a Santos, tutte quelle persone che mi hanno conosciuto per quello che sono e mi hanno accettato cosí. La maggior parte di queste persone sono ancora qua con me dopo 13 anni, molte di loro sono diventate pilastri fondamentali della mia vita. Un enorme grazie a Benedetta Bracci, una persona diventata fondamentale nella mia vita, una persona che in quinta elementare, mi ha guardato dicendomi: "tu sei una persona speciale". Non dimenticheró mai queste parole. Un grazie a Laura Moreno, dopo 10 anni di amicizia ci siamo ritrovati nella stessa universitá a Milano e di nuovo a Padova dove ti sei laureata due settimane fa. Un grazie enorme a Giorgia Nisi per essermi stata vicino e aver sempre creduto in me. Un grazie enorme a Simone Grillini che ancora oggi é qua a subire i miei dilemmi del fantacalcio. Un grazie anche a Sofia Pesce e Alessia Milone per tutti i momenti che abbiamo passato insieme. A Santos ho troppe persone da ringraziare, ringrazio Leonardo Ferrari, Claudia Ferrari, Leonardo Aragona, Viola Galli, Alice Pedalá, Mattia Saputo, Wilmer e Riccardo. Ringrazio tutte le persone dei nuovi gruppi di Davide Camnasio e Francesco Folloni conosciuti negli ultimi anni. Un grazie speciale anche a Elena Berruto e Giulio Meneghetti che mi hanno dato tantissimi consigli su come affrontare alcuni momenti della mia vita. Un grazie a tutti i genitori che mi vogliono bene e che continuano a credere in me come Paola, Alessandra, Ugo, Luca e a tutti quelli di cui mi sono dimenticato il nome. In particolare, vorrei ringraziare Franco Cavenaghi, una persona molto colta e intelligente che ha sempre creduto in me fin dall'inizio; quando gli parlavo di astronomia, sapeva sempre di cosa stessi parlando. Lo ringrazio per essermi stato vicino e aver creduto in me sempre, grazie davvero. Sicuro mi saró dimenticato qualcuno, ho conosciuto tantissime persone a Santos e ci vogliamo tutti bene, quindi vorrei dirvi grazie a tutti, sono qua grazie a voi, per molti anni siete stati la mia carica per l'anno a venire, grazie davvero. Grazie Santos e grazie per avermi fatto appassionare all'Universo.

Adesso, vorrei ringraziare due piccoli oggetti, il mio primo telescopio da 114 mm, per questo piccolo telescopio vorrei ringraziare ancora mia mamma che aveva due scelte come regalo di terza media: un cane o un telescopio. Tornando indietro, non so cosa sarebbe stato meglio, ma da lí a poco é diventato il mio migliore amico che ancora oggi mi accompagna qua a Padova. Vorrei ringraziare anche il mio secondo telescopio da 200 mm e scusarmi per aver trascurato quello piú piccolo, ma era bello aver l'opportunitá di osservare oggetti che prima non riuscivo a vedere. Vorrei ringraziare tutte le persone del gruppo astrofili di Villasanta (GAV) che mi hanno insegnato tantissimo. Ho fatto parte di questo gruppo per 7 anni e vorrei ringraziarli per tutte le conferenze del venerdí sera tenute ogni settimana, tutti i mesi dell'anno. Vorrei ringraziarli anche per tutte le serate osservative a cui mi hanno fatto partecipare con i miei due telescopi. In particolare, ringrazio i presidenti Marco Saini e Fausto Milani per la loro disponibilitá e immensa conoscenza che mi hanno donato. Ringrazio Luciano Tinelli per i suoi insegnamenti, sei stato il primo a spiegarmi come usare i vari dark, bias e flat e ora sono qua ad Asiago a usarli di routine. Ringrazio tutti i membri del gruppo. Un particolare ringraziamento ai membri del gruppo con cui sono andato a vedere le aurore boreali in Norvegia. Per ultimo, ma piú importante, ringrazio una persona che mi ha accolto subito benissimo e nel giro di poco tempo é diventato un secondo padre, Roberto Balocchi. Un secondo padre con cui mi sono divertito tanto, sempre presente nei momenti di difficoltá e che mi ha insegnato tanto, non solo sull'astronomia, ma anche sulla vita.

Ringrazio tutti i miei compagni delle superiori con cui sono cresciuto e maturato. Ringrazio tutti i miei professori delle superiori che mi hanno insegnato tanto, dandomi tante conoscenze, ma anche educato a livello didattico. Ringrazio la professoressa d'italiano Radi che mi ha aiutato tantissimo nel mio percorso scolastico e la ringrazio per tutte le volte che si fermava al pomeriggio ad aiutarmi e approfondire la sua materia. Una professoressa che ha sempre creduto in me e finite le superiori mi ha dato un bigliettino che ancora oggi porto con me: "un esempio di volontá e tenacia. Vedrai che l'esame andrá bene". Ringrazio la professoressa Cozza che, come la professoressa Radi, é stata fondamentale nel mio cammino scolastico. Ringrazio il mio professore di religione, Gibellato per tutte le esperienze passate con lui. Ringrazio la professoressa di fisica Malgrati e di scienze Consonni che con le loro conoscenze mi hanno preparato al mondo universitario e fatto amare queste bellissime materie. Il mio ringraziamento piú grande lo dedico a Virginia Salemi, nostra professoressa per un mese, nel giro di poco é diventata una delle persone piú importanti della mia vita, una seconda madre. Lei é sempre stata presente nei miei momenti di difficoltá, insegnandomi e aiutandomi tantissimo durante il periodo di fine scuola superiore e il mio percorso universitario. Vorrei ringraziarla anche per avermi sopportato e per tutte le esperienze fatte. Un immenso grazie a tre persone che sono diventate fondamentali per la mia vita, persone che puoi chiamare "amici veri", dovrei dire tantissime cose su di loro, ma non posso scrivere ringraziamenti piú lunghi della tesi: Jarno Campi, Ben Salem Sami e Riccardo De Marco. Tre persone molto diverse, ma con ognuna di esse ho vissuto esperienze bellissime, discorsi bellissimi e sono persone davvero importanti nella mia vita. Ringrazio la mia parrucchiera, Emanuela, per tutti i tagli diversi che le ho chiesto e i consigli ricevuti. Ho tante persone da ringraziare a Monza e le ringrazio tutte. Un grazie speciale a Gaia Colangelo che oltre ad avermi fatto conoscere per la prima volta l'amore e la sofferenza, ha sempre creduto in me e convincendomi a non iscrivermi ad economia e a continuare a seguire la mia passione: l'astronomia. Vorrei ringraziare tutte le persone che ho conosciuto all'interno del Jet, Mood e di JAN. In particolare, un grande grazie a Nicoló Allievi, una conoscenza iniziata al lavoro, a breve diventata una grande amicizia.

Ringrazio tutte le persone che ho conosciuto all'universitá di Milano, in particolare Matteo Lovato, Teresa La Morte, Benito Maciariello e Mattia Franco. Vorrei ringraziare un professore dell'universitá della Bicocca, Tommaso Tabarelli, oltre ad essere stato un professore molto colto, durante le sue lezioni mi ha insegnato a non mollare e a credere sempre nei miei sogni. Manca un'ultima persona conosciuta a Milano, un grazie speciale ed enorme a Lorenzo Fiaccadori, un ragazzo conosciuto a fisica, assieme ci siamo trasferiti all'universitá di Padova e iscritti ad astronomia.

E in poco tempo, siamo giá arrivati a Padova, ringrazio di nuovo Lorenzo Fiaccadori, un vero amico con cui ho vissuto 4 anni a Padova, abbiamo passato esperienze bellissime con tutti i nostri futuri amici. Ringrazio la prima persona che ho conosciuto a Padova, Giuseppe Vagnoni con cui si é formata una bella amicizia. Con lui, ho iniziato a giocare a calcetto a Padova, inoltre ringrazio tutte le persone che ogni settimana vengono a giocare con me. A Padova ci sono tante persone importanti e probabilmente non riusciró a scriverle tutte. In particolare, ringrazio Antonio Baggetta, Tania Machado, Sara Fogliacco e JP per essere diventate persone fondamentali per la mia vita, vi ringrazio per tutto il sostegno che mi date. Queste 4 persone sono punti di riferimento per la mia vita a Padova che non smetteró mai di ringraziare. Un grande grazie va dato a Santiago Javier che dopo avermi dato ripetizioni di analisi 3, é diventato un grande amico. Un altro grazie enorme lo do a Edoardo Fiesoli con cui ho passato tantissimi momenti insieme e vorrei personalmente ringraziarti per tutta la tua simpatia. Ringrazio anche Gianluca Morettini per le serate passate insieme e la sua simpatia in ogni cosa che dice; quando c'era Gianlu, tutti tornavano a casa con il sorriso. Vorrei ringraziare Roberto Balossi per essere diventato una persona importante sia all'universitá sia fuori. Grazie a te, ho risolto diversi dubbi e problemi che mi hanno permesso di superare gli esami. Un grazie anche a Gaia conosciuta un anno fa, ma che sta diventando una persona importante nella mia vita. Un grazie a tutte le persone con cui ho vissuto un'esperienza unica in Islanda. Un grazie ad Alessandra Mura aver condiviso assieme il nostro studio sugli oggetti del Sistema Solare e le osservazioni ad Asiago. Padova é diventata molto importante per me e vorrei ringraziare tutti, ringrazio quelli che non ho citato del gruppo dei Mocha (Gianmarco, Giuseppe, Emma, Maria, Enrico, Alexa e Vittoria), il gruppo di An Grappo (Alessia, Margherita, Linda, Bart, Martina, Ripalta, Simona, Vittorio e Vise), il gruppo Sbinnala (Federico, Sofia, Elena e Gabbo), il gruppo nuovo della magistrale (Daniele, Mattia, Ilaria, ecc), il gruppo del calcetto (Augusto, Leonardo, Joel, Matteo, ecc) e il gruppo dei dottorandi di Padova Irene Salmaso, Silvia Conforti e Biagio. Un grazie anche alle ultime persone conosciute come Nives, Meri, Ausilia, Simone e Fitim. Vorrei anche ringraziare delle persone che stanno diventando importanti da ottobre, i miei conquilini, ma ormai posso chiamarli amici: Carla, Paolo, Parisa, Silvia e Ale. Non mi sono dimenticato di quest'ultima persona che sto per citare. é diventata una delle persone piú importanti della mia vita, non solo per le esperienze, ma anche per gli insegnamenti e per le emozioni che mi ha fatto provare. Questa persona é riuscita a svestirmi da tutte le maschere che avevo iniziato ad indossare a Monza per farmi sentire accettato, ha tirato fuori l'Andrea Farina nascosto dentro di me. é riuscita ad aprirmi la mente e far uscire tutto quello che nascondevo facendomi provare emozioni e sentimenti profondi che difficilmente sarebbero usciti nella mia vita. Un grazie enorme per essermi stato vicino a Irene Albanese, un grazie per essere ancora qua e avermi sostenuto durante tutto il percorso universitario a Padova. Un grazie per tutte le esperienze che abbiamo vissuto e che vivremo, per tutti i discorsi, gli insegnamenti e le giornate/serate passate insieme. Sono sicuro di aver dimenticato alcune persone, ma tengo comunque a ringraziarvi anche se non ho scritto il vostro nome. Ringrazio inoltre tutti i genitori che ho conosciuto in questi ultimi anni e per i loro preziosi consigli che hanno arricchito il mio percorso. Padova é stata un'esperienza bellissima, un'esperienza unica, saró sempre debitore a questa cittá e a tutte le persone che la vivono, a tutte quelle persone che ogni giorno incontro e mi fanno sorridere.

Vorrei dedicare degli ultimi grazie, uno a Nova Cas 2021, una nova che mi ha fatto vivere un periodo speciale della mia vita e uno a Didymos, un asteroide che mi ha fatto appassionare a questo mondo dei NEAs. Un grazie speciale all'Universo, di cui mi sono innamorato e che ogni giorno mi fa alzare dal letto e mi fa battere forte il cuore. Un amore non platonico, ma reale e il suo essere misterioso mi porta a studiarlo giorno dopo giorno.

Questo é il mio percorso universitario, tutte queste persone hanno reso la mia universitá e la mia vita bella e serena. Quando qualcuno mi chiede cosa fai all'universitá, gli rispondo sempre che vivo l'universitá, gli esami non mi hanno dato molto, se non ansia. Tutte queste persone sono quello che hanno reso bella l'universitá, bello alzarsi dal letto per andare a viverle e io non smetteró mai di ringraziarle. L'avró giá ripetuto, ma queste persone mi hanno aiutato ad essere il ragazzo che sono, un ragazzo felice di vivere la sua vita serena alla scoperta di un Universo misterioso.

Per finire, vorrei ringraziare me stesso, vorrei ringraziare Andrea Farina che oltre ad aver vissuto momenti molto belli, ha lottato e sofferto per arrivare fino a qua e adesso ce l'ha fatta. Ce l'ha fatta a trovare una serenitá dentro di sé e a concludere questo percorso universitario. Ad Andrea Farina, vorrei dire grazie che ogni giorno si alza con il sorriso e cerca sempre di rendere felici le persone che lo circondano, ogni tanto trascurando sé stesso, vorrei dire grazie per avermi sostenuto in questi 25 anni di vita e aver avuto una forza immensa per essere arrivato qua. Vorrei ringraziarlo e dirgli che é forte, di continuare cosí e che anche i prossimi traguardi arriveranno e di mantenere questa serenitá trovata ultimamente. Gli auguro di essere sempre felice e continuare a vivere la vita come un sogno, un suo sogno, nel suo mondo.